Faculty of Materials Engineering, Silesian University of Technology, Poland

Faculty of Engineering and Architecture, Ghent University, Belgium

**Dissertation**

# Assessment of fracture development in thick-walled elements of power boilers after long-time operation

Author:

**Benard Kiptoo Kipsang**
MEng. (Hunan University, Changsha, China)
BEng. (Moi University, Eldoret, Kenya)

Promoter: dr hab. inż. Krzysztof Wacławiak
Co-promoter: prof. dr. ir. Wim De Waele

A thesis submitted in fulfilment of the requirements for the degree of Doctor of Philosophy (PhD) in Materials Engineering and Doctor of Engineering (PhD)

Katowice, April 2025

Refer to this dissertation as follows:

Kipsang, B.K. (2025). Thesis title. PhD thesis, Department of Material Technologies, Faculty of Materials Engineering, Silesian University of Technology, Poland and Department of Electromechanical and Metal Engineering, Faculty of Engineering and Architecture, Ghent University, Belgium.

| **Promoters** | **Author** |
|---|---|
| Krzysztof Wacławiak | Benard Kipsang |
| Wim De Waele | |

# DECLARATION

I do solemnly affirm that, except in instances where explicit acknowledgement has been provided, the intellectual content herein is solely the product of my PhD research that has been conducted exclusively since the start of my PhD studies under the supervision of Professor Krzysztof Wacławiak and Professor Wim De Waele. All editorial assistance has been duly acknowledged, and all ethical protocols and procedural guidelines have been adhered to with the utmost diligence. Additionally, I declare that this submission contains no material previously presented for the attainment of any academic qualification at any other institution. I acknowledge that barring explicit prior approval from Silesian University of Technology and Ghent University no portion of this scholarly work shall be submitted in any future qualification-seeking endeavor under my name.

The reproduction and publication of a digital form by the Silesian University of Technology and Ghent University will not violate any third-party rights, and I have not previously submitted it in its entirety or part for any qualification.

Benard Kiptoo Kipsang

# ACKNOWLEDGEMENTS

I express profound gratitude to Professor Krzysztof Wacławiak for accepting to be my supervisor and offering me the opportunity to study at Silesian University of Technology in Poland. His unwavering support, encouragement and guidance will always be in my mind. His ability to solve complex technical problems coupled with his boundless patience always kept me going through out my PhD thesis.

To my Ghent University supervisor prof. Wim De Waele, I extend my sincere appreciation for granting me an opportunity to pursue a joint PhD under his research group. His insights and experience in fracture mechanics provided invaluable input and the collaborative intellectual ecosystem that has made this work possible. I appreciate the indispensable contributions of Dr. Fahzad Farahani who facilitated the numerical simulation of this research and fine tuning of the digital Image correlation.

The efforts of the technical staff at SUT Mr. Bartos, along with Mr. Tonino and Mr. Sam at Ghent University ensured the specimens required for the empirical inquiry were available on time and well-machined. Their efforts, advice and experience ensured that this research had enough specimens and experiments to contribute to findings of this thesis.

Thanks, are also extended to the research groups I have attended who encouraged me, and many laughs. The moral support of my colleagues Dr. Goftila Sirata at SUT who gave me moral and professional support. Wangui at UGent was instrumental in ensuring I finished the research on time.

The Technical support and guidance of Mr. Robin Mote, Robin Departtere and Hassan in Instrumentation particularly on DCPD and DIC. They were always there to lend a hand when I needed help in Soete laboratory during my research visits. Gratitude is also addressed to many fellow researchers and PhD students at UGent and SUT.

# TABLE OF CONTENT

# LIST OF TABLES

LIST OF FIGURES

# LIST OF SYMBOLS AND ACRONYMS

| | |
|---|---|
| $\Delta a$ | Change in crack length |
| $\Delta a_{max}$ | Maximum crack growth |
| a | Crack or notch depth |
| $a_0$ | Initial flaw or notch depth |
| ASTM | American Society of Testing and Materials |
| AT | Arc-shaped tension |
| b | Remaining ligament thickness |
| B | Specimen thickness/width |
| $b_0$ | Initial remaining ligament ($W - a_0$) |
| BN | Net specimen thickness |
| BS | British standards |
| CCB | Circumferentially cracked bar |
| CMOD | Crack mouth opening displacement. |
| CT | Compact tension |
| CTOA | Crack tip opening angle |
| CTOD | Crack tip opening displacement. |
| CWPT | Curved-wide plate test |
| DCPD | Direct current potential drop |
| DENT | Double end notch tension |
| DIC | Digital image correlation |
| E | Young's modulus |
| FCG | Fatigue crack growth |
| FEA | Finite element analysis |
| FEM | Finite element modelling |
| FST | Full-scale test |
| G | Elastic energy release rate |
| GWe | GigWatt-electric |
| H | Daylight grip length |
| HAZ | Heat affected zone |
| HB | Brinell hardness |
| HRR | Hutchinson, Rice and Rosengren |
| ISO | International Organization for Standardization |
| J | J-integral |

| | |
|---|---|
| K | Stress intensity factor |
| LEFM | Linear elastic fracture mechanics |
| LLD | Load line-displacement |
| MT | Middle Tension |
| NTD | Non destructive testing |
| Q | Constrain parameter for J-Q theory |
| SBD | Strain based design |
| SEM | Scanning electron microscopy |
| SENB | Single edge notched bend specimen |
| SENT | Single edge notched tension specimen |
| SIF | Stress intensity factor |
| SUT | Silesian University of Technology |
| SWZ | Stretch width zone |
| TWh | TeraWatt-hour |
| UGent | Ghent University |
| W | Specimen width |
| $\delta$ | Stress |
| $\delta_{TC}$ | Sub-critical crack extension |
| $\delta_{Ti}$ | Crack initiation at 0.2 mm |
| $\eta$ | $\eta$ factor |
| $\nu$ | Poisson’s coefficient |

# SUMMARY

The global energy markets are transitioning from fossil fuels to renewable sources. However, the demand for conventional energy persists, with coal continuing to play a role in energy security. Over the next 10–15 years, a "transitional renaissance" of coal is anticipated. As power plants adapt to increased start-ups and shutdowns, components of power plants degrade due to ageing particularly under creep conditions, owing to this their structural integrity becomes a critical concern for safe operation and reliability.

This thesis studies the fracture behavior of material used in components of electricity-generating power plants after exposure to industry and laboratory ageing under high-temperature creep conditions. Its starts with an overview of the fracture mechanics field and power plant steel grade, their operating conditions, and a description of the degradation mechanisms that damage power plant systems and components. Experimental and numerical assessments were conducted on steel elements with over 100,000 operational hours to evaluate fracture toughness. The stress intensity factor (K) was analyzed using the arc tension specimen geometry. Effect of multiaxial stresses and mixed-mode fracture due to crack angle orientation or multi-axial stress are investigated. To overcome the limitations of traditional clip gauge method non-contact measurements by digital image correlation were used to measure fracture toughness under mixed-mode loading using SENT specimens.

Comprehensive experimental isothermal ageing and high-temperature accelerated creep degradation were carried out to examine the impact of ageing and thermal degradation on the trends of fracture resistance in power plant steel. Results indicate that fracture toughness varies across structural components, with the valve chamber exhibiting greater toughness than pipeline sections. A comparative analysis of SENT and AT specimens provided further insights into fracture behavior under different conditions. The study emphasizes the need for additional structural integrity assessments, such as finite element analysis (FEA) combined with creep and high-temperature testing, to predict remaining service life and enhance safety measures.

This research offers critical insights into the effect of creep and isothermal ageing on the durability of components in electricity-generating boilers, aiding decision-makers in assessing load-carrying capacity, potential hazards, and maintenance strategies. Furthermore, the study employs advanced experimental and numerical methods to assess fracture toughness. The research compares as received and degraded samples. The artificial ageing was achieved through laboratory accelerated creep and isothermal ageing, simulating actual power plant operating conditions. Three stages of degradation and a minimum of three crack tilt angles were examined to provide a comprehensive understanding of fracture behavior.

In addition to fracture mechanics, supplementary material characterization techniques, including hardness testing, microstructural analysis, Charpy impact testing, and fractography, were utilized to get more insights into fracture behaviour after degradation. The combination of full-size AT, SENT, and SENB specimens, along with numerical simulations, provided valuable insights into the fracture properties of heat-resistant steel after prolonged operation. Although it is beyond the scope of this thesis, the hope is that this work will assist in making informed decisions regarding the extension or upgrading of power plant components. The thesis concludes with a summary of main findings and suggestions for future research.

# STRESZCZENIE

Na światowym rynku energii obserwuje się przechodzenie z paliw kopalnych na źródła odnawialne. Jednak popyt na energię ze źródeł konwencjonalnych utrzymuje się, a węgiel nadal odgrywa znaczącą rolę w zapewnieniu bezpieczeństwa energetycznego. W ciągu najbliższych 10-15 lat spodziewany jest „przejściowy renesans" węgla. Ponieważ elektrownie dostosowują się do zwiększonej liczby rozruchów i odstawień, pogarszanie właściwości materiału, szczególnie w warunkach pełzania, staje się problemem przy ocenie bezpiecznej eksploatacji i przewidywaniu trwałości części i elementów bloków energetycznych.

Niniejsza rozprawa ma na celu zbadanie charakterystyki pękania wybranego materiału stosowanego w blokach elektrowni wytwarzających energię elektryczną, po długim okresie eksploatacji w warunkach pełzania w wysokiej temperaturze. Eksperymentalne i numeryczne badanie zostało przeprowadzone na elementach stalowych o ponad 100 000 godzinach pracy w celu oceny odporności na pękanie. Współczynnik intensywności naprężenia został przeanalizowany przy użyciu geometrii rozciąganej próbki łukowej.

Konstrukcje inżynierskie podlegają pękaniu w trybie mieszanym ze względu na orientację kąta pęknięcia lub istniejące naprężenie wieloosiowe. W związku z tym właściwe jest zbadanie zachowania i mechanizmu pękania stali żaroodpornej pod obciążeniem w trybie mieszanym. Bezkontaktowe pomiary za pomocą cyfrowej korelacji obrazu zostały wykorzystane do pomiaru odporności na pękanie pod obciążeniem w trybie mieszanym przy użyciu próbek SENT.

Przeprowadzono kompleksowe eksperymentalne starzenie izotermiczne i przyspieszoną degradację poprzez pełzanie w wysokiej temperaturze, w celu zbadania wpływu starzenia i degradacji termicznej na zmianę odporności na pękanie stali kotłowej.

Wyniki wskazują, że odporność na pękanie różni się w zależności od elementów konstrukcyjnych, przy czym komora zaworu wykazuje większą wytrzymałość niż sekcje rurociągu. Analiza porównawcza próbek SENT i AT dostarczyła dalszych informacji na temat zachowania podczas pękania w różnych warunkach. Wyniki badania wskazują na potrzebę dodatkowej oceny wytrzymałościowej, takiej jak analiza elementów skończonych (MES) w połączeniu z testami pełzania i testami wysokotemperaturowymi, w celu przewidywania pozostałej trwałości elementów kotła oraz poprawy jego bezpieczeństwa użytkowania.

Badania te prezentują krytyczny wgląd w trwałość kotłów wytwarzających energię elektryczną, pomagając operatorom kotłów w ocenie nośności, potencjalnych zagrożeń i strategii konserwacji. Charakteryzując degradację materiału poprzez równowagową analizę metalurgiczną, wyniki badań przyczyniają się do zapewnienia odporności bloków energetycznych w obliczu zmieniających się przemian w sektorze energetycznym.

Ponadto czynią opisane badania wykorzystując zaawansowane metody eksperymentalne i numeryczne do oceny obniżenia odporności na pękanie stali 14MoV6-3, kluczowego, tradycyjnego materiału w wielu istniejących elektrowniach. W pracy przebadano materiał w stanie nowym oraz zdegradowane poprzez przyspieszone pełzanie i starzenie izotermiczne, symulujące rzeczywiste warunki pracy. Zbadano trzy etapy degradacji i co najmniej trzy kąty nachylenia karbu, aby zapewnić kompleksowe zrozumienie zachowania podczas pękania.

Oprócz mechaniki pękania zastosowano dodatkowe techniki charakteryzacji materiału, w tym testy twardości, analizę mikrostrukturalną, testy udarności Charpy'ego i fraktografię. Połączenie pełnowymiarowych próbek AT, SENT i SENB, wraz z symulacjami numerycznymi, dostarczyło cennych informacji na temat właściwości pękania stali żaroodpornej po długotrwałej eksploatacji.

Chociaż wykracza to poza zakres niniejszej rozprawy, mam nadzieję, że praca ta pomoże w podejmowaniu świadomych decyzji dotyczących rozbudowy lub modernizacji bloków energetycznych elektrowni cieplnych.

# SAMENVATTING

De wereldwijde energiemarkten stappen over van fossiele brandstoffen naar hernieuwbare bronnen. De vraag naar conventionele energie blijft echter bestaan en steenkool blijft een rol spelen in de energiezekerheid. Voor de komende 10-15 jaar wordt een “overgangsrenaissance” van steenkool verwacht. Naarmate energiecentrales zich aanpassen aan meer opstarten en uitschakelen, wordt de degradatie van materiaaleigenschappen, vooral onder kruipomstandigheden, een kritisch punt van zorg voor een veilige werking en het voorspellen van de levensduur van componenten.

Dit proefschrift bestudeert het breukgedrag en de restlevensduur van materialen die worden gebruikt in componenten van elektriciteitscentrales na blootstelling aan veroudering in de industrie en het laboratorium onder kruipomstandigheden bij hoge temperatuur. Experimentele en numerieke beoordelingen werden uitgevoerd op stalen elementen met meer dan 100.000 bedrijfsuren om de breuktaaiheid te evalueren. De spanningsintensiteitsfactor (K) werd geanalyseerd met behulp van de geometrie van het boogspanningsmonster.

Technische constructies zijn onderhevig aan mixed-mode breuk als gevolg van scheurhoekoriëntatie of multi-axiale spanning. Daarom is het zinvol om het breukgedrag en -mechanisme van staal van krachtcentrales onder gemengde belasting te bestuderen. Contactloze metingen door digitale beeldcorrelatie werden gebruikt om de breuktaaiheid te meten onder gemengde belasting met behulp van SENT proefstukken.

Uitgebreide experimentele isotherme veroudering en versnelde kruipdegradatie bij hoge temperatuur werden uitgevoerd om de invloed van veroudering en thermische degradatie op de trends van breukbestendigheid in staal van energiecentrales te onderzoeken.

De resultaten geven aan dat de breuktaaiheid varieert over structurele componenten, waarbij de klepkamer een grotere taaiheid vertoont dan pijpleidingsecties. Een vergelijkende analyse van SENT en Arc-Shaped Tension (AT) specimens gaf meer inzicht in breukgedrag onder verschillende omstandigheden. Het onderzoek benadrukt de noodzaak van aanvullende structurele integriteitsbeoordelingen, zoals eindige-elementenanalyse (FEA) in combinatie met kruip- en hoge temperatuurtesten, om de resterende levensduur te voorspellen en veiligheidsmaatregelen te verbeteren.

Dit onderzoek biedt cruciale inzichten in de duurzaamheid van ketels die elektriciteit opwekken en helpt besluitvormers bij het beoordelen van de belastbaarheid, potentiële gevaren en onderhoudsstrategieën. Door materiaaldegradatie te karakteriseren met behulp van metallurgische analyse dragen de bevindingen bij aan het waarborgen van de veerkracht van energiecentrales tijdens de veranderende energietransities.

Verder maakt het onderzoek gebruik van geavanceerde experimentele en numerieke methoden om de degradatie van breuktaaiheid te beoordelen in 14MoV6-3 staal, een belangrijk materiaal in energiecentrales. Het onderzoek onderzoekt de huidige en gedegradeerde toestanden door versnelde kruip en isotherme veroudering, waarbij echte bedrijfsomstandigheden worden gesimuleerd. Drie stadia van degradatie en een minimum van drie scheurneigingshoeken werden onderzocht om een uitgebreid begrip te krijgen van breukgedrag.

Naast breukmechanica werden aanvullende materiaalkarakteriseringstechnieken gebruikt, waaronder hardheidstesten, microstructuuranalyse, Charpy-kerfslagproeven en fractografie. De combinatie van

AT, SENT- en SENB-exemplaren op ware grootte, samen met numerieke simulaties, gaven waardevolle inzichten in de breukeigenschappen van hittebestendig staal na langdurig gebruik.

Hoewel het buiten het bereik van dit proefschrift valt, hoopt men dat dit werk zal helpen bij het nemen van weloverwogen beslissingen over de uitbreiding of opwaardering van onderdelen van energiecentrales

# CHAPTER 1: INTRODUCTION, AIMS, OBJECTIVES AND SCOPE.

Fracture toughness refers to the resistance of brittle materials against the propagation of flaws when subjected to an applied stress. This concept posits that as the length of a flaw increases, the amount of stress required to induce fracture decreases. The material fracture toughness plays a critical role in determining the extent to which a flaw can lead to fracture [1]. The thickness of a component plays a pivotal role in determining the constraint conditions at the crack tip, with thinner components exhibiting plane stress conditions and thicker components displaying plane strain conditions.

Fracture has been a persistent issue for society since man discovered man-made structures [2]. One of the earliest recorded premature fractures in load-bearing structures is found in the Code of Hammurabi, established around 1754 BC by Hammurabi, the sixth king of the First Babylonian Dynasty, who ruled from 1792 BC to 1750 BC. However, the Code of Hammurabi did not offer any objective criteria to prevent structural failures and, instead, implicitly encouraged excessive overdesign [3]. It was not until the 1960s, when Irwin carried out extensive studies on crack-tip plasticity, contributing significantly to the development of the "Fracture Mechanics" discipline as is popularly known [4].

Many technological constraints have been overcome as engineering failure technologies have grown throughout time, the world's electricity supply is dominated by thermal power. Regulations are aimed to ensure that high-pressure power facilities operating at extreme temperatures have a sufficiently extended lifespan. The power station boiler's life and availability are determined by the state of its components under the most extreme temperature and stress conditions, which might cause damage or destruction sooner than others. Long-term use of high-temperature materials in power plant boilers can result in varying levels of creep, fatigue, and creep-fatigue coupling damage. Extreme conditions, such as high temperature, pressure, and tension fluctuations, can endanger the unit as shown in ruptured boiler tube in Figure 1(a) [5]. Approximately 70,000 hours of operation at a temperature of 540 °C caused damage to the welding that connected the collector to the communication tubes as shown in Figure 1 (b).

Crack formation is a severe concern for the structural integrity of power boiler components during their service life. Due to harsh operating conditions of cyclic thermomechanical stresses after prolonged periods of operation, fractures may form at areas of stress concentrations [6]. Such boiler failures can be caused by a variety of damage processes. This comprises failures caused by corrosion, graphitization, erosion, creep, and overheating [7].

Several studies have recently reported on failure cases in electric power facilities. Leakage caused by crack development of boiler tubes, especially superheater and re-heater tubes, is a major reason for boiler shutdown and withdrawal from the network [8]. For example, flat plate ends are a popular choice for pressure boilers since they are less expensive than dished ends. They are best suited for vessels with thicker walls, boilers with lower internal diameters, and pipes with non-circular cross sections. These flat boiler heads are less expensive and easier to manufacture than standard ellipsoidal heads but have a disadvantage of high-stress concentration at the pipe shell-flat plate cover junction [9].The presence of cracks or crack-like flaws in elements of power boilers can shorten their lifespan or cause catastrophic failure [10]. Regular boiler maintenance is required to prevent unexpected shutdowns [11].

FIGURE 1: Ruptured boiler tube (a) [5], damage to the welding that connected the collector to the communication tubes (b) [12].

Time-lasting creep alters the structure of the material so its properties. Combined with continuous high-temperature operation it cause changes in steel structure, including ferrite and pearlite composition [13]. Long-term high-temperature operation leads to increased carbide formation and coagulation, resulting in increased dislocation mobility, material creep, and changes in mechanical properties. Additionally, thermo-mechanical fatigue plays an important role [14]. To maintain the safe operation of power systems and to meet manufacturing requirements, suitable diagnostics for assessing the degradation of materials used in pressurized components are required. In installations that have outlived the expected working time of 100,000 hours—a milestone previously reached in Polish power plants in the 1980s—it is particularly important to preserve the integrity of materials functioning at temperature above critical levels. More than 90% of Poland's power plants are impacted by this situation; many of them have operated for more than 200,000 hours and are still planned for continuous usage [15].

With, and along with relaxation result in a complex history of operation. Fracture occurrence and growth have accompanied these processes since the beginning. As one may predict a lot of factors influence the service life of a component. Basic two are deformation caused by creep itself and the other is fracture occurrence and growth. Prediction of their relation is limited due to complexity of both. Some data are available from laboratory tests at normal or elevated temperature. Unfortunately, basic tests are uni-axial, whereas in real boilers it is always multi-axial. Fracture toughness measured by standards defines materials properties more closely than that of components, where the fracture occurs from multi-axial stress fields [7].

Power plants experience complex history of operation. The mechanical characteristics and structure of the material in its initial state and after service in the creep regime have been compared in several investigations. Internal flaws emerge because of structural alterations brought on by prolonged creep service. The material moves into the III creep stage, often known as fast creep, when generation processes and damage development occur.

Fractures initiate and grow during this this long complex history of operations. As one might expect, a variety of factors influence the service life of a component. The two basic types are creep-induced deformation and fracture incidence and growth. Because of their respective intricacy, their relationship is difficult to predict. Some data are available from laboratory testing conducted at normal or higher temperature. Unfortunately, basic tests are uniaxial, whereas actual boilers are always multiaxial. Fracture toughness assessed by standards is more closely related to material qualities than component properties, where fracture occurs due to multiaxial stress fields.

The threat of global warming has sparked an interest in finding methods for lowering $CO_2$ emissions. Because it produces a significant amount of $CO_2$, the energy industry has received special attention [16] . Steam turbines are used in fossil fuel-fired power stations to produce electricity. By raising the temperature and pressure of the steam entering the turbines, their thermodynamic efficiency may be enhanced. Following the Paris Agreement's ratification in December 2015 controls over greenhouse gas emissions have gained international attention [14].

Global attempts have been made to create steels that can be used in efficient fossil fuel-fired power plants. In this regard, ferritic alloys with a chromium content of 9 to 12 weight percent are the most promising materials, particularly for thick-walled parts like headers and boiler main steam pipes.

Studying the processes of defect accumulation and determining the primary fracture processes is essential because the long-term operation of the material may induce permanent changes in its structure, which may exacerbate the nucleation and accumulation of defects. Furthermore, altering the material's structure raises the possibility of an early fracture, necessitating the assessment of the fracture probability and facilitating the connection between the statistical properties and the material's fracture processes [17].

For the past several years, there haven't been many reported newly constructed units in the domestic power sector. It has forced electric energy producers to focus their primary efforts on keeping the current units operationally safe and available [18]. The findings of destructive testing, which is the focus of this study, on components after service provide the fundamental information source for the validation and growth of the materials database for the power sector.

The system for classifying structural alterations and internal damages resulting from extended service under creep conditions was created by the Institute for Ferrous Metallurgy, Gliwice, Poland. It is correlated with the life exhaustion extent, which is determined by the ratio of service time to time to destruction. This system enables the nondestructive matrix replica method to assess whether critical boiler elements are suitable for continued service [19] .

Considering the importance of power boilers in supplementing renewable sources, ensuring the safe use of conventional power units is related to the use of materials with mechanical properties that enable the transfer of high mechanical and thermal loads. It is essential to understand the fracture mechanisms of boiler steel after prolonged operation under multiaxial loading conditions through experimental studies. To replicate the actual operating conditions in power boilers, the material is artificially degraded in the laboratory, and its fracture toughness resistance is then measured.

Among these power units operated in Poland 90% have exceeded the design work time [20]. This time is calculated using the creep-rupture strength and based on a typical design time of 100,000 hours. Under 100,000 hours of operation, the creep is estimated to be in the primary and secondary stage. In primary stage, creep deformation is moderate and steady while dislocations accumulate. In the secondary stage, the creep rate accelerates as dislocations accumulate even more. After 100 thousand hours of operation, the commencement of the tertiary stage is predicted, and it is distinguished by fast acceleration of creep deformation, which frequently leads to material failure

[21] . Figure 2 depicts three stages of creep deformations. Creep increases significantly above 0.4 times the material's melting point. Even under continual stress, materials may gradually and constantly distort and ultimately fail because of thermal activation. Depending on the component, either deformation or fracture may limit the ultimate failure.

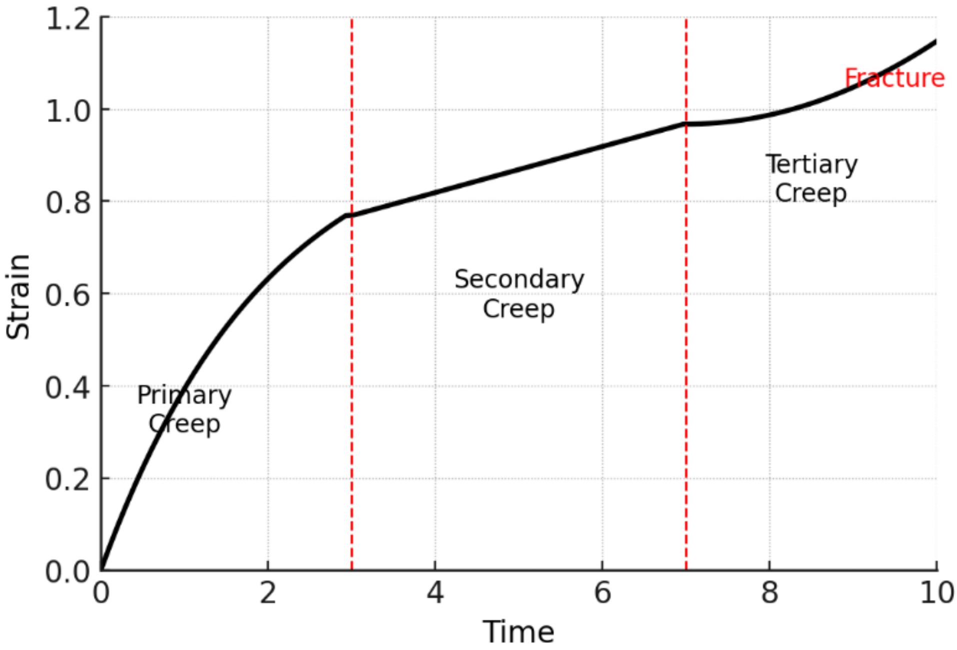

FIGURE 2: Stages of creep deformation [22].

In this period of paradigm shift in energy production from fossil fuels to renewable energy a steady power supply is essential for a functioning economy, able to meet the demands of industrialization. In December 2020, more than of Poland's electricity was generated from fossil raw resources, including hard coal, lignite, and gas as presented in Figure 3 [15]. Poland's energy transition is shifting away from coal, with renewables and gas playing an increasingly important role by 2050. However as presented in Figure 3 coal dependence is expected to continue in Poland past the year 2050 due to rising global energy demand, which cannot be met solely by non-fossil fuel sources [23]. Table 1 shows the changes and contributions of energy sources to electricity production (TWh) in Poland in 2019/2020 [24]. While alternative energy sources are expanding their contribution, which corresponds with global energy transitions towards more sustainable sources, the data indicates a small, less than 5% annual movement away from coal-based electricity production, notably hard coal, and lignite.

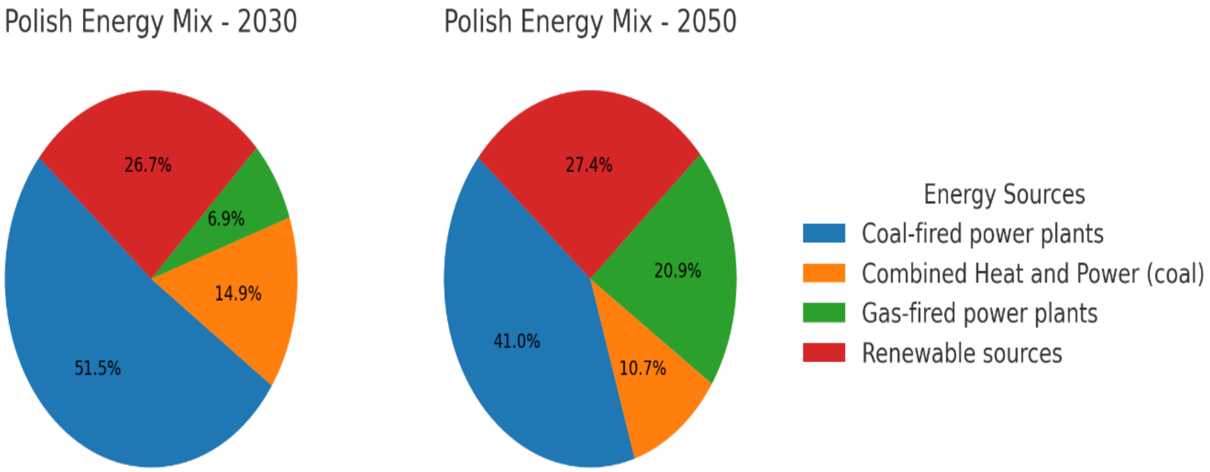

FIGURE 3: Forecasted energy generating capacities in Poland's energy mix for 2030 and 2050 (in GWe) [19].

Based on this there are significant challenges related to the wear and tear of power plant components that have been in operation for an extended period [25]. Given restricted economic opportunities, the integration of renewable energy sources such as wind and solar power plants within the existing systems is required for the continued operation of these power plants.

These changes lead to frequent equipment shutdowns, start-ups, and power generation oscillations, necessitating adaptation to the power demands of the plant. The ability to extend the service time over the intended work time, typically exceeding 200,000 hours, and recently even up to 350,000 hours, is the consequence of several safety features implemented at the design and manufacturing stage. To evaluate the current strength and durability of power installations, it is imperative to consider load variability issues, including the impact of loads on material fatigue life to a greater extent than was previously done during the design stage [26] .

TABLE 1 : Changes and contributions of energy sources to electricity production (TWh) in Poland in 2019/2020 [15]

| **Year** | **Total Production (TWh)** | **Hard Coal (TWh)** | **Lignite (TWh)** | **Other Sources (TWh)** |
|---|---|---|---|---|
| **2019** | 158.7 | 78.1 | 41.5 | 39.0 |
| **Share (%)** | 100 | 49.2 | 26.1 | 24.6 |
| **2020** | 152.3 | 71.5 | 37.9 | 42.7 |
| **Share (%)** | 100 | 46.9 | 24.9 | 28.0 |
| **Change (%)** | 95.9 | -4.8 | -4.8 | 12.3 |

In harsh conditions, creep-resistant steels need to remain dependable for extended periods. The significance of material integrity evaluation in the power generation business has been presented in [27] where leaks in boiler tubing caused approximately 20% loss of power production at power stations, leading to forced outages. The mechanical and creep properties, which are typically those of the virgin state (i.e., as-received condition), are the basis for power plant component design lifetimes. On the other hand, ageing in service might cause the actual material qualities to vary, and plant operating conditions could be altered to accommodate an unforeseen demand. Thus, it is essential to create high-quality databases of pertinent creep features for power plant life management and design. Extending plant life without compromising reliability is crucial, especially for essential components that are frequently exposed to harsh conditions. Crack growth monitoring systems have been devised that use quantified fracture to predict the remaining service life of steam boiler components, enabling advanced predictive maintenance.

Predicting and preventing component failures significantly improves the safety of power plant operations, protecting both personnel and infrastructure. Enhanced monitoring and predictive maintenance allow for more efficient resource use, scheduling maintenance based on actual component conditions rather than fixed intervals, leading to cost savings. Understanding the fracture mechanics and durability of components extends their service life, reducing the frequency of replacements and associated costs [28].

Extending the life of boiler components through better design and maintenance reduces the need for new parts, lowering resource consumption and waste. Preventing unplanned shutdowns and improving operational efficiency reduces emissions and the overall environmental footprint. Power plant operators benefit from predictive maintenance technologies and more dependable boiler components, which increase operational efficiency and safety. Materials testing facilities might use advanced testing processes to give more precise and dependable services. Component makers employ my research findings to create more durable and reliable parts. Existing maintenance techniques focus on time-based timetables and basic uniaxial testing, which fail to account for complicated multiaxial stress conditions. Figure 4 presents the pessimistic situation of the amount of coal that will be mined for power production in Poland in future. The graphic indicates a long-term reduction and eventual phase-out of lignite mining in Poland, most likely due to environmental restrictions, reduced reliance on coal, and increased use of renewable energy. Bełchatów, the largest producer, has a continuous decline but will remains operating the longest, due to inadequate implementation of diversification plans. Most of the lignite production will be used for electricity generation in the next 30-40 years [23]. While smaller mines will close earlier. The question arises by the year 2050 will the existing power plant infrastructure be structurally sound to be reliable for power generation? This research offers a more accurate assessment of fracture toughness by incorporating multiaxial stress fields and using both experimental and numerical methods. This leads to better real-world condition understanding and more reliable component life predictions.

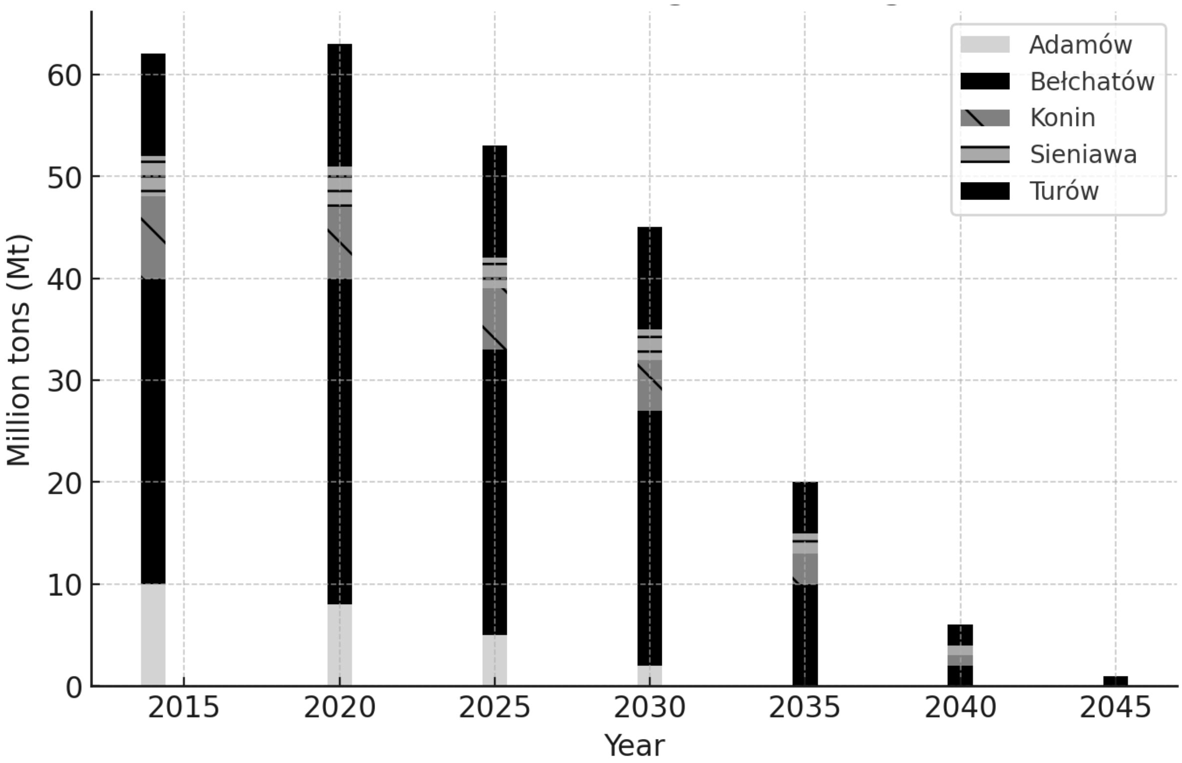

FIGURE 4: A pessimistic scenario for Polish lignite mining [24].

Microstructural changes have been widely used as a qualitative means of assessing the state of deterioration of the structural integrity of power steel components. The fracture behavior of the components is rarely examined. The experimental results produced in this research describe the crack propagation behavior of creep-resistant steel used in thermal power plants. Therefore, work can provide a means of determining the residual life of power plant components after long periods of operation.

### 1.1 Aims and Objectives

This research mainly aims to investigate and understand the effect of ageing caused by long time operation on fracture behavior of low alloy power boiler steel grades. To achieve this main objective Several specific objectives were set for this thesis. The specific objectives of this research are as follows.

1. To investigate the ageing mechanism of low alloy molybdenum vanadium power plant steel grade in boiler conditions after a long period of operation and imitate those conditions in laboratory set-up.
2. To understand the fracture behavior of power steel under mixed-mode loading and its applications to the structural integrity assessment.
3. Implement a reliable non-contact experimental method to determine ductile tearing resistance of power steel under various in-plane loading.
4. To investigate the mode mixity (i.e., loading combination) effect on the fracture resistance of mild steel and further identify the factors that influence the sensitivity of the fracture resistance of steel to mode mixity from the point of view of microstructure and material properties.
5. Investigate the relationship between ageing conditions and fracture toughness and discover the fracture resistance degradation mechanisms of creep-degraded power steel.
6. The investigate the difference between isothermal degradation and creep-degraded on loss of fracture toughness.

## 1.2 Scope and thesis layout

This research aims to investigate the effect of creep and thermal degradation on fracture characteristics of molybdenum vanadium low alloy steels. The scope of the research is summarized as follows:

1. This research uses chromium-molybdenum-vanadium (Cr-Mo-V) low alloy steel grade from Poland and the Czech Republic commercial and industrial markets and to some extend G17CrMoV5-10 (L17HMF) cast steel from decommissioned turbine. The steel grade conforms to Polish standard (PN-75/H-84024). Due to the differences in chemical components, fracture characteristics of other power plant steel grades may be significantly different.
2. This research investigates virgin as received, creep degraded, isothermal degraded and steel degraded in actual industrial conditions.
3. The experimental fracture toughness tests were done at room temperature. No tests were done at elevated or operating temperature of the studied material.
4. The classification of degradation and ageing level is based on creep properties of the steel grade found in the literature while the isothermal degradation is based on Arrhenius equation.
5. This research investigates steel under pure mode I and mixed-mode I/III loading. The effect of mode II is not studied.
6. SENT, SENB and AT specimen geometries were used for testing fracture.

The structure of this thesis is as follows:

**Chapter 2** establishes the theoretical framework applied in this research. The history, theoretical foundations and experimental methodology used in fracture toughness testing of low-constrained geometries are discussed. It provides a brief overview of ferritic-bainitic (pearlitic), martensitic, and austenitic steels used in power boiler pressure elements, including an overview of the properties and historical developments.

**Chapter 3** explores the relationship between fracture resistance, steel ageing, and geometry shape, reporting variation of fracture toughness in two parts experiencing different operation parameters and geometrical dimensions (valve and piping sections). Both experimental and numerical methods are applied.

**Chapter 4** presents a comprehensive experimental program investigating the fracture behavior of creep-resistant steel under mixed-mode loading. It examines the effect of crack tilt angle on fracture resistance and analyzes the sensitivity of the crack tilt angle to mode mixity.

**Chapter 5** applies the CTOD parameter to investigate effect of short term thermal creep on facture toughness. Additional material characterization techniques like Charpy V-Notch impact test and microstructural examination are used to get better insights on effect of ageing.

**Chapter 6** investigates the relationship between fracture resistance and the ageing of steel. Techniques of accelerated isothermal and accelerated creep ageing are presented. The effect of material degradation on ductile tearing resistance is reported.

**Chapter 7** concludes the thesis with key findings and recommendations for future research.

# CHAPTER 2: LITERATURE REVIEW

To accomplish the objectives and aims of this thesis, this foundation chapter gives a technical review of recent advancements in fracture mechanics theory and test methodologies for metallic materials. It also covers the principles of fracture mechanics and its role in structural integrity assessment. It introduces core concepts like SIF, J integral, CTOD, standardization, and recent breakthroughs in testing low-constrained geometries, which are the primary specimens used in the tests. The review discusses the most important fracture mechanics parameters employed in this thesis, the CTOD, from the fundamental concept and formulation to experimental estimation, test methodologies, and standardization processes. It also discussed the impact of long-term service and creep ageing on power plant steels like 14MoV6-3, P91, and P92.

## 2.1. Fracture Mechanics Principles

### Introduction

A fracture is the splitting of an object into two or more portions. Fracture toughness is a material property that describes the resistance of a material to fracture in the presence of flaws on the other hand yield strength of a metal is the amount of stress it can withstand before deforming. Fracture mechanics is a technique of characterizing the fracture behavior of a sharp notch in a member in terms such as stress and flaw size that can be used by design engineers. When designing a component or structure, it is common to assume that the material is isotropic and flaw-free. In the real world, all materials have imperfections, either internally indicative of missing atoms or fabricated discontinuities, holes, notches, cutouts, and radii [29]. Characterizing the toughness of a material is just one facet of fracture mechanics. The link between toughness, stress, and fault size must be mathematically understood to apply fracture mechanics concepts to design.

Historically, numerous accidents have occurred because of a failure to address fracture mechanics [30]. Catastrophic structural failures on tankers and cargo ships, which were mostly built in the United States during World War II, are the most well-known examples. We now have a better understanding of material breakdowns and know how to avert them because to World War II. Fatigue leads to catastrophic brittle breakdown of steel, which can happen at high speeds of up to 2100 m/s. [29]. Brittle fracture is not as common as yielding, buckling, and fatigue loading but when they occur, they are more costly in terms of human life and property damage.

Material-forming processes like machining, and welding will always introduce imperfections in form of notches, flaws, discontinuities, or other stress concentrations. Therefore, in addition to traditional material properties like yield strength and elastic modulus notch toughness must be put into consideration during the design of structures. Notch toughness is defined as the ability of a material to absorb energy in the presence of a sharp notch, especially during impact loading. Unlike toughness, there is no notch and loading are slow.

One of the most widely used method for measuring notch toughness is the Charpy V-notch (CVN) impact specimen test. Notches have a significant effect on the behaviour of a structure. The presence of a notch on a ductile material can make them to be brittle in-service loading. Service conditions like low temperature and impact loading can impede the ability of a material to yield or to flow freely around a notch hence making it to be brittle [31].

Fracture mechanics has the advantage of stress analysis in the vicinity of the crack. Fracture mechanics provide the best available technique for accounting quantitatively for the factors of the degree of reliability of a structure against failure by fracture as it can determine the notch toughness of a material using fracture mechanics type tests, nominal stress and flaw size and geometry.

In Linear-elastic fracture mechanics (LEFM) stress concentration occurs in the presence of a discontinuity or a hole which reduces the surface area of the load-bearing surface hence increasing the stress in the vicinity. Theoretical stress concentration factor $K_t$ is the ratio of the maximum local stress at the discontinuity $\sigma_{max}$ to the average stress $\sigma_{av}$ as presented in Equation (2.1).

$$Kt = \frac{\sigma_{max}}{\sigma_{av}} \qquad (2.1)$$

The theoretical stress concentration factor takes only the geometry of the material into consideration but in the practical world the ratio of maximum to nominal stresses is affected by the nature of the material used (metallurgical structure, inelastic behavior, anisotropy, inhomogeneity etc.) and hence it is called effective stress concentration factor $K_e$.

$K_t$ is mostly used in static stress analysis while $K_e$ is used in repeated loading like fatigue. For elastic material, the relationship of $K_t$ and $K_e$ is presented in Equation (2.2).

$$K_t = K_e \qquad (2.2)$$

Stress concentration is a location in an object where the stresses are significantly higher than the surrounding regions. Most of the time extremely sharp notches and cracks are present in materials due to fatigue loading, fabrication technique, welding, defects etc. For this small notch, the value of the theoretical stress concentration factor tends to infinity. Therefore, it becomes meaningless. In this scenario, the stress intensity factor is used.

$K_I$ is the most applied stress intensity factor. It forecasts the intensity of stress near the tip of a crack caused by a remote load or residual stresses. $K_{IC}$ is the critical value of the stress intensity factor, and it is used to measure fracture toughness. The brittle fracture occurs during unstable crack growth. This is when stress intensity factor $K_I$ reaches critical value $K_C$ the same way yielding occurs when stresses reach a certain limit called yield stress. It is a material property just like yield strength and it depends on temperature, loading rate and constraints. The stress intensity factor is proportional to the nominal applied stress and the square root of the crack size a.

The total useful life of a component is determined by the time it takes to initiate a crack and propagate it from the subcritical dimension to the critical dimension. Engineering Critical Assessment (ECA) methodologies based on fracture mechanics and applicable to structural components rely on the idea that a single parameter characterizing the crack driving force describes the material's fracture resistance [1]. An accurate and dependable determination of fracture toughness is critical for assessing equipment failure. Griffith's pioneering work a century ago established the concept of toughness as a measure of fracture resistance. It grew incredibly quickly matured. In the second half of the twentieth century, it became an essential tool in developing advanced transportation, civil construction, and power systems [32]. Its literature is currently extensive [5], [6].

Fracture toughness is the measure of the resistance of a material to local failure near a defect [4]. Early fracture assessments relied on the energy approach, which defined fracture as occurring when the energy available for crack growth is sufficient to overcome the material's resistance [7]. The increasing population and civilization have put pressure on the energy resources of fossil fuels. This has led to the shifting of exploration to offshore and extreme polar regions where the resources are unexploited. These environments are unfriendly to humans and materials; hence periodic inspection might be rare. Therefore, it is essential to include structural strength in the presence of cracks in strength analysis.

Presently fracture toughness tests are mostly carried out following the ISO and ASTM 3 standards, which are the most accurate methods for measuring fracture toughness [2]. The most critical parameters in fracture mechanics are the stress intensity factor K (or its equivalent partner, the elastic energy release rate G), the J integral, the crack-tip opening displacement (CTOD), and the crack-tip opening angle (CTOA) [33]. Fracture toughness experimental measurement and standardization are critical in applying fracture mechanics techniques to structural soundness analysis, damage tolerance design, fitness-for-service evaluation, and residual strength analysis for various engineering structures.

Many approaches have been used to examine fracture mechanics, including energy to cause failure, stress analysis, small-scale causes of fracture, applications of fracture, computational methods, etc. Table 2 provides a simple study of fracture mechanics based on the material parameters of the fracture.

TABLE 2: A simplified table for the fields of fracture mechanics [34]

| **Category** | **Material Property** | **Parameter** |
|---|---|---|
| Linear Elastic Fracture Mechanics (LEFM) | Linear, time-independent | Stress intensity factor(K), Energy release rate(G) |
| Elastic-Plastic Fracture Mechanics | Non-linear, time-independent | J- Integral, Crack tip opening displacement (CTOD) |

### Linear Elastic Fracture Mechanics (LEFM) and Elastic-plastic fracture mechanics

LEFM primarily deals with linear-elastic deformation when the stress is within the yield limit. The fracture toughness parameter for LEFM is K, the crack tip stress intensity factor; this K parameter is labelled $K_{Ic}$ at failure. K can be calculated using the load and crack length values. The $K_{Ic}$ values are a material property determined by ASTM standards. The $K_{Ic}$ values are determined from a point on the K-R curve and are a material property. The K-R curve is a plot of the parameter K versus crack extension. It demonstrates that as the crack grows, the resistance to its growth, R, decreases until a steady state is reached. The K-R curve is an abbreviation for the crack growth resistance curve [35].

When the linear method's limits are not complied with, non-linear fracture methods must be used. To determine whether LEFM or EPFM should be used, a parameter labeled stress ratio is used. The Rsc is for compact specimens, while the Rsb is for bend specimens. The stress ratio is a value that compares the nominal crack-tip stress to the yield strength of the material.

In fracture analysis, non-linear fracture includes deformation from elastic and plastic components. Non-linear fracture mechanics methods are more complicated than LEFM methods; the inclusion of plasticity complicates the analysis.

### The J integral

The J integral is a fracture toughness parameter used in nonlinear fracture mechanics to quantitatively describe the change rate in total potential energy. It is calculated using load, load-line displacement, and crack length. The J-R curve, a plot of J versus ductile crack extension, a, is the basic fracture toughness characterization by the J integral for ductile materials.

A single value of toughness is frequently defined to simplify the analysis of fracture potential. A construction procedure determines a point on the J-R curve to obtain single-point toughness. This point is labelled $J_Q$, a provisional value that becomes $J_{IC}$ when the standard's criteria are met.

The multiple specimen technique and the single specimen method are the two main methods for developing R curves. The multiple specimen technique consists of testing five or more identical specimens, each loaded to a different point on the load versus displacement curve. The specimens are loaded to the desired point, then unloaded, and finally heated to mark the oxidation of the crack growth. After that, the specimens are cooled in liquid nitrogen and broken open. On the fracture surface, the initial and final crack lengths are measured optically. The J value at the final load point is calculated based on this. The J-R curve is plotted using these values, J, and crack growth, Δa.

Because each test is expensive, it is preferable to use as few specimens as possible. A specimen must be created, pre-cracked, and tested for each test. The fabrication and pre-cracking of the specimens can be time-consuming. The test's accuracy is also affected by the number of samples tested. The greater the number of samples tested, the better the $J_Q$ result.

The single specimen's method for constructing J-R curves necessitates the preparation and testing of only one specimen. To determine crack growth, the specimen must be equipped with crack monitoring equipment. Optical measurements, compliance methods, or an electrical potential system can all be used to monitor a crack.

The single specimen method necessitates continuously or discretely measuring or calculating crack growth for the specimen and then plotting the J versus Δa curve. The single specimen test method has the advantage of requiring only one specimen to be constructed and tested to determine the entire R curve.

Only the compliance method is accepted by ASTM among the various single specimen methods for determining the J-R curve. To create elastic slopes, the compliance method employs unloading and reloading. A compliance calibration equation is used to relate these slopes to crack length. The J-R curve can be calculated using individual crack length measurements and J values calculated at each point.

Whatever method is used to monitor crack growth, a corresponding J value must be calculated for each point on the R curve. J is divided into elastic ($J_{el}$) and plastic ($J_{pl}$) components for estimation purposes as presented in Equation (2.3).

$$J = J_{el} + J_{pl} \qquad (2.3)$$

The $J_{el}$ elastic is computed from the elastic stress intensity as presented in Equation 2.4.

$$Jel = \frac{K^2(1-V^2)}{E} \qquad (2.4)$$

Where v is the poisons ratio and E is Young's Elastic Modulus.

Equation (2.5) presents the ($J_{pl}$) computed from the plastic component.

$$Jpl = \frac{\eta Apl}{Bb0} \qquad (2.5)$$

bo represents the initial ligament length, Apl is the area under the load-displacement curve. Exclusion lines are drawn at crack extension (Δa) values of 0.15 and 1.5 mm to compute $J_Q$, a provisional $J_{IC}$ from the R curve. These lines have a slope of $2\sigma_y$, which roughly corresponds to the component of crack extension caused by crack blunting rather than ductile tearing. At a maximum value of J, a horizontal exclusion line is defined as.

$$Jmax = \frac{b0\sigma y}{15} \qquad (2.6)$$

$\sigma_y$ is the flow stress, calculated as the average of yield and tensile strengths. All data that fall within the exclusion limits are fit to a power-law expression.

$$J = C1(\Delta a)^{C2} \qquad (2.7)$$

C1 and C2 are constants. The $J_Q$ is defined as the point at which this Equation intersects a 0.2 mm offset line. If all the other validity criteria are met, $J_Q = J_{IC}$ if the following size requirements are met.

$$B, bo > \frac{25JQ}{\sigma y} \qquad (2.8)$$

**CTOD as Parameters of the R curve**

Wells proposed displacement of the crack faces as an alternate fracture criterion when considerable flexibility occurs before to failure. He attempted to apply LEFM to structural steels with low and medium strength levels. These materials were too ductile for LEFM to be used, but Wells observed that the crack faces moved apart with plastic deformation. As the material's toughness grew, so did the degree of crack blunting.

This observation resulted in the creation of the crack-tip-opening displacement parameter (CTOD) [1], [22]. Wells aimed to enhance the stress intensity factor method by adapting it from a purely elastic condition to an elastic-plastic condition through the development of the CTOD approach. Unlike linear elastic fracture mechanics (LEFM), which is mostly based on stress intensity factors, CTOD provides a physical and more direct assessment of crack tip deformation, making it especially useful for analyzing ductile fracture in materials with high plasticity before failure [36] .

CTOD assesses the physical opening of a crack at its tip by measuring the displacement between two spots on either side of the fracture. It is especially useful in assessing fracture resistance in materials subjected to thermomechanical loading since it considers both elastic and plastic contributions to crack propagation. One of the main obstacles to the CTOD as a property of material is the lack of a single, universally recognized definition; that is, there is disagreement over which crack flank displacement most accurately represents the material's fracture toughness [37]. CTOD is described using a variety of definitions. The opening of the original crack tip when the crack opens due to loading is one of the most well-known definitions for CTOD. It is a crack tip displacement measure in which the original crack tip (produced by machining or fatigue pre-cracking) is blunted as the crack opens, resulting in a finite displacement at the original crack tip [23]. The 45° CTOD at the crack tip is an alternate definition for CTOD. CTOD is defined as 45 based on the displacement of the crack face's intercept and a pair of imaginary lines set at 45° from the blunted crack tip as proposed by Shih in 1981 based on J-CTOD conversion.

Measuring fracture toughness and crack extension in situ or with mixed mode loading is difficult since the typical displacement measurement gauge may not be available. Following this approach, it was proposed to employ the CTOD5 technology developed by the GKSS research centre Geesthacht in Germany to assess fracture toughness [38] . This technique allows for the immediate creation of the CTOD-R curve if the crack extension is present. The main CTOD definitions for fixed and developing cracks are shown in Figure 5.

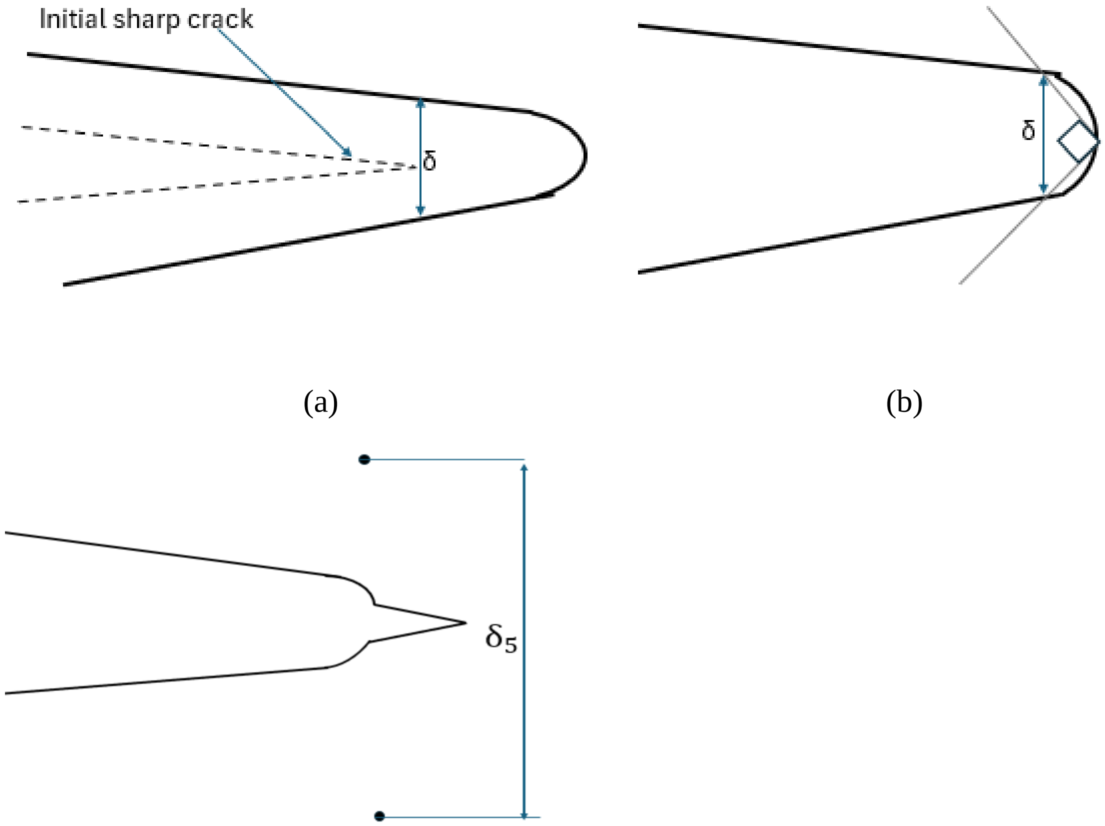

(a) (b)

(c) $\delta_5$ (CTOD5)

FIGURE 5: Schematic representation of crack tip-opening displacement: at the original tip (a), at the intersection of a 90° vertex with the crack flanks (b), $\delta_5$ (CTOD5) (c)

## CTOD Testing

The $K_{IC}$ test can only be used on the lower shelf of toughness in structural steels and welds due to the strict limits on plastic deformation. The $J_{IC}$ and J-R curve test methods allow for significantly more plastic deformation, but only on the upper shelf. The CTOD test is the only standardized method for measuring fracture toughness in the ductile-brittle transition region. Like the $J_{IC}$ and J-R curves, experimental CTOD estimates are obtained by separating the CTOD into elastic and plastic components. The elastic CTOD is calculated as follows:

$$\delta_{el} = \frac{K^2(1-v^2)}{2\delta_y E} \qquad (2.9)$$

The plastic component is obtained by imagining the specimens rotating around a plastic hinge.

$$\delta_{pl} = \frac{r_p(w-a)vp}{r_p(w-a)+a+z} \qquad (2.10)$$

Where z is the knife-edge height $r_p$ is a rotational factor a constant between 0 and $v_p$ is the plastic displacement. The plastic rotational factor is given by $rp = 0.44$ For SENB specimens.

The CTOD standard test method applies to both ductile and brittle materials, as well as steels in the ductile-brittle transition. The $\delta_c$ Critical CTOD at the onset of the unstable fracture without prior stable crack growth. This corresponds to the lower shelf and lower transition region of steels where the fracture mechanism is pure cleavage. $\delta_u$ - Critical CTOD at the onset of unstable fracture which has been preceded by stable crack growth. In the case of ferritic steels, this corresponds to the "ductile thumbnail" observed in the upper transition region.

$\delta_i$ - CTOD at the initiation of stable sack growth. This measure of toughness corresponds to value $J_{IC}$. $\delta_m$ - CTOD at the maximum load plateau. 'This occurs on or near the upper shelf of steels [39]. As with the $J_{IC}$ standard, the R curve can be generated by either a single or multiple specimens' procedure. CTOD values are plotted against the physical crack extension, and vertical exclusion lines are drawn at 0.15 and 1.5mm of crack extension. The data are then fitted to an offset power-law expression presented in Equation (2. 11)

$$\delta = C1 + C2(\Delta a)^{C3} \qquad (2.11)$$

Where C1, C2 and C3 are constants with $C2 \geq 0$ and $0 \leq C3 \leq 1$, and C1 is the intercept on the Y axis and might be 0. The initiation toughness $\delta i$ is then defined at the CTOD value corresponding to $\Delta a$=0.2 mm.

Current testing guidelines and standards use a plastic hinge model to measure CTOD values. The approach assumes that the test specimen rotates around a plastic hinge positioned on the crack ligament, allowing the CTOD to be estimated using a simple geometric relationship between the plastic displacement at the crack mouth. This research employs the CTOD evaluation procedure based on the Double Clip Gauge approach and the $\delta_5$ methodology as provided by Schwalbe and co-workers at GKSS. The DIC system monitors the movement of two nodes placed 5.0 mm apart (2.5 mm up and down) and symmetrical to the initial crack tip (CTOD-$\delta_5$) during tension tests. Schwalbe noted that if one considers that the gauge points across which $\delta_5$ is measured are situated within the HRR field, then the $\delta_5$ parameter can be correlated to the $J$-integral.

## 2.2. Recent advances in fracture toughness testing and standardization.

Although many studies have examined fracture toughness measurement and standardization since its inception in the 1960s, most of the advances have been incremental and there have not been any big breakthroughs. This literature review summarizes the incremental advances made in the last two decades in fracture mechanics. The testing methods for materials in low-constrain conditions like pipes and other pressure vessels is presented. SENT specimen test method progress is discussed and compared. Also, the fracture toughness testing of nonconventional geometries, sizes and materials is discussed. This review is expected to serve as a summarized technical review of fracture toughness testing, evaluation and standardization for metallic materials in terms of the linear elastic fracture mechanics as well as the elastic–plastic fracture mechanics. It focusses on recent improvements in fracture toughness testing and evaluation, for greater knowledge and implementation of proper fracture parameters and fracture toughness test methods.

### Loading modes

Mixed mode fracture occurs when a structure or body experiences inclined cracks or multiaxial stress. A crack has three primary loading conditions as shown in Figure 6, Mode I, II, and III loading. Cracks may be subjected to multiple forms of loading during real-world operations. The principal load is applied as a tensile stress normal to the crack plane, tends to open the crack tip in mode I loading; in mode II in-plane shear tends to slide the crack faces with respect to each other while in mode III, the crack tip is subjected to out-of-plane shearing.  Mode, I loading is commonly used to assess fracture toughness. The stress intensity factor is usually given a subscript to denote the mode of loading, ($K_I$, $K_{II}$ and $K_{III}$ for modes I, II and III.

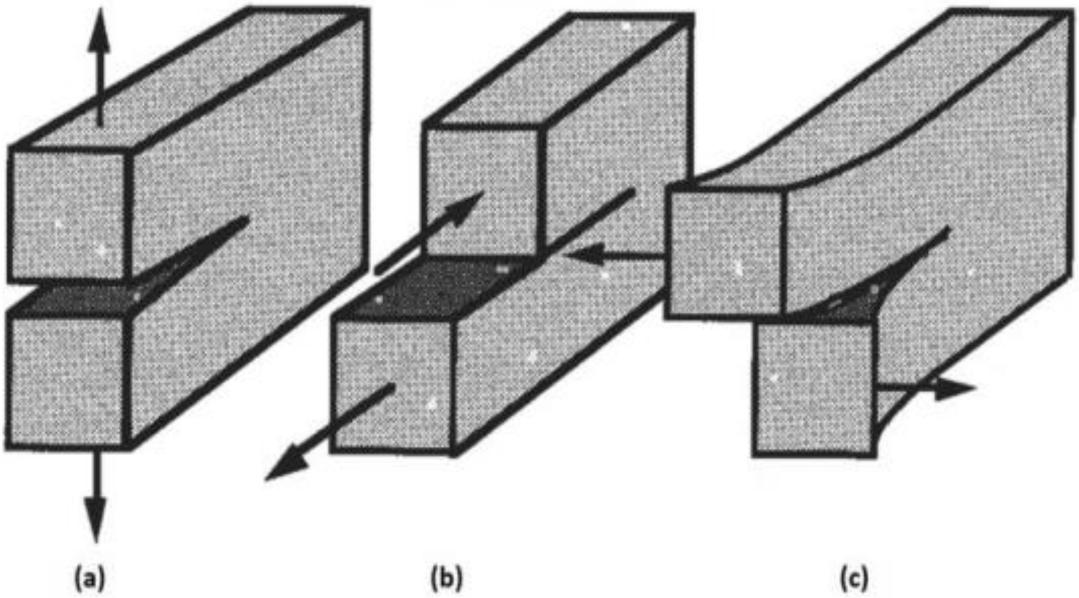

FIGURE 6: crack loading mechanisms, (a) mode i (b) mode ii and (c) mode iii (adopted from [1]).

Adding mode II or mode III loads to ductile metals can significantly reduce total fracture toughness, while less ductile metals are unaffected [40]. Currently, there is no standard testing method for overall fracture toughness of metals under mixed mode loading. Difficulties in establishing mixed mode fracture toughness include detecting local deformation near the crack, monitoring crack extension length, and lacking a common approach for determining fracture start. The biggest difficulties are with the experimental setups and the analysis of test outcomes.

Developing a testing technique that includes specimen design, resistance curve analysis, and fracture toughness determination is highly suggested. SINTAP (1999) and BS7910 are fracture mechanics-based procedures for assessing structural integrity. They use a two-criterion failure diagram (FAD) to evaluate the interaction between fracture failure and plastic collapse.

### Advancements in standardization

There are various fracture toughness test standards in use today for determining the fracture toughness of metallic materials. ASTM E1820 and ISO 12135 are two of the most widely used standards. Several studies have examined the suitability of various standards for varied materials [41]. Because of obvious differences between the ASTM E1820 and ISO 12135 standards, namely the blunting line Equation, fitting Equation of the J-R curve, and valid data points, the results show that different procedures result in varying fracture toughness values for the same material. As a result, it is still unclear which fracture toughness test standard is more useful for particular under certain conditions in technical applications.

Zhang et. al compared the $J_{IC}$ values calculated using the ISO and ASTM standards [42]. Their variations were primarily due to the range of qualified data, the function of the construction line, and the regression line Equation. These disparities lead to different fracture toughness, $J_{IC}$, values through using two standards, with the one tested using ISO standard lower.

### Fracture toughness testing Standards employing SENT specimens.

Toughness measurements are increasingly using specimen geometries that mimic real-world defect geometry [43]. One noteworthy example is the geometry of the SENT specimen has been found to have a much closer resemblance in terms of crack tip constraints to flaws in pipes than that of the SENB specimens [9]. In 2014 The British standard BS 8571 was published as the only standard that currently establishes the test method for determining fracture toughness in metallic materials employing a single edge notched tension SENT specimen [44] . This is in terms of (crack tip opening displacement, (CTOD) and J (the experimental equivalent of the J-integral). The CTOD can be measured directly from the mouth of the specimen or estimated from a clip gauge extensometer.

The 2018 revised version of the standard brought about the following main changes: the clamped load J equations were consolidated to provide a single formula for all specimen dimensions, the crack shape validity error was fixed, annexes were added to provide guidance on crack path deviation and for testing specimens with non-sharp notches and the allowed range of $a_0/W$ was reduced [45]. As shown below in Figure 7, the specimen can be loaded by either clamping or pins.

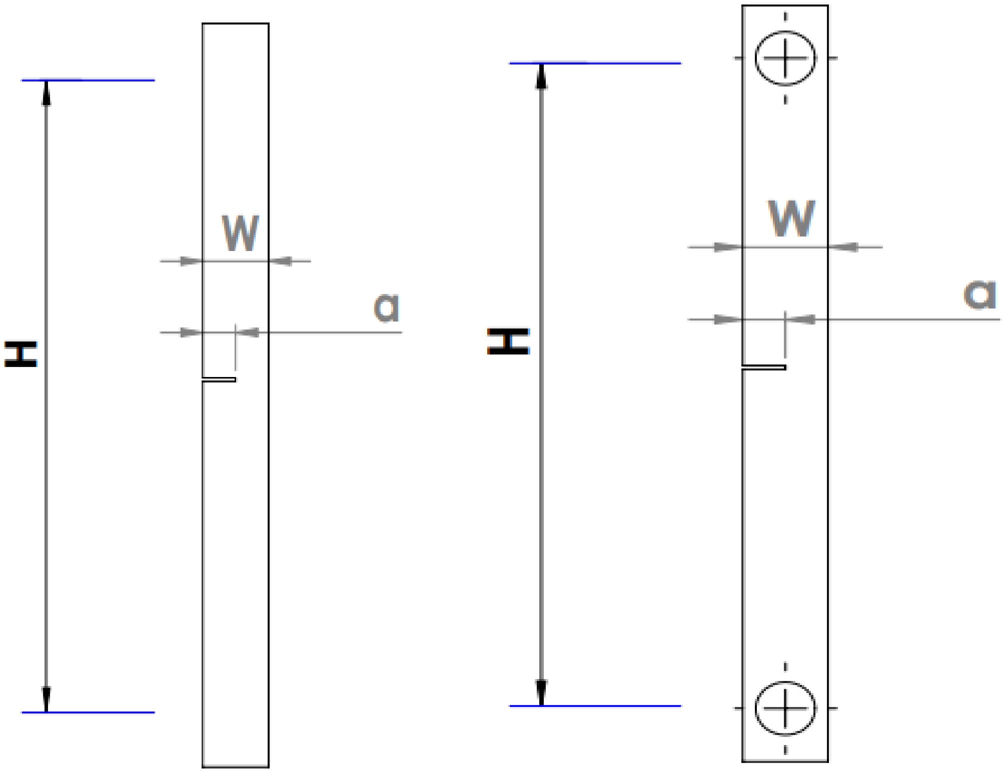

FIGURE 7: Clamped single edge notched tension specimen and a directly pin-loaded single edge notched tension specimen [46].

### Advancements in specimens ’configurations

Compact tension (CT) specimens, single-edge notched bend (SENB) specimens in three-point bending, middle-cracked tension (MT) specimens, disk-shaped compact (DCT) specimens, and arc-shaped tension (AT) specimens are the five different types of fracture test specimens. This is according to fracture mechanics test standards including ASTM E1820 and ISO 12135 [12]. Most of the standardized specimens suggest specific relationships between thickness (B), width (W), and initial crack size ($a_0$). The ligaments of the other specimens experience both stress and bending, except for MT specimens [47]. High-constraint specimens tend to produce conservative toughness estimates when utilized to assess the fracture toughness characteristics of onshore pipelines subject to geotechnical stresses, which might contain faults related to low-constraint loading. As a result, material selection and pipeline design expenses increase unnecessarily.

In the recent past, circumferentially cracked bar (CCB) specimens for CTOD fracture toughness determination in the upper shelf regime has also been reported [13]. Because of its radial symmetry, this geometry is elementary in design, can be scaled according to the availability of materials, and is free of three-dimensional effects. Wang [48] provided the following $K_I$ Equation for V-notched circumferentially cracked bar under remote tension.

$$K_I = \frac{0.932P\sqrt{D}}{d^2\sqrt{\pi}} for 1.2 \leq \frac{D}{d} \leq 2.1 \qquad (2.12)$$

where P is the maximum load, d is the minimum diameter at the V-notch, and D is the remote bar diameter. For SENT specimen testing table 3 summarizes the geometries and their requirements used by various standards [49] .

TABLE 3: Acceptable geometry of major published sent testing methods.

| **Standard** | **Specimen Cross Section** | **$a_o$/W Ratio** | **Side groove Requirement** |
|---|---|---|---|
| BS8571:2018 | 0.5 ≤ W/B ≤ 2 | $0.2 \leq a_0/W \leq 0.5$ | 5% suggested |
| DNV-RP-F108 | (B = 2W) × W | $0.2 \leq a_0/W \leq 0.5$ | None |
| ExxonMobil | (B = W) × W | $0.25 \leq a_0/W \leq 0.35$ | 5% required |
| Canmet Materials | (B = W) × W | $0.25 \leq a_0/W \leq 0.5$ | 5–7.5% required |

Early fracture assessments relied on the energy approach, which defined fracture as occurring when the energy available for crack growth is sufficient to overcome the material's resistance [7].

Wallin proposed a master curve method with a corresponding reference temperature based on the weakest link theory and the Weibull statistics theory to describe the statistical scatter statistical size effects, and temperature dependence of cleavage toughness in the transition region and on the lower shelf [14]. Using the relationship, the parameter $K_{JC}$ is derived from individual $J_C$ test data at the onset of cleavage fracture as presented in Equation 2.13 [31].

$$K_{JC} = \sqrt{(\frac{EJc}{1-v^2})} \qquad (2.13)$$

where E is the Young Modulus of elasticity, v is the Poisson's ratio and $J_C$ is determined at the cleavage instability point using the fundamental ASTM E1820 technique under circumstances of plane strain.

**J and CTOD estimations for clamped SENT specimens**

In their work, E. Wang et al. [48] compared three existing methods for computing J and CTOD and proposed a complementary plastic η factor (ηpl) approach for clamped SENT specimens with H/W = 10 by carrying out simulations using 2D and 3D FEAs [15]. They found out that the plastic η factor ($\eta_{pl}$) is affected by specimen geometric configurations (a/W, B/W, in both plain-sided and side-grooved geometries) and strain hardening properties (n). Their new approach showed a greater agreement than the other three conventional methods. The absolute error in this new method was reduced to less than 10%. Their findings indicate that the complementary ηpl approach developed is a useful and accurate method for predicting ηpl values for clamped SENT specimens with $0.3 \leq a/W \leq 0.7$ and B/W = 1 and 2.

B.P. Pherson investigated the current fracture toughness test procedure to see if there is a simpler, less complicated way to obtain the $J_{IC}$ value from a fracture toughness specimen test recorded. The current method of construction of $J_{IC}$ curve is complex and requires a detailed computer program or spreadsheet. The findings demonstrated that a fracture toughness specimen's load and displacement record can be used to estimate a $J_Q$ value, a provisional value for fracture toughness, $J_{IC}$.

G.H. Donato et al. [50] discussed the creation of J and CTOD estimate algorithms based on plastic eta factors and plastic rotation factors for deep and shallow cracked bend specimens. Two methods are considered: (i) estimating J and CTOD from plastic work, and (ii) estimating CTOD from the rotational factor of plastic. When the CTOD is used to describe the material's fracture resistance, a comparable formulation also holds.

The earlier development, which was based on the eta-factor, is still in close contact with current standards for determining experimental J-values using common fracture specimens with deep cracks. These analyses then yield precise values for η-factors and $r_p$ -factors that can be applied to various specimen geometries and material properties. The findings presented here are like those described in a previous study by Kirk and Dodds [51], which also discusses the development of an estimation technique for J and CTOD using SE(B) specimens.

Stretch zone width ($\Delta a_{SZW}$) can be used to calculate the value of CTOD at the beginning of the subcritical crack initiation, $\delta_{Ti}$ [39]. Japanese scholars first put forth this approach, which was later standardized in the ISO standard ISO-12135:2016 same technique. Furmańczyk et al. [52] evaluated various methods' capability to determine the value of crack tip opening displacement (CTOD) at subcritical crack initiation, $\delta_{Ti}$. The experimental results were compared to those obtained through numerical calculations. The CTOD was measured on SENB specimens made of S355JR steel that had been heat-treated in a laboratory. The ASTM E1820 standard provides a procedure for estimating CTOD at 0.2 mm subcritical crack extension. The ASTM E1820 [53] procedure determines $\delta_{TC}$ based on crack mouth displacement data representing an average value along specimen thickness. Gown et. al examined the J-Integral resistance curves of a base metal for high-strength steel pipes using the single-specimen technique with clamped SENT specimens. The technique is the same as ASTM E 1820 for CT and SENB specimens.

**Advancements in factors affecting the value of fracture toughness; crack tip constrain.**

The depth, shape, and geometry of the notch, as well as the specimen thickness and geometry, load, and forces mode, all influence the degree and effects of crack tip constraint [54]. Shallow cracks have a lower constraint than deep cracks, and shallow cracks are more likely to be found in real structures. J. Kang et. al [55] established that fracture toughness reduces parabolically as the crack tip constrains as shown in Figure 8.

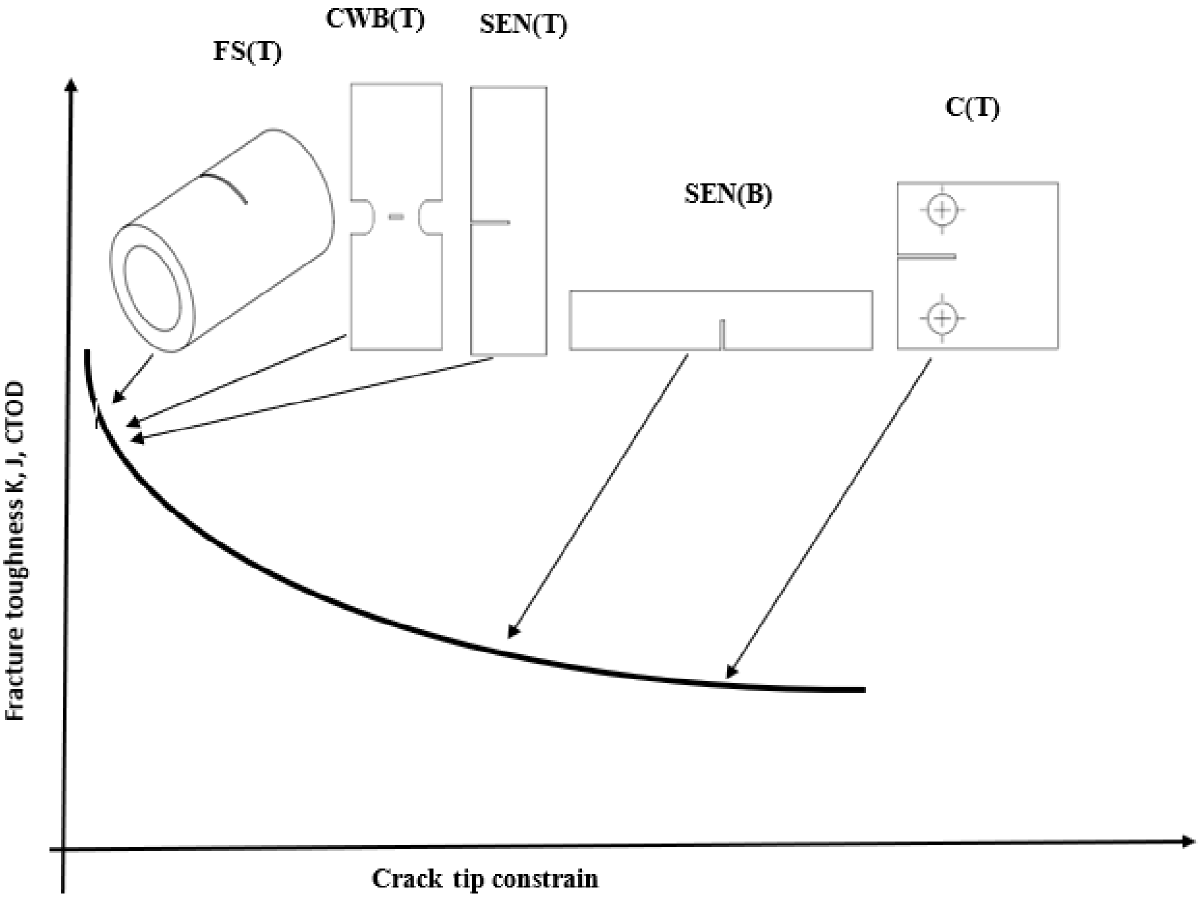

FIGURE 8: Diagrammatic representation of the relationship between specimen geometry and fracture toughness and constraint [56]

### The effect of notch depth and strain rate on CTOD values in fracture tests of structural steel elements

During fracture toughness testing the test objective determines the position and configuration of the notches; first, the shape and process origin of the material (plate, tube, square or rectangular bars), rolling direction, and the regions of interest in the welded joint are defined [57]. Kowalski et al. [21] investigated the effect of notch depth difference, within the standards' allowable range, on the recorded CTOD values of a given material. The analysis was carried out by numerically modeling the destruction of specimens with various notch geometries and then verifying the numerical results in laboratory tests.

The results show that the CTOD test can determine steel ductility. They also discovered that caution should be exercised when comparing CTOD values obtained for specimens whose geometry fits relevant standards but differs by an $a_0/W$ ratio. This is significant because even modest changes in this ratio significantly impact the critical tip notch opening displacement CTOD.

W. K. Nowacki et al. investigated the effect of strain rate on ductile fracture [58]. A new methodology for assessing the influence of strain rate on ductile fracture was proposed. The recording of temperature evolution during deformation can provide additional information for determining the shear banding contribution function and the onset of ductile fracture.

In [59] the impact of strain rate and stress triaxiality on the fracture properties of ductile metals was investigated. It was discovered that the degree of stress triaxiality in the specimen had a significant impact on the ductility of all three materials, with the ferrous materials showing the strongest dependence and the aluminum alloy the weakest. They found out that although the fracture modeling experiments were successful, more research is necessary before such models may be used outside the scope of conditions for which they were developed. A future, more thorough investigation into the behavior of ductile fracture will focus on the impact of temperature, including both high and low temperature.

### Influence of in-plane constraints on the crack tip opening displacement for SENB specimens under predominantly plane strain conditions

The effect of geometry constraint is well documented in the literature. Lowering the constraint increases fracture toughness, and vice versa [9]. M. Graba [24] investigated the influence of in-plane geometric constraints represented by Q-stresses on the crack tip opening displacement for SENB specimens subjected to primarily plane strain conditions. He used the results to develop a new formula for calculating the value of the coefficient $d_n$(n, б0/E, a/W) while accounting for the effect of in-plane constraints on the strain hardening exponent n, the ratio б0 /E, and the relative crack length $a_o$/W.

In [60] a hybrid solution for determining the selected fracture parameters for SENB specimens dominated by plane strain is proposed by Graba. The influence of material properties and relative crack length on three fracture mechanics parameters: the J-integral, the CTOD, and the displacement of the point of application of the force vLL, calculated for selected elastic-plastic material configurations, is discussed in this thesis. New analytical equations were presented based on FE calculations.

The new hybrid formulas presented here enable estimating selected parameters of elastic-plastic fracture mechanics with varying degrees of accuracy with actual experimental data.

J. Kowalski investigated the effect of specimen geometry on the CTOD value for VL-E36 shipbuilding steel experimentally and numerically. The presented findings indicate that specimen cross-section geometry significantly affects CTOD. The yields obtained with BxB type specimens are lower than those obtained with Bx2B type specimens.

For both cases studied by J. Kowalski, the relative crack length $a_0$ /W significantly affected the CTOD value. It is linear in both cases. It is significantly smaller for BxB specimens than specimens with a Bx2B cross-sectional ratio. According to these findings, the CTOD results obtained for elastic-plastic fracture mechanics cannot be treated as material constants because their values depend on the type of specimen used, how it is loaded, and the relative crack length.

### Advancements in fatigue crack growth testing

Fatigue is arguably the most successful use of fracture mechanics  [61]. A structural component's fatigue life is typically divided into two periods: crack initiation and crack growth. The fracture mechanics parameters Stress Intensity Factor (SIF), K, J integral, and CTOD are considered a crack driving factors for the prediction of fatigue crack propagation [27]. According to Ž. Božić et. al the stages in fatigue crack growth can be represented by the schematic diagram shown below in Figure 9.

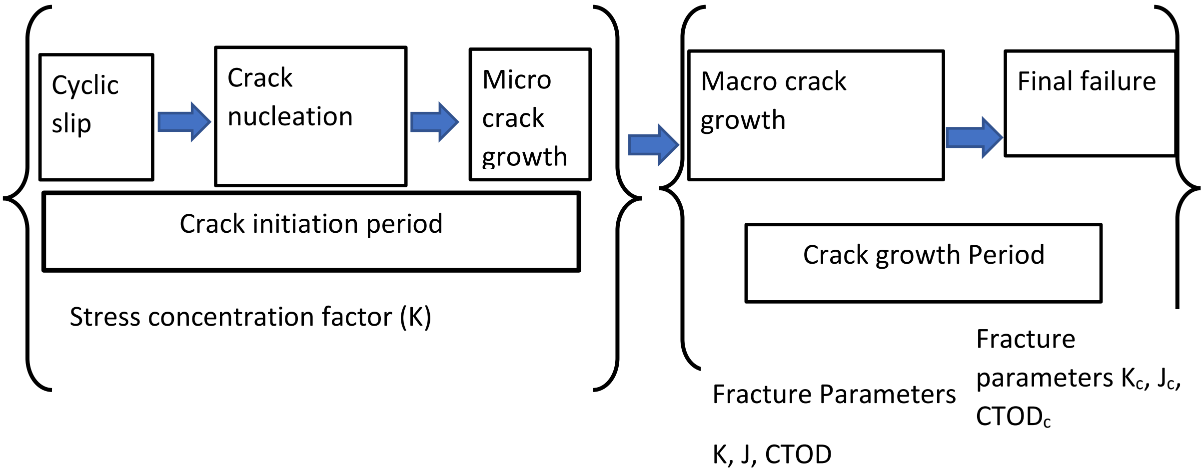

FIGURE 9: Stages in the fatigue life (based on [27]).

The finite element method is the most widely used computational method for calculating stress intensity factors in cracked geometries [35]. Although they have been successfully used for the simulation of mixed-mode FGC in complex geometries, the main disadvantage is that the FEM mesh must conform to the geometry of the crack. As a result, each time the crack propagates, the mesh must be updated for each crack increment, which is difficult.

K. Hectors et al. [62] presented a Python-based numerical framework for arbitrary three-dimensional fatigue crack propagation using the X-FEM method to solve this conundrum. To determine the stress intensity factor solutions, the framework employs the Abaqus X-FEM solver. A B-spline formulation with C1 continuity for the crack faces is used to accurately describe the crack front and crack plane in three dimensions. The crack advancement is simulated iteratively using a predefined Δamax. A new crack front extension algorithm was used to improve automated crack advancement along with sharp corners. The proposed algorithm combines standard linear or polynomial extrapolation extension methods with a mesh boundary detection method based on the Möller–Trumbore algorithm. A reliable solution to the failure of level set construction from the explicit crack face geometry was implemented to improve the reliability even further.

### Fatigue crack growth standards

ASTM published a standard test method for determining fatigue crack growth rates from near-threshold to $K_{max}$ controlled instability [63]. In this test procedure, notched specimens pre-cracked in fatigue to an appropriate standard are subjected to cyclic stress. To determine the crack growth rate, the crack's size is measured as a function of the number of fatigue cycles that have passed, either visually or through an equivalent approach.

Results are stated in the linear elasticity theory's crack-tip stress-intensity factor range (K). Materials that can be tested using this test method are not restricted by thickness or strength as provided as the specimens are thick enough to resist buckling and large enough to maintain a majority elastic state during testing.

### Monitoring of crack size

There are several methods for measuring the length of cracks [64]. They have been discussed extensively in numerous publications. Clip gauges are the most popular, simple, and affordable option [6]. Numerous non-destructive testing (NDT) techniques are available, such as potential difference (PD), optical, compliance, ultrasonic, acoustic emission, eddy current, and alternating current field

[65]. This dissertation used PD approaches for its experimental work because it have several advantages and a lot of room for future improvement [65]. Compliance techniques, which are based on the correlation between the length of a fracture and the strain that results, have been utilized extensively for long-term crack monitoring but become less sensitive for small cracks. Optical methods such as marking the fracture surface or tracking the crack tip extension using a travelling microscope, can accurately forecast crack lengths but require visual access making continuous monitoring impractical.

Boroski et al. [66] presented a method for determining the length of fatigue cracks in compact tension specimens. Fatigue VIEW system was used for this purpose, which consists of two high-resolution video cameras and dedicated software. It was created in collaboration with the UTP University of Science and Technology in Bydgoszcz at the Institute of Maintenance Technology–National Research Institute in Radom.

The FatigueVIEW system, in its basic configuration, allows you to observe the research object using two video cameras. Using two video cameras is intended to enable 3D analyses or to using two video cameras to enable 3D analyses or improve the accuracy of 2D analyses. A fatigue crack was detected in a CT-type specimen using a digital image correlation method, and its length was monitored as a function of the number of load cycles. The used research-measurement system enabled machine operation control for fatigue tests with crack lengths, such as stopping the cyclically variable loading after the specimen reached the desired length.

Monitoring crack extension during the test, particularly at low and high temperature, is one challenge material testing [20]. The optical method for measuring crack length can be used to calibrate the compliance method for measuring crack length in cryogenic conditions. S. Naib et al. [67] at the University of Gent, Belgium used Single Edge notched Tension SENT specimens to investigate heterogeneous weld crack growth resistance and evaluate available techniques for measuring tearing behavior. The mob9-point method, Direct Current Potential Drop technique, and normalization data reduction technique was used to measure crack growth.

A minimum distance between the current input and output pins and the notched section is proposed to promote current homogeneity across the specimen width. According to their findings, DCPD is a reliable technique for understanding crack behavior in the heterogeneous region because it indicates variations in resistance curves and is also an effective method for predicting final crack extension. By comparing the potential drop across the notch to a reference voltage measurement taken far from the notch, it is possible to minimize the impact of unwanted variations in current and material resistivity (i.e., with temperature) (dual-probe technique). The findings demonstrated that both the plain-sided and side-grooved square-section-SE(T) specimens may be used to represent the Johnson Equation, which expresses the relationship between potential drop increase and relative fracture depth [68].

While simpler to use, the normalized data reduction method does not reveal the irregular shape of tearing resistance curves seen in heterogeneous welds. When a crack path deviation exists, DCPD analysis is related to crack extension.

### Advancements in fracture toughness testing of unique materials shapes, geometries, and advanced materials: Fracture toughness of welds

According to several fitness for service (FFS) assessment methodologies, the fracture resistance of the weld metal (represented by a J-R curve) is a crucial input for structural integrity analyses of load-bearing welded components [67].

The presence of local strength and toughness variations (heterogeneity) within a weld region complicates the assessment of welded structure integrity [13]. The J-R curve for welded joints is determined experimentally by testing small, laboratory fracture specimens according to ISO 15,653-specified practices. The calculation of crack driving force and extension as the test progresses is required for post-processing single specimen SENT test results. This is based on the ASTM E1820 [11] for J-evaluation for homogeneous metallic materials, which has been extended to weldments with yield strength mismatch ratios M in the range of 0.5 to M to 1.25. Here, M is described as:

$$M = \frac{\sigma_{yWM}}{\sigma_{yBM}} \qquad (2.14)$$

where $\sigma_{YWM}$ and $\sigma_{yBM}$ are the tensile strengths of weld metal and base metal, respectively.

Conventional testing procedures frequently use three-point bend specimens with deep, thorough fractures ($a_o/W \geq 0.5$) to assess the cleavage fracture toughness of ferritic steels, particularly pipeline steels and their weldments [69]. Toughness measurements from high-constraint specimens are typically conservative. Leading to unnecessarily high material selection and pipeline design costs. Single-edge tension SENT specimen geometries, which have a less crack-tip constraint, are thus preferred for use with pipeline base metals, girth welds, and heat-affected zones.

In welded joints, the notch must ensure that the crack or pre-crack tip grows through the microstructure of interest. Several methods for testing homogeneous materials have been investigated and proven reliable. However, published data suggest that the accuracy of these methods may degrade when testing welded joints.

Because most brittle regions are located at the HAZ, some suitable options for assessing these regions exist, such as joints with "V" or "K" shapes, where one of the sides is perpendicular to the plate surface [70]. The HAZ could be evaluated using compact miniaturized specimens for both "V" symmetrical shapes and K shapes, as shown in the schematic weld joint cross view in Figure 10 for SENB specimen and figure 11 for CT specimen.

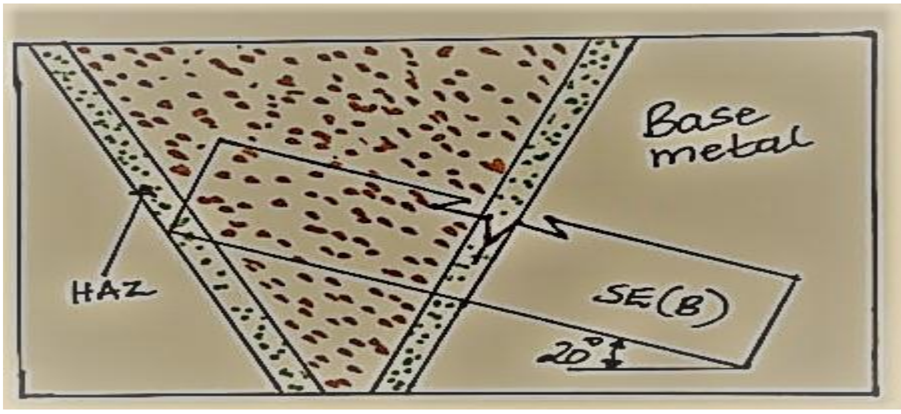

FIGURE 10: Design options for notches in fusion weld joints, (SENB) specimens.

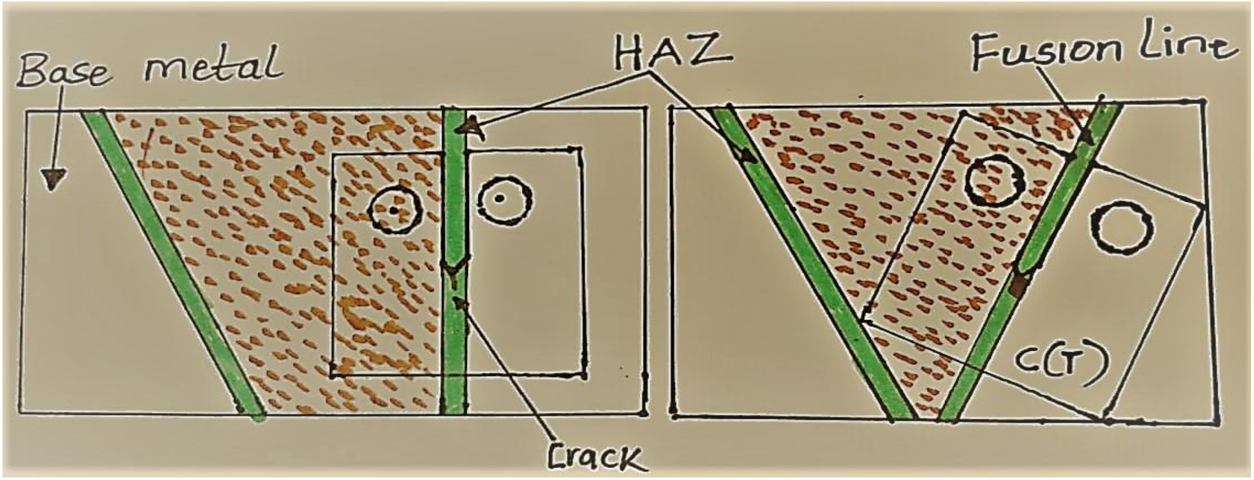

FIGURE 11: Design options for notches in fusion weld joints in compact tension specimen [6].

R. G. Savioli et al. [71] examined the use of ή methodology and suggested improvements in J and CTOD estimation formulas for C(T) fracture specimens, including overmatched weldments. They introduced a broader set of ή factors applicable to the structural, pipeline, and pressure vessel steels for a wide range of crack sizes (as measured by the ($a_o$/W) ratio) and material properties, including different levels of weld strength mismatch.

**Advances in fracture toughness for pipes and pressure vessels**

Long-established fracture mechanics test standards, such as ASTM and ISO 12135, focus on measuring fracture toughness using laboratory specimens with high constraints, such as (CT) specimens, SENB, and disk-shaped specimens. Toughness measurements from high-constraint specimens are typically conservative. Leading to unnecessarily high material selection and pipeline design costs [72].

Previous studies have found that the SENT specimen, as well as the type of connection with the test machine (clamping) and the value H/W = 10, provide a reasonable match to the constraint conditions of a circumferential crack in a pipe subjected to tensile loading under strain-based design conditions [73]. Modern line pipe steels are becoming increasingly tough, critical elastic stress intensity factors KIC cannot be used to characterize fracture toughness. Therefore, EPFM theory is then used. The tearing resistance curve can be used to describe the fracture toughness of a material. This curve can represent the CTOD, in mm or J-integral J, in N/mm as a function of the ductile crack extension of Δa, in mm [33] but CTOD tests have been used the most to assess fracture toughness in the pipeline industry . Safety requirements imposed by respective codes, the design of pressure vessels and boilers is strictly regulated [35]. The specified vessel wall thickness is determined so that the stresses created in the structure remain within the elastic limit for the design pressure and design temperature. This avoids excessive plastic deformations or ruptures when the yield point exceeds a certain threshold.

In 2006 Det Norske Veritas published recommended practice in fracture control for pipeline installation methods introducing cyclic plastic strain [74]. It gives guidance on how to test and analyze pipeline girth welds that are subjected to cyclic plastic deformation, such as during reeling technique installation but also for other scenarios with significant plastic strains.

Cracks in a pressure vessel can reduce its strength. When a fracture crack reaches a critical size, it can cause rapid growth of existing damage and, eventually, sudden failure. It should be noted that such failure typically occurs under stresses much lower than the material yield strength.

Szybiski et al. [9] research focused on determining the impact of crack presence on stable vessel operation. They were most interested in the cracks in the vessel's inner wall because they are difficult to identify and monitor. The impact of various parameters such as crack length, orientation, and fracture toughness was considered. Detailed numerical results were obtained using the finite element code ANSYS for various crack sizes and locations. The cracks in the weld joining shell and end plate, as well as cracks in the groove area, where the maximum stress concentration appeared, were numerically studied. The results show that boilers with cracks are at risk of premature failure.

Minnebruggen conducted an experimental-numerical investigation into the feasibility of spirally welded pipes in a strain-based design context [75]. He concludes that spirally welded pipes exhibit promising behavior for use in a strain-based design project. The current design guidelines for tensile strain capacity and pressure correction factor are concluded to be valid because they predict a lower bound value in terms of strain capacity.

### Elastic-plastic fracture parameters for DENT plates under plane strain conditions

Gabra [76] presented a comprehensive numerical analysis of DENT plates. The study included using a finite element model to verify the limit load solution. The yield stress, σ0, the strain hardening exponent, n, and the relative crack length, a/W, were considered in the elastic-plastic material analysis and their effects on the values of the J-integral, CTOD, and the load line displacement, vLL. He proposed new Equations for calculating limit loads.

### Fracture toughness evaluation at the micro-scale and for miniaturized specimens

The definition of stress includes a reliance on a scale. The traditional definition of stress as force per area is based on using a reference cross-section or volume. It is an obvious consequence that fracture toughness, as defined by stress distribution analysis, must also be a scale-dependent quantity [77].

For most structural materials, it is challenging and occasionally impossible to measure a valid KIC because of the strict size criteria of ASTM E 399 [78]. Active research is being done on interface fracture and nanoscale fracture due to issues faced in the microelectronics industry [2]. J. Ast et al. [79] summarized the approaches proposed and used to address the challenges mentioned above, focusing on micro-cantilever and micro-pillar test configurations. They discovered that two different toughness evaluation methods had been developed for this micro-level. Micro-pillar splitting and micro-cantilever bending are two examples.

Ion beam milling is frequently used to fabricate specimens in both situations, giving the samples specific characteristics. Layers of altered material are introduced due to the inevitable implantation of ions and the accompanying ion beam modification of the material structure. These layers, despite being relatively thin (about 50 nm, as a guide), may change the material response compared to that of a parent or virgin material.

The small punch (SP) technique was proposed for radiation embrittlement studies in 1981 [80]. Many researchers extensively developed this technique to estimate the potential for residual life assessment of components during service [81].

### Brittle fracture criteria for bi-material structures and composites

The growing use of composite materials in machine construction necessitates a strong need for modeling and evaluating their strength. Mieczkowski et al. present experimental and theoretical results of verifications for composite materials with interfacial cracks in their paper [82] Griffith, McClintock, and Novozhilov's fracture hypotheses were chosen. The theoretical, critical load values derived from each hypothesis were compared to experimental data, which included uni- and multi-axial loading conditions.

The Griffith criterion, which considers proportions between normal and tangential stresses at the interface, produced the most accurate findings. The everyday hoop stresses regarded as a damage function yielded the most detailed findings for the Novozhilov criterion. In contrast, the maximum primary stresses treated as a damage function offered the correct values of the binding force for the McClintock criterion.

Recent advancements in fracture toughness testing both regarding the elastic-plastic and linear elastic fracture mechanics are discussed in this article. Fracture mechanics is now viewed as a well-established engineering discipline due to its quick expansion and appeal to address practical problems. Instead of huge discoveries, current research creates incremental advancements.

Now, fracture toughness tests are mostly carried out following the ISO and ASTM E1820 standards, which are the most accurate methods for measuring fracture toughness. For each standard, the advances that have been made in specimen geometry, crack measurement techniques, size, size requirement, and validity criterion were discussed. According to this review, fracture toughness testing, experimental evaluation, and standardization for metallic materials are still experiencing changes and improvements after more than 50-year history of the development of fracture mechanics theory. Mode, I load is still the most popular mode of loading in fracture measurement.

Over the years, various fracture toughness parameters, assessment criteria, and experimental techniques have been proposed and modified progressively. There are still challenges in the correct measurement of crack size especially in FCG. The use of fracture mechanics will always be of great importance to the advancement of the modern world since an accurate and dependable determination of fracture toughness is critical for assessing equipment failure.

### 2.3. Power plant steel-grades

Power engineering steels are a range of construction alloy steels dedicated to pressure components operating at elevated temperature [83]. Heat-resistant steel (ferritic and austenitic) is commonly utilized for key components in power plants. In 1950, carbon steel boilers in thermal power plants had operating pressures and temperature of 4 MPa and $370^0$ C, respectively. However, after 1955, the development of molybdenum steel (Mo) allowed for higher pressures and temperature of 10 MPa and $480^0$ C. From 1960-1970, the developed chromium molybdenum (Cr-Mo) steel alloy increased temperature to $566^0$ C and pressure to 17-26 MPa [28]. Figure 12 illustrates how Mo and Cr affect the creep rupture strength of low alloy vanadium molybdenum steels (0.3%Mo, 1%Cr-0.5%Mo, and 2.25%Cr-1%Mo) at $500^0$ C and $550^0$ C after 100,000 hours [16].

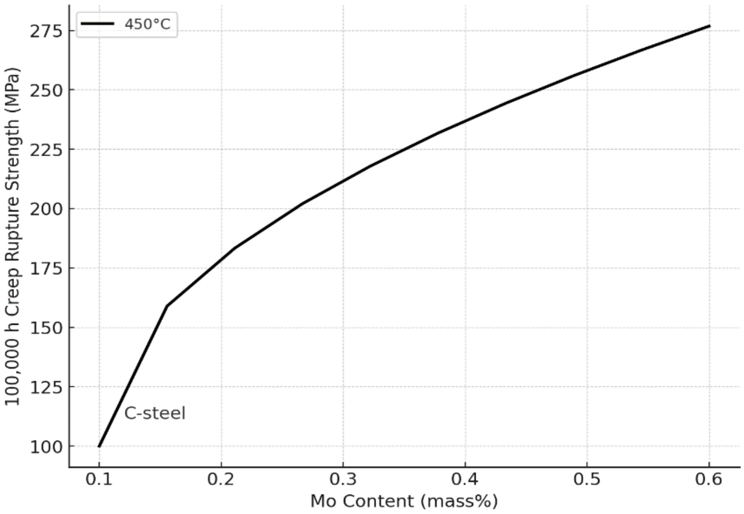

FIGURE 12. The creep rupture strength of a Mo-V steel at $450^0$ C as a function of Mo content after 100,000 hours [22].

In the late 1970s, 14MoV6-3 steel (DIN) became a popular steel grade for steam pipelines (temperature up to $540^0$ C and pressure up to 45 bars for a service life of 100,000 hours). The material exhibits appropriate mechanical properties at both room and high temperature, including plasticity, tensile strength, notch impact strength, and elongation. It has favorable physical and chemical characteristics, including a high heat capacity with little linear thermal expansion, corrosion resistance when exposed to fumes, and oxidation resistance when water vapour is present.

This was because it provided significant benefits over previous generations and allowed for reduced pipe wall thickness [84]. The equivalent grades of 14MoV6-3 steel are presented in Table 4.

TABLE 4. Equivalents of 14MoV6-3 for different standards and countries

| **Jurisdiction standard** | **Steel grade equivalent of 14MoV6-3** |
|---|---|
| Poland (PN) | 13HMF |
| BS EN 10028-2 | 10CrMo9-10 |
| Germany (DIN EN 10216-2, EN 10028-2) | 10CrMo9-10 |
| European Union (EN 10273, EN 10222-2) | X12CrMo5 |
| USA (ASTM A335, A213, A387) | A335 P11 / A335 P12 / A387 Gr. 12 |
| Russia (GOST 20072-74, GOST 5520-79) | 15CrMo |
| China (GB/T 5310, GB 713) | 12Cr1MoV |

14MoV6-3 is referred to as 13HMF in Poland, the Czech Republic, Slovakia, and other Central and Eastern European nations—especially those impacted by steel standards from the previous Soviet era—frequently employ this name style. It is a high-strength martensitic stainless steel that is commonly used in high-temperature applications such as boilers and heat exchangers. The "13" in its name refers to its chromium content, which is around 13%. The "HMF" stands for High-Manganese Free-Cutting steel.

The mechanical properties of 13HMF steel, also known as X13CrMoSi5-1, depend on the specific condition and treatment of the material [83]. However, some typical mechanical properties are:

Tensile Strength: 550-800 MPa

Yield Strength: 340-550 MPa

Elongation : 10-25%

Hardness: 229-341 HB

Impact Strength: Good, with a minimum impact value of 27 J at -20°C

These values are approximate and may vary based on the material's heat treatment, processing, and composition [85]. Figure 13 below show the creep rapture strength of 14MoV6-3 at four different temperatures. The higher the temperature the lower the creep rapture strength.

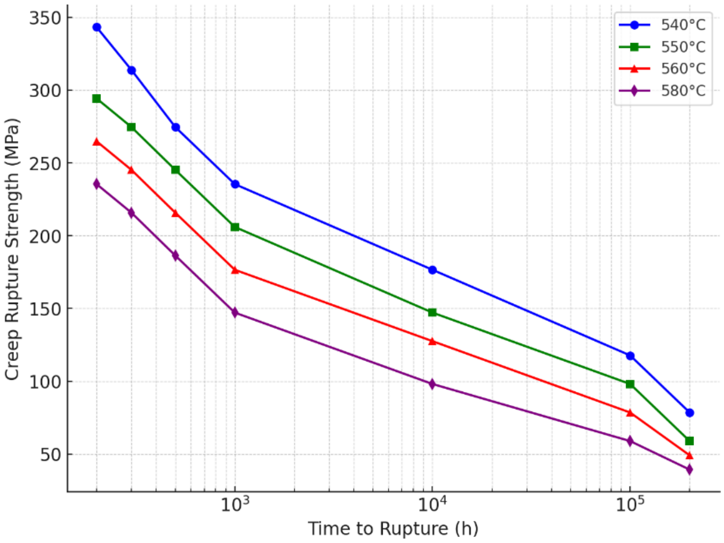

Figure 13. Creep rapture strength of 14MoV6-3 [86].

### Ageing of power plant steel materials

The International Atomic Energy Agency (IAEA) has provided the following technical definition of aging. The term "aging" refers to the ongoing, time-dependent deterioration of materials brought on by typical operating and transient circumstances. Degradation is used in this thesis as a synonym for material aging [28]. Most of the electrical power-generating plant components for both conventional and nuclear power plants operate at high temperature for extended periods. To determine the influence of long-term thermal ageing on the behavior of material it must be subjected to temperature in the range of 600 °C and 650 °C in the absence of stress then examine the evolution of microstructure [30]. The creep deformation and fracture mechanisms for materials under low levels of stress behaved differently from those under high stresses.

The ageing of the materials must be taken into consideration when estimating the lifespan of a structure or its components. The ability of a material to withstand an applied load can be significantly reduced by ageing mechanisms like corrosion, fatigue, and others by reducing its mechanical properties [87].

The fracture toughness of power plant steel can be impacted by ageing and creep at high temperature. Ageing can cause changes to the microstructure and mechanics of the material, while creep can cause deformation over time and result in decreased fracture toughness. The extent of the changes will depend on factors like temperature, stress, and material composition. Further experiments are needed to fully understand the effect of ageing and creep on the fracture toughness of 13HMF steel [88].

The 9Cr-1Mo (P9), 9Cr-1Mo-V-Nb (P91), 9Cr-1Mo-1W-V-Nb (E911), and 9Cr-0.5Mo-1.8W-V-Nb (P92) steels, which are utilized for thick section components of steam/fossil power plants in the working temperature range of 580-650 °C and pressure of 230 bars to 300 bars, are among the advanced creep-resistant materials [59]. Because of its high resistance to radiation and oxidation, P91 steel is considered a candidate material for out-of-core and in-core components of Gen IV reactors. P91 steels are used in petrochemical plants' high-pressure steam headers and piping as well as in power plants ultra-supercritical boilers' steam headers and superheaters [89]. For many decades, 9-12% Cr steels have been used as pipe materials in power plants all over the world. The prefixes P and T refer to plate and tube product forms of the steel, respectively.

Among the strongest steam pipe steel currently on the market is advanced tungsten and boron-modified 9% Cr martensitic steel (ASTM Grade P92) [90]. 620 $^{0}$C is its maximum application temperature. Because of this, it is now acknowledged as one of the leading candidates for high-temperature components of these plants [91].

## Historical developments

The invention of heat-resistant steels with high creep strength and acceptable creep ductility significantly improved power plant efficiency. The importance of material properties was not recognized until steam turbine bolts were damaged in the 1930s. This revealed that the strength of steels used in power stations at higher temperatures is heavily influenced by creep behavior throughout operation [21].

The application of single alloy molybdenum-vanadium steel dates to before World Conflict II, and the steel appears to have stood the test during the conflict. The challenging post-war supply situation played a significant role in the growth of this low-alloy, low-cost steel produced by West German Edelstahl and Roehren Werke. The creep rupture strength of steel 14MoV6-3 was superior to that of the higher alloyed steel 10CrMoV9-10 used in West Germany [92]. The easily weldable ferritic-pearlitic steels 15Mo3 and 13CrMo4-5, the ferritic-bainitic steel 10CrMo9-10, the less easily weldable bainitic-ferritic steel 14MoV6-3, and the high-alloy martensitic steel X20CrMoV12.1 were among the low alloy steels engineered in the 1930s and 1940s that successfully met the material requirements, primarily short-term creep rupture strength for power plant materials. Many thermal power plants still use conventional methods with maximum steam temperature of 540 $^{0}$C and pressures of 18.6 MPa, resulting in up to 33% power unit efficiency. These alloy steels were used for coils, temperature regulators, superheater chambers, and pipework that operated under creep conditions. Table 2 presents the innovative materials utilized to manufacture supercritical boilers.

Power production plants face environmental and economic constraints, leading to a focus on developing high-efficiency, low-emission systems. If the thermal efficiency of power plants can be increased, fuel Conserves fuel and reduces pollution [93]. Figure 14 compares the maximum service temperature for a 1,00,000-h stress rupture strength of 100 MPa between the stress rupture strengths of the new power station steels and the currently utilized steels. It is evident that as the steel composition becomes more complicated, the maximum service temperature rises.

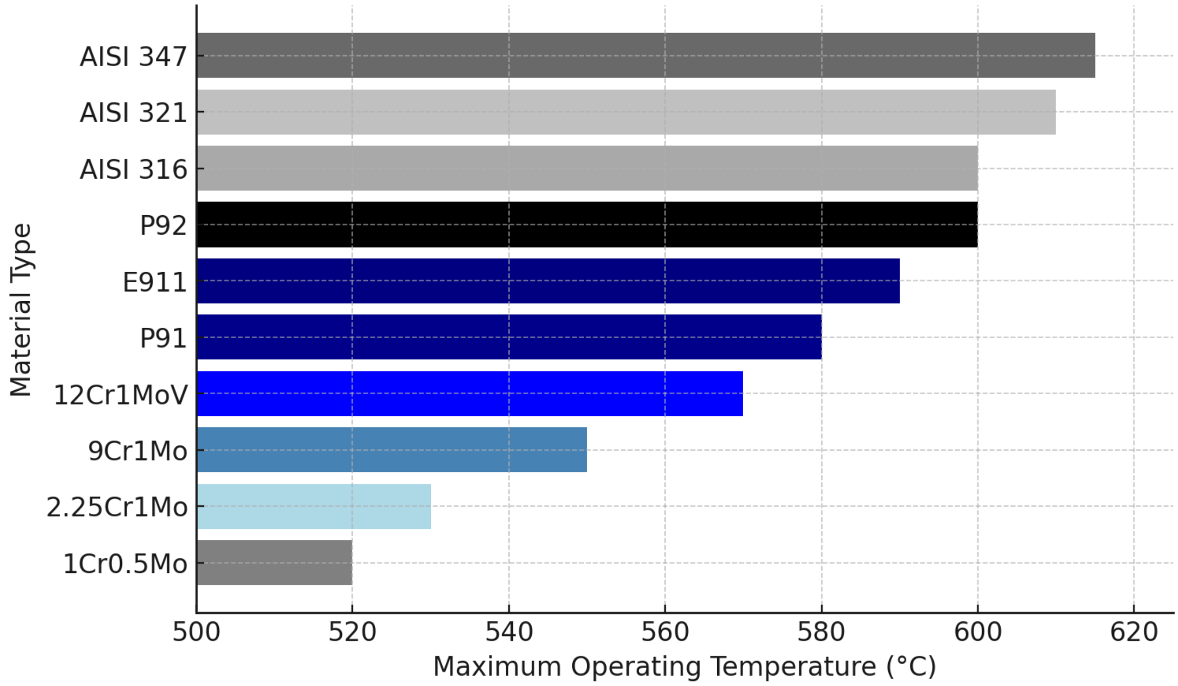

FIGURE 14: Stress rupture strengths of the currently utilized and the newly created power station steels [93].

The use of 9% chromium steel as parts of fast-breeder nuclear reactors attracted a lot of interest in the 1970s. The Oak Ridge National Laboratory created improved steel based on the well-known Fe9Cr1Mo steel which was in use since the 1950s in petrochemical plants. This improved steel was then included in the ASTM specifications under the designation P91 (ASTM 1986) [94]

Since the 1970s, experimentation has focused on developing steel processing procedures that produce improved characteristics than X20CrMoV12.1 steel. The steel NF616 (Nippon Steel 1991), which is now known as P92 in the ASTM specification, is a product of Nippon Steel's steel development program in Japan. P92 steel is a modified form of P91 steel with additions of 1.5–2.0 weight percent tungsten, a reduction in molybdenum from 1 to 0.5 weight percent, and additions of 0.001-0.002 weight percent boron. Compared to P91 steel, P92 has a higher temperature creep rupture strength. Table 5 and show a comparison of their composition and creep properties respectively.

According to Table 6 P91 and P92 have similar carbon content (0.07-0.13%), which adds to their strength and hardness. P91 has 0.85-1.05% Mo, but P92 contains just 0.35-0.55%. The reduced Mo content in P92 allows for more tungsten (W), which improves long-term creep resistance while increasing high-temperature strength and stability. The operating temperature, pressure, and creep life requirements of a component in a thermal power plant determine whether P91 or P92 is used.

TABLE 5: Steels presently used for critical and thick wall components of boiler.

| **Steel name** | **Composition** | **Temperature of application** | **Application/boiler part used** |
|---|---|---|---|
| T/P23, T/P24 | 2.25Cr–Mo, V, Ti, Nb, B, W | up to 550°C | Membrane walls |
| T/P91, T/P92, E911, PB2 | 9%CrMoV, W, Nb, N, B, Cu | up to 600°C | Superheater chambers, steam pipes, superheater coils |
| HCM12(A), EM12M, VM12, MARB2 | 12%CrMoV, W, Co, Nb, N, B, Cu | up to 620°C | Superheater coils, steam pipes |
| Austenitic steels & Ni superalloys | Austenitic matrix with improved composition | Withstands 560–700°C | Superheater elements, pipes, turbine regulator valves |

TABLE 6: The chemical properties of P91 and P92 steel-grades [95]

| Grade | C | Mn | P | S | Si | Cr | Mo | W |
|---|---|---|---|---|---|---|---|---|
| P91 | 0.07-0.13 | 0.3-0.6 | 0.02 | 0.01 | 0.2 -0.5 | 8-9.5 | 0.85-1.05 | - |
| P92 | 0.07-0.13 | 0.3-0.6 | 0.02 | 0.01 | 0.2-0.5 | 8-9.5 | 0.35-0.55 | 1.5-2 |

Despite being used for more than 20 years, there is every indication that the 9% Cr steels have high long-term stability since very few damages have occurred or been reported. According to Brett et al, leaks in British power plants occurred quite early due to failures in the heat-affected zone of P91 welding seams in high-pressure collectors. Another account of the disastrous P91 pipe disruption in the high-pressure line of the Chinese power plant Huadian Datong, which was brought on by manufacturing errors and quality problems, is available [96].

P92 steel has been the subject of several studies to examine the evolution of microstructure by holding steel specimens for a variety of times from short to relatively long periods in the absence of stress at temperature in the range of 600 °C and 650 °C to determine the influence of long-term thermal ageing on the behavior of steel [30]. In their study [31], experimental testing and numerical simulation results revealed that steel P91 exhibits good thermal ageing resistance and maintains high ductility even after extended thermal exposure (11,000 h at 650 °C).

G. Sasikala et al. [[97]] measure the fracture toughness parameter J for 0.2 mm crack extension, $J_{0.2}$ of P91 steel after accelerated thermal ageing (2900 h at 923 K). It was observed that thermal ageing of P91 material even for extensive durations has marginal effect on $J_{0.2}$. Pandey et al [59] measured impact of strain rate and notch geometry on the tensile characteristics and fracture mechanism of creep strength enhanced ferritic P91 steel.

Sklenicka et al [90] investigated the impact of short-term ageing in the past on the mechanical and creep characteristics of P92 steel. Yan et. al [98] found out that the toughness of G115 steel drops from 115 J toughness rating to just 36 J after the first 300 hours of the ageing process, and then nearly stabilizes as the ageing time is increased to 8000 hours.

### Ageing oxidation resistance

The resistance of a material to high-temperature corrosion, oxidation in the presence of water vapour, and spallation of the oxide coating is the second most important factor in determining its suitability for use in supercritical boilers. The boiler rupture caused by a flaw in the welding division, corrosion, overheating, and material degradation has devastating consequences. Chromium is the element responsible for oxidation resistance [93]. Increasing chromium concentration improves corrosion resistance, with a significant increase observed at chromium levels above 20%.

Coal ash corrosion differs from other fuels as it is influenced by flue gas $S_O2$ levels and ash $Na_2SO_4$ and $K_2SO_4$ content. In high concentrations, $Na_3Fe\ (SO_4)_3$, $K_3Fe(SO_4)_3$, and other basic iron sulfates can develop on the tube surface, causing severe corrosion. As the flue gas rises, ash collects on tube surfaces, leading to corrosion. It is especially severe on surfaces at a 45° angle with the upward flow of flue gas.

Yamada et, al. [99] aged the as-received SCS14A steels by first holding at 1100 C for 7.5 hours and then quenching them in water for homogeneity. Then, they were aged in an electric furnace in the air for up to 30,000 hours at temperature between 350 and 400 C. This was followed by recovery heating (RH) at 550 C for one hour after ageing to specifically remove the phase decomposition.

Vargars-Arista et, al [100] carried out the ageing of weld metal at 250 +/- $5^0$C using a Carbolite resistance oven with a digital controller. Byun et, al [101] used four large muffle furnaces (MTI Co. Model KSL-1200XL) to thermally age the CASS materials over an extended period. Using a K-type thermocouple that has a precision of 1 °C, a programmable controller was used to regulate the temperature of each furnace chamber. The temperature in the chamber varies spatially by roughly 5 °C. In the large capacity furnaces with the temperature controls set at 290, 330, 360, and 400 °C, the eight CASS materials and the two reference wrought materials were thermally aged for up to 30000 hours.

### Artificial accelerated ageing of specimen at elevated temperature

The quest to increase the design lifetime of fossil fuel power plants that operate for a long time at high temperature necessitates knowledge of the remaining component lifetimes. Without knowledge of the mechanical properties that exist after the period of operation (the actual mechanical properties), it is impossible to estimate residual lifetimes because the material's properties can deteriorate over time due to service loading and temperature ageing [81]. Accelerated ageing has been applied in various studies to simulate actual conditions [69].

Accelerated ageing has developed to meet the challenge of evaluating the integrity of long-service components and predicting plant life, scheduling, repairing, and replacing welds and old components, calculating the cost of component deterioration, cost of normal service, peak service, plant cycling, and safe periods of plant life extensions, and removing the cost of expensive full-size specimen tests [102]. Orlova et al [103] used high-temperature creeping to investigate microstructural development during high-temperature creeping of 9% Cr steel.

Modern fossil-fuel power plants have components made of ferritic steels with 1–12 weight per cent Cr and 0.5–1 weight per cent Mo that are intended for an operating temperature of up to 600 C. Over the past 20 years numerous studies on the mechanical properties and fracture toughness on P91 and P92 metals have been done. The processes of high-temperature creep deformation of P92 steel have been widely reported. From the survey there is not much data or research work on the effect of creep on fracture toughness degradation over a long time of operations.

### Assessing the residual reliability and durability of the operational elements of the power plant under creep conditions.

The industrial concept of failure often differs significantly from the textbook definition. In industrial definition, a component is considered to have failed when it is no longer capable of performing its intended function safely, reliably, and affordably. Any of these characteristics can indicate failure [104]. Although catastrophic component failures are rare, they have a significant impact on human lives in addition to the expenses of repairs, replacement power, and legal fees.

It is possible to categorize the general components of a remaining-life-assessment technique for a frequently observed failure scenario into regions as shown in Figure 15. Region I is associated with early, microscopic damage events that precede the onset of a macroscopic crack. These occurrences include the creation of creep holes and microcracks, the coarsening of precipitate phases, and dislocation rearrangements. The macrocrack’s propagation is correlated with Region II.

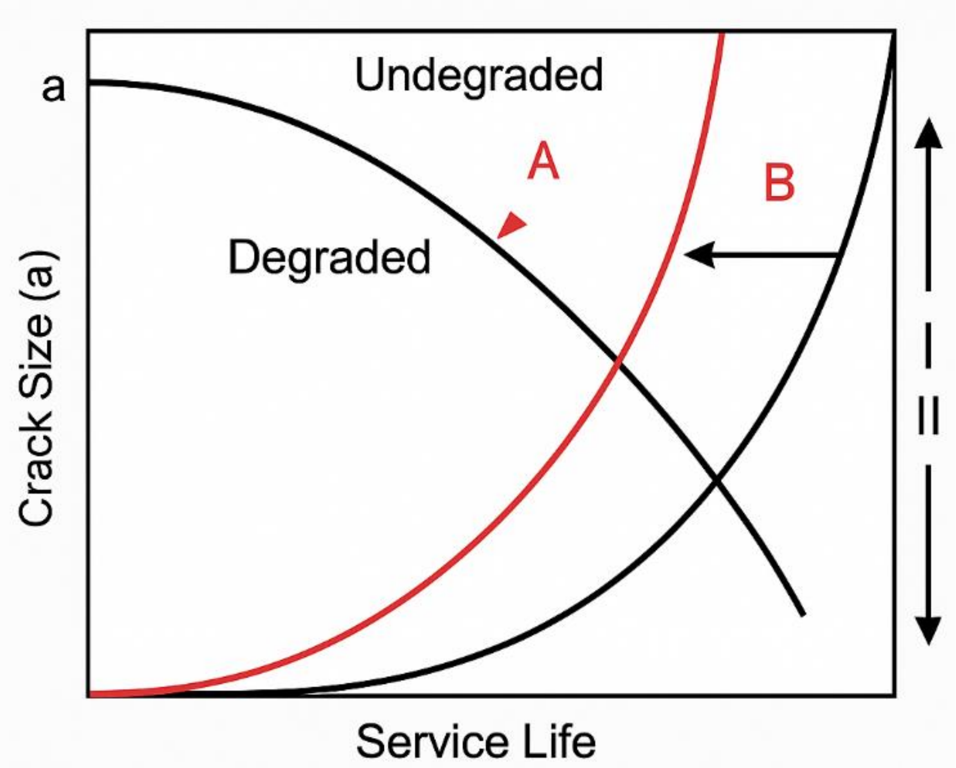

FIGURE 15: A typical failure scenario including crack initiation and propagation is illustrated using a remaining-life-assessment approach [104].

In area II, cracks expand until they reach critical size at which fast fracture takes place. Conventional NDE techniques are used for crack detection and sizing in region II. When crack initiation governs a component's failure, the component may be retired if any defects are found during an inspection or, more conservatively, if calculations indicate that a crack may have begun. Although creep or creep fatigue may cause cracks to begin and spread, another mechanism may be responsible for the final failures. One common failure scenario in heavy section components is the beginning and propagation of cracks at high temperatures during steady state operation, followed by brittle fracture at low temperatures during start-stop transients. Failure can also result from loading at low temperatures, such as hydrotesting pressure vessels and pipes or overspeed testing spinning parts at low temperatures.

Monitoring the structural integrity of components allows for the prediction of the duration for extended safe operation. According to Polish Standards PN-75/H-84024 (1975), the estimated lifetime of an element is based on material durability assessed in a creep test, which considers oxidation resistance, elements must last between 100,000 and 200,000 hours of use. In industrial applications, residual life typically accounts for 0.6-0.8 of overall life, with 1.0 indicating failure. In Europe, there are fewer experimental assessments for austenitic steel components under long-term creep circumstances [85].

Non-destructive testing assesses geometric aspects through response methodologies and hardness assessments. Non-destructive physical approaches are also employed to determine magnetic characteristics. Metallographic tests objectively analyze a material's microstructure and internal flaws. Figure 16 presents the schematic chart for assessing the state of a material and determining the residual durability of the operational elements under creep conditions. This method is used to assess functionality of important and critical parts used in pressure and turbine areas of the power boiler, which operate under the high temperature and pressure conditions, i.e. the superheater parts and main steam pipes.

The Institute for Ferrous Metallurgy, Silesian University of Technology, and RAFAKO S.A., Poland have developed testing criteria to evaluate a material's strength and integrity based on microstructural state. Ashby's fracture mechanism map for face-centered cubic (FCC) metals and alloys, with axes of normalized stress $\sigma/G$ and homologous temperature $T/T_m$, identifies the dominant mechanism that leads to fracture in less time than other mechanisms. In practice, the fracture mechanism map is more essential than the deformation mechanism map as it provides instructions for evaluating damage and estimating remaining life of plant components. The creep regime has three fracture mechanisms: intergranular, transgranular, and rupture.

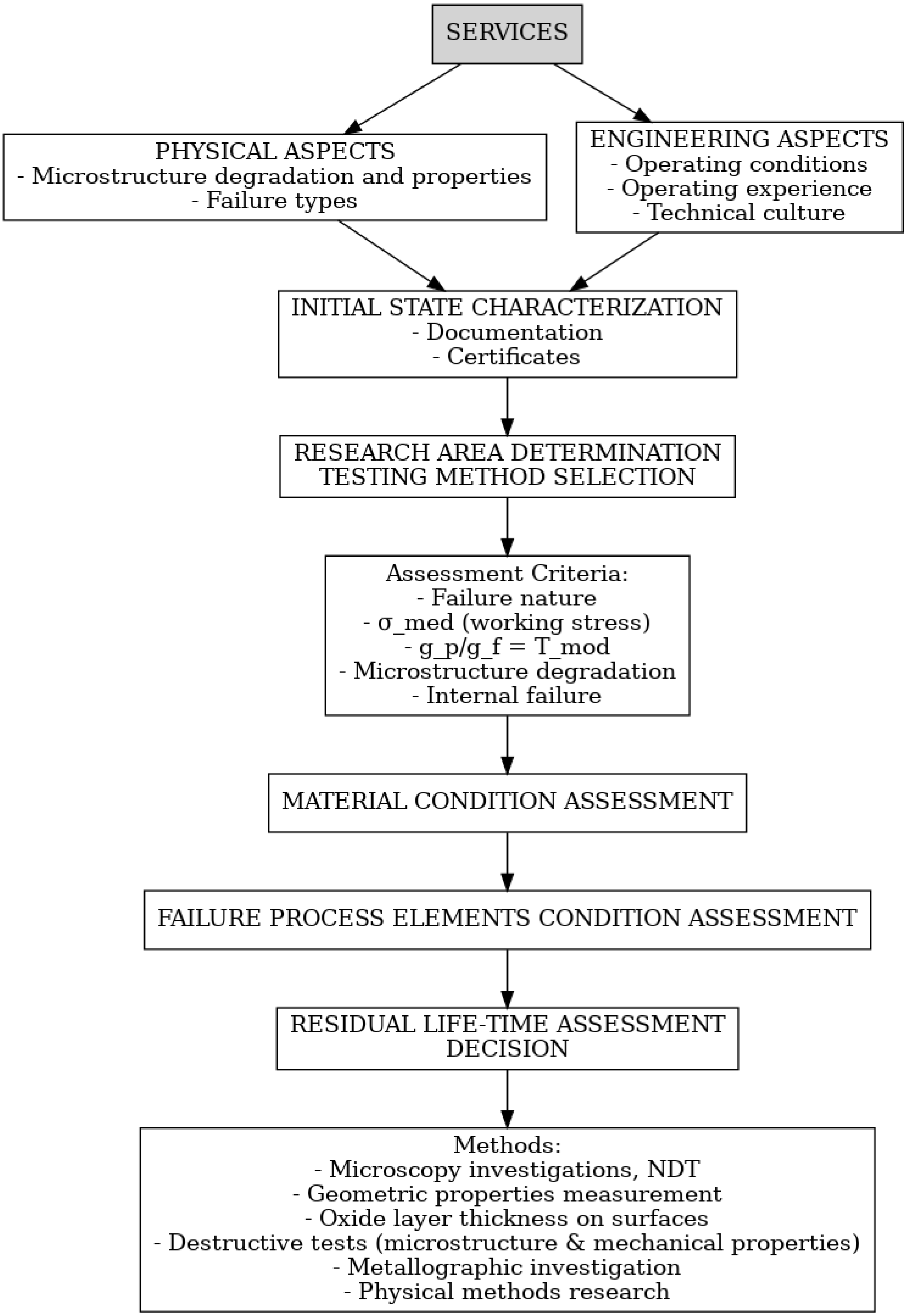

FIGURE 16: Methodology for evaluating the structural integrity of power plant materials and components [86].

## 2.4. Summary

The fracture toughness concept has been used for decades to assess material reliability in structures, but it has recently gained attention due to decreased service life caused by material degradation during operation. The $K_{IC}$ critical stress intensity factor is largely theoretical and constant among standards.

To address environmental and energy saving concerns, power plants have recently increased their steam conditions. Since 1960, various studies on heat-resistant steels for boiler and turbine applications have been carried out. Among the different steels produced for advanced steam cycles, significant development has been made in 9-12% Cr steels for boiler pipework and turbine components, as well as austenitic steels for superheater and reheater tubing. The most current 9-12% Cr steels have a creep rupture strength of 140 MPa at 600°C for 100,000 hours. To increase creep strength, alloying with tungsten reduces the amount of molybdenum present.

For reliability of power plants material must withstand continuous high-temperature operation, demanding specialized testing methods. The long-term creep service of the component, which is influenced by temperature and pressure, causes the material structure to alter, its functional qualities to deteriorate, and damage processes to emerge. The primary causes of the changes in qualities that restrict life are precipitation and transformations of carbides, changes in the shape of carbides, modification of the chemical composition of the substrate, and disintegration of the pearlite/bainite or tempered martensite areas (depending on the grade of steel).

Understanding material degradation mechanism enables improved predictive maintenance plans and reduces unexpected shutdowns. Computational modelling, non-destructive methods (NDT), and safety precautions are used to objectively assess a material's state. The assessment method and measurement vary based on the component type and function. In Polish power plant the assessment of integrity of components is done by assessing structural degradation using microstructural investigations in a scanning electron microscope, phase composition analysis of precipitations, hardness measurement are mostly used to assess the state of the material after long-term service. The use of carbide precipitation processes, as well as phase composition and carbide type content using X-ray phase analysis, for evaluating the condition of materials used in the pressure part of power boilers beyond the design work time, has the limitation of representing a very small microstructural area.

In Europe, there are fewer experimental assessments made of components made of austenitic steel subjected to long-term operation under creep conditions. There is limited research on the fracture toughness of ferritic–bainitic (pearlitic), martensitic and austenitic steels designed for use in pressure elements of power boilers Considering elastoplastic fracture behaviour, creep, and heat degradation. In this regard, the purpose of this work is to study the service life effect on the fracture toughness structure of power plant steel grade. Material degradation over time is mostly determined by creep flaws. Regardless of the degree of structural degradation, these flaws are crucial and decisive in determining an element's suitability for continued operation. The ageing of the materials must be taken into consideration when estimating the lifespan of a structure or its components. The ability of a material to withstand an applied load can be significantly decreased by a variety of ageing mechanisms, such as corrosion, fatigue, and others, by reducing its mechanical properties, such as tensile strength, yield strength, ductility, etc. Additionally, during the manufacturing process, small flaws can develop into cracks that may lead to component failure. It's crucial to comprehend how ageing affects a material's crack resistance.

# CHAPTER 3: FRACTURE TOUGHNESS VARIATIONS IN STEAM BOILER COMPONENTS AFTER A LONG PERIOD OF OPERATION

Long-term high-temperature and high-pressure operations cause microstructural changes in boiler tubes that reduce their load-bearing capacity and shorten their useful lifetimes. Failure happens when the load-bearing capacity drops below a critical threshold that is determined by the tube's geometry and operational characteristics. The SIF escalates with an increase in external loading. Once the SIF surpasses a critical threshold, the crack within the component initiates its growth. This critical threshold is known as the fracture toughness, denoted as $K_C$ or $K_{IC}$, which characterizes the material resistance to the unstable propagation of cracks. The thickness affects the constraint conditions at the crack tip with thin components having plane stress conditions and thick components having plane strain conditions. Plane strain conditions give the lowest fracture toughness value, which is a material property as depicted in Figure 17 below.

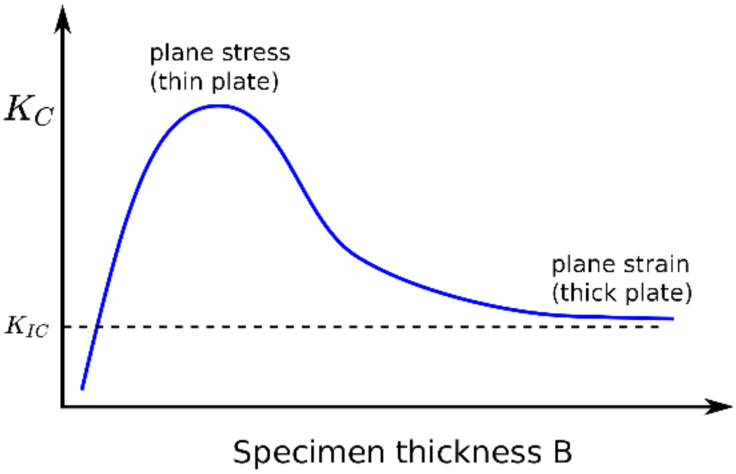

FIGURE 17: Impact of specimen thickness on fracture toughness.

The thermal mechanical fatigue loading on materials operating for long times over 20 years causes changes in the microstructure of the materials. This in turn affects the fatigue properties and crack resistance properties. This may cause crack formation and growth in the areas with stress concentrations. For chemical and energy plants most equipment have exceeded its design life of 100, 000 hours. It is therefore important to decide whether to keep them in operation. To do this new information on the status of the materials is needed. The technical state of the equipment used in the power industry may vary based on their history of operation [8]. The durability and structural integrity of elements subjected to high pressure and temperature are greatly compromised after long periods of operations [5]. Steam turbine unit malfunctions include pressurized parts, such as the tubing, piping, and pressure vessels that make up the system’s steam-generating section.

Creep, fatigue, creep-fatigue, and thermal fatigue are the main ways that high temperature components fail [105]. Even though these mechanisms may cause cracks to start and spread in heavy section components, startup-shutdown transients at low temperatures may ultimately result in failure. Power plants designed to supply the basic load are routinely powered down and then backed up. Variations in the steam temperature caused by power variations put components under thermo-mechanical stress, which causes material degradation and, ultimately, their failure [106]. Issues on the phenomena of fatigue and creep are well-known in the literature, but only as model fatigue processes carried out on suitable equipment from the initial state of the tested alloys. This calls for the regulation of ductile fracture propagation and safe pressure pipeline loading. In this situation, a safety standard for fracture arrest must be devised. Residual lifetime estimation is impossible without knowledge of mechanical properties after the actual time of operation [17]. Long-term use of several components necessitates a tailored strategy due to their unique operation. Evaluating the status of these plants becomes a research endeavor, with methodologies tailored to the operational circumstances and loading history [107]. Fracture toughness is therefore another important factor to consider. Considerable gains have been made both with respect to crack initiation and crack growth via the foregoing methods. Applying laboratory data to forecast component life has often been stymied by failure to model actual pressures, strain cycles, section size effects, environmental effects, and long-term degradation effects.

Large-scale chemical, thermal, nuclear, and petroleum sectors all make substantial use of creep-resistant steels. Resistance to environmental attack, creep rupture strength and ductility of the weld metal and heat affected zone, resistance to creep deformation and rupture, and sufficient ductility of the base material to prevent abrupt failure and to permit the material to deform rather than fracture in areas of high stress concentrations are some of the crucial factors to be considered when choosing such steels. According to the literature [8], steam pipeline failure is determined using static tensile tests, including tensile strength ($R_m$), yield strength ($R_{p02}$), elongation (A), and Vickers hardness (V), which are correlated with operating time. For analyzing toughness properties, a Charpy-V impact test is preferred compared to fracture toughness because it is relatively easy to perform.

Long term service exposure can reduce material toughness, leading to fast crack propagation and catastrophic brittle failure. Low-allow chromium, molybdenum, and vanadium cast steels are used to make the frames and valve chambers of steam turbines. When steel casts are operated at high temperatures for an extended period, certain processes take place that weaken their structure and reduce their useful qualities. Changes in the shape and type of carbides are among the primary causes of structure degradation, which in turn leads to a decline in crack resistance and a fall in creep resistance [108]. Turbine casings may break due to toughness losses caused by temper embrittlement, creep embrittlement, or stress relief cracking. To prevent fracture propagation, either machining (grinding) or welding should be used to fix the casing early on [109].

Researchers in a paper from 2006 [110] investigated the condition of the intermediate pipes of a steam turbine. They assessed the status of low cycle fatigue and Crack growth rate of the pipeline material after a long time of operation in elevated temperature conditions and stresses commonly experienced in chemical industrial plants. For tests done both at room and elevated temperature, they concluded that there is an increase in the fatigue life of the used specimen. the probable cause of this phenomenon is that long operating periods at elevated temperatures cause microstructural changes accompanied by dislocation movements and stress relaxation at the microscale level. This leads to an increase in the plasticity of the material and a reduction in strength. This is observed by both results of basic mechanical properties, cycle strain curves, and low cycle fatigue. An increase in relative elongation and narrowing was found to be caused by the long-term operation. In addition, the old material showed lower stress saturation compared to the new material when tested at the same level of strain amplitude.

The low fatigue strength of the new material compared to aged should be subjected to detailed analysis and research considering the structural condition of the crack formation process. The increase in the low cycle fatigue caused by long-term operation in thermal and mechanical stress does not necessarily imply an increase in the quality of the material over time. This is because the properties represent the global conditions of the material whereas the process of failure or fracture of pipes caused by the formation and growth of cracks are of local nature. Therefore, the improvement of fatigue life should not be taken on a face value to mislead meaning the properties of materials have improved [111].

They did a finite element analysis of equivalent stress distributions determined under the assumption of constraints on the thermal freedom of the pipelines and wear. They found out that the thermal expansion of the turbine produces a displacement of the pipeline connection points with the turbine along the Z-axis (boiler-turbine direction) and vertically (Y-axis). The magnitude of the displacements in the Z-axis was chosen based on data collected by the system that monitors the turbine operating parameters. The wear estimate was accomplished by assuming two types of boundary conditions specified by the displacements of the valve chambers in the computations. Hypothetical displacement values were expected to occur following the unit's rehabilitation operations in the scenario of improper delivery of live steam and warmed steam pipes to the valve chambers.

In another study [84], premature fracture of steam pipelines made of 14MoV6-3 steel specified for 100,000 hours of service life at 540 °C was investigated. They determined that the stress intensity factor ($K_{IC}$) was reduced by 17%. A review of the literature demonstrates that radial fracture toughness testing for pressure vessels and pipes is difficult due to the challenge of obtaining a standard specimen. As a result, arc-shaped specimens are frequently used to measure the thickness direction of pressure vessels [112].

Early service termination is the result of a complex stress state that includes torsion and/or bending components. The quick degradation of the microstructure demonstrates this fact, as well as the early creation of voids and the appearance of internal damage processes [113]. To forecast the date of the next technical inspection, decommissioning, or to fully justify continued equipment operation in the presence of a crack or after the end of its design lifetime, its structural integrity should be known [18]. The material's fracture behavior data is required for integrity assessment due to its loading range [15]. This ensures the prevention of brittle fracture; therefore, this work presents the state of fracture toughness of the components. The fracture toughness of pressure vessels and pipe material can be different for varying orientations.

The major study given in this chapter was published in international Journal of Pressure Vessels and Piping (Wacławiak K., Kipsang B., Farahani B. V., De Waele W.) [10].

## 3.1. Materials and methods

### Materials background

The tested materials were taken from a decommissioned 18K360 steam turbine unit with a 360 MW capacity that was operating at 535$^0$C and a pressure of about 15 MPa. The specific parts are the straight section of the primary steam pipeline connecting the valve chambers to the high- and medium-pressure parts of the turbine (hereafter referred to as the pipeline section and the valve chamber unit). Figure 18 present the valve chamber where the samples where extracted. The chemical composition of the sample steel after a long period of operation is given in Table 7.

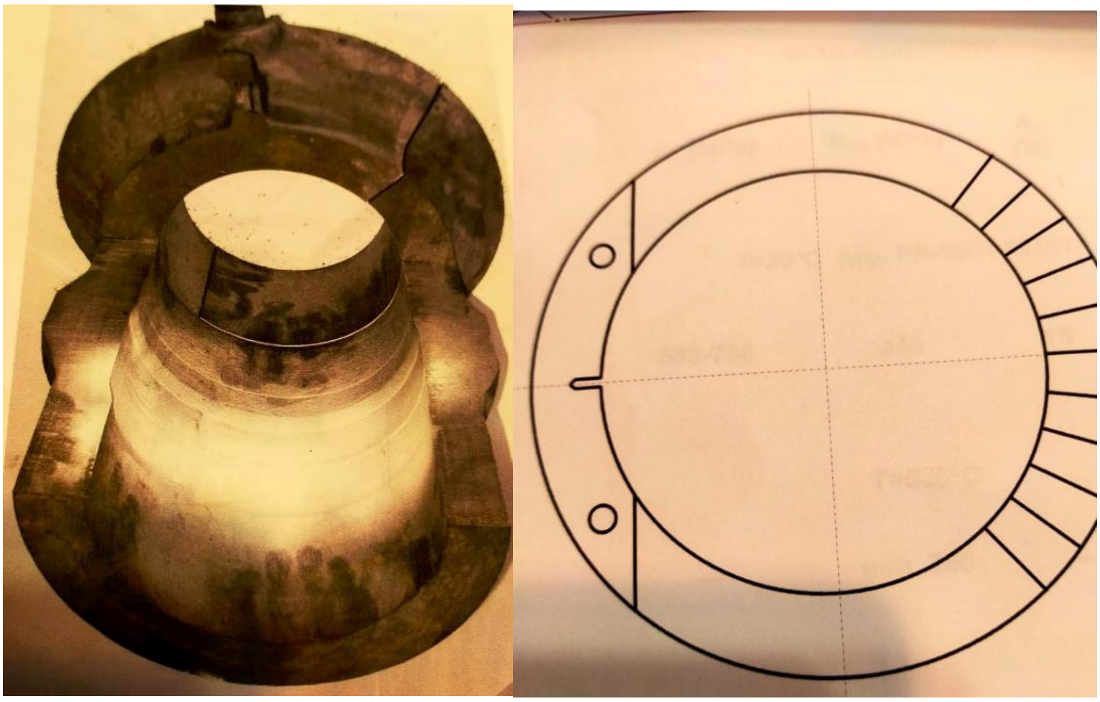

FIGURE 18. The valve chamber where the specimens were extracted.

The valve material is made of G17CrMoV5-10 (L17HMF) cast steel, while the pipeline is 14MoV6-3 steel (13HMF) grade. The dynamic loading of the steam pipeline causes a transverse pressure gradient while sections with rapid changes in the flow direction, such as the valve, become heavily loaded. Pressure oscillations can lead to it exceeding 10% of the operating pressure. Every experiment was repeated three times to check the statistical reproducibility of the experimental results.

The system was withdrawn from service after 105,000 hours of operation; during this time, there were 278 shutdowns for maintenance services. Distortion and cracking can cause damage to the high-pressure turbine casings. Distortion can be caused by heat gradients, quick startup and shutdown cycles, or load changes causing damage to the high-pressure turbine casings. These distortions can be caused by heat gradients, quick startup and shutdown cycles, or load changes.

TABLE 7: The nominal chemical composition of the sample materials 13HMF steel and l17HMF (wt.%) [17], [114].

| **Element** | **C** | **S** | **p** | **Mn** | **Si** | **Cr** | **Ni** | **V** | **Mo** | **Cu** | **Al** |
|---|---|---|---|---|---|---|---|---|---|---|---|
| 13HMF | 0.15 | 0.012 | 0.025 | 0.49 | 0.29 | 0.36 | 0.04 | 0.26 | 0.59 | 0.016 | <0.005 |
| L17HMF | 0.15 | 0.018 | 0.012 | 0.65 | 0.26 | 1.60 | - | 0.30 | 1.17 | - | - |

**Experimental procedures**

Only the radial pipe properties were examined. Three samples from each of the two sections were tested for statistical robustness. The standard arc-shaped tension specimens with a width-to-thickness ratio of 2:1 was machined for the fracture toughness test.

Specimens were machined out of cylindrical geometries. The axis of the specimens was parallel to the pipes' axis. The crack of the specimen measures was normal to the circumference, and the propagation direction was radial; the reference direction of the arc-shaped specimen is designated C-

R [19]. The samples were extracted according to the scheme in Figure 19 with individual sections of the component delivered for testing. Table 8 presents the dimensions of the specimens from Valve and pipe samples.

TABLE 8: Geometrical dimensions of the arc-shaped specimens

| Component | **Thickness B [mm]** | **Width W [mm]** | **Chord L [mm]** | **Offset X [mm]** | **Crack length a [mm]** |
|---|---|---|---|---|---|
| Valve | 18 | 36 | 222 | 18 | 18 |
| Pipeline | 20 | 40 | 250 | 20 | 20 |

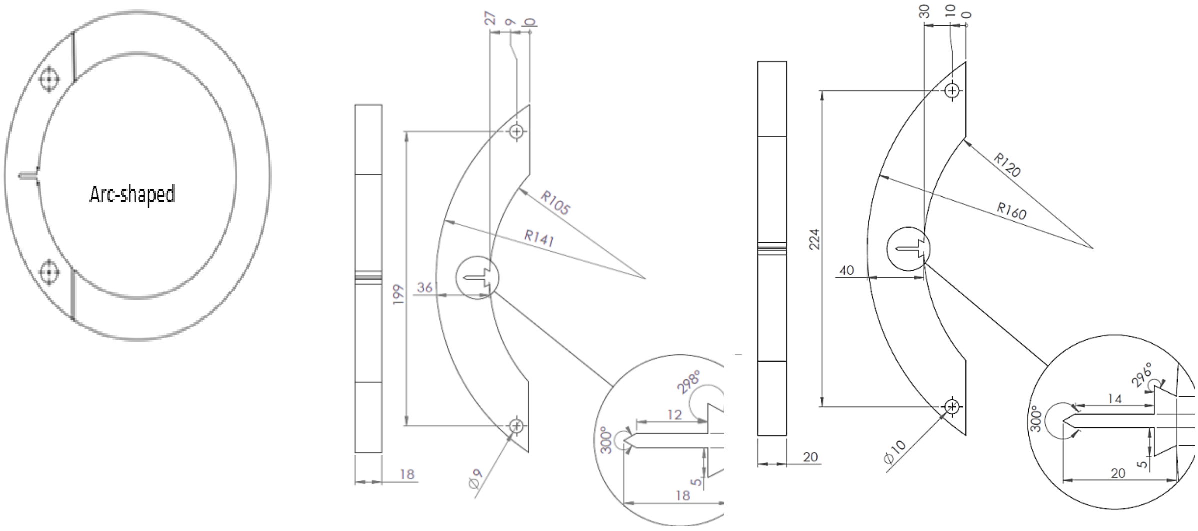

(a) (b) (c)

FIGURE 19: Analyzed specimens: location of the sample in the components (a), schematics diagram of the arc-shaped specimen of the valve (b), and pipeline specimen (c).

Fatigue pre-cracking was undertaken using a sinusoidal waveform of stress ratio R = 0.1, where R = σmin/σmax is used with an initial crack depth ratio of $\frac{a_0}{W} = 0.5$. Fracture toughness tests were conducted at room temperature at a constant crosshead speed of 274 N/s. Hence, a quasi-static nature was ensured using a hydraulic MTS Landmark universal testing machine with a load cell capacity of 100 kN. Special clevises were used for attachment, as shown in Figure 20.

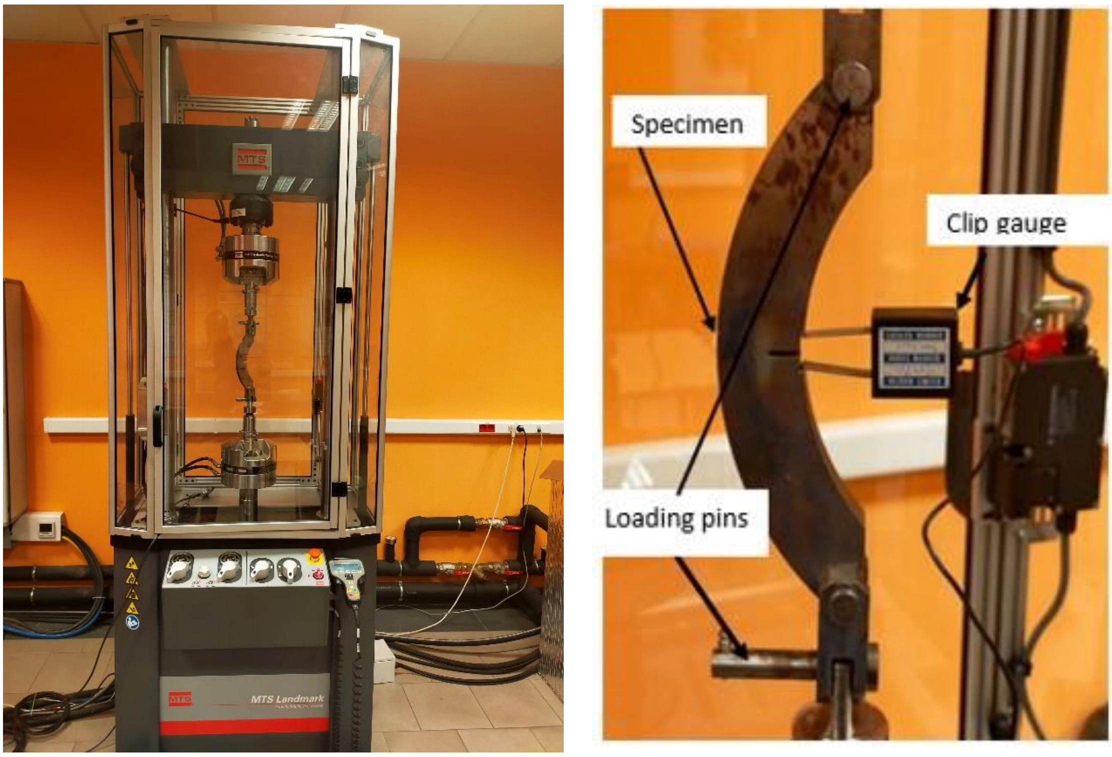

(a) (b)

FIGURE 20: Experimental set-up: MTS Landmark testing machine (a) and clevis and clip gauge extensometer (b).

The load and mouth opening displacement were measured and recorded with an Instron AR/1627-1 clip-gauge extensometer of 10 mm gauge length as shown in Figure 21. The specimen had suitable integrally machined knife edges.

Samples were prepared for microstructural analysis using normal metallographic techniques of grinding and polishing. Waterproof SiC emery papers were employed to polish the specimens' surfaces. Polishing with 3 and 1 µm diamond suspension on a disc polisher resulted in a mirror-like surface. This facilitated improved microstructural observation. Samples were nital-etched for microstructural analysis. Light microscopy was used to analyze the microstructure of the specimens, including both pipe and valve components.

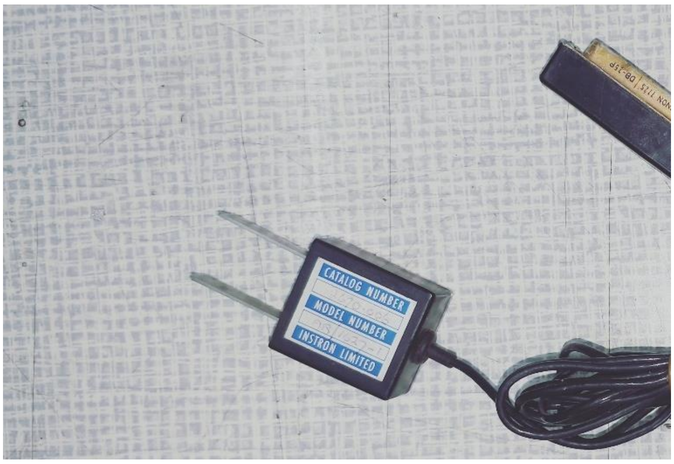

FIGURE 21: INSTRON AR/1627-1 clip gauge used for measuring the load line displacement.

### Numerical modeling

The numerical assessment was conducted using the FEM formulation, which is extended to the principles of linear elastic fracture mechanics (LEFM). The finite element model was created and analyzed in Abaqus/Standard and configured as a shell model with the specimen thickness defined as the mid-surface for the analysis. The notch was modeled using a contour integral definition based on the maximum energy release rate criterion. This approach calculates the fracture toughness while considering the presence of 20 contour integrals located ahead of the crack tip.

To obtain an alternative solution, the model was solved through FEM with formulation simulated in Abaqus (Dassault Systèmes Simulia Corp, Johnston, RI, USA). The geometry of the studied numerical models is depicted in Figure 22. In Figure 23 the FE mesh assigned to the model and the boundary conditions application. As seen in this figure, two reference points, $RP_1$ and $RP_2$, were allocated to the model being kinematically coupled with the corresponding holes in the top and bottom specimen's sides to simulate the applied load and fixation for restricting displacement along the X and Z axis and rotation in the Y axis respectively. The FE mesh includes a total number of 4184 nodes and 4045 linear quadrilateral elements of type S4. A denser mesh was assigned to the notch region where the fracture toughness was calculated. A coarse mesh of was used for the rest of the model to reduce computational cost.

The standard pin loaded SENT specimen is outlined in BS 8571:2018 [45], as shown in Figure 24. It is made by the material conforming to the mechanical properties Presented in Table 9. Following the BS 8571:2018 standard, a reference solution for the fracture toughness of the pin loaded SENT specimens, denoted$K_{IC}^{REF}$ (the critical stress intensity factor) is calculated.

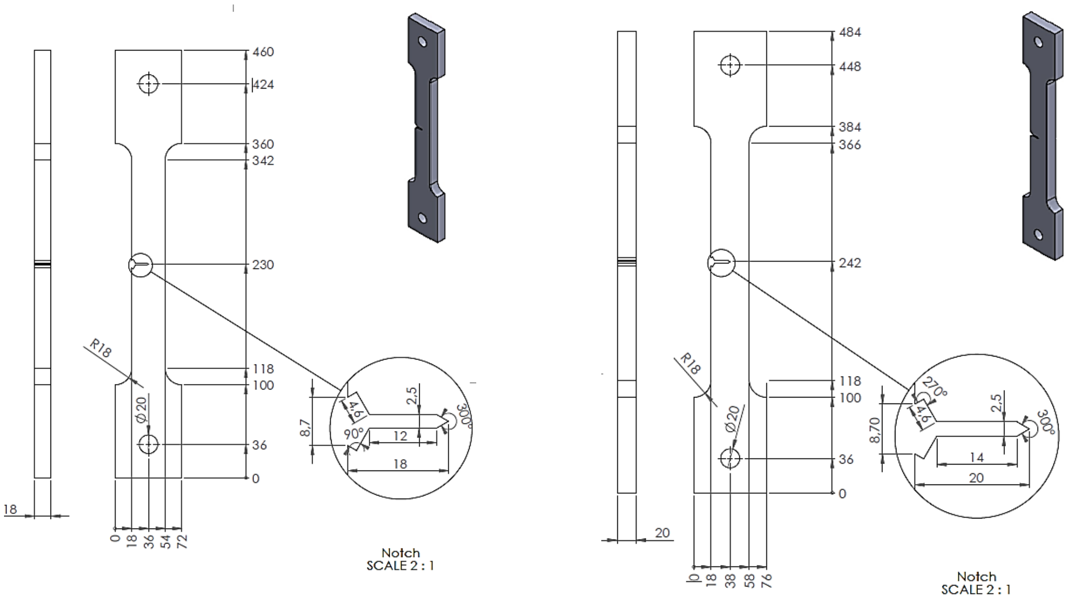

a) b)

FIGURE 22. Single edge notch tension, SENT, specimen, a) valve and b) pipe.

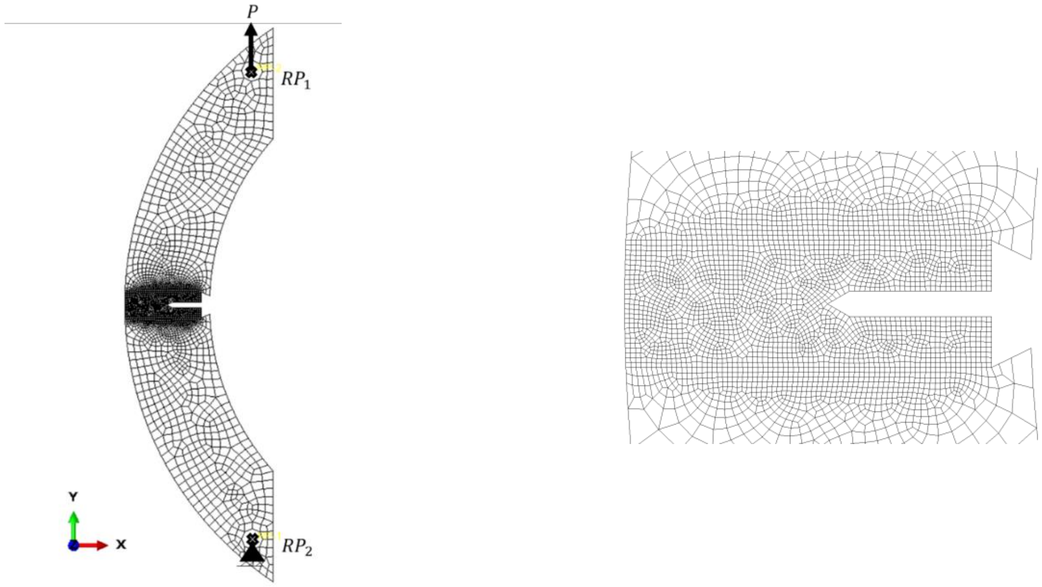

FIGURE 23: FE mesh of the at model with detail on the notch zone.

TABLE 9: Mechanical properties used in numerical modeling.

| Property | Value |
|---|---|
| Young’s modulus | $E = 190 \times 10^3, MPa$ |
| Poisson’s ratio | $\upsilon = 0.29$ |
| Yield stress | $R_{p0.2} = 365, MPa$ |
| Ultimate tensile strength | $R_m = 490 - 690, MPa$ |
| Density | $\rho = 7900, \quad \frac{kg}{m^3}$ |

The SENT specimens of dimensions presented in Table 10 were for numeric simulations.

TABLE 10: Reference fracture toughness obtained for the sent specimen.

| **SENT - Valve** | **SENT – Pipe** |
|---|---|
| $W = 36, mm$ | $W = 40, mm$ |
| $B = B_N = 18, mm$ | $B = B_N = 20, mm$ |
| $a_0 = 18, mm$ | $a_0 = 20, mm$ |
| $P = 17.5, kN$ | $P = 18.5, kN$ |
| $K_{IC}^{REF} = 18.15$, MPa·m$^{1/2}$ | $K_{IC}^{REF} = 16.38$, MPa·m$^{1/2}$ |

The FEM within the Abaqus simulation framework was implemented. Figure 25 illustrates the FE mesh that was applied to the model, along with the implementation of boundary conditions. Two reference points were introduced, denoted as $RP_1$ and $RP_2$. These reference points were strategically positioned within the model to establish kinematic coupling with the corresponding holes located on the top and bottom sides of the specimen. This set-up effectively defined the conditions for simulating the applied load and fixation, and alternative solutions for the given problem to be explored. The FE mesh comprises a total of 4028 nodes and 3904 elements. These elements consist of 3832 linear quadrilateral elements of type S4R and 72 linear triangular elements of type S3. Notably, a finer mesh has been specifically defined within the notch region to capture details with higher resolution.

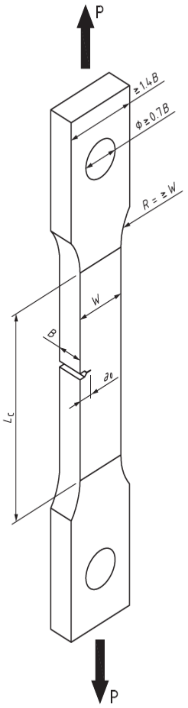

Figure 24: Directly pin-loaded single-edge notched tension specimen.

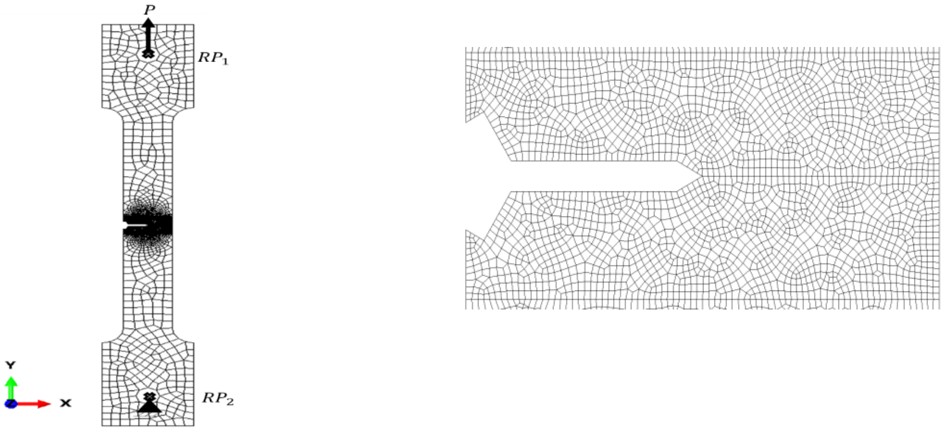

FIGURE 25: FE mesh of SENT model with detail on the notch zone.

## 3.2. Results

### Experimental determination of fracture toughness

During the experimental test, the force–mouth opening displacement curve is recorded, and the $P_Q$ value is determined. Figure 26 presents a plot of the results. The figure shows stable crack propagation during the increasing of the load. The fracture toughness results are summarized in Table 11 and Table 12 for the pipeline section and the valve chamber, respectively. It is noticeable that there is a significant difference between the fracture toughness of the pipe tube material and the valve chamber material.

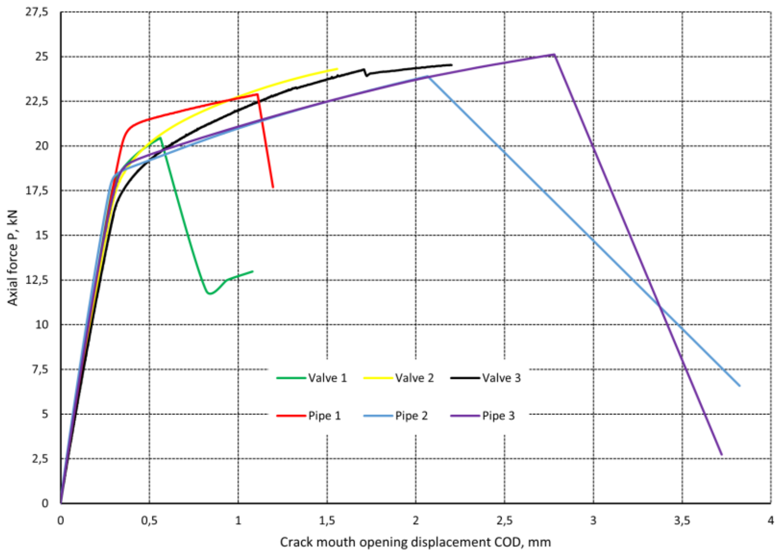

FIGURE 26: Load–line displacement curves of the tested specimens.

The fracture toughness, $K_Q$, is calculated using the following Equations (3.1) and (3.2) (provided in the standards [53]):

$$\boldsymbol{K_Q} = \frac{\boldsymbol{P}}{\boldsymbol{B}\sqrt{\boldsymbol{W}}}\left(\frac{3\boldsymbol{X}}{\boldsymbol{W}} + 1.9 + 1.1.\frac{\boldsymbol{a}}{\boldsymbol{W}}\right)\left[1 + 0.25\left(1 - \frac{\boldsymbol{a}}{\boldsymbol{W}}\right)^2\left(1 - \frac{\boldsymbol{r1}}{\boldsymbol{r2}}\right)\right]\boldsymbol{f}\left(\frac{\boldsymbol{a}}{\boldsymbol{W}}\right), \qquad (3.1)$$

where:

$$\boldsymbol{f}\left(\frac{a}{W}\right) = \frac{\frac{\sqrt{a}}{W}}{(1-\frac{a}{W})^{3/2}}\left[3.74 - 6.30\frac{a}{W} + 6.32\left(\frac{a}{W}\right)^2 - 2.43\left(\frac{a}{W}\right)^3\right]. \tag{3.2}$$

Here, P is the critical fracture load, PQ (applied to specimen) B is the thickness of the specimen, W is the specimen width, a is the crack length, and X is the loading hole offset.

TABLE 11: Experimental results of the pipeline component arc-shaped tension specimens.

| **Parameter** | **Specimen 1** | **Specimen 2** | **Specimen 3** | **Average** |
|---|---|---|---|---|
| $P_{max}$, kN | 22.88 | 25.11 | 23.90 | 23.96 |
| $P_{Q}$, kN | 19.00 | 18.5 | 18.00 | 18.50 |
| $P_{max}/P_Q$ | 1.20 | 1.35 | 1.33 | 1.29 |
| $K_Q$, MPa·m$^{1/2}$ ($K_Q \neq K_{IC}$) | 71.13 | 69.25 | 67.38 | 69.25 |

TABLE 12: Experimental results of the valve chamber arc-shaped specimens.

| **Parameter** | **Specimen 1** | **Specimen2** | **Specimen 3** | **Average** |
|---|---|---|---|---|
| $P_{max}$, kN | 20.45 | 24.40 | 24.53 | 23.13 |
| $P_Q$, kN | 18.00 | 17.5 | 17.00 | 17.50 |
| $P_{max}/P_Q$ | 1.14 | 1.39 | 1.44 | 1.32 |
| $K_Q$, MPa·m$^{1/2}$ | 78.94 | 76.75 | 74.56 | 76.75 |

### Results of numerical modelling

Table 13 reports $K_{IC}^{REF}$ calculated for different applied loads, $P$, for AT specimens on the valve and pipe specimens. Numerical simulations are conducted, and the results of the longitudinal displacement and stress fields for AT specimens and valve shape have been extracted, as depicted in Figure 27 and Figure 28 respectively. When examining the displacement fields, one can infer that as the applied load increases, the maximum displacement in the loading direction also increases.

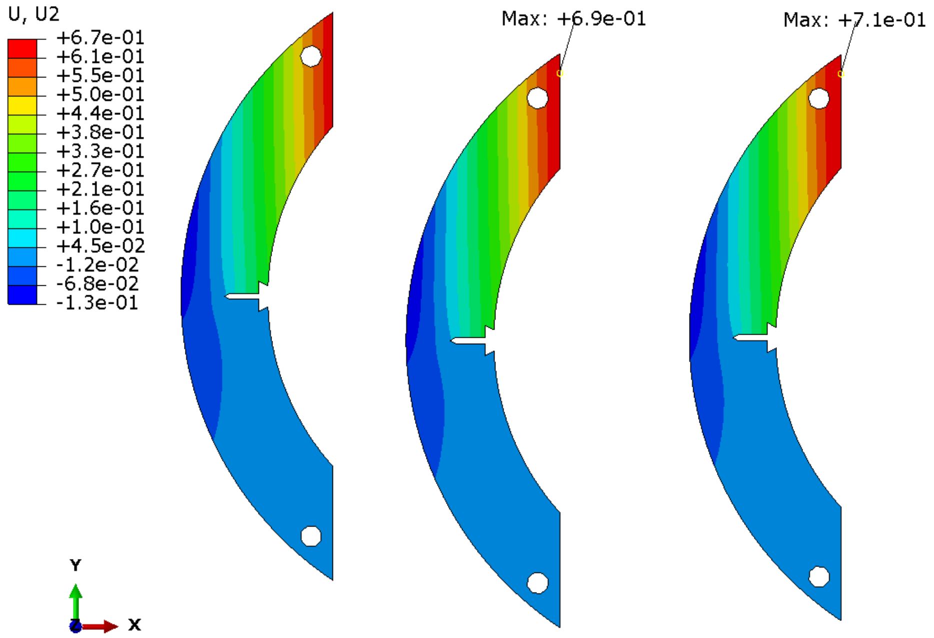

a) b) c)

FIGURE 27: Longitudinal displacement obtained from the fem model for at specimen and valve shape for different loading conditions: a) 17, b) 17.5, and c) 18 kN, values in mm.

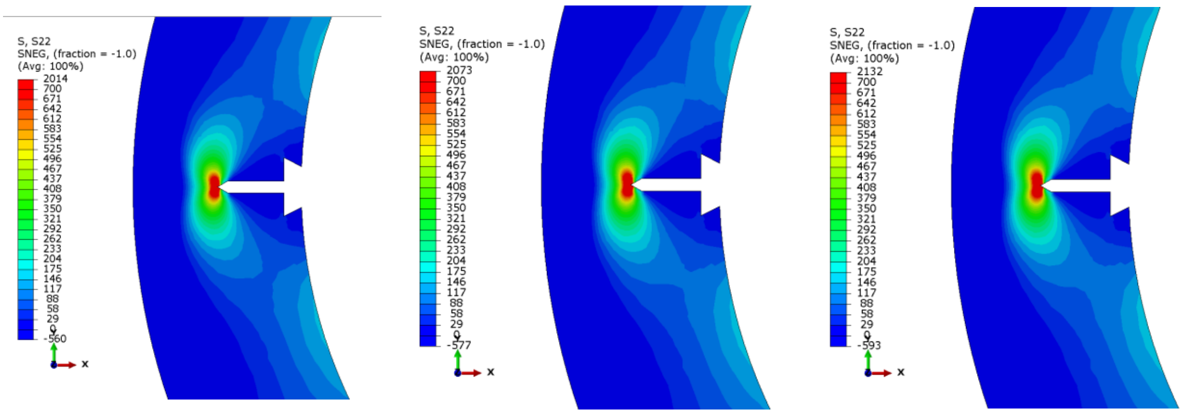

a) b) c)

FIGURE 28: longitudinal stress field obtained from the fem model for at specimen and valve shape for different loading conditions: a) 17, b) 17.5, and c) 18 kN, values in MPa.

The stress profiles indicate that the crack tip is responsible for the highest stress value, primarily owing to the stress gradient. As the applied load increases, the maximum stress value also rises, and this peak stress value is associated with a single node located at the crack tip. In the area of peak stress, it can be stated that voids begin to nucleate, and the region between the crack tip and the voids exhibits behavior like a specimen under tension. Consequently, micro-voids develop within this region, coalesce, and contribute to the extension of the crack.

The longitudinal displacements and stress fields obtained from the FEM model for AT pipe specimen for different loading conditions for the pipe model are presented Figure 29 and Figure 30 respectively.

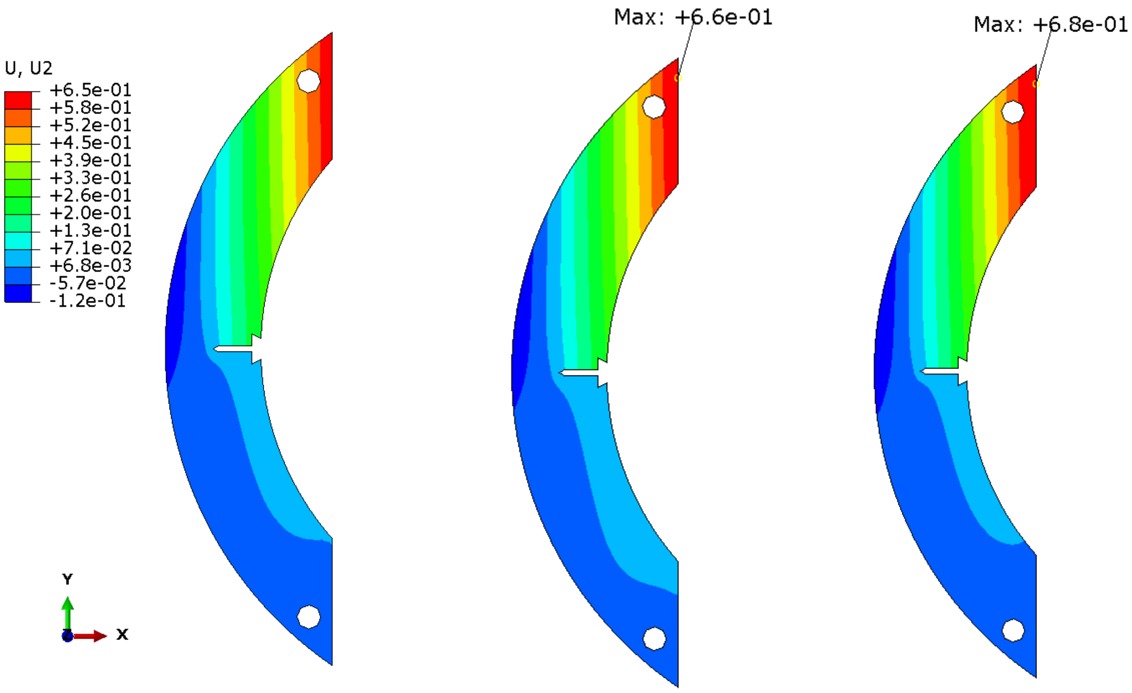

a) b) c)

FIGURE 29: Longitudinal displacement obtained from the FEM model for AT specimen and pipe shape for different loading conditions: a) 18, b) 18.5 and c) 19 kN, values in mm.

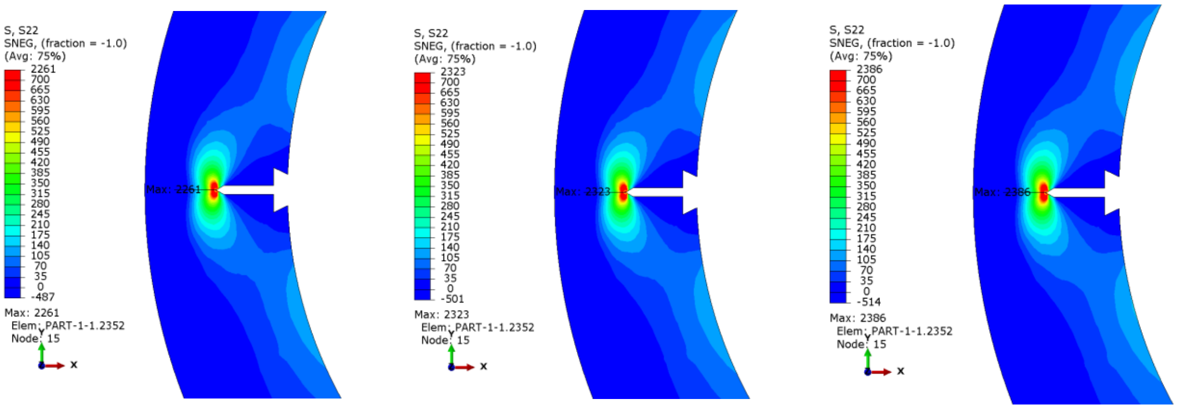

a) b) c)

FIGURE 30: Longitudinal stress field obtained from the FEM model for AT specimen and pipe shape for different loading conditions: a) 18, b) 18.5, and c) 19 kN, values in MPa.

TABLE 13: Numerical fracture toughness $K_{IC}$, MPa.$m^{1/2}$ obtained from FEM for AT Specimens and different contour integrals.

| | **AT, Valve** | | | **AT, Pipe** | | |
|---|---|---|---|---|---|---|
| **Contour** | $\boldsymbol{P} = 18, kN$ | $\boldsymbol{P} = 17.5, kN$ | $\boldsymbol{P} = 17, kN$ | $\boldsymbol{P} = 19, kN$ | $\boldsymbol{P} = 18.5, kN$ | $\boldsymbol{P} = 18, kNs$ |
| 1 | 68.98 | 67.06 | 65.15 | 65.22 | 63.51 | 61.79 |
| 2 | 74.86 | 72.78 | 70.70 | 68.09 | 66.30 | 64.50 |
| 3 | 75.64 | 73.54 | 71.44 | 68.76 | 66.95 | 65.14 |
| 4 | 76.11 | 74.00 | 71.88 | 69.21 | 67.39 | 65.57 |
| 5 | 76.51 | 74.38 | 72.26 | 69.52 | 67.69 | 65.86 |
| 6 | 77.12 | 74.98 | 72.84 | 70.08 | 68.23 | 66.39 |
| 7 | 77.61 | 75.46 | 73.30 | 70.54 | 68.69 | 66.83 |
| 8 | 77.87 | 75.70 | 73.54 | 70.76 | 68.90 | 67.04 |
| 9 | 77.97 | 75.80 | 73.64 | 70.89 | 69.03 | 67.16 |
| 10 | 78.08 | 75.91 | 73.74 | 70.97 | 69.10 | 67.23 |
| 11 | 78.14 | 75.97 | 73.80 | 71.03 | 69.16 | 67.29 |
| 12 | 78.17 | 76.00 | 73.83 | 71.07 | 69.20 | 67.33 |
| 13 | 78.20 | 76.03 | 73.85 | 71.09 | 69.22 | 67.35 |
| 14 | 78.24 | 76.06 | 73.89 | 71.11 | 69.24 | 67.37 |
| 15 | 78.25 | 76.07 | 73.90 | 71.14 | 69.27 | 67.40 |
| 16 | 78.26 | 76.08 | 73.91 | 71.14 | 69.27 | 67.40 |
| 17 | 78.26 | 76.09 | 73.91 | 71.15 | 69.28 | 67.41 |
| 18 | 78.26 | 76.09 | 73.92 | 71.16 | 69.28 | 67.41 |
| 19 | 78.27 | 76.10 | 73.92 | 71.16 | 69.29 | 67.42 |
| 20 | 78.27 | 76.09 | 73.92 | 71.15 | 69.28 | 67.41 |

Following the numerical solutions, the average fracture toughness was computed and compared with the reference solution proposed by the ASTM standard. Their results are presented in Table 14 and Table 15.

TABLE 14: Fracture toughness obtained for AT valve specimen for different applied loads.

| **Load $\boldsymbol{P}, \boldsymbol{kN}$** | $\boldsymbol{K_{IC}^{FEM}}$, MPa.m$^{1/2}$ | $\boldsymbol{K_{IC}^{REF}}$, MPa.m$^{1/2}$ | **Deviation** (%) |
|---|---|---|---|
| **18.0** | 77.15 | 78.94 | -2.26 |
| **17.5** | 75.01 | 76.75 | -2.27 |
| **17.0** | 72.87 | 74.56 | -2.27 |

TABLE 15: Fracture toughness obtained for AT pipe specimen for various applied loads.

| **Load $\boldsymbol{P}, \boldsymbol{kN}$** | $\boldsymbol{K_{IC}^{FEM}}$, MPa.m$^{1/2}$ | $\boldsymbol{K_{IC}^{REF}}$, MPa.m$^{1/2}$ | **Deviation** (%) |
|---|---|---|---|
| **19.0** | 70.26 | 71.13 | -1.22 |
| **18.5** | 68.41 | 69.25 | -1.21 |
| **18.0** | 66.56 | 67.38 | -1.21 |

The deviation is calculated according to the expression:

$$\left[\frac{K_{IC}^{FEM}-K_{IC}^{REF}}{K_{IC}^{REF}}\right]100\% \qquad (3.3)$$

The numerical simulations of the SENT specimen have been carried out, and the $\boldsymbol{K_{IC}^{FEM}}$ calculated for a total number of 20 contour integrals as presented in Table 16.

Table 16: Numerical FEM fracture toughness $K_{IC}$, MPa.m$^{1/2}$ obtained for SENT specimens and different contour integrals.

| | **SENT Valve** | **SENT Pipe** |
|---|---|---|
| **Contour** | $\boldsymbol{P} = 17.5, kN$ | $\boldsymbol{P} = 18.5, kN$ |
| 1 | 12.08 | 12.17 |
| 2 | 17.23 | 15.70 |
| 3 | 17.57 | 15.78 |
| 4 | 17.73 | 16.01 |
| 5 | 17.81 | 16.03 |
| 6 | 17.94 | 16.14 |
| 7 | 18.03 | 16.23 |
| 8 | 18.08 | 16.27 |
| 9 | 18.10 | 16.29 |
| 10 | 18.12 | 16.30 |

| | | |
|---|---|---|
| 11 | 18.13 | 16.31 |
| 12 | 18.14 | 16.31 |
| 13 | 18.14 | 16.32 |
| 14 | 18.15 | 16.33 |
| 15 | 18.15 | 16.33 |
| 16 | 18.15 | 16.33 |
| 17 | 18.15 | 16.34 |
| 18 | 18.15 | 16.33 |
| 19 | 18.15 | 16.33 |
| 20 | 18.15 | 16.35 |

Table 17 presents a comparison of the fracture toughness results obtained from both the reference and FEM solutions for the SENT geometry. Note that $K_{IC}^{FEM}$ represents the average value of the results presented in Table 16. Figure 31 and Figure 32 accordingly present the longitudinal stress and displacement contours for the SENT specimens, respectively.

Table 17: Fracture toughness obtained for SENT specimens.

| | **SENT – Valve** | **SENT – Pipe** |
|---|---|---|
| **Load** $\boldsymbol{P, kN}$ | 17.5 | 18.5 |
| $\boldsymbol{K_{IC}^{FEM}}$, MPa.m$^{1/2}$ | 17.71 | 16.01 |
| $\boldsymbol{K_{IC}^{REF}}$, MPa.m$^{1/2}$ | 18.15 | 16.38 |
| **Deviation** (%) | -2.44 | -2.28 |

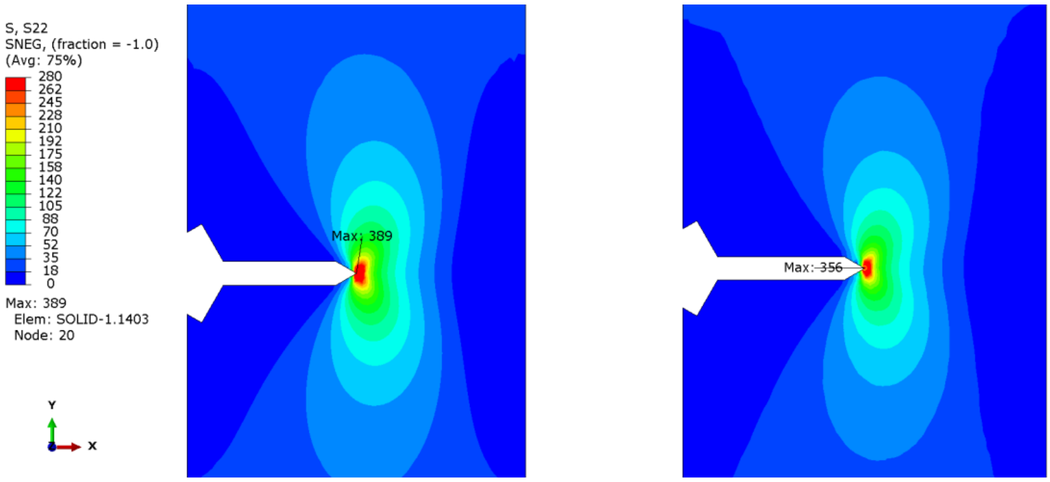

FIGURE 31: Longitudinal stress field obtained from the FEM model for SENT specimen: a) valve and b) pipe shape, values in MPa.

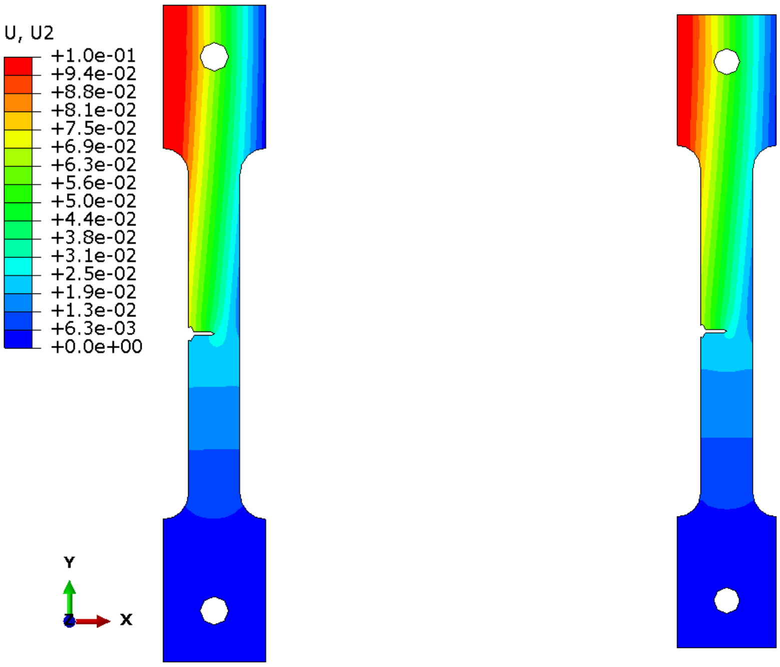

(a) (b)

FIGURE 32: Longitudinal displacement profile obtained from the FEM model for SENT specimen: valve (a) and pipe (b), values in mm.

## Fractography and microstructure

To a certain degree, fracture analysis can also be used to assess how the mechanical properties of corroded steel have degraded, and the fracture morphology can always provide crucial details and significant information about the fracture behaviors. To examine the fracture surface, the tested specimens were broken by uniaxial tensile loading. A metallographic examination of the fractured surfaces of the specimens reveals the mechanism of the failure in the two materials. Figure 33 shows the fractured surface of the pipe material and the valve chamber material scanned by a digital camera. Microdelaminations and cleavage fragments indicate steel embrittlement. The valve has a brittle trans-crystalline fractured structure, while the pipeline has a brittle intergranular fracture structure.

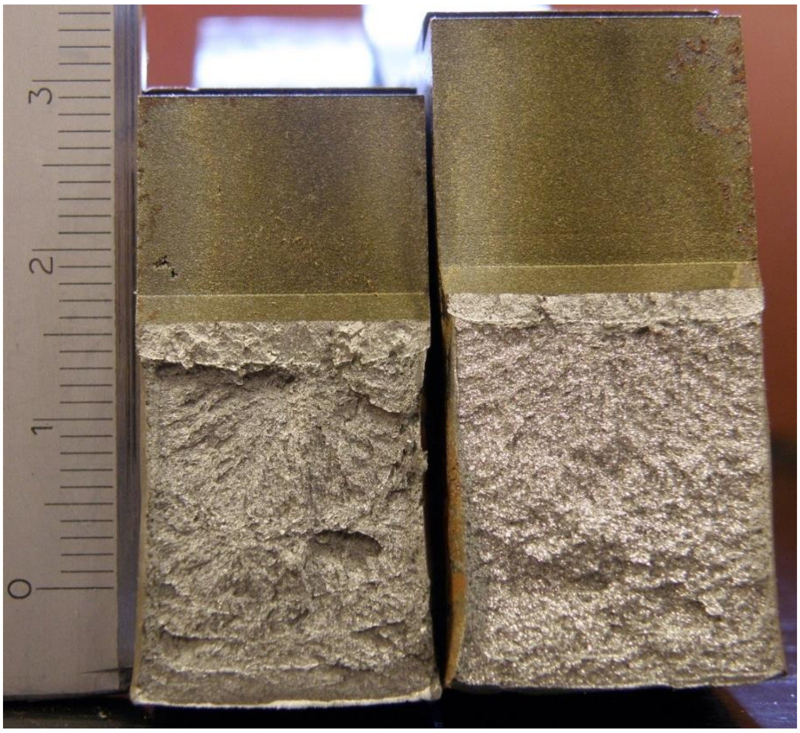

(a) (b)

FIGURE 33: Fractured surfaces of the valve a) and pipeline b) components.

The results of the investigations of the microstructure under light microscopy in the form of material structure images are presented in Figure 34. For the pipe specimen, no discontinuities or micro-cracks are observed in the structure. No initiation of damaging processes is observed either but there is precipitation in bainitic areas. For the valve specimen, the microstructure of cast steel's bainitic-ferritic structure is visible. The rare appearance of needle-shaped bainite forms may suggest the existence of lower bainite in the microstructure. For this reason, for an assessment of the life of constructional components, the material might be concluded to have been compromised but since it’s a qualitative assessment it can’t be concluded how much degraded it is. The fracture toughness results provide additional quantitative material property to establish the structural integrity of the material.

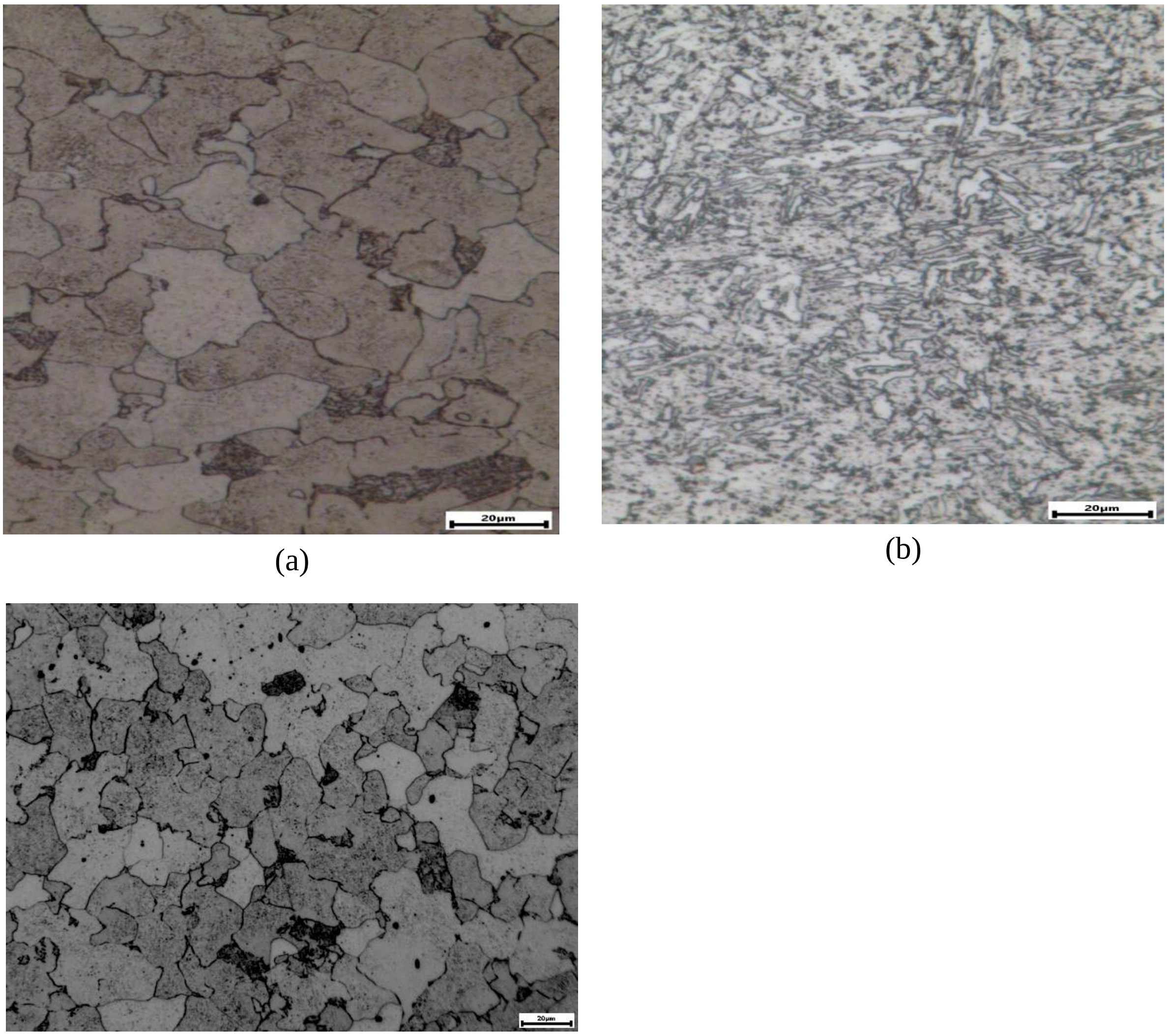

(a)

(b)

(c)

FIGURE 34: Microstructure of the tested components under a light microscope at a magnification of 50X: pipeline material (a) valve material (b) and virgin pipe material (c).

### 3.3. Discussion

The load-displacement curves show the presence of considerable ductility before fracture in both the valve and pipeline specimens. None of the specimens met the ASTM validity criteria of $\frac{P_{max}}{P_Q} \leq 1.10$ or $W - a > 2.5\left(\frac{K_Q}{\sigma_{YS}}\right)^2$ for $K_Q$ to be $K_{IC}$, hence, it is a ductile fracture. The average $K_Q$ from all the specimens are consistent, showing homogeneity in the material. It can be seen from the load-displacement curves that there is no significant difference in the curves of the valve chamber and pipeline section.

The authors of previous papers investigated the fracture toughness of the same components using single-edge notch bend specimens (SENB) for both the valve and the pipeline material [110]. They determined that the fracture toughness of the pipeline and valve material are 45.7 and 62.8 MPa.m$^{1/2}$, respectively. These findings are consistent with the results of this work in terms of the valve having a higher fracture toughness value compared to the pipe. It is also noticeable that the SENB specimen has lower values of fracture toughness compared to the arc tension specimen. This could be due to a difference in crack tip constraints, according to ref. [22] since different specimen geometries have various crack tip constraints. During sampling for the SENB specimen, the load is axial, while for the arc-shaped specimen, the loads are radial, as depicted in Figure 35. The arc-shaped specimen is designated C-R while the SENB specimen is designated L-R as stipulated in the ASTM standard for fracture testing. This could be another reason for the difference in fracture toughness in the orientation of the specimens.

Pipeline specimens have higher values of Pmax, $P_Q$, and average fracture toughness, while the valve chamber specimens have a higher $P_{max}/P_Q$ ratio. The difference in the fracture toughness results could be attributed to the difference in the materials. The valve material is G17CrMoV5-10 (L17HMF), while the pipeline material is 14MoV6-3 (13HMF) steel. Steam line material properties are dependent on the progression of precipitation processes, as well as on the growth of grains and the development of microstructure changes and structural discontinuities that result from prolonged exposure to high temperature [115]. An observation of the fractured surface showed that the fractured specimen of the valve chamber is brittle transcrystalline, while that of the pipe is brittle intercrystallite. The small and shallow dimples that fracture the surface of the pipe material indicate low toughness even though the morphology appeared somehow ductile [116]. For the valve material, the cleavage facets with little to no dimples on the fracture surface morphologies indicated that the samples primarily failed in the cleavage mode.

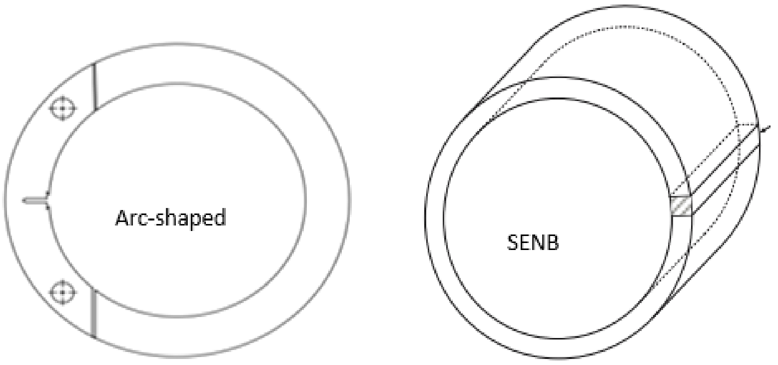

FIGURE 35: A schematic diagram showing the sampling position of the arc tension and SENB specimens.

The 13HMF low-alloyed steel has an initial microstructure that consists of bainite and ferrite, with a tiny proportion of pearlite [85]. After a lengthy exploration, as seen in Figure 34, the final structure is ferrite with somewhat homogeneously distributed precipitations inside the grains and chains with considerable precipitation on their edges [117]. Long-term increased temperature operation results in a considerable increase in ferrite grain size. According to the model of stages in the degradation of the structure of power plant materials proposed by literature [118] for low-alloy 14MoV6-3 steel, the degradation process is not yet in its final stage as there were no creep micro-voids [119].

The studied L17HMF cast steel has a bainitic-ferritic structure. The microstructure is identical to the structure of new castings. The long-term operation has not contributed to the decay of the bainite areas, nor has there been coagulation of precipitates. Conventional evaluation of durability uses metallographic tests of structure degradation so-called changes to the structure of, respectively, perlite, bainite, or martensite, the development of precipitation processes and development of internal damages as well as checking with the magnetic or ultrasonic method to see whether there are cracks in these elements.

This work assumes the presence of a crack and attempts to estimate the risk of its spontaneous development in turbine operating conditions. The stress singularity at the crack tip is recognized by the presence of infinite stress at this location, and the stress components at the crack tip exhibit multivalued characteristics. Cracks most often occur on the inner surface of pipelines due to corrosion and have a circumferential direction. Testing was undertaken at room temperature, and only the internal sudden pressure loads were considered. Yet, for real conditions of power plants, the elements operate at elevated temperature of up to 535 °C, and there are multiaxial loads influenced by creep, thermal elongation of creep (thermal stresses), and dead weight of intermediate pipes. At this temperature, it is well known in the literature that an increase in temperature leads to an increase in fracture toughness; therefore, the present values are conservative.

Calculations of fracture toughness derived from pressure can only provide preliminary information about the expected loads the material can withstand before uncontrolled brittle fracture. A comprehensive assessment of the object's durability should be supplemented with material tests enabling the determination of the actual degree of material wear in the most intensive areas of the analyzed element. Depending on their loading range, the results may be used to estimate the operational reliability forecasts in the presence of a crack. The results can also be correlated to indentation-based fracture toughness testing and a correlation factor used to predict future fracture strength during continuous operation.

The established methodology of material state evaluation and evaluation of its suitability for further operation, and prediction of further safe operation can allow for the optimal use, in terms of operation and economic factors and safety conditions, of structural components of power installations subjected to long-term operation in conditions of increased temperature, stress, and aggressive environment . In the absence of enough samples for experimental assessment, a numerical assessment may be used as numerical results were found to be closely aligned with the experimental results. The presented steam pipelines and valves may be safely used for years, if "continuous monitoring" of key material properties is followed to prevent substantial uncontrolled failure; it is also important to check the material's strength condition.

Potential uncertainties relating to the experimental and numerical evaluation methods used in this work mostly arise because testing was undertaken at room temperature, yet the actual operating conditions are at an elevated temperature of 535 °C. Furthermore, the present thesis considers the influence of impact loads on fracture toughness over time, including creep, increased temperature, and fatigue. Unfortunately, the true history of the mentioned processes cannot be mimicked because real boilers undergo randomly required startup and shutdowns, apart from the planned operations. So, the separation of factors like creep, fatigue, and thermo-mechanical fatigue is impossible.

Another potential limitation is that the tests were completed using uniaxial tension, while thermomechanical multiaxial loading is present in actual power plants. In future work, specimens with tilted notches will be used to test the effect of multiaxial loading since a tilted notch experiences both type I and type III crack opening modes. Additionally, ductile tearing resistance should be implemented to calculate the exact point where the crack initiation occurs.

### 3.4. Summary and conclusion

This study presents an experimental and numerical assessment of the fracture toughness of steam boiler components, which have been in operation for more than 100,000 h. The materials tested are components of two different parts of a steam turbine unit: the pipeline section that connects the headers with turbines, which is made of 13HMF steel, and the valve chamber section, which is made of L17HMF steel grades. The experimental assessment used full-size arc-shaped tension specimens (AT). AT and single-edge notch tension (SENT) specimens are used for numerical assessment. The finite element method (FEM) formulations are developed and examined in Abaqus, which is set up as a shell model with the specimen thickness designated as the mid-surface for the analysis. The notch is modeled using a contour integral definition based on the maximum energy release rate criterion. The fracture toughness is quantified using the stress intensity factor ($K_I$), and the results are compared. The valve chamber is found to have a higher fracture toughness than the pipeline section. The effect of specimen geometry is also noticeable, and the fracture toughness of SENT and AT specimens are compared. The numerical FE simulations showed the longitudinal stress field around the crack tip. With an average Pmax of 23.96 and 23.13 kN respectively, the pipeline components of the AT specimens could withstand slightly higher values of Pmax compared to valve specimens. Additionally, the valve chamber specimens have a higher $P_{max}/P_Q$ ratio. This shows they experienced more ductile fractures compared to pipe components.

Despite this, the valve specimens have superior fracture toughness compared to pipeline specimens, i.e., 76.75 and 69.25 MPa.m$^{1/2}$, respectively. The average KQ from all the specimens is very consistent, with 3.75 and 4.38 MPa m$^{1/2}$ for the pipe and valve samples, respectively. This demonstrates there is uniformity in the material from which the samples were extracted.

The numerical results closely align with the experimental results, with a maximum deviation between experimental and numeric of –2.27% for valve and –1.21% for pipe specimens. The stress singularity at the crack tip is recognized by the presence of infinite stress at this location, and the stress components at the crack tip exhibit multivalued characteristics. As the thickness of the specimen increases, the stress state becomes more plane-strained and, hence, toughness decreases. The findings of the microstructure of 14MoV6-3 reported in this chapter primarily support earlier findings, although with prolonged use at high temperatures, the ferrite grain size also significantly increases in addition to the microstructure evolution previously discussed. A degraded bainitic-ferritic structure was observed in the G17CrMoV5-10 cast steel following operation.

The findings provided insightful information about the fracture behavior of 13HMF and L17HMF steel after long periods of operation, which will be very helpful when deciding to extend the service life or upgrade power boilers to meet the increased demand for renewable energy sources of equipment. In the analyzed instance, continued operation of the assessed components for the following years is viable and safe, even in the presence of minor cracks, provided there is continuous monitoring of essential material to avoid or at least reduce the probability of an uncontrolled failure.

# CHAPTER 4: INVESTIGATION OF MIXED MODE I/III FRACTURE BEHAVIOUR OF 14MoV6-3 POWER PLANT STEEL

In the ongoing shift in the energy demands from traditional sources to renewable carbon zero conventional electricity generation methods, such as thermal power, are still needed to supplement renewable sources, especially during peak demands [120]. This frequent powering on and shutting down causes severe thermal fatigue as they were designed to operate continually. Therefore, monitoring power engineering steel pipes is crucial for maintaining safety and reducing operating costs caused by the acceleration of damaged dynamics [121].

Engineering Critical Assessment (ECA) procedures adopt fracture mechanics concepts to assess the criticality of structural defects. They are commonly applied to derive tolerable defect sizes during installation and operation [85]. Fracture failure of structures poses significant damage to the equipment dependability, hence the ability to tolerate a fundamental amount of damage is a demand for critical components [122]. Fracture toughness is often evaluated using the critical stress intensity factor ($K_{Ic}$), J-integral and CTOD ($\delta$).

Although both metrics are acceptable for measuring fracture toughness for metals that are extremely tough to be measured by the Stress Intensity Factor, the oil and gas sector currently prefers CTOD-R curves instead of J-resistance measurements for defect evaluation [123]. The choice between $J$-integral and CTOD ($\delta$) depends on the ease of obtaining fracture toughness and crack driving force in the given application. The CTOD can be measured as either $\delta_{90}$ or $\delta_5$. As an illustration, $\delta_5$ refers to the displacement between two fixed measurement locations on the specimen surface 5 mm apart on both sides of the fracture tip. To perform a typical $\delta_5$ test, a clip gauge is used to determine the CTOD and record displacement as loading capacity directly increases. This approach requires direct contact with the specimen, which is not feasible for specimens with a tilted notch [38].

Engineering structures typically experience mixed mode fracture due to irregular or inclined internal cracks [124], the oblique orientation of fractures, or multiaxial stresses. Pre-existing cracks are often subjected to variable tensile, shear, torsional stresses, or an arbitrary combination of them, which may cause serious fracture failures [125]. According to the literature [126], metals experience mixed-mode fracture hence to evaluate and estimate the lifespan and residual, a thorough understanding of ductile fracture behaviour under mixed-mode I/II/III loading conditions is required. While mode-I fracture mechanics is somewhat mature [127], mixed mode fracture mechanics remains challenging, especially for ductile materials under multiaxial stress, as there is no consensus or standard for determining the fracture toughness of elastoplastic materials over a mixed mode loading condition [128]. While numerous research has been published for in-plane, mixed-mode I/II fracture [129], the state-of-the-art lacks concrete study including experimental, analytical, and computational investigations into mixed-mode I/III, II/III, and I/II/III fractures. For example, Jin et al. [130] reported that mixed mode fatigue cracks can initiate at stress levels below the pure mode I threshold, and the fatigue crack growth rate (FCG) in mixed mode can take place quicker than in pure mode I. Therefore, it is only prudent to study mixed-mode fracture. Engineering structures like pressure vessels, pipelines, and airplanes often fail under complex loading. In these circumstances, strain energy release rates must be decomposed into mode I, II, and III components [131].

Experimental optical techniques, such as DIC, play a crucial role in fracture mechanics by providing non-contact, full-field measurements of deformation and strain. These methods enable detailed analysis of crack initiation, propagation, and stress distribution in engineering structures, offering valuable insights into material behaviour under various loading conditions. The DIC is increasingly being employed in laboratories offering very accurate results (with noise < 1/100 pixels) [64] by recognizing the surface structure of measured objects in digital format photos and assigning coordinates to image pixels. It then aims to maximize the correlation between subgroups in photographing specimens at various deformation phases. In DIC, a random speckle pattern is applied to the specimen surface, and images are captured before (reference) and after (distorted) deformation. Subsets of these images, containing portions of the speckle pattern, are tracked, and compared to measure displacement and deformation. While the subsets are analysed and correlated, they are not necessarily "observed concurrently" but rather compared sequentially to determine changes between the reference and distorted states. Matching greyscale distributions within subsets is possible since the pictures' grey value remains constant. This allows for quantifying deformation at all points inside the region of interest. By comparing the quantitative deformation of a subset of reference and distorted pictures, displacement can be calculated in the desired direction. After determining displacement, the derivation may be used to compute strain [132].

Several research works present the DIC application to evaluate the CTOD of a visible crack tip in small-scale fracture toughness experiments with through-thickness notches [133]. It has been demonstrated in literature that CTOD can be estimated using DIC and separated into elastic and plastic CTOD components using an offset compliance approach [134]. The evolution of fatigue damage has indeed been investigated in for 14MoV6-3 (13HMF) power engineering steel using DIC. Farahani et al. [122] used a full-field three-dimensional optical technique to measure the deformation fields and to obtain SIF at different crack lengths. They verified their DIC experimental work using FEM implemented in ABAQUS, and they found the DIC method for characterizing displacement fields to be a relatively straightforward and cost-effective optical technique. Yan et al. [135] implemented an automated polariscope and three-dimensional photoelasticity to calculate the mode III SIF of 14 mm thick cast blocks of epoxy resin (MY750). The results show that for mode I loading the in-plane strain components do not consistently follow the singularity trends predicted by the Hutchinson-Rice-Rosengren theory (HRR) theory.

Few extensive investigations have been conducted on the performance of the DIC approach in measuring the fracture toughness of tilted notches [136]. This might be due to the cumbersome and sophisticated experimental methods employed in mixed mode I/III. One critical criterion for evaluating the success of the DIC approach in mixed-mode fracture analysis, particularly in the presence of out-of-plane displacements, is its ability to generate reliable, high-sensitivity data while minimizing noise. This aspect, nevertheless, has not been completely investigated.

This chapter implements the 3D-DIC method to measure the full displacement field on one surface of the specimens during loading condition and stable tearing processes on the standard configuration SENT specimens with different tilt angles to provide a mixed mode I and III opening. The DIC approach is specifically used to measure the crack length and the crack tip opening. To identify the fracture initiation site, strain is measured close to the crack tip. It is necessary to consider mixed-mode fractures, owing to the disordered internal microcracks and the complex stress conditions in pressure vessels in power boilers. The 3D-DIC system is used instead of the 2D one, since by its design, it can detect out-of-plane displacement [128]. SENT specimens come in two varieties: pin-loaded and clamped at the far end. In the literature [123], strain-based design (SBD) technique indicates that pipes having circumferential fractures under tension or bending are of primary concern, therefore this work chooses clamped SENT specimens. In addition, strain gages are installed at the back of the specimen to measure the strain behavior. The testing methods for elastoplastic materials' fracture resistance under mixed-mode stress can benefit from the work in this chapter.

## 4.1. Material and methods

The investigated material is bainitic–ferritic 14MoV6-3 heat-resistant steel. It was supplied by Třinecké železárny (Třinec, Czech Republic) in the form of a 10-meter-long cylindrical rod with an as-received state condition: (normalization at 940–960 °C and tempered at 700–730 °C). According to the manufacturer certificate, the material has Young's modulus of 190 GPa, a Poisson's ratio of 0.3, a yield strength of 332-353 MPa, and ultimate strength of 591-593 MPa. The chemical composition is presented Table 18 and conforms with the Polish Standard (PN-75/H-84024).

TABLE 18: Chemical composition of the commercially acquired 14MoV6-3 steel according to manufacturer's certificates [weight %].

| Element | C | Mn | Si | P | S | Cr | Al | Mo | V |
|---|---|---|---|---|---|---|---|---|---|
| % | 0.15 | 0.61 | 0.24 | 0.03 | 0.007 | 0.60 | 0.018 | 0.453 | 0.318 |

SENT specimens were extracted from the round bars according to the British standard BS 8571:14. The advantage of this specimen geometry is that mixed mode I/III loading can be introduced by changing the crack angle [137]. All the specimens have an equal initial notch length of 5 mm generated by fine milling in two steps to reach the desired dimensions as shown in Figure 37. No fatigue pre-cracking was done since this would make controlling the initial fracture depth difficult, and proclivity of the fatigue pre-crack to rotate towards mode I orientation. Previous work in [73] has shown at that it does not make any difference to do fatigue pre-cracking for adequately ductile materials. Three notch tilt angles, $\varphi=0°$, to represent pure mode I loading and $\varphi=22.5$ and 45° to represent mode mixed mode I/III loading as shown in Figures 36 and 37 at least two tests were performed for each notch angle as presented in Table 19.

TABLE 19: Details of tested SENT specimens.

| Specimen reference | Notch angle $\varphi$ (°) |
|---|---|
| N1-22.5 | 22.5 |
| N2-22.5 | 22.5 |
| N3-22.5 | 22.5 |
| N4-0 | 0 |
| N5-0 | 0 |
| N6-45 | 45 |
| N7-45 | 45 |
| N8-45 | 45 |

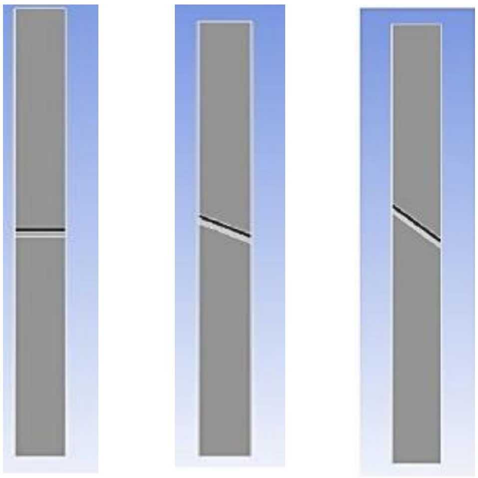

FIGURE 36: Different detailed side views of the crack inclination angle of the specimens.

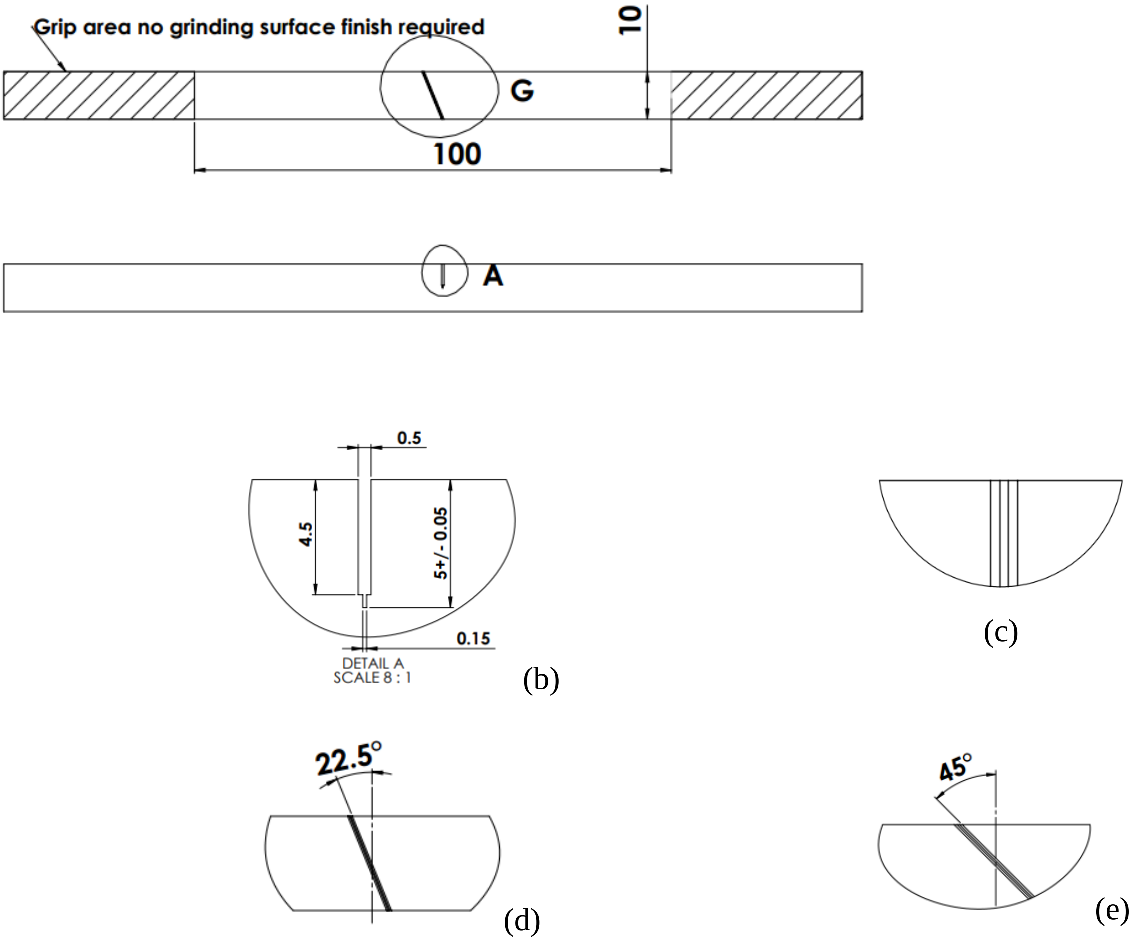

FIGURE 37: Single edge notched tension (SENT) specimen geometries notch details.

Figure 37 (b) and (c) show the details of the machined notch showing the two-step milling. Figure 37 (d) and (e) show the details of the 22.5 and 45-degree tilted notches respectively.

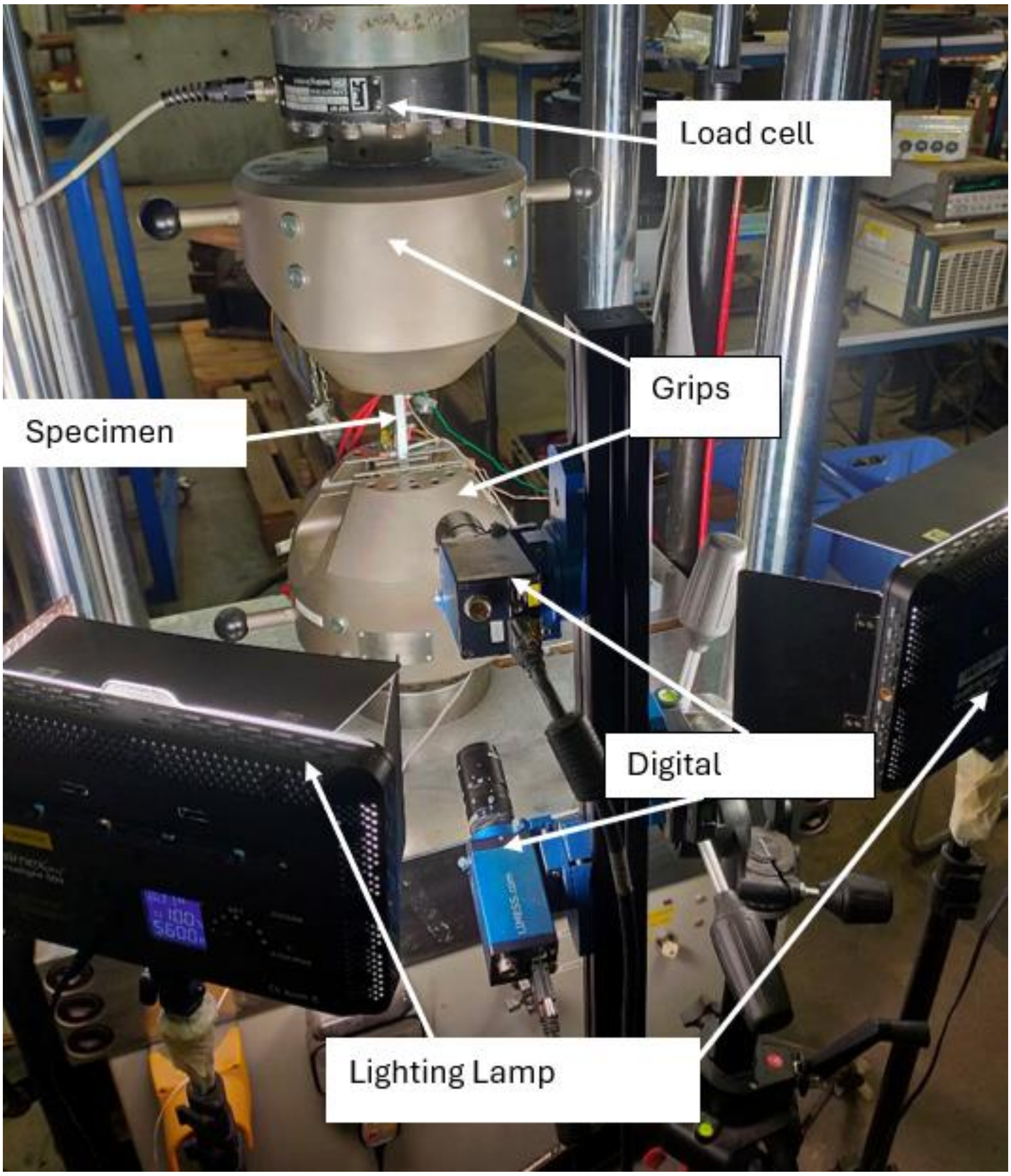

FIGURE 38: Experimental setup of SENT specimens under quasi-static tensile loading.

The experimental apparatus of the 3D-DIC is shown in Figure 38, which includes two synchronized digital cameras, two stable light sources, a loading system, and a DIC computer. Experiments have been performed using a servo-hydraulic ESH 100 kN universal testing machine through a displacement-control mode at room temperature with a constant displacement rate of 0.002 mm⁄s.

Experimentally, Direct Current Potential Drop (DCPD) method was used for ductile crack extension ($\Delta$a) measurements during testing. A reference voltage drop measurement is recommended to account for current leaks and electrical conductivity variations [73]. After the test, the specimens were cooled in liquid air to enable brittle fracture of the remaining ligament allowing for the observation of fractured surface. Using the nine-point average method outlined in ISO 12135:2016 [138], the original crack and the stable crack extension were measured as shown in Figure 39 With the help of Keynse surface analysis   machine.

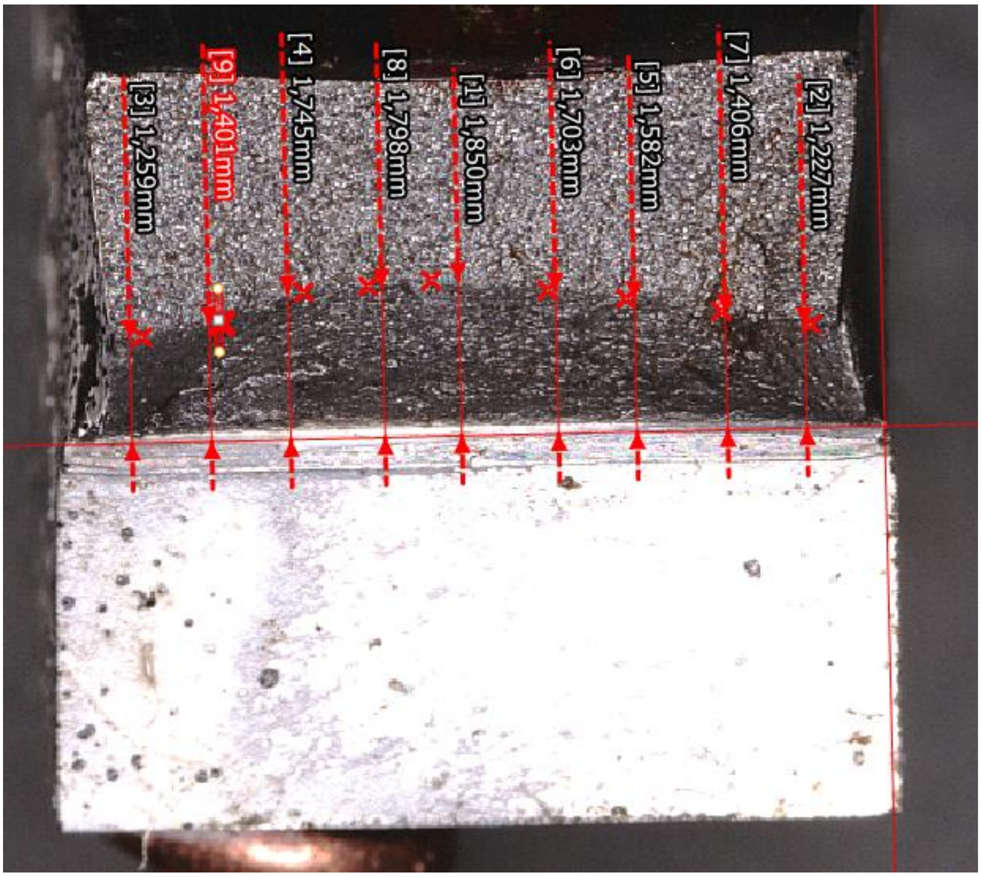

FIGURE 39: Typical post-test fracture surfaces illustrating crack extension area, with nine-point average estimation using Keyence instrument.

### Digital image correlation analysis

In this study, a 3D DIC was used to document the experimental data. To comply with the principles of DIC, the specimen surface was prepared by spray-coating it with a matte white base layer, followed by applying random speckles of matte black paint to create the necessary high-contrast pattern for accurate measurements. Figure 40 illustrates various specimen sides in which (a) the back of the specimen, equipped with strain gauges and the current supply connections for the DCPD measurements; (b) the side of the specimen, where DIC images were captured, showing the crack opening and the applied speckle pattern; and (c) the front of the specimen, highlighting the copper pins used for voltage drop measurements. To ensure the integrity of the speckle pattern and prevent brittle fracture of the paint during loading, the interval between painting and testing was limited to a maximum of 24 hours.

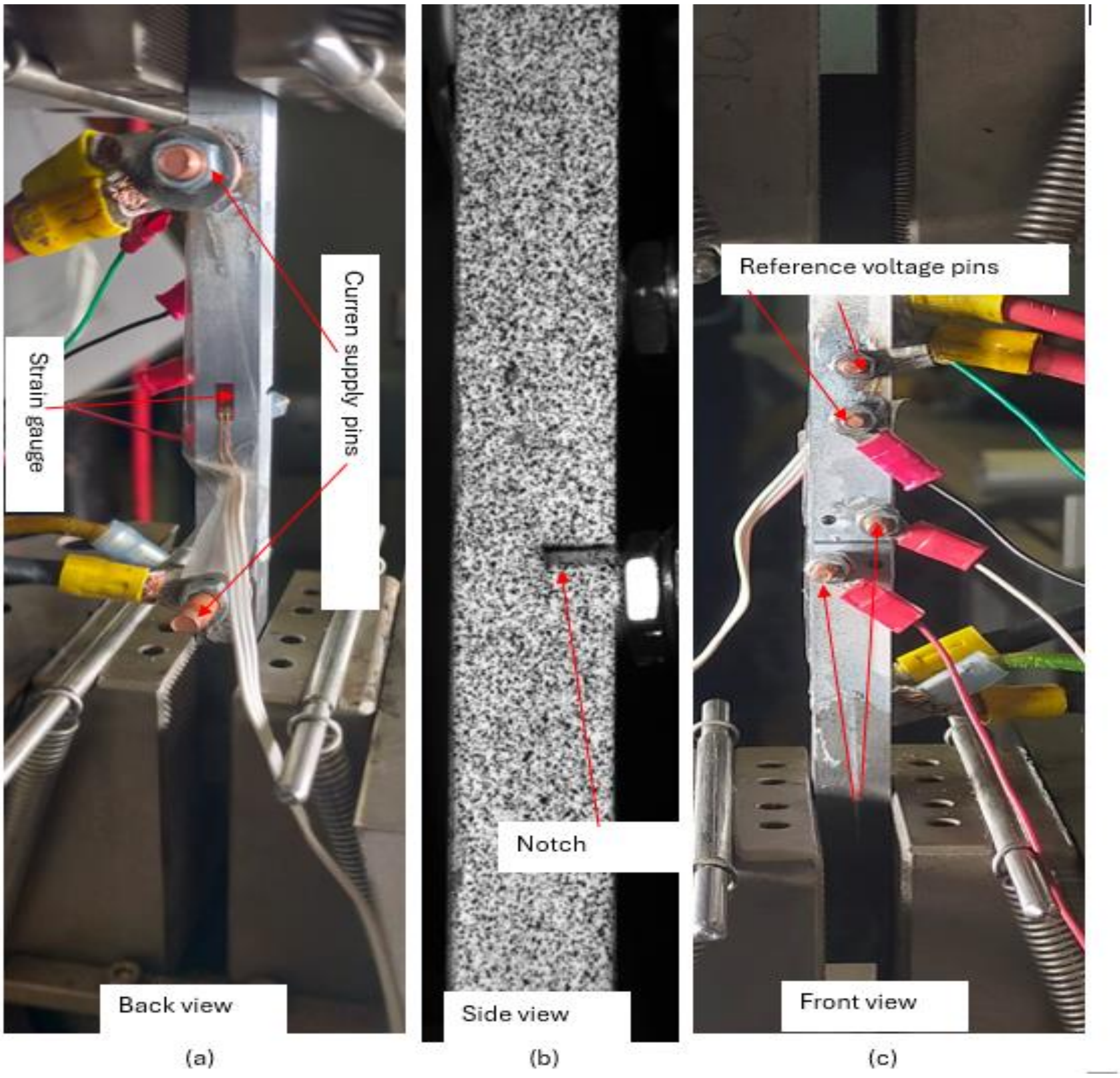

FIGURE 40: Image of the specimen mounted between the grips.

The working distance between the camera and the specimen surface was about 400 mm. The speckle size ranged between 1.00 and 6.00 pixels, 0.03–0.16 mm as recommended in the literature [139]. The 3D-DIC system comprised a RICOH FL-CC7528-2M 2.0 Mega Pixel Lens with a 75mm focal length. Before testing, calibration was performed using a checkerboard calibration plate of 3x3 mm. Besides, VIC-3D v7 software was used to process DIC images automatically at a frequency of 1 Hz. The reference pictures of undeformed specimens at zero load were used to compare with each image.

TABLE 20: Digital image correlation (DIC) parameters

| Parameter | Value |
|---|---|
| Subset size | 25 |
| Step size | 7 |
| Image filtering | none |
| Pixel size | 6 pixels |

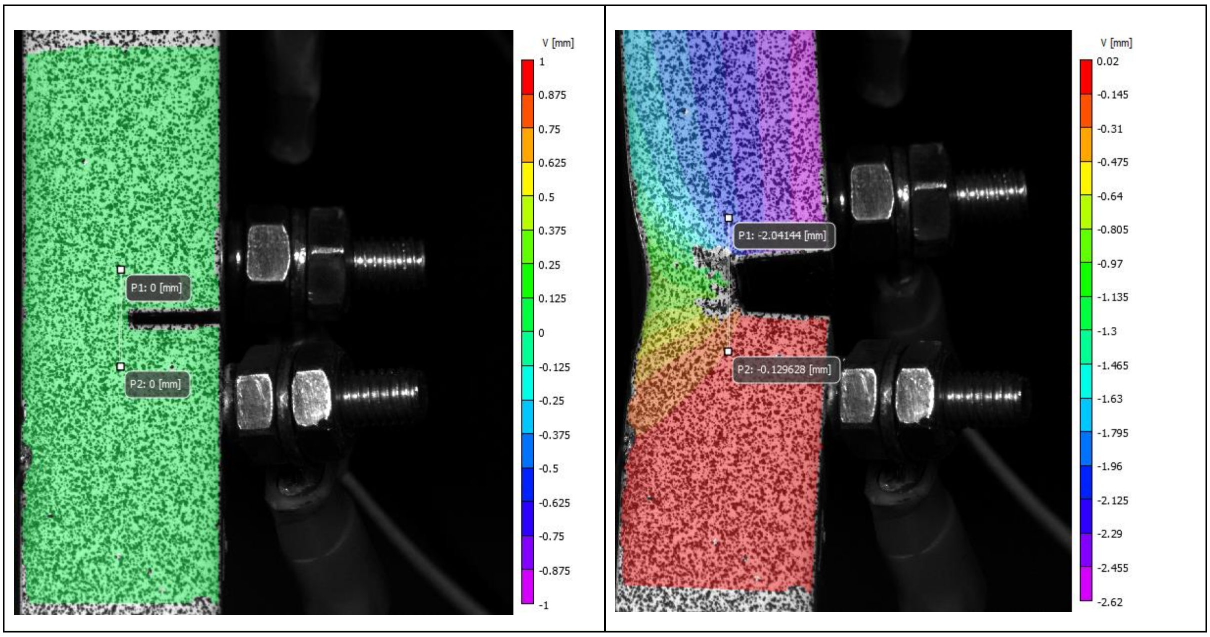

FIGURE 41: Setpoints for measuring $\delta_5$ shows the two points selected on the specimen surface on the upper and lower sides of the crack tip with a span of 5 mm.

Figure 41 shows points where vertical (in-plane, along the y-axis) displacement is measured using the DIC virtual extensometer for mode I opening. Equation (4. 1) presents the calculation of the total $\delta_5$ under mixed-mode loading calculated by measuring the opening components, as described in the literature [126], where $\delta_5$ total is the CTOD under mixed mode loading conditions, and $\delta_I$ and $\delta_{III}$ are modes I and III, respectively.

$$\delta_{5total} = \sqrt{\delta_I^2 + \delta_{III}^2} \qquad (4.\ 1)$$

### The mode-I SIF Calculation from DIC

As there is no standardized method to determine the fracture initiation under mixed-mode loading, the robustness of experimental results collected from DIC is examined by acquiring the Mode I SIF. For determining the SIF based on the experimental results, a numerical iterative over- deterministic algorithm [140] was used as extensively described in [141]. This approach requires identifying the crack tip [142] and the deformation field to serve as input for the algorithm. The methodology integrates the stress fields into Muskhelishvili’s Equations which theoretically describe the stress distribution around the crack tip. One significant advantage of this methodology is its ability to use unlimited data points, thereby minimizing deviations in the results. Additionally, it is enhanced by the application of Singular Value Decomposition (SVD), which accelerates computational analyses while maintaining a stable orthogonal basis.

To determine the mode-I SIF from the DIC data, $\Delta K_I^{DIC}$, the point coordinates and their deformation tensor are extracted within the DIC problem domain for any given measured crack length. Then, a window with specified dimensions of 3×3 mm is selected, ensuring a gap beyond the crack tip. This gap accounts for the plastic zone size, which had been previously calculated for each crack length. Since the SIF is valid only in the linear elastic regime, incorporating this gap ensures that the SIF formulation can be accurately applied.

### Numerical simulations

Finite Element Analysis (FEA) was conducted to evaluate and validate the experimental results, ensuring the reliability of the experiments. Three-dimensional elastic plastic FEAs were performed using ABAQUS© to simulate the mechanical response of SENT specimens. The geometries were prepared in SolidWorks©, and a Python script was implemented and imported into ABAQUS© to develop a model replicating the notched SENT specimen used in the experiments.

In the elastoplastic analysis, the Stress Intensity Factor (SIF) cannot be directly determined, as it is only applicable under Linear Elastic Fracture Mechanics (LEFM) conditions. Instead, the J-Integral is calculated and subsequently used to derive the SIF. The SENT specimen was modelled under idealized plane stress conditions. As a guideline, accurate LEFM results require a finely meshed region around the crack tip to capture the stress and deformation fields effectively [143].

All specimens had a spider mesh put near the crack tip, with a mesh size of approximately 0.1 mm in the fracture initiation area. The crack region was allocated an appropriate mesh configuration, as illustrated in Figure 42. The total number of elements ranged between 15,000 and 20,000, depending on the crack size. A mesh sensitivity analysis was performed to ensure an optimal mesh size, good convergence, and correct numerical results. Table 21 presents the mechanical properties applied.

TABLE 21: Material properties of 14MoV6-3

| | |
|---|---|
| Young’s modulus, GPa | 190 |
| Poisson’s ratio, - | 0.29 |
| Yield stress $R_{0.2}$, MPa | 365 |
| Ultimate tensile strength, MPa | 490-690 |
| Density, kg/m$^3$ | 7900 |

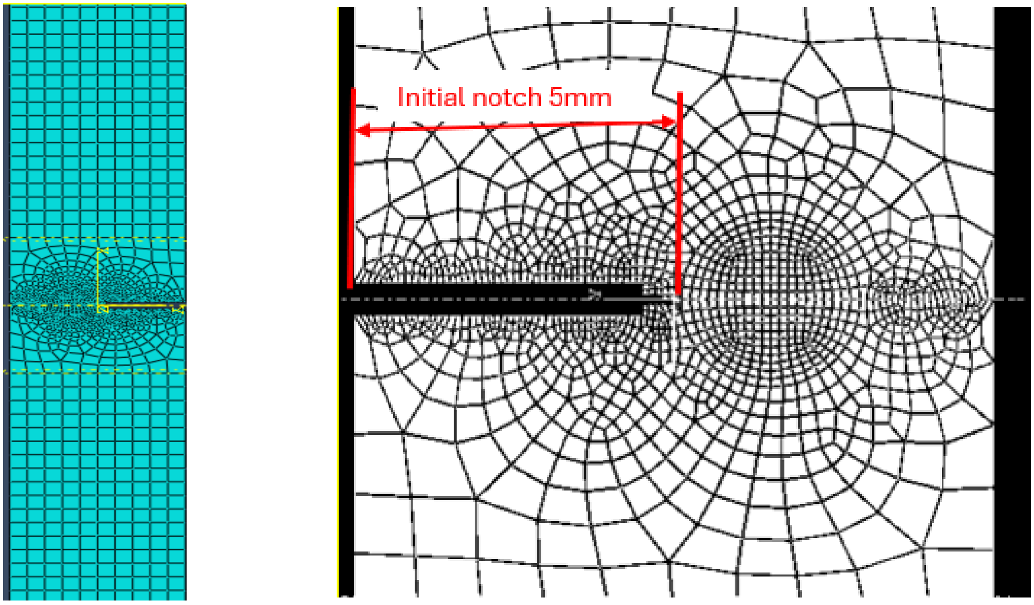

FIGURE 42: FE mesh of SENT model with detail on the notch zone.

## 4.2. Results

Figure 43 presents the calculated mode III CTOD of the three-notch orientations. It can be inferred that $\delta_{III}$ of specimens correspond to $\varphi=0$ degree is negligibly small as compared to the ones with tilted notches. Thus, Table 22 shows the contributions of the mode III CTOD to the total CTOD at maximum loads. The larger the notch tilt angle, the larger the mode III opening while φ =0 notches contribute a negligible % of mode III opening.

TABLE 22: Contributions of CTOD III to total CTOD at maximum loads

| Specimen code | I, mm | III, mm | $\delta_5$ Total, mm | $\delta_5$ % of mode III of the total |
|---|---|---|---|---|
| NS4-0 | 0.98 | 0.00 | 0.98 | 0.71 |
| NS5-0 | 0.97 | 0.02 | 0.97 | 2.97 |
| N1-22.5 | 0.93 | 0.29 | 0.97 | 30.65 |
| N2-22.5 | 0.88 | 0.45 | 0.99 | 45.99 |
| N3-22.5 | 0.92 | 0.33 | 0.98 | 34.61 |
| N6-45 | 1.35 | 0.77 | 1.55 | 49.47 |
| N7-45 | 0.98 | 0.62 | 1.16 | 53.41 |
| N8-45 | 1.05 | 0.57 | 1.20 | 48.14 |

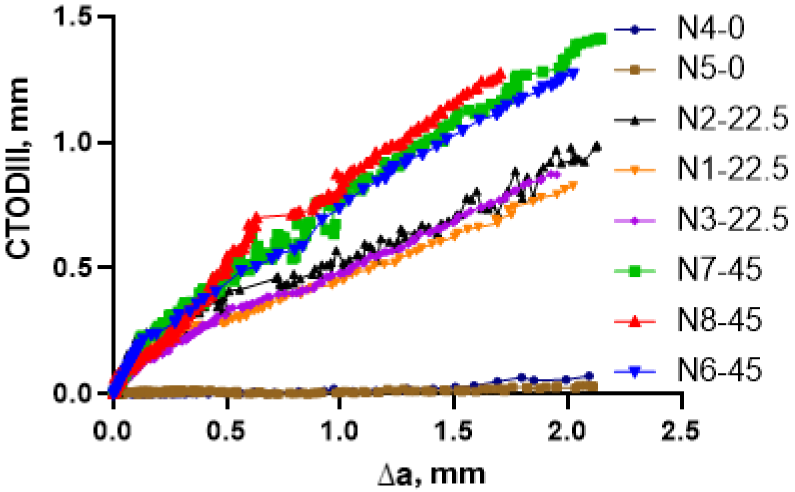

FIGURE 43. Mode III $\delta_5$-R curves under different loading angles.

The contributions of $\delta_I$ and $\delta_{III}$ to $\delta_5$ total N6-45 which has a tilt notch of 45° is presented in detail in Figure 44. While Figure 44 (a) may suggest that the contribution of mode III remains uniform throughout crack growth, Figure 44 (b) reveals a different trend: during the initial stage of the fracture process, the $\delta_I/\delta_{III}$ ratio increases, then decreases, before eventually stabilising. This indicates that the contribution of mode III opening varies during the loading process and is not constant throughout.

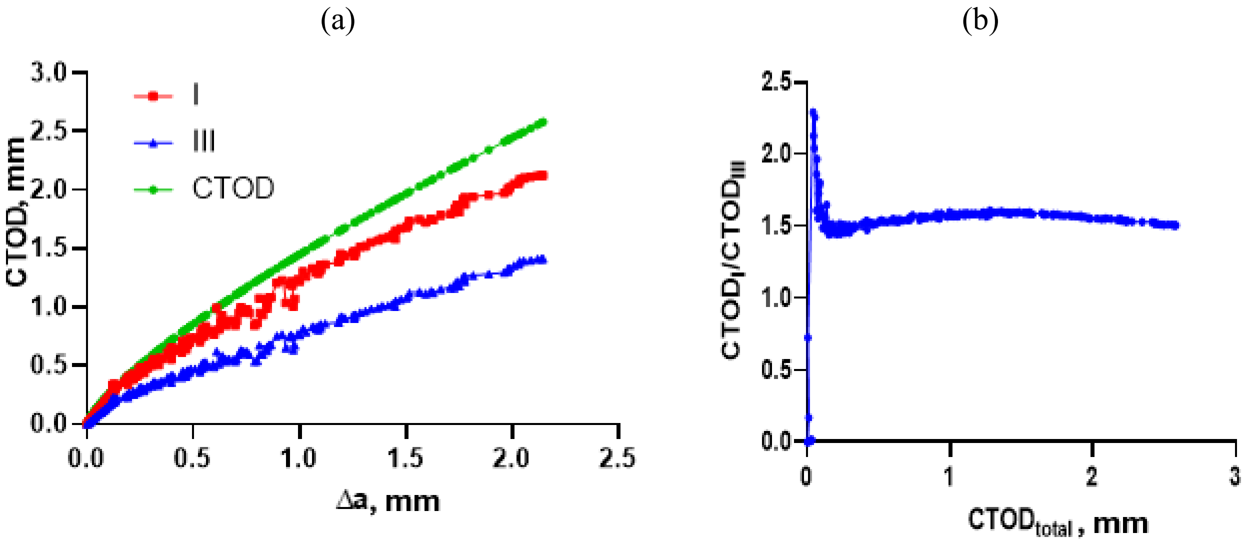

Figure 44: CTOD resistance curve of specimen N7-45 (a), contribution of mode I to ratio of CTOD I/III (b).

Figure 45 presents the comparison of mode I $\delta_5$ for specimens with notch angles $\alpha = 0$ and 45°. It is noticeable that for $\varphi=0°$ specimens, the crack tip opening displacement $\delta_5$ is not smooth. Their mode I opening is kinked at maximum loading while the 45-degree tilt notch has a smooth and always rising curve. The kinking of the resistance curve means from that point the crack grows without an increase in CTOD.

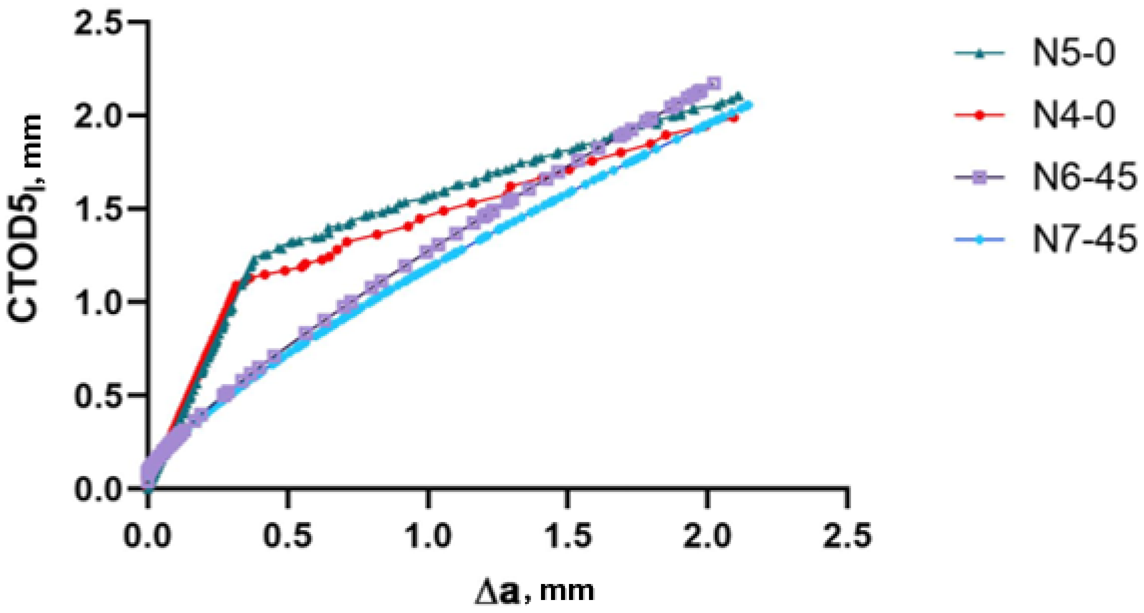

FIGURE 45: Resistance curves of mode I CTOD.

Figure 46 presents the comparison of the CTOD total of two samples with $\varphi=0°$, and one sample considering $\varphi=45°$. In this regard, the $\varphi=45°$ notch specimen exhibits a rising R curve while for the straight notch specimens, the R curves are flat. In metals, a rising R curve is typically associated with the growth and coalescence of microvoids.

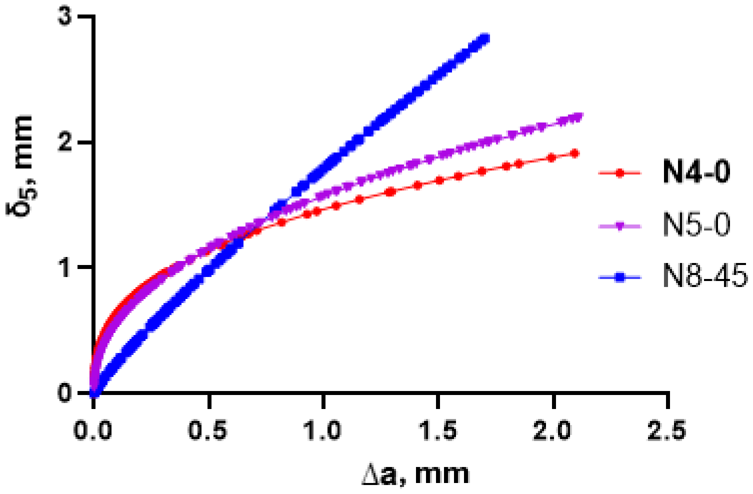

FIGURE 46: $\delta_5$ total crack extension resistance curves (R-curves).

Moreover, Figure 47 shows the force vs. CTOD curve of the tested specimens. The specimens with tilted notches can tolerate slightly higher loads at the same CTOD compared to straight-notched specimens. Furthermore, there is a little kinking-like yield point valley for the samples including a 45-degree tilted notch.

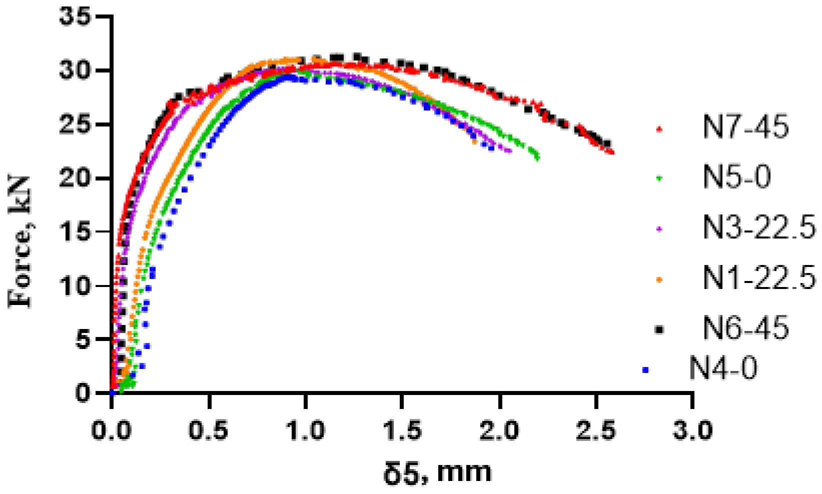

FIGURE 47: Force vs CTOD curve for evaluated SENT specimens.

Table 23 presents the maximum force withstood by every tested specimen before fracture. Although the difference in maximum tolerated loads is small, the 45-degree notched specimens fractured at higher loads followed by 22.5-degree notched while straight-notched specimens carried the lowest loads before fracture, respectively.

TABLE 23: Maximum force for the tested specimens.

| Tilt angle, ° | 0 | 22.5 | 45 |
|---|---|---|---|
| Tested specimens | 29.42<br>30.03<br>- | 31.08<br>29.48<br>30.17 | 30.73<br>30.72<br>31.26 |
| Average max force, kN | 29.73 | 30.24 | 30.90 |

From experimental DIC analysis, the data was processed Using the VIC 3D software. Figure 48 presents the contour plots of equivalent von-Mises strain around the crack tip of tested specimens at maximum loading. For these strains, the VIC-3D software uses a principal plane strain formulation as presented in Equation (4. 2) [135].

$$\varepsilon_{vonMises} = \frac{\sqrt{2}}{3}\sqrt{(\varepsilon_1-\varepsilon_2)^2+(\varepsilon_2-\varepsilon_3)^2+(\varepsilon_3-\varepsilon_1)^2} \tag{4.2}$$

Where $\varepsilon_1, \varepsilon_2, \varepsilon_3$ are the principal strains.

Under mode I loading, the spread of the strain contour has the traditional symmetrical kidney bean-shaped plastic zone. Under mixed mode I/III loading the strain field looks like a distorted rhombus with two asymmetrical lobes. These two lobes appear different in size and shape with distortion more pronounced in the 45° tilted notch.

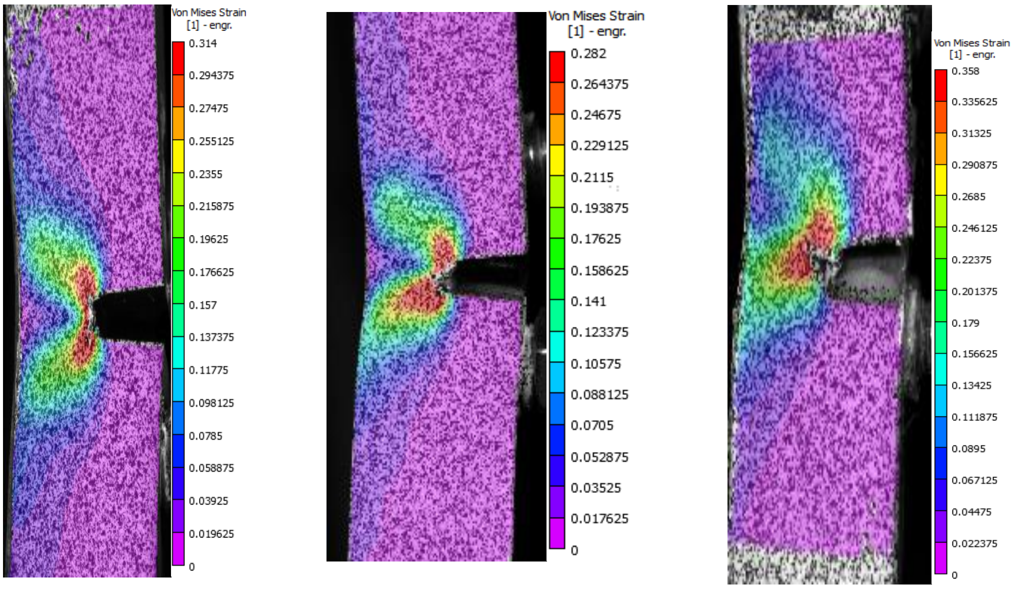

(a) (b) (c)

Figure 48. Von-Mises equivalent strain contours around the crack tip on the specimen surface at maximum loading obtained by DIC: straight notch (a), 22.5-degree notch (b), 45-degree notch (c).

The variation of forces in terms of strain measured by the strain gauges, mounted at the ligament of the specimens, is obtained as plotted in Figure 49. All the curves begin with a sharp increase in force, followed by compression strains then plateau as strain increases and then finally tension. This shows that elastic deformation occurs first, followed by plastic deformation or stability at greater strains. Straight-notched specimens experienced the most compressive strains while 45-degree tilted specimens experienced the most tensile strains.

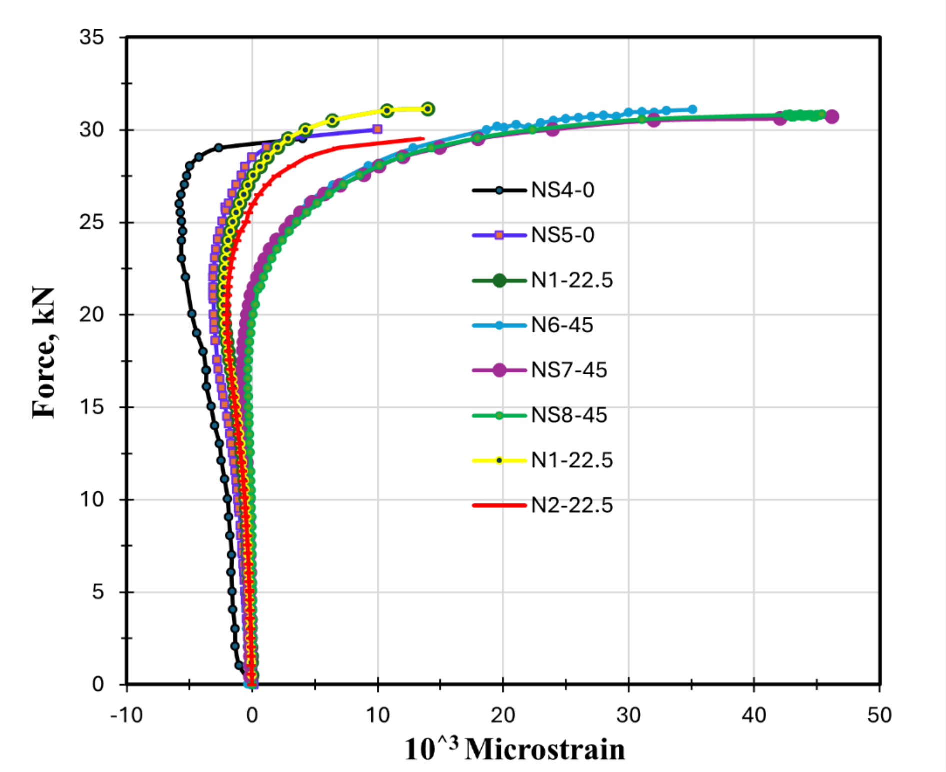

FIGURE 49: Force variation in terms of strain for different tested samples.

To get more insights into the material response under loading condition, SEM analyses was performed using X-ray spectrometer (FEI Quanta 200) at 500X magnification. So, Figure 50 presents the fracture surfaces scanned by SEM of different combinations of in-plane loading. Fractured surfaces normally consist of three different crack propagation stages. Stage I is related to the unstable crack initiation; stage II involves stable cracking propagation and stage III corresponds to the final fracture. Nevertheless, this work deals with stage II related to the stable tearing surface. As a result, the nature of tearing was investigated, and the impact of crack angle on tearing processes was defined using literature references [144].

The fracture surfaces of specimens with mode I loading dominance are packed with roughly equal axial dimples that are closer to one another whereas under mixed mode I/III loading (22.5- and 45-degree notched specimens) the fracture mechanism is essentially shearing as shown by the presence of typical microvoid coalescence characterized by dimples that are relatively small compared to pure mode I.

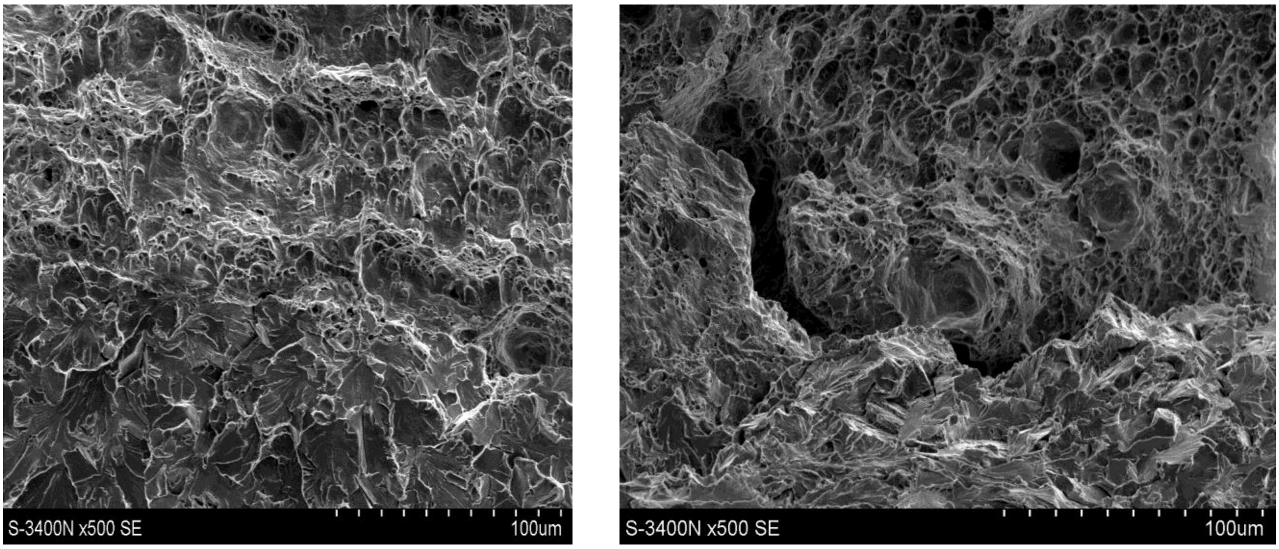

a) NS-4 b) N1-22.5

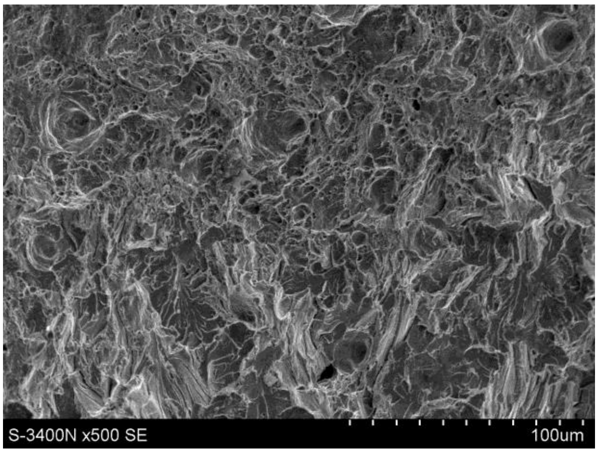

c) N6-45

FIGURE 50: SEM fractography assessment on the fractured surfaces: pure mode I fracture surface (a), fractography of mixed mode I/III fracture surface (b, c).

Figure 51 presents the fractured surface morphology of the specimens after postmortem examination. The straight notched specimen has forward tunnelled crack front caused by plane strain crack growth occurring in the middle of the specimen. A reversed thumbnail tunnelling crack front was formed in the 45-degree slant notch like the specimens with side grooves while the 22.5-degree slant specimens exhibit a uniform crack propagation through thickness.

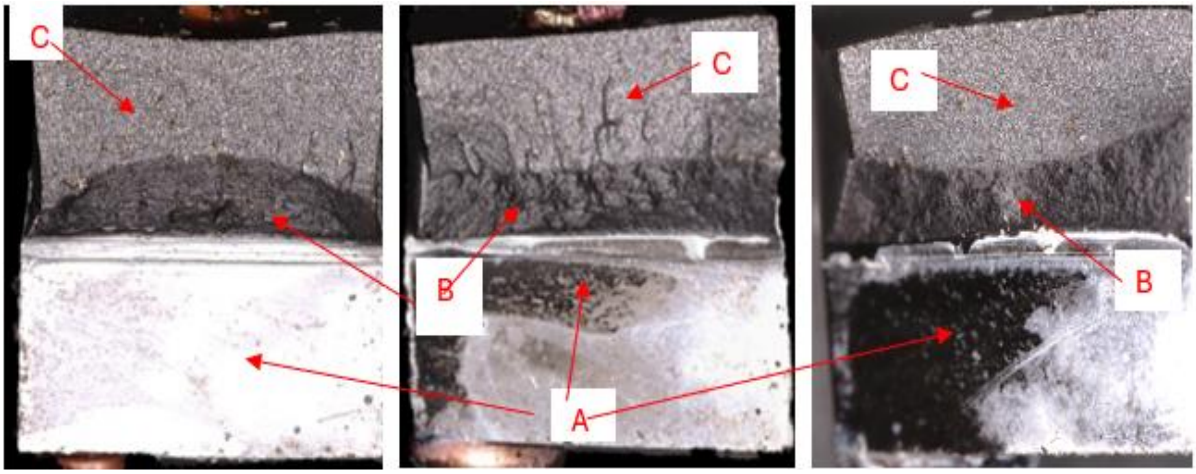

a) straight notch b) 22.5° notch b) 45° notch

FIGURE 51: Fracture morphology of specimen surfaces after the experiment, where A is saw cur surface, B is the ductile crack growth area, and C is the brittle fractured surface post-mortem.

Furthermore, Table 24 presents the crack extensions measured using the DCPD, DIC, and post-mortem extermination after brittle fracture using liquid air. The DIC crack measurement was done by assuming the place of the highest strain to be the crack tip. For 75% of tested specimens, the final crack extension is less than the maximum crack extension limit of 2mm allowed by BS 8571 Standard.

TABLE 24: Final crack extensions measured by DCPD, DIC, and post-mortem 9-point average.

| Specimen number | DCPD, mm | DIC, mm | Δ9 points, mm | Error DCPD, % | Error DIC, % |
|---|---|---|---|---|---|
| NS4-0 | 2.26 | 2.47 | 1.98 | -14.14 | +24.74 |
| NS5-0 | 2.00 | 1.22 | 1.54 | -29.89 | +20.00 |
| N1-22.5 | 2.02 | 1.84 | 1.80 | -12.16 | -2.22 |
| N2-22.5 | 2.13 | 1.92 | 1.94 | -9.90 | 1.03 |
| N3-22.5 | 1.95 | 1.87 | 1.81 | -7.83 | -3.31 |
| N6-45 | 2.02 | 2.65 | 2.03 | 0.62 | -30.54 |
| N7-45 | 2.15 | 2.32 | 2.03 | -5.86 | -14.28 |
| N8-45 | 1.71 | 2.31 | 1.94 | 11.98 | -19.07 |

### Plastic zone size

The sharp tip of the fatigue pre-crack can generate a relatively small plastic zone to obtain conservative values of fracture toughness. For our test no fatigue Precracking was used as the saw cut was small and the material was ductile enough. To determine the mode-I SIF from the DIC data the plastic zone size ($r_p$) along the crack line is determined using Irwin's hypothesis which assumes small-scale yielding near the crack tip. Therefore, in the case of plane strain condition, Irwin suggested to use the following formula of Equation (4.3):

$$r_p = \frac{K_I^2}{6\pi\sigma_Y^2} \qquad (4.3)$$

Consequently, in this study, $r_p$ was calculated on all measured crack lengths for the SENT with the straight notch as reported in Table 25 for two crack lengths: before crack initiation and after crack initiation indeed.

TABLE 25: Plastic zone size for different crack lengths, plane strain condition

| Δa, mm | a mm | $\Delta K_I^{ref}$, MPa.mm$^{0.5}$ | $r_p$, $mm$ |
|---|---|---|---|
| 0.2044 | 5.2044 | 2481.833 | 2.6 |
| 0.2981 | 5.2981 | 2554.774 | 2.9 |

Figure 52 shows the longitudinal strain and stress contours related to the first measure crack length extracted from a 3×3 mm² window near the crack tip, ensuring a gap corresponding to the plastic zone size. These data were inputted into the over deterministic algorithm to compute the SIF. Mode I SIF therefore was calculated for different crack lengths and the obtained results from DIC have been compared to the reference solution obtained from the BS8571-2018 standard as presented in Table 26. The values calculated from the over deterministic algorithm produced a reasonable difference from the experimental analytical value with both cases being less than 2% proving thus the robustness and reliability of the DIC and DCPD crack prediction.

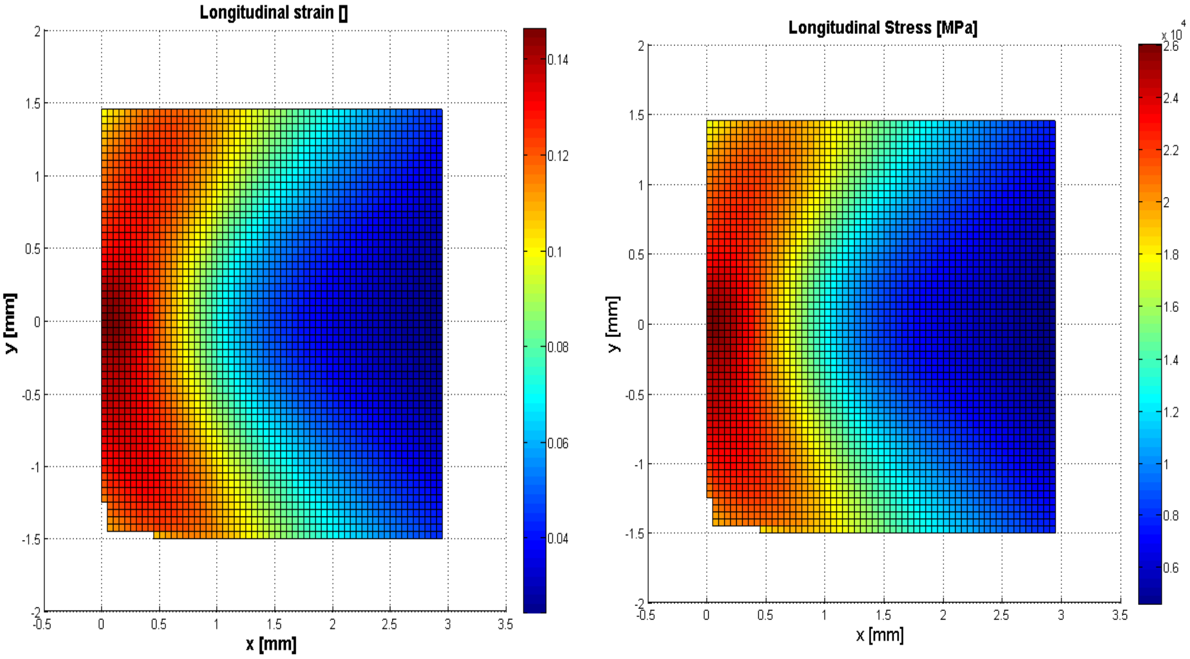

a) b)

FIGURE 52: Input data from the first measured crack length in the over-deterministic algorithm to compute SIF: longitudinal strain (a), and longitudinal stress variation (b).

Table 26: Mode-I SIF calculation for the φ = 0°

| Δa, mm | a, mm | F, kN | $K_I^{ref.}$, MPa.mm$^{1/2}$ | $K_I^{DIC}$, MPa.mm$^{1/2}$ | Deviation, % |
|---|---|---|---|---|---|
| 0.2044 | 5.2044 | 28.6 | 2481.8 | 2503.7 | 0.9 |
| 0.2981 | 5.2981 | 29.4 | 2554.8 | 2599.3 | 1.7 |

In this case deviation is calculated with Equation (4.4), where $K_I^{DIC}$ and $K_I^{ref.}$ is the Stress Intensity Factor from the DIC over-deterministic algorithm and SIF from the analytical experimental calculation respectively.

$$\left[K_I^{DIC} - K_I^{ref}/K_I^{ref}\right]x100 \qquad (4.4)$$

**Comparison of experimental and numerical results**

Stress Intensity Factors (SIF) for corresponding loads were calculated using Equation (4.5) provided in BSI standard BS 8571:2018 [80] for the SENT specimen geometry.

-

$$J = J_{el} + J_{PL} = \frac{K^2}{E'} + \frac{\eta U_P}{Bb_0} \qquad (4.\ 5)$$

where: $U_P$ is the area under the plastic part of the load versus the CMOD curve, N/mm; $K$ is the stress intensity factor, $E$is Young's modulus, $\eta_p$ is a dimensionless function of geometry, $B$ is the specimen thickness; $b_0$ is the specimen ligament.

The calculated experimental SIF according to the BSI standard is compared with the one derived from the J integral calculated from FEA at specific loading points as provided in Table 27. All numerical results closely followed the experimental data to the maximum load for all specimens.

TABLE 27: Fracture toughness J integrals were obtained for different applied loads.

| J from FEM analyses | $a = 0.2\ mm$ | $F_{Max}, kN$ | $a = 1.5\ , mm$ |
|---|---|---|---|
| 1 | 187.6 | 580 | 242 |
| 2 | 181.2 | 578 | 238 |
| 3 | 190.7 | 590 | 254 |
| 4 | 186 | 597 | 246 |
| 5 | 190.5 | 567 | 250 |
| J (average) FEA, N/mm | 187.2 | 582.4 | 246 |
| J from experiments, N/mm | 194.6 | 669.6 | 254.5 |
| variation, % | 3.8 | 13.0 | 3.3 |

### 4.3. Discussion

Overall, the DCPD technique accurately estimates crack development in both straight and tilted notches. The results of DCPD crack growth prediction presented in Table 24 inferred that the potential drop signal was unaffected by crack front shearing, which often restricts its use to mixed-mode fracture experiments [128]. This can be shown in the DCPD % error in column 5 in Table 24, where all except one specimen exhibited a percentage error higher than 15%, slightly exceeding the recommended threshold. The rest had a percentage error below the 15% limit prescribed by the ISO12135 standard validity requirements indicating that the DCPD method remains a reliable tool for tracking crack growth.

Figure 43 presents the calculated mode III CTOD for the three-notch orientations, revealing that the scatter in mode III CTOD between specimens of identical notch angles is limited. This consistency demonstrates that DIC provides robust and reliable measurements of out-of-plane displacements. These findings align with the conclusion of a previous study [140], which also used DIC to measure the mixed mode I/II fracture characteristics of mild steel. That study confirmed the accuracy of DIC in capturing in-plane displacement fields and fracture behaviour, further establishing it as a reliable method for determining fracture resistance curves across various loading modes. These results highlight the versatility and precision of DIC, particularly when applied to both in-plane and out-of-plane fracture analyses.

The observations in Figure 44 (b) regarding the mode ratio $\delta_I/\delta_{III}$ show a rapid increase during initial loading, followed by a decrease, and finally reaching a stable, uniform state. This behaviour is closely linked to the turning and twisting of the specimen, which influence the relative contributions of tension (mode I) and shear (mode III) during fracture. As the specimen twists, mode-III fracture dominates initially, but as loading progresses, the influence of mode-I increases. A previous studies in [141] has also addressed a similar stabilization of the mode ratio at peak loading, noting that the twisting-induced mode-III cracking occurs in a non-coplanar manner, while mode-I cracking is coplanar with the loading direction. As a result, once torsional effects diminish, the ratio of mode I to mode III CTOD stabilizes, leading to a more uniform fracture behaviour as tearing progresses. This stabilization signifies the point at which the shear and tensile contributions to crack growth balance out, providing insight into the underlying mechanics of mixed-mode fracture.

The observation of Figure 43 of the straight-notched specimens having negligibly mode III CTOD as compared to the specimens with tilted notches is consistent with findings of [145]. When the notch is straight ($\varphi = 0°$), the specimen fails under pure tension (mode I), when the notch is tilted there is presence of mixed mode loading and this leads to the specimens withstanding larger maximum loads compared to straight notched specimens as shown in Table 23 materials' response to ductile tearing resistance behaviour is influenced by the mode-mix effect brought by notch tilt angle even when the material type, loading mode, specimen shape, and crack dimensions are the same. This is depicted in Figure 26 where the resistance straight-notched specimens that experience mode I loading are relatively flat compared to the 45-degree tilted specimens that experience mixed mode I and mode III loading.

Table 22 illustrates the contributions of the mode III CTOD to the total CTOD at maximum loads. The larger the notch tilt angle, the larger the mode III opening while straight notches contribute a negligible percentage of mode III opening. From this table, the total CTOD is reduced by the introduction of mode III openings. This agrees with the findings reported in [47] where it was concluded that the dominant stress state in the fracture process has a significant role in crack propagation inside structural components. Another study [146] also shown that mode I/III fracture toughness is significantly lower than mode I fracture toughness at each temperature. The pronounced bending of the ligament of straight notched specimens as depicted by micro stains in Figure 49, suggests there is a larger opening of the crack mouth opening compared to tilted notched specimens.

From an energy point of view, tensile fractures absorb less energy, whereas shear cracks absorb more energy [147]. From comparing the resistance curve of straight, 22.5, and 45-degree notch slant angles, it is evident that the more the tilt angles are, the flatter the resistance curve is. This suggests that in the case of a slanted notch, the crack growth remains stable compared to a straight notch as a flatter R-curve corresponds to a steadier fracture propagation. In contrast, a straight notch, with its rising R-curve, indicates less stable crack growth. This finding contrasts with the fracture testing results on structural steel reported in [84], where an increase in shearing load (i.e., mode II loading) was found to reduce the overall toughness.

The findings reported in [137] showed that while the imposed mode III loading component reduced the mode I SIF needed for crack initiation, the combined mode I - mode III loading had a higher total stress intensity factor than the mode I case. This suggested that fracture initiation was more difficult in the combined mode I/III orientation than in mode I.

The crack angle also caused different response on ligament deformation behaviour and strain as shown in Figure 49 For the early loading stage, all the ligaments were subjected to the compressive force caused by the bending-dominated load acting on the net section of the specimen resulting in negative strain. However, it is noticeable that straight-notched specimens that experienced pure mode I loading experienced the highest magnitude of ligament bending while the 45-degree tilted which experienced the highest ratio of mode mix experienced the least bending. This behaviour has been linked to the low constraint level developed at the crack tip [47]. Most elements in the 45-degree tilted notch are subjected to axisymmetric tension which reduces the crack speed and delays the fracture process by shear lips formation. This phenomenon has also been observed in single edge notch bend (SENB) specimens straight-notched specimen initially subjected to a combined tension-compression loading mode along the remaining ligament, being opening stresses at the crack-tip side and compressive forces at the ligament point. The tilted notch specimens experience little bending at the ligament and deflect in the out-of-plane mode III opening due to mixed mode I/III loading [148]. Particularly the 45-degree tilted notch specimen experiences tensile dominating conditions which is why it exhibits two advancing crack fronts on the edges as shown in Figure 49 by strain gauge behaviour, accounting for the observed reverse tunnelling effect in Figure 51.

The typical contour plots of von Mises equivalent strains around the crack tip of tested specimens at maximum loading obtained from DIC are presented in Figure 48. Under mode I loading, the near-crack tip plastic deformation field spreads out in a fan from 45 to 135 degrees from the fracture plane, resulting in the characteristic kidney bean-shaped plastic zone. Under combined mode I/III loading, the near fracture tip deformation field spreads out in a fan, while the mode III-induced component is limited to the crack route [149]. This significant variation of the plastic deformation field near the crack tip is the main cause of the difference in fracture resistance. These findings agree with the one reported in [150] where it was concluded that the mode III loading component reduces the dominating strain component ($\varepsilon_{\theta\theta}$) upstream of the fracture tip and raises strain singularity compared to the mode I situation.

Crack-tip conditions determine how the crack propagates along the remaining ligament [144]. The variation in the shape of the crack front for the three loading angles is shown in Figure 51. For the 0-degree crack angle, the main crack growth occurs in the middle of the specimen thickness. When a near-tip material point is under mode I loading, it is subjected to a large opening stress causing elongation in that direction and lateral contraction due to the Poisson ratio. The surrounding material will prevent it from happening giving rise to a triaxial stress state [79], because of the stress state at the crack tip with tilt notch introducing or mimicking a plane stress condition, primarily due to the absence of an out-of-plane (through-thickness) stress component. According to previous study [10] microvoid coalescence causes an edge fracture in a plate to expand quicker in the centre due to increased stress triaxiality, creating a tunnelling effect. The edges of the tilted crack introduce a second crack tip to enhance uniform fracture propagation, thereby partially reducing tunnelling. the 45-degree tilted notches introduced reverse tunnelling like the one observed in the literature [146]. The pronounced reversed thumbnail crack front observed in the 45-degree tilted notch is similar to the specimen where side groves are present as observed by previous authors [51]. Another observation from the fractured specimens is the tendency of the tilted notches to grow straight without any fork formation as reported by [151], where they found that arbitrary cracks will be subjected to symmetric and antisymmetric loading leading to fork formation. The absence of a tunnelling effect in the 22.5-degree angle fractured surface suggests low-stress triaxiality meaning the stress distribution along the remaining ligament is relatively uniform.

The observations on the fractured surface of mode I and mixed mode fracture in Figure 50, show how the interplay between local separation processes and large-scale plastic dissipation heavily influences the mechanism of void formation and coalescence. According to literature [144] the presence of dimple-like structures denotes ductile failure. The observed widespread big dimples on the specimen with an angle of 22.5 indicate a higher ductility fracture [152]. The straight notches specimen undergoes intergranular crack growth. At the same time, mixed-mode loading causes both a mixture of transgranular and intergranular fracture with an increase in the crack angle indicating α reduces the fraction of intergranular fracture compared to the transgranular fracture [153]. The intergranular fracture occurs when cracks propagate along the grain boundaries. Typical cleavage features such as river patterns and secondary cracks were visible in the mode I fracture. Cao [40] confirmed that it is difficult to form a large primary void because more energy will be consumed, creating a void of a larger size. The formation of the primary void with a larger size causes a higher resistance to the propagation of the crack as observed in Figure 50, the difference in the size of the primary void is the main cause of different fracture toughness for straight and tilted notches.

The plastic zone, which forms around the crack tip due to localized yielding, is directly influenced by the SIF, serving as a critical indicator of the crack driving force and the extent of non-linear deformation in the material. After passing through the plastic zone, the material transitions to a linear elastic behaviour, where the SIF characterizes the stress and strain fields around the crack tip. Referring to the results gained based on the over-deterministic algorithm in Table 25 and Figure 52 there is a lot of plastic deformation accumulated ahead of the crack tip. This plastic area is getting larger as the crack propagates and can be considered as a gap in the calculations. The size of this gap ahead of the crack tip indicates that 14MoV6-3 steel grade undergoes a lot of yielding before the onset of fracture. As a comparison, the J-integral obtained from the numerical simulations and calculated from the experiment had an insignificant difference as shown in Table 27. Furthermore, the SIF attained for mode I loading using a robust over-deterministic numerical algorithm deployed in a mathematical routine, produced closely agreeable values to the one obtained from experimental load and crack extension. At the present there is no standard available for measurement of the Stress Intensity Factor for slanted notches.

### 4.4. Summary and conclusion

Considering the complex stresses in power boiler piping and the oblique orientation of cracks, mixed mode I/III loading plays a significant role in crack propagation during service. This research investigates the fracture characteristics of 14MoV6-3 power plant steel under mixed mode I/III loading. Experimental techniques are implemented using the 3D full-field Digital Image correlation (DIC) tool to measure the Crack Tip Opening Displacement (CTOD) in quasi-static loading conditions. Single Edge Notch Tension (SENT) specimens are used to assess tilted notches' effect on their tearing resistance. Three different notch angles 0, 22.5, and 45 degrees are assessed. The contribution of mode III CTOD to crack opening is quantified. In all cases, it can be inferred that the fracture toughness under mixed mode I/III loading is slightly higher than the under mode I loading.

Numerically, the problem is solved using the finite element method, FEM, formulation extended to the fracture mechanics theory in which J-Integral is acquired and compared to the experimental solution, a good agreement is then verified. The mode-I Stress Intensity Factor (SIF) is calculated from the DIC data using the overdeterministic algorithm to obtain an alternative solution and assess the experimental campaign's robustness. Therefore, a comprehensive comparison is drawn amongst all acquired results. Furthermore, the fracture resistance (R-curves) of the different notch angles is experimentally evaluated. In this thesis, the mixed-mode (I/III) fracture in 14MoV6-3 power steel is investigated using SENT specimen including tilted notches. The effects of inclination angle are studied. There is no standard for obtaining CTOD in SENT testing using slanted notches. Limitation arises during fracture evaluation when the crack is angled, making clip gauge examination problematic. Thus, DIC technique is used to quantify the fracture parameter $\delta_5$.

Owning to the obtained results, the following conclusion will be drawn:

- CTOD measurements of 14MoV6-3 steel on the SENT specimen yielded satisfactory results.
- SENT specimens with tilted notches can be used to determine the fracture toughness of mixed mode I/III. In this regard, the DIC is robust to assess the mixed mode I/III during ductile fracture.
- The parametric study shows that there exists a strong influence on crack tilt angle on $\delta_5$. Increasing the tilt angle leads to an increase in the mode III opening component.
- Specimens with straight notches had a relatively lower fracture toughness. Fracture toughness strength increases with loading angle modes I+III.
- From the fracture surface observations, the tilt angle affects the shape of the crack front.
- There was no apparent change in the failure mechanism with the introduction of the mode III loading component. Mode III shear did not play a significant role in the failure process which was mostly influenced by mode I tensile stresses.
- The potential reason for the increase in fracture toughness with increasing mode III loading was redundant work due to the change in fracture mechanism from cleavage under mode I loading to ductile under mixed mode I/III loading.

# CHAPTER 5: INFLUENCE OF SHORT TERM ELEVATED TEMPERATURE CREEP ON FRACTURE TEARING RESISTANCE

The design lifetimes of power plant components are determined by their mechanical and creep qualities, which are typically those of the virgin state (i.e., as received). However, the actual material qualities may fluctuate due to ageing in service, and plant operation conditions may be altered to fulfill an unexpected need [154]. Thus, the creation of high-quality databases of relevant creep features for power plant design and life management is critical. The molybdenum-vanadium steel grade 14MoV6-3 (EN 1.7715) is ferritic-pearlitic steel that has been widely employed in power plant installations to manufacture boilers and steam pipelines intended for steam temperature up to 540 °C [155]. This is due to their excellent elevated temperature properties allowing reduction of pipe wall thickness [156]. It also offers other better creep resistance, lower weight, lower manufacturing costs due to reduced amount of welding and ease of handling and transportation than grades of previous generation [116].

Despite their creep resistant properties incidences of boiler pipes made of low alloy molybdenum vanadium steel grade has been reported to break prematurely [157]. Failures are generated by the combined effects of temperature, fatigue loading, and harsh environment and are typically exhibited as through-the-thickness fractures, resulting in pipeline leaking before break. Engineers prefer to replace existing broken 14MoV6-3 steel pipes with new ones constructed of various steel grades rather than repair them. Surface flaws are repaired by grinding until the indication is no longer visible. Long-term use of 14MoV6-3 steel in creep circumstances results in microstructure alterations. This is known as thermal ageing, and it is a problem for many steel components. Thermal ageing, in general, reduces the ductility and hardness of steel and aggregates with time. Accurate prediction of ductile fracture behavior is vital in structural integrity assessments of crucial engineering structures operating in a fully plastic environment such as boiler pipe systems [158].

Creep strength and fracture resistance are the most important determinants of the appropriateness of high-pressure steam pipeline materials [10]. Creep is typically to blame for 30% of all tube failures in boilers and reformers [159]. The fatigue and creep phenomena for power steels are well documented in the literature, but only as model fatigue processes carried out on proper equipment from the initial state of the tested alloys. However, cracks in the elements can form during long-term operation under cyclic loads and environmental factors. One disadvantage of ferritic steels is the likelihood of a shift in fracture mechanism from ductile to cleavage [16]. Boiler tube creep fractures are thought to be the cause of 10% of all power plant failures. In thermal power equipment in general, and the major steam pipes in particular, metallographic analysis and hardness measurements are routinely employed to validate the present technical status of operated steels. Steel structure research focuses largely on grain and carbide size, carbide distribution inside grains and along their borders, and pore density.

According to a literature survey done in [160] it was reported that literature data do not provide much information on low-alloy energy steels about service life. Considering the wide use of 14MoV6-3 steel for many components of power boilers at temperature up to 540$^0$C. Some efforts have been put to research effect of creep and long-term operation on 14MoV6-3 steel [155], but no literature could be found to measure resistance curves after long periods of operations. In a study by [160] degradation of microstructure and strength properties of heat-resistant steels operating under variable loads was investigated. Considering this, it is critical to get more insights on the influence of creep ageing on the fracture toughness of materials used in power industry infrastructure and materials extracted from power plants. Research by [161] experimented on impacts of exploitation time and temperature on resistance to brittle fracture of low-alloyed Cr-Mo steel A-387 Gr. They concluded that exploitation time impacted the resistance to crack propagation and other mechanical properties.

The currently used method (Office of Technical Inspection Guidelines, Poland) of estimating the safe life of materials based on the microstructure of metallographic replicas is a has limitations due to the inability to determine the degree of advancement of precipitation processes or the degree of deformation. As a result, defining the procedure for assessing the degree of material deterioration at the substructure level becomes critical. Experimental measurements and assessments of fracture toughness are critical for mechanical structure performance and quality [162]. The fracture toughness resistance curve is useful in assisting strain-based design and pipeline integrity evaluation [55].

To forecast the date of the next technical inspection, decommissioning or to fully justify equipment to continue operating in the presence of a crack or after the end of its design lifetime its structural integrity should be known. The material's fracture behaviour data are required for integrity assessment due to their loading range.

Understanding the microstructural evolution and fracture behavior of materials during creep exposure, especially early phases of loading, can help design creep-resistant steels and enhance creep-life prediction tools. However, to our knowledge, there is currently no systematic fracture behavior of 14MoV6-3 steel during very short-term isothermal ageing, which could replicate an early stage of creep loading of high temperature components. The purpose of this work is to further elucidate creep-strength deterioration of 14Mo6-3 steel following short-term static annealing. Previous research initiatives on the fracture behaviour of 14MoV6-3 were done using SENB and CT specimens which provide over-conservative figures due to their high crack tip. However, fracture behaviour of 14MoV6-3 employing SENT specimens after a lengthy period of operations is still absent. In this work, experimental crack tip opening displacement (CTOD) methodology is used to assess the ductile tearing resistance curves using SENT specimens. Creep ageing is performed on virgin steel to various stages of ageing.

The main results of this chapter was published in [56].

## 5.1. Material and methods

### Materials

The study was carried out using ferritic -pearlitic steel described in Chapter 4. The spectrometry of chemical composition of the as received material was accomplished and it was found to conform to conditions prescribed in the European standard EN-10216-2. According to the manufacturer's certificates, the pipe was normalized at $1050^0$C/1 hour/air cooling and tempered at $780^0$C/140 minutes/air cooling. This state is now referred to as the as-received state (AR).

The yield strength, ultimate tensile strength, and elongation of the as received and the aged 14MoV6-3 steel where evaluated using static tensile test according to ASTM standard [163]. For the new as received material the results were compared with standards requirement and manufacturers certificates. Mechanical properties of the examined steel from manufactures certificates and from our testing results are presented in Table 28.

.

Table 28: Mechanical parameters in as-received condition, manufactures certificate and according to the standards EN-10216-2 at room temperature.

| | **Ultimate tensile strength, MPa** | **Yield strength, MPa** | **Elongation (%)** | **Energy of impact, J/cm$^2$** |
|---|---|---|---|---|
| Manufactures certificates | 591- 593 | 332-353 | 28.8-29.2 | 169-174 |
| As received | 559-562 | 343-373 | 23% | 174-198 |
| EN-10216-2 | 460–610 | > 320 | > 20% | |

### Accelerated creep ageing

The specimens were machined to get the standard specimen size and create threads for griping during creeping. The rod-like creep ageing specimens were machined along the rolling direction (RD) of the rods. These were specimens of 12 mm square cross-section and a gauge length of 140-180 mm and a thread of 16M as shown in the Figure 53.

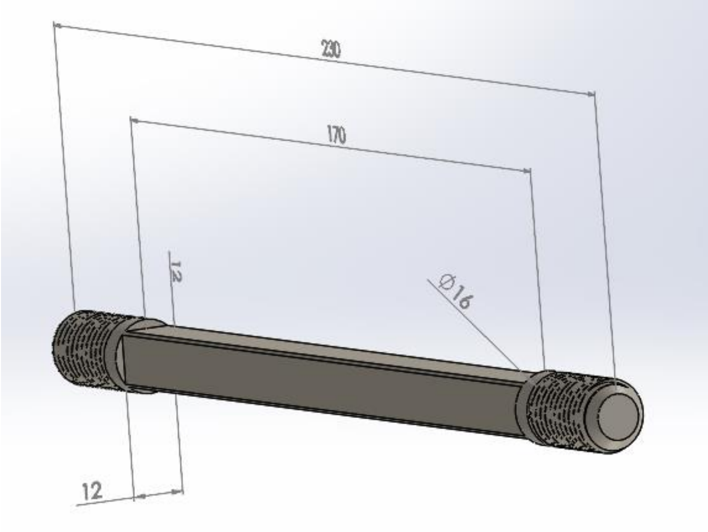

FIGURE 53: The creep specimen

Ageing was done to replicate the operating conditions of the primary steam pipeline of boiler power plants. These components can fail or wear out much earlier than others. They are known as boiler key parts. Among critical elements, those that function above the limit temperature, i.e., in creep mechanism operating circumstances, deserve special consideration. The functioning of power boiler components in the main steam cycle is deemed important because the steam is delivered to the turbine via the supply system. (e.g., heaters, superheaters, drum). Therefore, the water is converted into steam with the high pressure and temperature requirements for powering the engine (15 MPa, 540 C) [160].

To imitate the elevated temperature working conditions of the material accelerated ageing was performed to degrade the structure of the materials using Kappa 05DS Zwick machine fitted with a furnace. 12 mm square-shaped specimen with a length of 170 mm where machined for all creep tensile testing. Creep tests were conducted atmospheric conditions at constant temperature of 540°C and as this is the operating temperature of boilers made with the studied steel grade. The temperature during thermal ageing was maintained at ± 2 °C. Creep elongations were continuously measured, using a linear variable differential transducer, recorded digitally and computer processed.

According to literature the creep time to rapture of 14MoV6-3 steel is presented as 242 MPa at 480 hours. To prevent the rapture of the specimen, the stress to rapture was reduced by 30% hence the creep pressure was 169 MPa for the three stages of ageing namely 120, 240, and 480 hours. This represented 10% of the expected lifespan. of the steel grade at those operating conditions of temperature and stress. Table 29 shows the codes used to name the specimens according to their stage of ageing. For statistical robustness three specimens were prepared for each condition of ageing.

TABLE 29: The name codes of the specimens showing their aged state.

| Specimen description | Code |
|---|---|
| New as received | NS1, NS2 and NS3 |
| 120 hours ageing creep | 10-120 and 12-120 |
| 240 hours creep ageing | 3-240, 6-240 and 6-240 dot |
| 480 hours creep ageing | 4-480, 5-480 and 7-480 |

### Specimen geometry

Fracture toughness testing was performed using SENT specimens all having dimensions of B=W =10 mm and the daylight grip length (H) is equivalent to 10W and a/W = 0.5. The use of deeply cracked specimens of a/W =0.5 is to guarantee conditions leading to high crack-tip constraint with limited scale plasticity and to compare the results with previous work in the literature. All SENT specimens with crack-oriented perpendicular to extrusion direction were used as shown in Figure 54 as stipulated in British standard BS:8571 2018. A two-step milling procedure was used to machine the initial cracks such that the final root radius of the crack was 0.15 mm. Four holes of diameter 1.9 mm and 3 mm depth were drilled 4.5 mm from the notch for attaching the clip gauges.

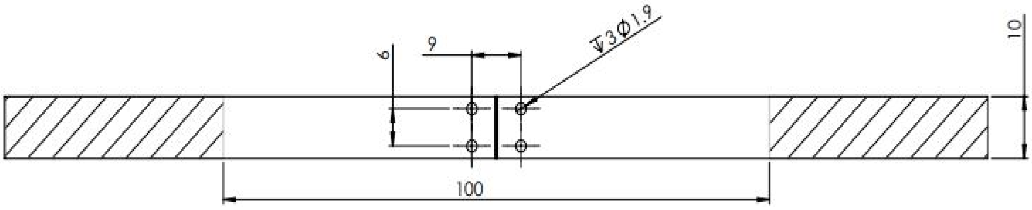

FIGURE 54: Schematic drawing (out-of-scale) showing the dimensions of the SENT test specimen.

### SENT tearing resistance test procedure.

No fatigue pre-cracking was done since this would make controlling the initial fracture depth more difficult, and it is not necessary for adequately ductile materials [73]. At least two identical samples were tested for each condition of ageing. The test setup is as shown in Figure 55. The current pins on the specimen were positioned to ensure a uniform potential field hence the potential drop across the crack is independent of the pin’s location. Figure 56 (a) shows the specimen with pins welded on to the specimen.

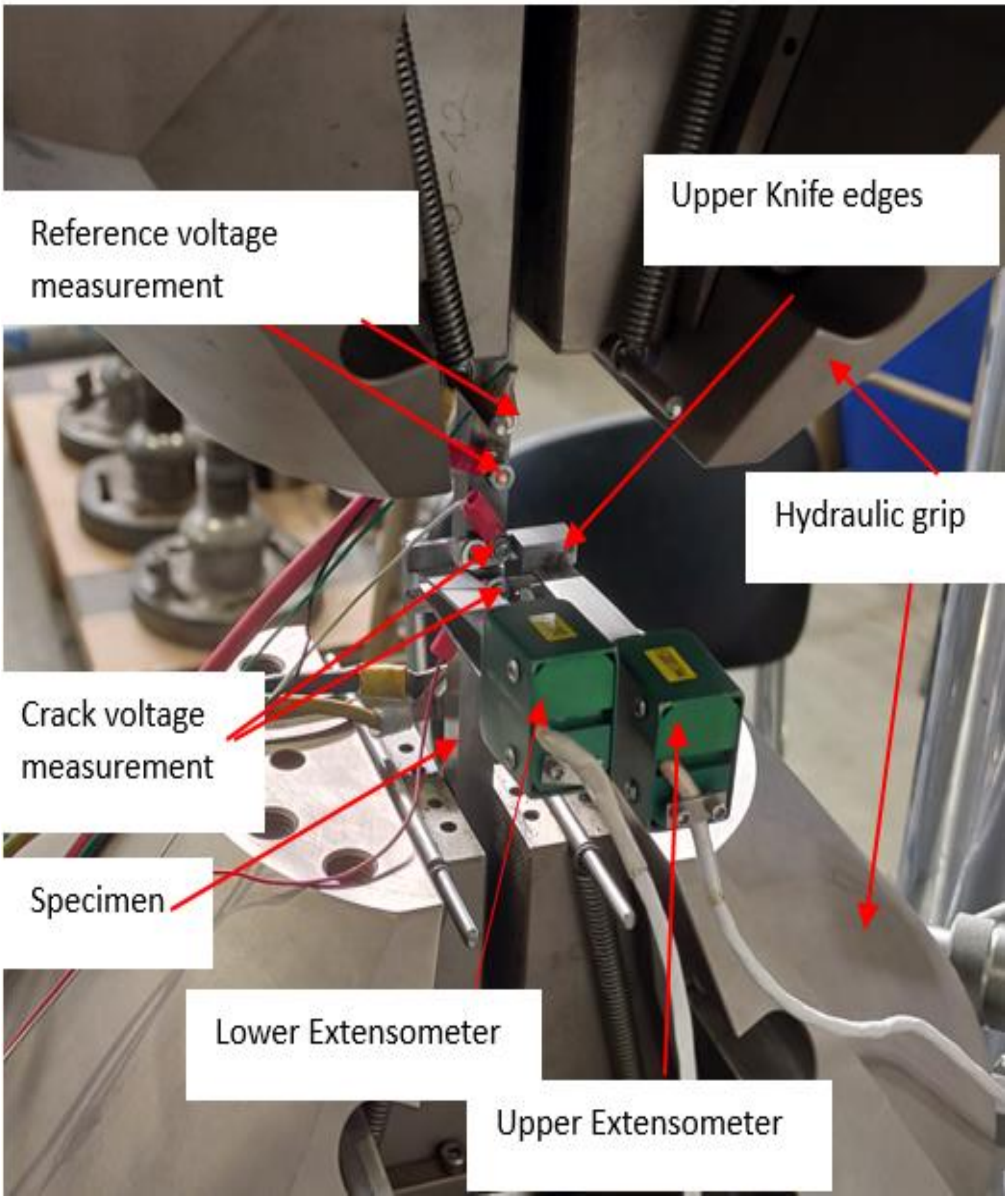

FIGURE 55: The SENT specimen testing setup.

The tests were carried out at room temperature at Soete Laboratory at Ghent University Belgium using a 100 kN servo hydraulic testing machine. The clamping approach for griping was used using pressure of 5 MPa. Tensile loading was applied to the specimen under quasi-static displacement control at a loading rate of 0.01 mm/s [164]. A double clip gauge approach was used to compute the crack mouth opening displacement (CMOD). The crack growth was measured using both the direct current potential drop method (DCPD) and unloading compliance (UC). The supplied current was 25A ensuring there is high crack density given the good conductivity of steel. The unloading regime was done following the procedures by ASTM E1820-18a.

After attaining a load level equal to half of $F_m$, where $F_m$ is given by Equation (5.1). Six unloading cycles in the elastic regime were performed in each test to allow the specimen to “bed in” as described in ISO standard.

$$F_m = \frac{1}{2}\frac{б_{0.2}+б_{UTS}}{2}(W - a_o)B_e \tag{5. 1}$$

where: Be= B since there were no side grooves. The unloading at the plastic region was done after equal crack openings.

The tests were carried out past the maximum load until the load fell below 80% of the maximum measured value to acquire enough fracture development.

There are three definitions for CTOD [25]. For this work the 90° intercept method as also called UGent method [25] is applied. The CTOD was calculated from the double clip gauge data performed by means of Equation (5.2.

$$CTOD = 2\frac{V_2(a_O+h_1)-V_1(a_O+h_2)}{(V_2-V_1)-2(h_2-h_1)} \tag{5.2}$$

For the estimation of crack growth using the unloading compliance the correction factor (F) as suggested by Shen et al [165] was applied. Compliance to crack size is expressed represented in Equation (5.3) as a ratio of a/W as follows.

$$\frac{a_i}{W} = 1.6485 - 9.1005U_i + 33.025U_i^2 - 78.467U_i^3 + 97.344U_i^4 - 47.227U_i^5 \tag{5.3}$$

Where U is expressed in Equation (5.4) as.

$$U = \frac{1}{1+\sqrt{B_{ef}C_{icorr,i}E}} \tag{5.4}$$

Where E is the Young’s modulus, $C_{icorr,i}$ is the corrected compliance and $B_{ef}$ is the effective thickness which in our case equals B because there are no side grooves.

The fracture surfaces of the studied specimens were heat tinted in an oven at 200°C for 2 hours to analyze them. They were then cooled in liquid nitrogen before being brittle fractured. The nine-point average technique as shown in Figure 5.3, was used to get an average final crack length. This was used to validate the crack length measurement obtained by UC and DCPD.

Tensile tests were performed to characterize the mechanical properties of the as received and the creep aged materials. Hereto, round bar specimens with a gauge diameter and gauge length of 6 mm and 4 mm respectively were used. Figure 56 (b) shows the specimen used for tensile testing. At least two specimens were tested for each ageing condition using Zwick/Roel Z100 universal testing machine. Testing was done according to ASTM standard. A clip-on extensometer was used to record load elongation data in the elastic zone.

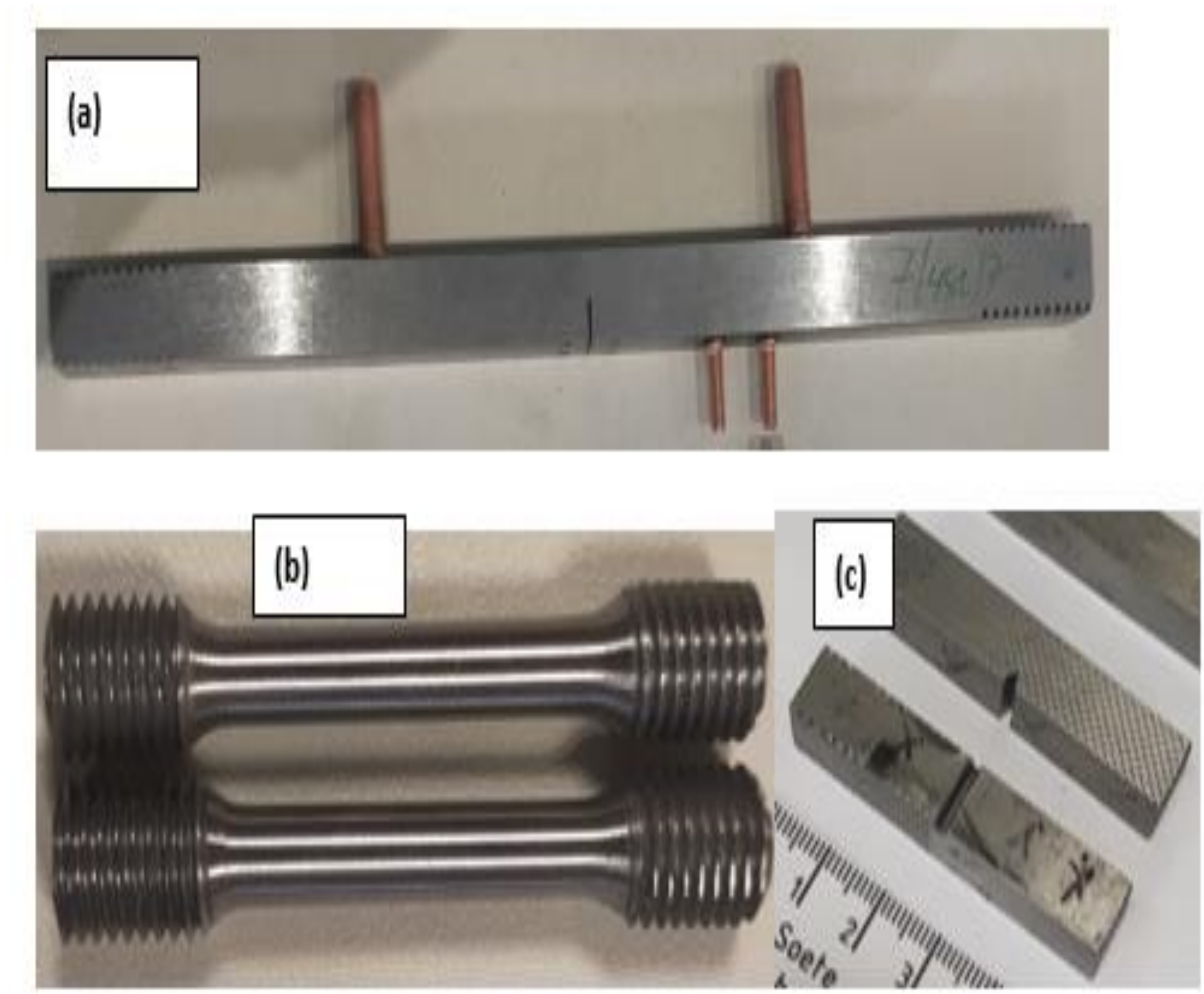

FIGURE 56: Images of SENT specimen (a), round specimens for static tensile test (b), threaded samples and Charpy impact specimens (c).

A set of Charpy-V notch (CVN) impact specimens for each ageing period was extracted in the same orientations as for SENT specimens. Impact toughness testing was carried out at room temperature according to ASTM E-23 where V-notched specimens of 10x10x55 mm in size, was loaded to impact bending by Charpy pendulum. Figure 56 (c) shows the specimen used for Charpy impact test. Microstructure characterisation and fractographic analysis of both aged and crept specimens were performed by means of light, transmission and scanning electron microscopy. To investigate decrease of impact toughness due to creep ageing two specimens at each stage of ageing were selected for impact testing. The hardness of steel samples was measured using Zwick ZHV hardness apparatuses on polished specimens of 10 mm thick after being used for SENT testing.

## 5.2. Results

### Mechanical properties

Figure 57 presents the stress–strain curves for the new and aged specimens tested at room temperature. The characteristics of obtained tensile curves at room temperature correspond to typical stress strain curve of ductile metallic material even after the longest period of ageing which is 480 hours.

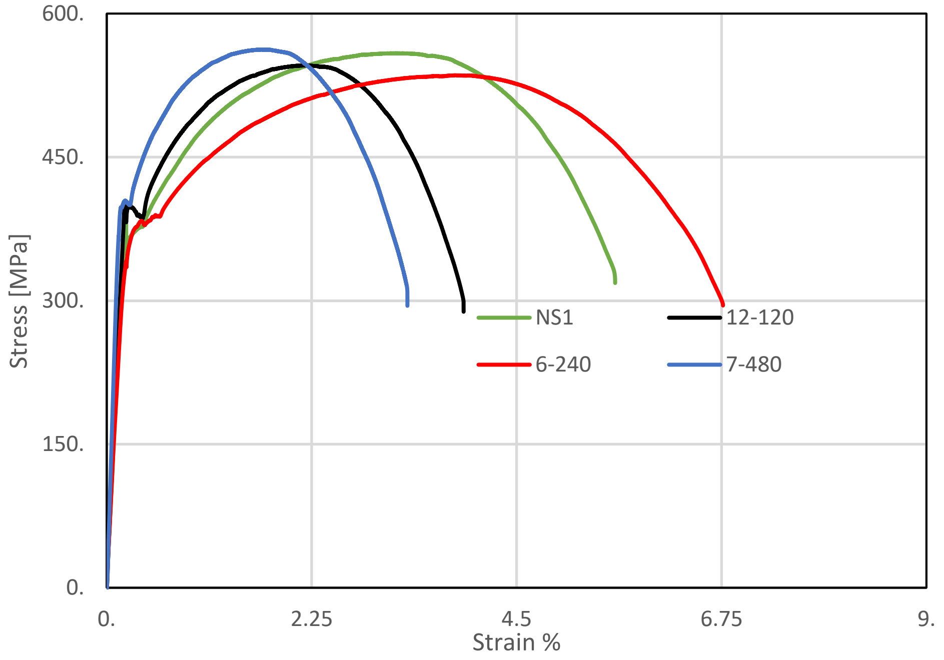

FIGURE 57: Stress strain diagram of new and aged specimens.

Tensile testing results of specimens of the new and aged specimens at room temperature are given in Table 30

TABLE 30: Results of mechanical properties of tensile testing

| Ageing period, hours | Yield Strength, MPa | Tensile strength, MPa | Young Modulus, GPa |
|---|---|---|---|
| 0 | 373 | 559 | 184 |
| 120 | 401 | 551 | 200 |
| 240 | 391 | 539 | 200 |
| 480 | 404 | 556 | 169 |

According to the results presented in Table 30 and Figure 58, its noticeable that the yield strength and tensile strength are insensitive to ageing time, as there is no significant change across the different stages of ageing. The yield strength and tensile strength are maintained at all stages of ageing at a value higher than required minimum value of 320 and 460 MPa respectively for the material according to EN 10216–2 Seamless steel tubes for pressure purposes - Technical delivery conditions - Part 2: Non-alloy and alloy steel tubes with specified elevated temperature properties.

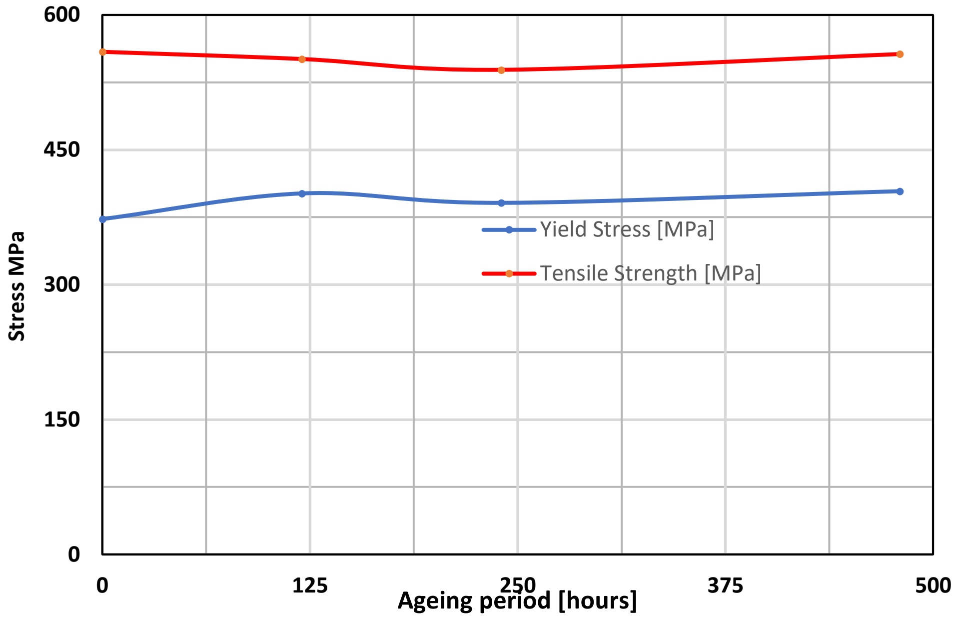

FIGURE 58: Average yield strength and tensile strength of the specimens after different stages of ageing.

### Load- CMOD curves

The load-CMOD curves for the SENT specimens are shown in Figure 59. No unstable fracture or unstable propagation phenomena, often known as "pop-in" phenomena, were noticed during the loading procedure, and the load remained stable even after reaching its maximum value.

It can be seen from the figure that the maximum loads of the aged specimens are higher than those of the new as received specimens. The average maximum loads were 29.3, 31.6, 31.3 and 29.7 for the new, 120, 240, and 480 hours of ageing respectively as shown in Table 5.4. That represents a 3-7% increase in maximum load in aged specimens. Also notably is that the as received unaged specimens have higher CMOD at maximum loads compared to aged ones. There is no significant difference in the maximum loads among 120, 240 and 480 hours of ageing.

During testing, there was substantial visible yielding and fracture blunting in specimens made of both new as received and aged specimens.

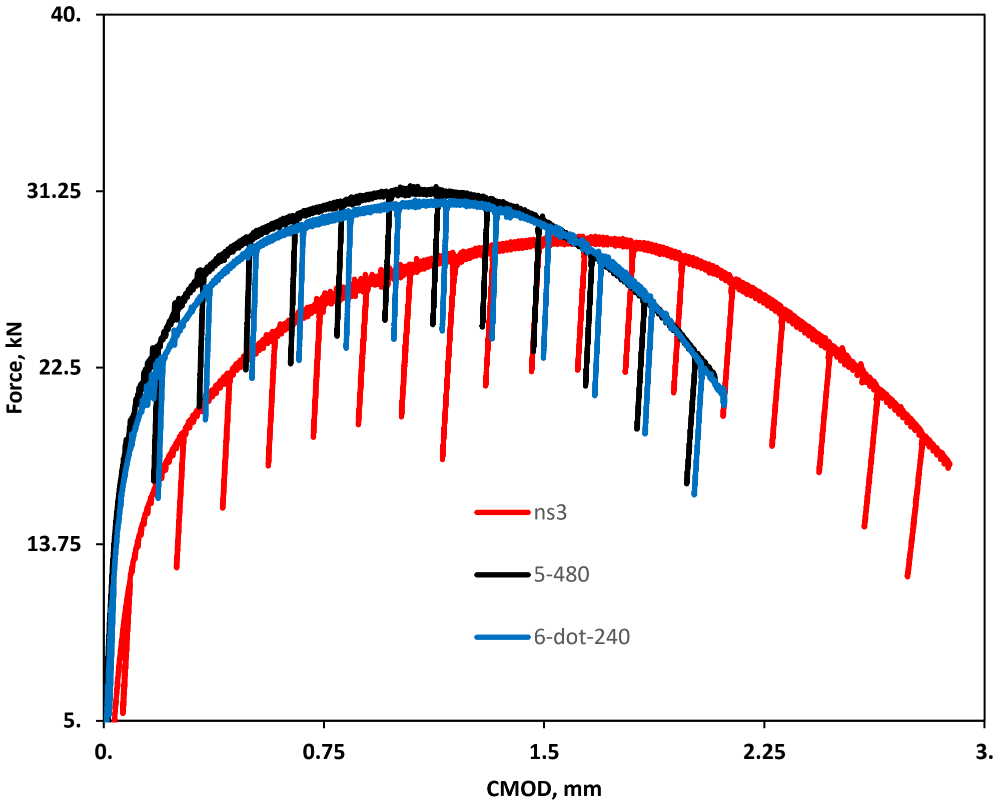

FIGURE 59: The records of load vs CMOD curves obtained from the SENT tests of specimens from new, 120, 240 and 480 hours of ageing.

### Resistance curves

The physical measured final crack extension and UC and DCPD predicted final crack length values were compared to determine the applicability and reliability of the method of DCPD and unloading compliance for crack size assessment. Figures 60 and 61 present the resistance curves as plotted using the DCPD data for crack growth together with final crack growth observed from postmortem examination of the specimens' fracture surfaces. In some specimens there is a very good correlation between the curves plotted using the UC and the DCPD data. Also notable is the expected trends of rising superior resistance to ductile tearing for new specimens compared to the aged specimens. In addition, it was seen that there is no significant difference in the resistance curves of 120 hours, 240 hours, and 480 hours of ageing. They exhibited similarly lower fracture toughness values.

Figure 62 presents the resistance curves of specimens plotted in one graph plotted using the DCPD data for crack growth. The results showed the trends of superiority of resistance to ductile tearing for new specimens compared to the aged specimens. There is no significant difference in the resistance curves of 120 hours, 240 hours, and 480 hours of ageing. They exhibited similarly lower fracture toughness values.

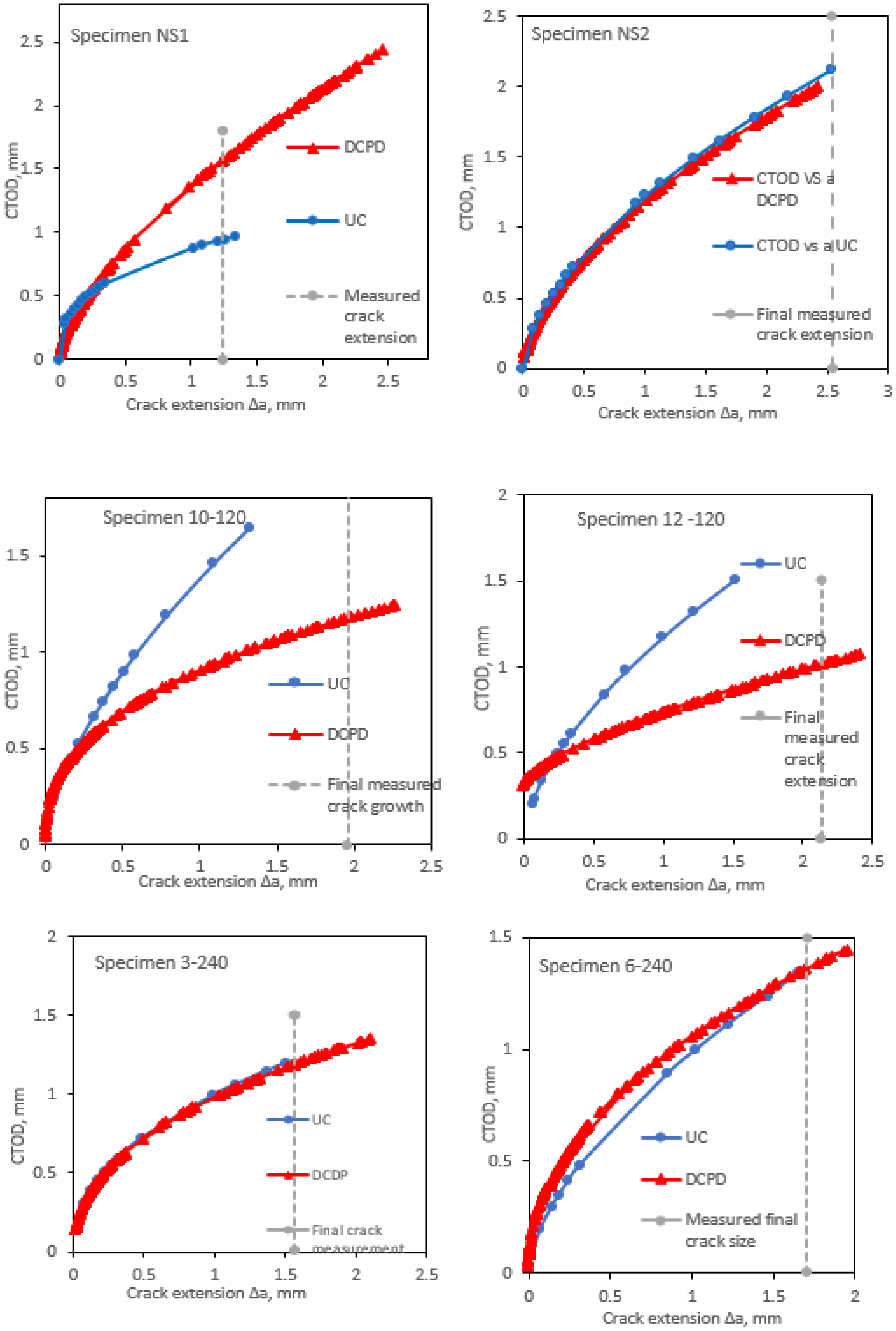

FIGURE 60: Resistance curves of new specimens and those aged to 120 and 240 hours were constructed from DCPD and UC data.

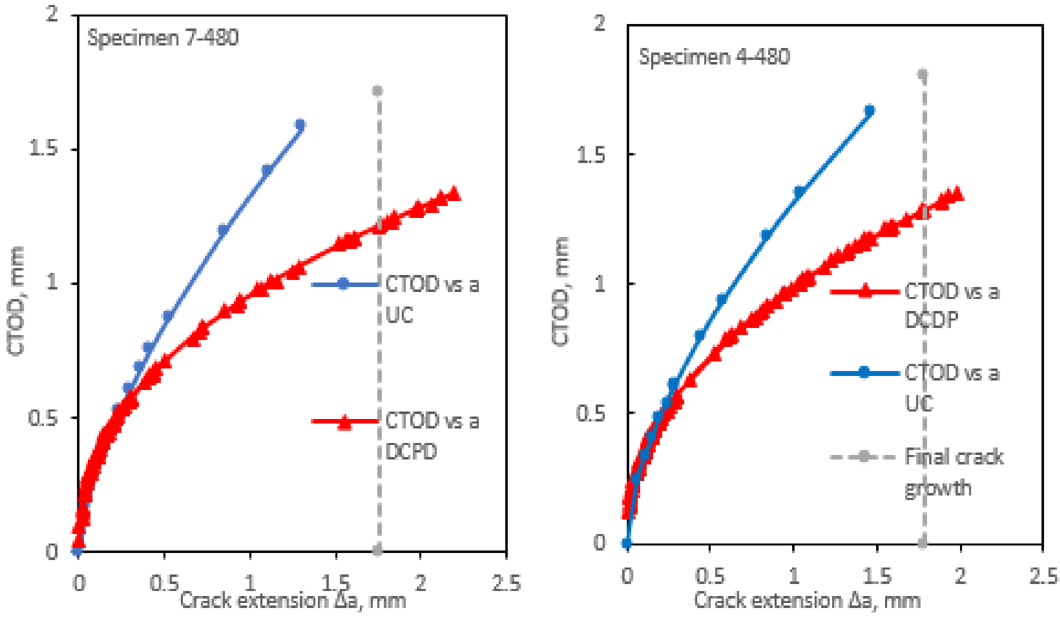

FIGURE 61: Resistance curves of new specimens and those aged to 480 hours constructed from DCPD and UC data.

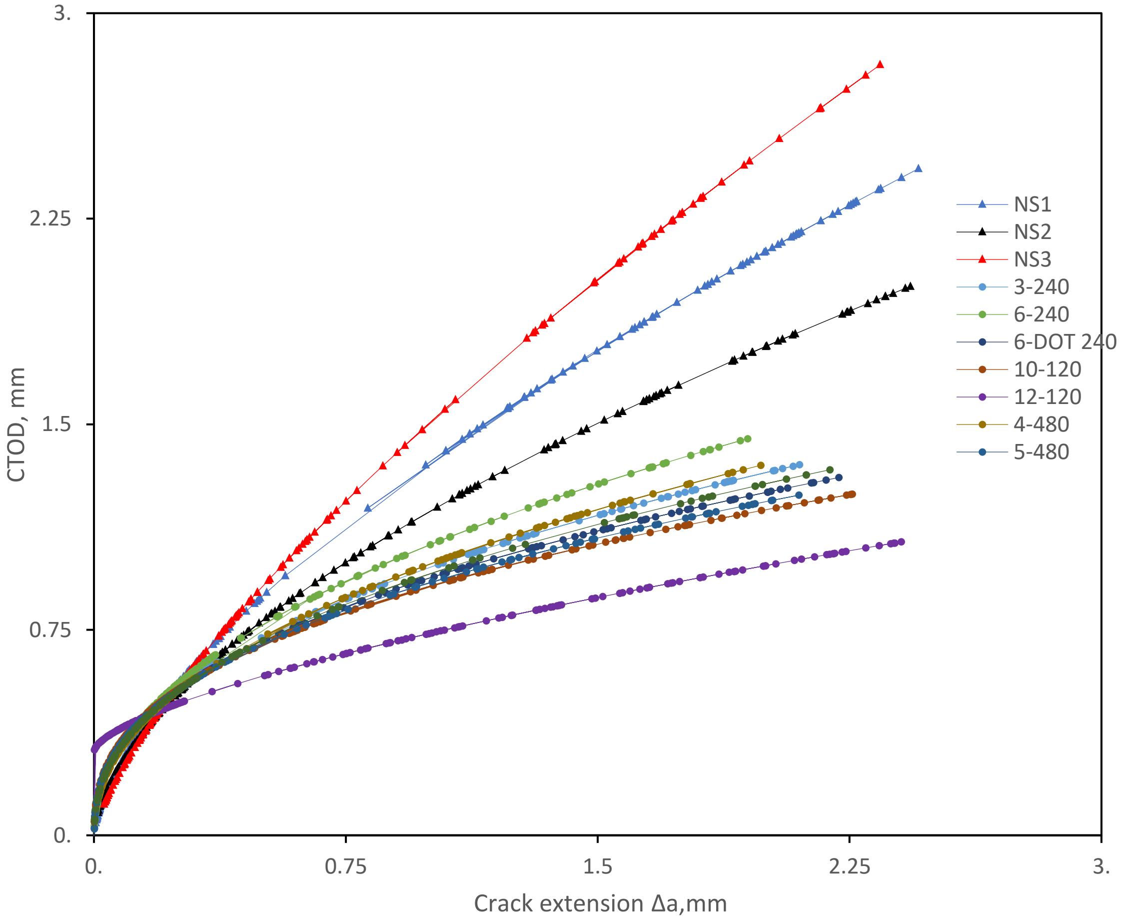

FIGURE 62: Comparison of resistance curves obtained from specimens of various aged conditions plotted using DCPD data.

Table 31 shows the crack size as determined by the fracture surfaces and indirectly estimated using the DCPD and Unloading compliance approach. More specimens meet the 15% percentage error qualifying criteria for valid test in DCPD data compared to Unloading compliance. To this end DCPD will be used for the analysis and comparison of the results as it has better reliable results.

TABLE 31: Errors in DCPD and UC final crack size measurements.

| **Specimen** | **N1** | **N2** | **N3** | **10-120** | **12-120** | **3-240** | **6-240** | **240-6dot** | **4-480** | **5-480** | **7-480** |
|---|---|---|---|---|---|---|---|---|---|---|---|
| 9-point average, mm | 1.24 | 1.757 | 2.49 | 1.96 | 2.14 | 1.569 | 1.71 | 1.77 | 1.78 | 1.78 | 1.75 |
| UC final crack, growth, mm | 1.33 | 2.53 | 2.82 | 1.32 | 1.52 | 1.50 | 1.65 | 1.40 | 1.46 | 1.36 | 1.30 |
| DCPD final crack growth, mm | 2.45 | 2.432 | 2.34 | 2.25 | 2.4 | 2.1 | 1.83 | 2.21 | 1.98 | 2.02 | 2.19 |
| DCPD % error | 97.2 | 38.43 | -6.19 | 14.77 | 12.2 | 33.81 | 7.44 | 25.27 | 10.92 | 13.5 | 24.92 |
| UC % error | 7.09 | 44.1 | 13.04 | -32.72 | -28.9 | -4.12 | -3.1 | -20.7 | -17.99 | -23.7 | -25.7 |

TABLE 32: Relationship between the ageing stage and maximum loads, crack initiation CTOD and resistance curves efficiencies.

| **Specimen code** | **MAX force, kN** | **Equations of CTOD-R curve** |
|---|---|---|
| NS1 | 29.86 | $1.3622(\Delta a)^{0.6455}$ |
| NS2 | 29.02 | $1.1815((\Delta a)^{0.5943}$ |
| NS3 | 29.01 | $1.506(\Delta a)^{0.734}$ |
| 10-120 | 31.73 | $0.9093(\Delta a)^{0.3856}$ |
| 12-120 | 31.50 | $0.3102+0.426735(\Delta a)^{0.6592}$ |
| 3-240 | 29.51 | $0.977967(\Delta a)^{0.4368}$ |
| 6-240 | 28.66 | $1.0602(\Delta a)^{0.4675}$ |
| 6DOT-240 | 30.80 | $0.9394(\Delta a)^{0.413154}$ |
| 4-480 | 30.49 | $0.9899(\Delta a)^{0.4526}$ |
| 5-480 | 31.51 | $0.9222(\Delta a)^{0.400}$ |
| 7-480 | 32.02 | $0.954292(\Delta a)^{0.42688}$ |

The Equation of the resistance curve shows in Table 32 shows the new specimens have a value of more 1 in the value of L in the Equation $CTOD = m + l(\Delta a)^{X}$. This indicates higher values of CTOD for new specimens compared to aged specimens. There is no significant difference in CTOD at crack initiation among aged specimens.

Table 33 presents the fracture initiation toughness at 0.2 mm crack initiation as defined in BS 8571 :2018 standards measured using both DCPD and unloading compliance data.

TABLE 33: CTOD fracture toughness initiation values derived from DCPD and UC resistance curves.

| **Specimen** | **NS1** | **NS2** | **NS3** | **10-120** | **12-120** | **3-240** | **6-240** | **240-6dot** | **4-480** | **5-480** | **7-480** |
|---|---|---|---|---|---|---|---|---|---|---|---|
| δ (mm) at DCPD$_{,0.2}$ | 1.2 | 1.13 | 1.4 | 0.71 | 0.59 | 0.77 | 0.82 | 0.70 | 0.79 | 0.59 | 0.60 |
| δ (mm)at UC Δa$_{0.2}$ | 0.65 | 0.93 | 1.08 | 0.72 | 0.57 | 0.64 | 0.63 | 0.58 | 0.68 | 0.60 | 0.59 |

## Hardness

Hardness values of the steel in the AR and the aged conditions are shown in Figure 63. Despite considerable scattering due to micro- structural heterogeneity of the materials, a slight increase of hardness with increasing ageing time can be observed. According to the manufacturer’s certificate the material has hardness between approximately values of 163 and and170 HB. The values for the new specimens found in this study are slightly higher but close to those in the manufacture’s certificates. This may be because of the effects of machining. For the aged materials creeping increases the hardness by 3% for 240 and 480 hours ageing and it’s unchanged for 120 hours of ageing.

The average hardness values in the 240 and 480 hours of ageing are slightly higher than those of new and 120 hours of ageing.

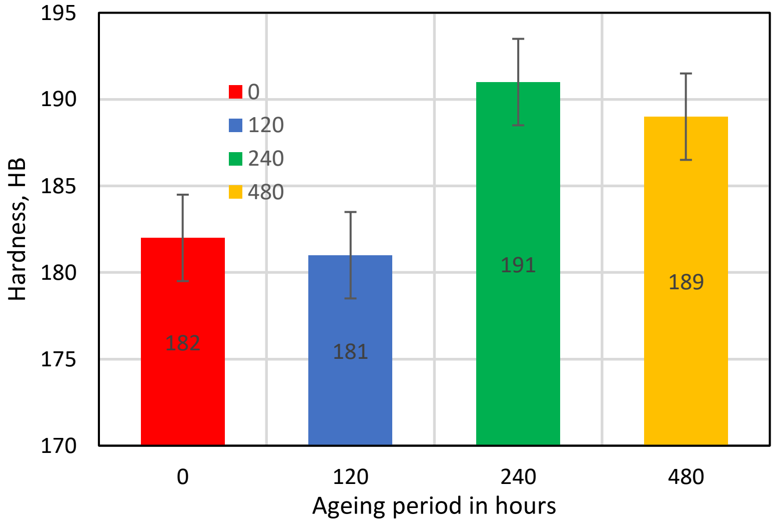

FIGURE 63: The distribution of hardness in the four stages of ageing.

### Charpy V-notch (CVN) impact energy data

Results of average values 2 specimens each condition of impact toughness of new and aged materials are presented in Figure 65. From the results it is notable that the total impact energy (impact toughness) increases slightly compared to new material and is maximum for 240 hours of ageing while there is no difference in average values of new material and 120 hours of ageing. Figure 64 shows the appearance of the specimens after fracture. All specimens both new and aged showed significant ductility.

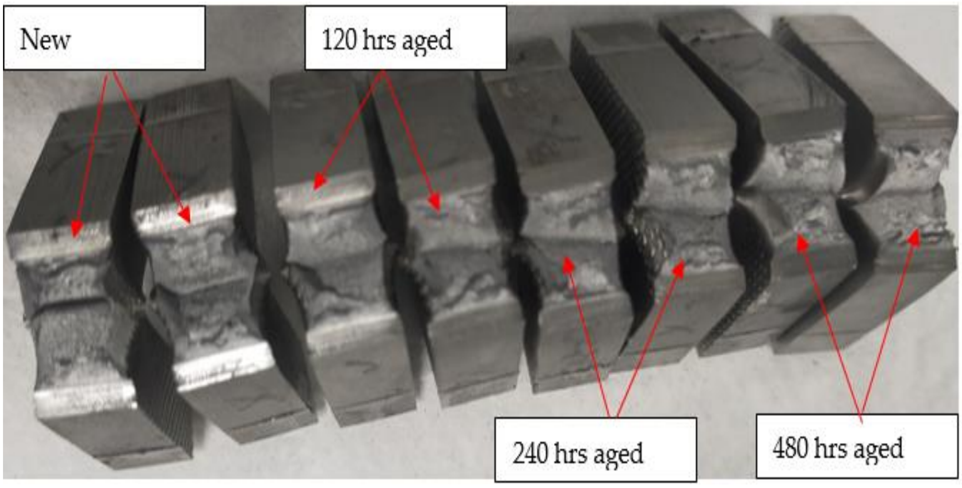

FIGURE 64: Images of specimens after Charpy impact test.

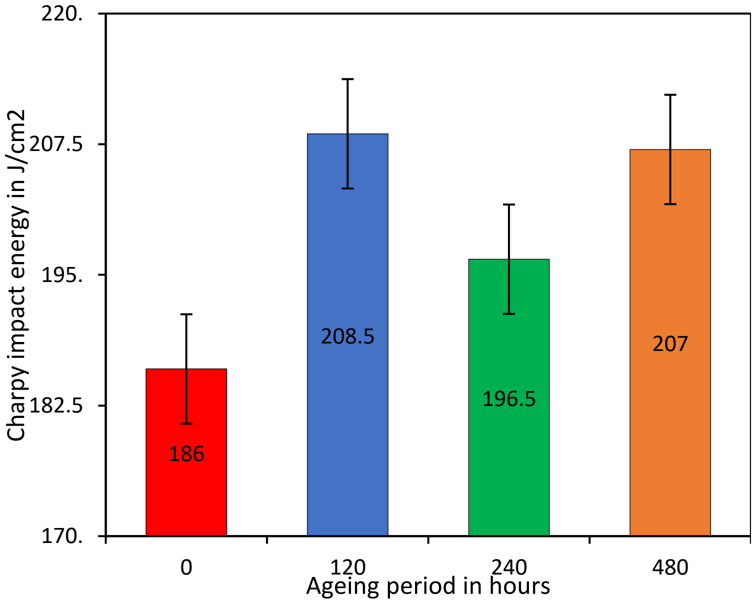

FIGURE 65: Charpy impact energy of the studied specimens

It has been found that the predominant ductile fracture of 14MoV6-3 steels specimens in the initial condition remained the same and did not transform to brittle in the aged state. Also, the lateral expansion and the shear area remained the same across all the stages of ageing.

### Fractured surfaces characterization

To investigate the effect of ageing on microstructure of the material S-3400N scanning electron microscope (SEM) was used to extract fractography of the specimens from all the four stages of ageing at different magnifications. A comparison of microstructure of new material and aged materials 14MoV6-3 was done at different magnifications. Figures 66 and 67 show the microstructure of new and aged specimens at magnification of 50X and 1kX respectively. SEM at magnification of 50X and 1kX has not revealed significant differences in image of the observed structure for the sample areas. It is apparent that there is no noticeable change in microstructure after ageing even up to 480 hours. The surfaces observed in both the new and aged specimens are typical of cleavage in a polycrystalline material. The river patterns observed at the magnification of 1kX of several lines converging like tributaries of a river is typical of cleavage fracture.

According to literature in its original condition, the structure of 14MoV6-3 steel is a blend of ferrite and bainite. Used steel deteriorates due to grain coarsening caused by exposure to high temperature and pressures creating voids between grains at various places which can be found consistently dispersed across the studied region.

Figure 68 show the height map of the fracture surface of (a) new specimen NS3 (b) 12-120 (c) 6-240 and (d) 5-480 captured using the Keynes surface analysis equipment. The measured surface roughness of the fractured surfaces is also similar for the examined specimens and does not show significant differences.

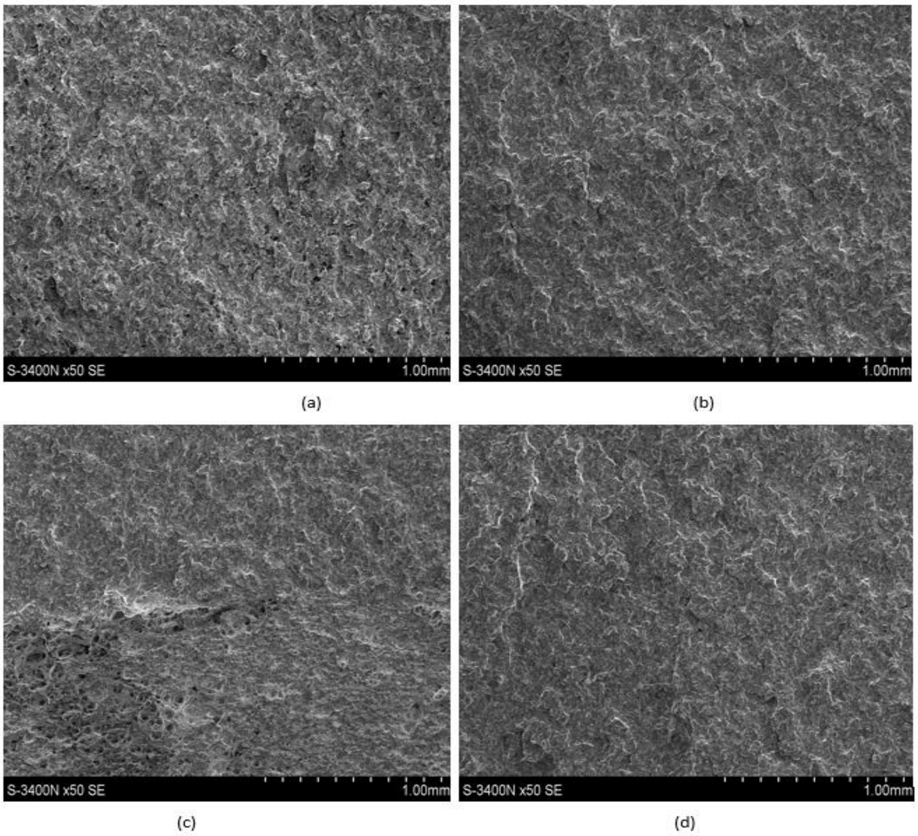

FIGURE 66: The images of microstructure of new (a), 120 hours of ageing (b) 240 hours of ageing (c) and 480 hour aged (d) material with the magnification of 50X

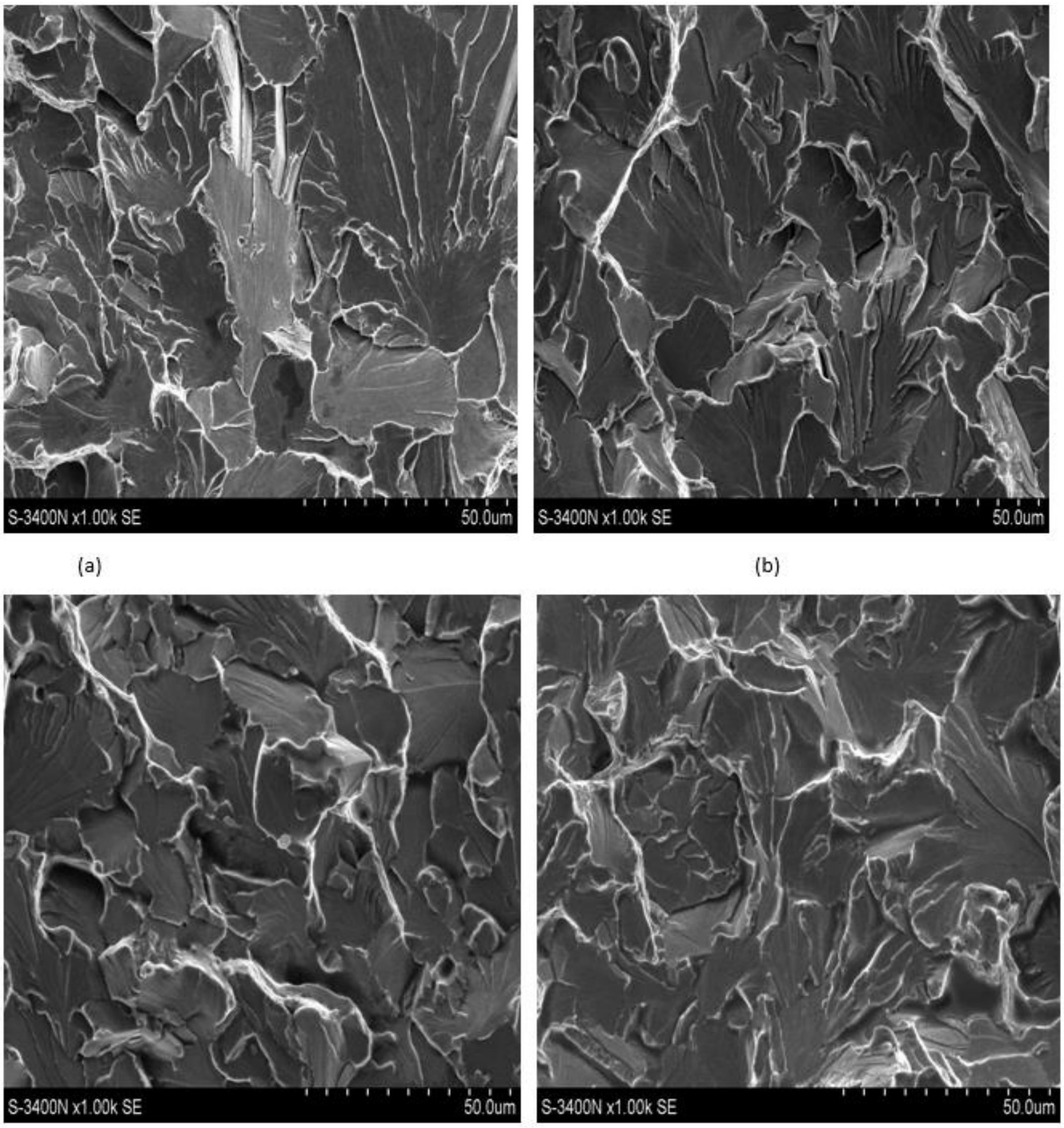

(a) (b)

(c) (d)

FIGURE 67: The images of microstructure of new (a), 120 hours of ageing (b), 240 hours of ageing (c), and 480 hour-aged (d) material with the magnification of 1kX.

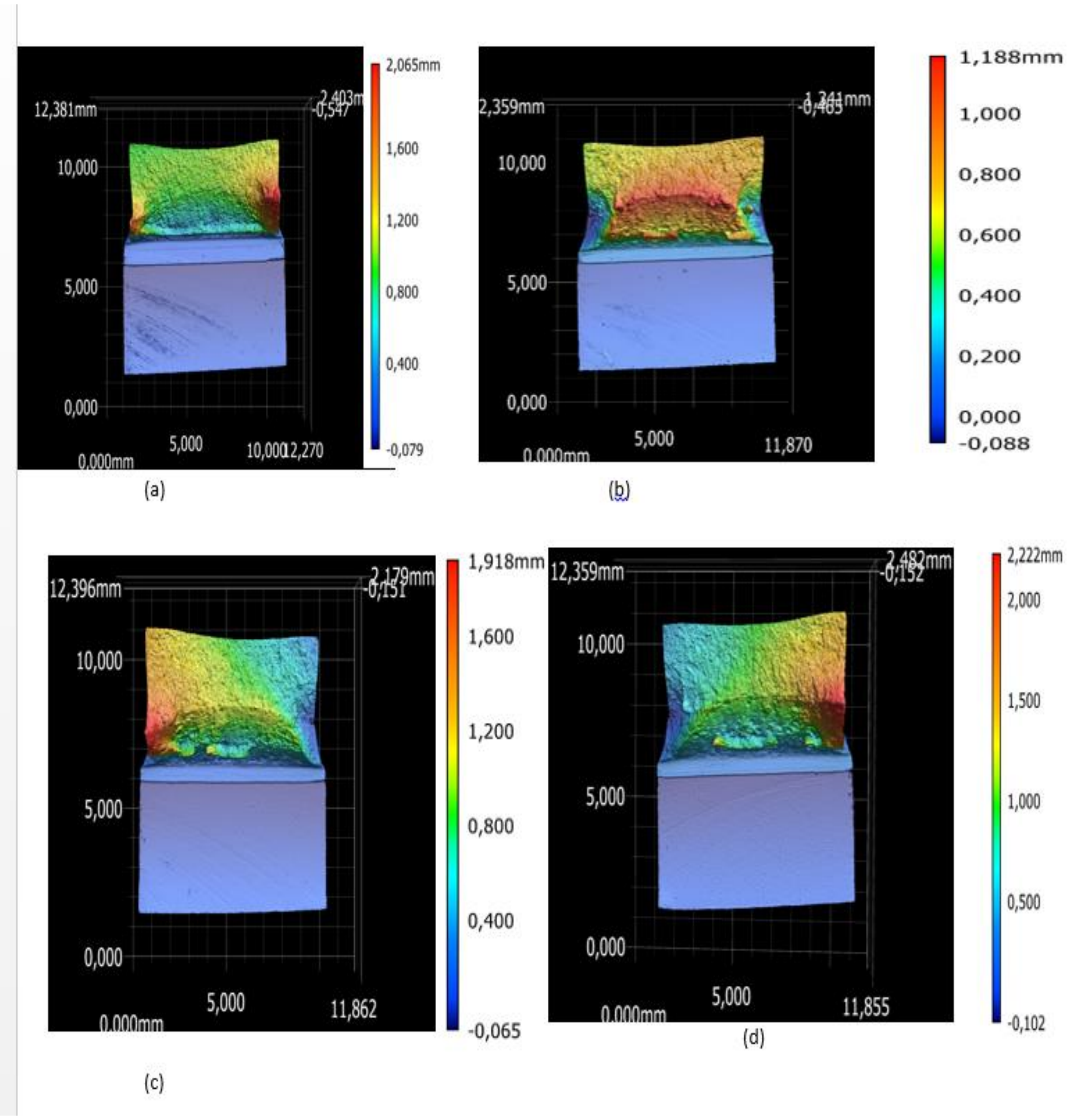

FIGURE 68: Height map of the fracture surface of (a) new specimen NS3 (b) 12-120 (c) 6-240 and (d) 5-480

In Figure 69 images of crack mouth opening at the end of the SENT testing of (a) new specimen NS3 (b) 12-120 (c) 6-240 and (d) 5-480 are presented. It can be observed that in all the stages of ageing the crack propagates in two lines. Then one stops after maximum load and the other one proceeds propagating until failure of the specimen. The fracture of all types of specimens occurs along the path with minimal resistance.

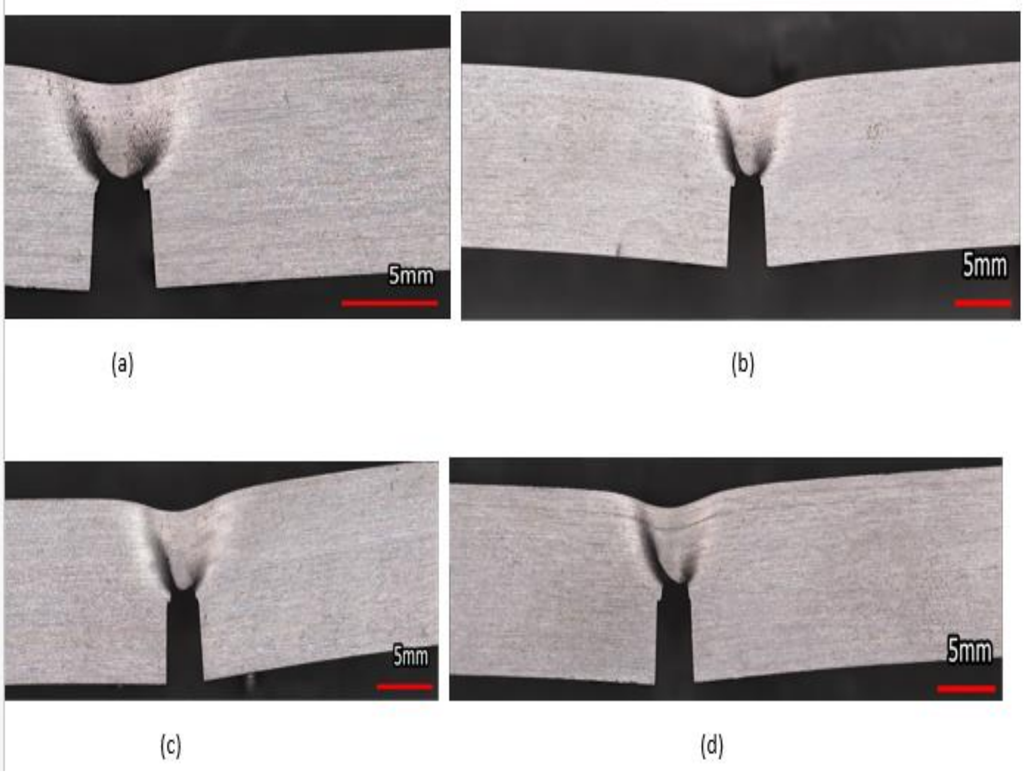

FIGURE 69: Images of crack mouth opening at the end of the SENT testing of new specimen NS3 (a), 120 hours aged 12-120 (b), 240 hours aged 6-240 (c) and 480 hours aged 5-480 (d).

From figure 69 the crack propagates in two edges. Then one stops after maximum load and the other one continues.

**Characteristics of the crack front**

Figure 70 shows the crack front profile of fractured specimens from different stages of ageing. As already reported for any homogeneous material [166] symmetrical curved crack front was observed in all specimens. Therefore, the nine-point technique as provided for in the BS 8571:2018 straightness criterion was applied. Except for specimen 12-120, all test results meet this validity criteria. Based on nine measurements taken on the specimen fracture surface, an average crack length is calculated. If the difference between any of the center seven final crack length measurements does not exceed 20% of the average crack length determined by the test, the test is declared valid.

Notably, all the specimens had almost similar parabolic crack front which is effect of tunneling caused by high constrain at the middle of the crack compared to the edges. The creep ageing did not have effects on crack front profile as all stages of ageing despite the limited blunting that was observed in the testing. These findings are in line with the hardness and Charpy impact test which did not show any change due to creeping.

FIGURE 70: Fracture surface showing the crack front of new and aged specimen.

To summarize the results Table 34 present as summary of the average percentage change of measured properties of aged specimens compared to the new as received specimens. Its observable that of all the four parameters CTOD was the most affected by ageing.

TABLE 34: A summary of the average percentage change of measured properties of aged specimens compared to the new as received specimens.

| | ***120 hours*** | ***240 hours*** | ***480 hours*** |
|---|---|---|---|
| % Change of CTOD at $\Delta a_{0.2\text{ mm}}$ | -48% | -39% | -47% |
| % Change of maximum force | 7.9% | 1.2% | 7% |
| % Change of Charpy energy | 12.1% | 5.6% | 11.3% |
| % Change of hardness | -0.54% | 4.9% | 3.8% |

### 5.3. Discussion

The obtained results of tensile testing of new and aged specimens shows that even after creeping for 480 hours the yield stress and tensile strength are still as high as those of new material as prescribed in European standard EN 10216-2 for Seamless steel tubes for pressure [167]. In previous work it was reported that in comparison to the as received material, both tensile strength and hardness decreased considerably after ageing. It was reported in literature that long-term service exposure on the elevated temperature tensile strength of low alloy steel with molybdenum leads to decline in tensile strength caused by the change in the interaction solid solution strengthening due to carbon and molybdenum [92]. It is therefore plausible to say that even the highest ageing period of 480 hours done in this work was not adequate to imitate the long-term operating conditions.

The unloading compliance was found to greatly underestimate the crack size. The crack growth estimations based on unloading compliance most likely might have been affected by the plastic deformation in the specimens ’arms. Much of the previous development work for CTOD testing standards was centered on high strength and structural steels, which have relatively high yield strength to ultimate tensile strength (Y/T) ratios ranging from 0.7 to 0.95. For greater strain hardening materials with lower Y/T ratios, such as stainless steel, the conventional CTOD formulae in BS 7448 have been known to be less accurate that explain the less accuracy of UC in measuring crack length aged specimens. This might be another possible reason because the problem was not experienced in new specimens.

Many tough materials do not fail catastrophically at a specific value of J or CTOD. Instead, these materials exhibit a rising R curve, with J and CTOD increasing with crack growth. Unstable crack propagation is less likely in materials with steep R curves. The results indicated that the new specimens have a more rising R-curve as compared to the aged ones. The aged specimens although their R curves are rising less, they still exhibit a degree of stable crack growth and typical resistance curve for a ductile material. These results agree with previous findings in [69] where it was confirmed that the toughness of the material decreases significantly after thermal ageing, which means a lower resistance required during crack propagation.

The difference in values of CTOD values between the new and aged specimens at 0.2 mm crack initiation is because there is a small amount of apparent crack blunting of aged specimens. The new specimens experience a lot of blunting hence higher values of CTOD at crack initiation. The absence of blunting in the aged was explained in [116] where the presence of soft ferrite matrix in the microstructure increase blunting of low alloyed steel at crack tip hence increasing toughness.

Charpy impact toughness did not reduce after ageing. This finding agrees with previous studies. According to [168] it was concluded that impact toughness is almost the same for new and used steel. Another paper [116] reported that the impact toughness of steel which had undergone normalization was made tougher than tempered, quenched, and tempered steel while in [169] it was reported that after service period of 168,000 hours at 540°C impact strength remains as satisfactory. The show of ductility during the SENT fracture testing and Charpy impact testing indicate that even after 480 hours of ageing the specimens still have a lot of structural strength and residual life remaining. Steam line material creep ageing is caused by the progression of precipitation processes, as well as on the growth of grains and the development of microstructure changes and structural discontinuities that result from prolonged exposure to high temperature. It can therefore be deduced that the near end life of operation was not properly imitated. In previous work [156] it has been found that the predominant ductile fracture of 14MoV6-3 steel specimens in the initial condition transforms to predominantly brittle in the aged state. Damir et al. [117] reported that impact toughness value of steam line material 14MoV6-3 is primarily determined by the development of precipitation processes, as well as the formation of microstructure alterations and structural discontinuities, as well as grain growth, which occur over a long period of exploitation at extreme temperature. They reported a very low value of total impact energy (impact toughness) at room temperature 20°C.

The CTOD at 0.2 $\Delta a$ crack initiation of aged materials was observed to be longer than for aged material. This difference was related to the amount of blunting before crack propagation. For the new material there is a lot of blunting prior to crack initiation seen from data of DCDP and CMOD. The observations in previous studies [170] where it was reported that microstructure changes occur after long periods of creep. Zieliński et al. [13] observed significant structure degradation after long periods of operation they which indicates an accelerated creeping process which results in formation of single voids and their coalescence in the final stage, forming a characteristic system of crack chains which initially include one grain. It was concluded that specimen from new material possesses a coarser surface with large craters with some inclusions and areas of micro voids located inside or around them. The aged after long time of operation the microstructure of the specimens should have larger craters and dimples.

But for this work the images of microstructure and crack front where almost identical with no evidence of shift to cleavage fracture even after creep as reported by Dzioba et al [171]. The surfaces observed was the cleavage crack where a pattern resembling a river is formed by a propagating crack forms parallel planes to accommodate a twist mismatch. The tearing in between planes will join and tributary like convergence is formed since several cracks require more energy to propagate. Probably, one of the reasons for this is inadequate creep ageing. The presence of fine and relatively deep trans granular dimples mixed with intergranular dimples clustered in very narrow areas parallel to the long axis direction of the lamellas suggests that the fracture process involves both ductile and Brittle fracture and that the creeping mechanism was not adequate to imitate end of life after long periods of operation.

## 5.4. Summary and conclusion

This work investigates the degradation of the ductile tearing resistance of 14MoV6-3 steel grade due to creep ageing at elevated temperature. Creeping durations of 120, 240, and 480 hours at a temperature of $540^0$ C and stress level of 169 MPa were selected on specimens machined from as-received materials. The creep ageing of 480 hours at this condition represents 10% of its lifespan. SENT specimen testing was done using unloading compliance and DCPD methods to measure crack growth. The tearing resistance degradation was evaluated for the as-received condition and every stage of ageing. The maximum loads, the CTOD at crack initiation and resistance curves were compared for each stage of ageing. Charpy impact and hardness tests and microstructural examination were performed to get more insight into degradation after accelerated creep ageing. As received unaged specimens resulted in the highest $\mathrm{CTOD}_{90}$ at $\Delta a_{0.2\ \mathrm{mm}}$ crack initiation fracture toughness value of 1.24 mm with the aged specimens having lower values by 48, 39 and 47 % for the 120, 240 and 480 hours of ageing respectively. The new material exhibited a more rising resistance curve typical of structural metallic compared to aged specimens. Charpy impact and hardness results revealed they were slightly enhanced while yield stress and tensile strength remained unaffected. Microstructural analysis with SEM showed microstructure remained relatively consistent after ageing. Creeping stress should be increased to imitate closely near end of service life. Tilted notches should be used to investigate the effect of multiaxial loads on tearing resistance.

The deterioration of 14MoV6-3 steel caused by creep was examined by comparing the properties of new and aged steel. The accelerated thermal ageing tests were performed on the as-received material from 0 h to 480 h to investigate fracture properties. Resistance curves of SENT specimens were determined using both the direct current potential drop method and the unloading compliance approach. To provide more insight of steel properties degradation due to elevated temperature creep stresses Charpy impact, hardness test and microstructural examination was also done. It was concluded that:

I. The specimens show good mechanical properties even after ageing to 480 hours. Yield stress and tensile stress fulfill the requirements of the standards.

II. DCPD provided a better crack prediction compared to UC.

III. The character of the curves exclusively changes depending on after ageing but there is no significant difference in CTOD-R curves of 120, 240 and 480 hours of ageing.

IV. The CTOD-R curves indicate that new material has high toughness compared to specimens from all the all stages of ageing and their shapes are characteristic of structural metallic materials (rising CTOD-R curves). From CTOD-R curves, it can be concluded that the crack initiation ranges of new specimens are double that of aged specimens. It is apparent that the crack growth resistance of 14MoV6-3 steel is reduced with creep ageing.

V. No significant change in hardness was found after ageing. The hardness properties of the new specimens agree with those reported in the literature. Charpy impact strength and hardness measurements although increases slightly for aged specimens remained relatively consistent after ageing.

VI. Fractography analysis of all the samples from all ageing periods reveals that they have a similar appearance.

VII. The observed life exhaustion extent of the material based on fracture toughness parameter CTOD is much higher than compared to that of the hardness, Charpy impact energy and CTOD at crack initiation the creep ageing had the highest impact compared to other parameters.

It is possible to conclude that additional experimental studies are needed with increased creep stress or duration. Also, in actual power plants the materials are subjected to multiaxial loading, to this end there is need to investigate the effect of multiaxial loading by use of tilted notched the results presented here has shed some light on the effect of creep ageing on crack growth resistance for 14MoV6-3 steel.

# CHAPTER 6: INVESTIGATING THE SENSITIVITY OF CRACK TIP OPENING DISPLACEMENT TO AGEING MECHANISMS IN 14MoV6-3 STEEL

The thermal power industry, a traditional cornerstone of electricity generation, is increasingly scrutinized for its environmental impact. Consequently, power producers are prioritizing the extension of the operational lifespan of existing infrastructure rather than investing in new installations, especially amid the global paradigm shift toward renewable energy sources [172]. Extending the service life of ageing equipment must ensure continued power generation efficiency, enhanced operational flexibility, and adaptability to frequent start-ups and variable loads, as dictated by evolving boiler cycle demands. These requirements often exceed the design norms of legacy systems, necessitating advanced strategies for performance optimisation and structural integrity assessment [5]. The high temperature and thermomechanical operating conditions subject power plant equipment to various ageing mechanisms, defined as the progressive, time-dependent degradation of materials under operational service conditions. Materials subjected to persistent stress at extreme temperature in severe conditions degrade gradually, which can eventually lead to catastrophic failure.

Thermal, nuclear, chemical, and petroleum operations require creep resistant steels that must be dependable for extended periods of time in harsh conditions of high temperatures. The design lifetimes of power plant components are determined by their mechanical and creep qualities, which are typically those of the virgin state (i.e., as received). However, material qualities may vary over time and plant operations may be altered to accommodate unexpected demands [173]. The service life of these power plants should be done while ensuring plant reliability, which relies significantly on the performance of critical components often exposed to elevated temperature, and thermomechanical loads. Thus, creating high-quality databases of pertinent creep features for power plant life management and design is essential. Enhancing accurate creep-life prediction techniques may need a deeper comprehension of the microstructural evolution and creep behaviour of materials over the whole creep exposure, including after long ageing periods. Published work [26] reported that like other steels in this class, 14MoV6-3 steel's resistance to fracture may be diminished if creep causes the grains and carbides along their boundaries to enlarge over time. Typically, operating degradation along the grain boundaries weakens the section with the least fracture resistance, which is when steam pipeline components collapse.

Dynamic recovery, dynamic recrystallization, precipitate coarsening, and other processes that lead to softening and a reduction in creep resistance are typical examples of microstructure evolution. The formation of creep voids and cracks, frequently at grain boundaries, is a component of damage evolution. Plastic deformation is irreversible, with both time-dependent and time-independent components. Creep denotes the time-dependent component of plastic deformation. Creep is the slow and continual plastic deformation of materials under long-term strain. Creep can occur at any temperature above absolute zero Kelvin, but it is typically associated with time-dependent plastic deformation at temperatures above $0.4T_m$ (absolute melting temperature). This is because diffusion can aid creep at higher temperatures. Elevated-temperature components utilized under creep conditions are designed utilizing allowed stress under creep conditions, which is typically estimated based on 100 000 hours creep rupture strength at the working temperature but can potentially be 200 000-300 000 h creep rupture strength.

Creep strength and fracture resistance are the most important determinants of the appropriateness of high-pressure steam pipeline materials [174]. Creep is typically to blame for 30% of all tube failures in boilers and reformers [175]. The fatigue and creep phenomena for power steels are well documented in the literature, but only as model fatigue processes but not carried out on proper equipment from the initial state of the tested alloys [176].

Cracks in power elements can form during long-term operation under cyclic loads and environmental factors [177]. Therefore, fracture toughness of critical components is critical for safe operation, especially after creep damage caused by operating conditions. Understanding how fracture toughness deteriorates and the underlying mechanisms might inform material selection and development decisions [72]. Boiler tube creep fractures are thought to be the cause of 10% of all power plant failures. At present, several methods of assessing creep damage have been developed only for virgin materials [178]. In thermal power equipment in general and the major steam pipes in particular, metallographic analysis and hardness measurements are routinely employed to validate the present technical status of operated steels. This normally focuses largely on grain and carbide size, carbide distribution inside grains and along their borders, and pore density.

Despite experimental studies demonstrating that metallic materials, including pipeline steel, undergo creep at elevated temperature, the effects of high-temperature creep (RTC) on pipeline steel fracture properties are still relatively unexplained [20]. The primary information source for assessing life and residual life is still creep tests. Their drawback, though, is that it takes such as long testing times and high expenses to get the test results. To reduce the time required to conduct these tests and evaluate life duration, the so-called shortened creep tests, which run anywhere from a few dozen hours to a maximum of three to five thousand hours, are used.

Understanding the microstructural evolution and creep behavior of materials throughout their exposure, including early phases of loading, can aid in the creation of creep-resistant steels and enhance creep-life prediction tools. The decision to allow long-lived materials to continue to be in use in the power industry is based on rigorous diagnostics, which include microstructure degradation, and corrosion processes [167]. This is a major limitation of metallographic testing as it overestimates the loss of mechanical strength in addition to having limitation of the necessity to reduce the examined area to a very limited area compared to the actual component dimension. However, there is currently no comprehensive study on the impact of creep on fracture toughness during short-term isothermal ageing and accelerated creep.

This study investigates the impact of high-temperature creep and isothermal ageing on the fracture toughness of 14MoV6-3 steel. Ageing is accomplished by subjecting specimens to creep and high-temperature exposure for durations of up to 10 weeks (1680 hours) using accelerated degradation testing. The research complements traditional fractographic and metallographic analyses typically conducted on polished cross-sectional surfaces of tested components, where defect density is often detected by chance. While fractures generally propagate along paths of least resistance—characterized by the highest defect density—fracture surface analyses offer a more comprehensive approach. They enable the identification of both manufacturing and operational flaws, as well as insights into the mechanisms driving defect coalescence. The findings of this study are critical for evaluating the long-term fracture resistance of 14MoV6-3 steel in power plant applications, particularly under prolonged high-temperature operating conditions.

## 6.1. Materials and experimental methods.

### Materials

The studied steel grade is the same still grade used in Chapter 4. The material was supplied as a half-meter-long pipe, normalized at 940-960 °C and tempered at 700-730 °C. It's used in thick-walled components of pressure components of power boilers notably the elbow portions of primary steam pipes. This material is made of 14MoV6-3 low-alloy steel and meets EN 10216-2:2013 European Standards for seamless steel tubes for pressure tubes with specified high-temperature characteristics and Polish Standards (PN-75/H-84024).

### Creep ageing

Most of the electrical power-generating plant components for both conventional and nuclear power plants operate at high temperatures for extended periods of time. To determine the influence of long-term thermal aging on the behavior of material it has to be subjected to high temperatures in the range up to 650 °C in the absence or presence of stress then examine the evolution of microstructure [179]. The creep deformation and fracture mechanisms for materials under low levels of stress behaved differently from those under high stresses. Creep testing can be performed at either continuous load or constant stress. Engineering steel creep tests are often conducted at constant temperatures and tensile loads for ease of experimentation.

The creep degradation test was performed in atmospheric conditions using the 50 kN capacity Kappa 050 DS Zwick/Roell creep testing machine fitted with controlled furnaces as shown in Figure 71. It contains the complete test setup of the creeping equipment, comprising of a control system, data acquisition system, electric heating furnace, temperature control, and monitoring system.

Specimens for creep degradation were machined into Standard Single Edge Notch Tensile Specimens (SENT) without a notch with a total length of 180 mm, and a gauge length of 100 mm between two gripping ends, the specimen featured a square cross-section of 12 mm as shown in figure 72 (b). The specimen's two ends were threaded to accommodate M16-threaded gripping jaws. The furnace, configured with three distinct heating zones, maintained a uniform temperature throughout as shown in Figure 72 (c). Temperature monitoring was achieved using five thermocouples: three were strategically placed within the furnace at the upper, middle, and lower regions, while two additional surface thermocouples monitored the specimen directly.

FIGURE 71: The 50 kN capacity kappa 050 ds Zwick/Roell creep testing machine fitted with controlled furnaces.

(b) (c)

FIGURE 72: Creep test setup and instrumentations on the test specimen

The parameters for accelerated creep were chosen to be $650^0$C at a tensile stress of 60 MPa and an ageing period of 100 hours. These parameters are higher than its operating parameters of $540^0$ C and pressure of 15 MPa [101] accelerating degradation to simulate long operating conditions. Using a K-type thermocouple that has a precision of 1 °C, a programmable controller was used to regulate the temperature of each furnace chamber. The temperature in the chamber varies spatially by roughly 5 °C.

### Isothermal degradation

Iso-thermal ageing (annealing) was implemented to accelerate artificial microstructural degradation at an elevated temperature, higher than the material's actual operating temperature. This conditions the microstructure to be like that of material subjected to long-term service at the operational temperature [173].

The as-received rods of 30 mm and 20 mm diameters were thermally aged in an atmospheric environment using a temperature-controlled electric furnace at $650^0$ C. Three ageing periods were selected, 4,8 and 10 weeks. 10 weeks is approximately equivalent to operating at a service temperature of $540^0$C for 17 years according to Arrhenius's equation provided in Equation (6.1) [180]. This equation provides a relation between temperature and time where the activation energy (enthalpy), refers to the diffusion process which dominates such a treatment without loading.

$$In(\frac{T_a}{T_n}) = -\frac{E}{R}\left(\frac{1}{T_2} - \frac{1}{T_1}\right) \qquad (6.1)$$

Where $T_a$ is the calculated accelerated ageing temperature, $T_n$ is the actual natural or operational ageing temperature, E is the activation energy in kJ/Mol, R is the gas constant, $T_l$ is the natural ageing time and $T_2$ is artificial ageing time. In this case $T_l$=540°C, and $T_2$=650°C. After machining the specimens were machined into SENT specimens for fracture toughness testing.

Thermo-Calc software, a multielement thermodynamic calculation software package was used to simulate the structural changes resulting from thermal treatment to help understand the phase stability in the different temperature ranges (Thermo-Calc Software, Stockholm, Sweden). Such software requires a thermodynamic database (TCFE database) of parameters which describe the lattice stabilities and the interaction parameters to predict dissolution and precipitation behavior of various precipitation phases and the mole fraction of all phases according to temperature. Other systems include: MatCalc, the Monte Carlo method, and the Ising model.

### Specimens and testing

After the thermal and creep ageing treatment, SENT specimens were machined in longitudinal (L-T) orientation having W=B = 10 mm and a daylight grip length (H) of 10 W. Specimen surfaces were also fully machined to meet the tolerances and surface finish specified by ISO 12135. The nominal initial-crack-size-to-width ($a_0$/ W) ratio of 0.5 was machined for all specimens using a thin saw in two steps with a final notch radius of 0.15 mm. The specimens were neither fatigue-pre-cracked nor side grooved. Fatigue pre-cracking would make the control of initial crack size difficult, nonetheless, previous studies by [30] reported that it is not necessary to have sufficient ductile materials.

### Fracture toughness quantification

The current study employs the Digital Image Correlation (DIC) technique to measure the specimens' displacement and strain field as implemented in Chapter 4 as shown in Figure 74. These methods eliminate the need for a crack mouth opening displacement (CMOD) or load-line displacement gauge, as CMOD can be derived from surface point displacements. This method is beneficial for tilted notches as clip gauges are impractical. δ5 was measured optically on the test specimen using a DIC virtual extensometer placed at a distance of ± 2.5 mm from the crack tip on the crack tip line parallel to the loading axis as suggested in Chapter 4. Two more pairs of points placed ±2.5 mm apart, at the same distance from the crack path were added to measure out-of-plane displacements since the extensometer only measures in-plane displacement during deformation. This method offers a convenient way of constructing the δ-R curve with the measured crack extension Δa. The DIC parameters used can be found in Table 35. Measurement of crack extension was done using the Direct Curren Potential Drop method (DCPD) as implemented in Chapter 4.

Table 35: DIC parameters.

| **Parameter** | **Value** |
|---|---|
| Calibration plate | 3 x 3 mm |
| Subset size | 23 pixels |
| Image filtering | none |
| Pixel size | 6 pixels |
| Strain resolution | 30 µstrain |

Figure 73 presents the servo hydraulic ESH 100 kN universal testing machine used to perform mechanical loading. This was done in displacement mode with a constant crosshead displacement rate of 0.12 mm/min corresponding to an average stress intensity factor K-rate of 0.2 MPa $m^{1/2}$ s −1 ensuring quasi-static fracture. Loading continued beyond the maximum force but stopped when the force reduced to 80% of the maximum force to provide a crack extension as provided in BS8571 standards which limits the maximum crack to 20% of the specimen ligament ($W-a_0$). For different ageing conditions and three crack orientations (α = 0°, 22.50, and 45°). 17 specimens were tested in total.

Table 36 summarizes the performed tests. The specimens with tilted notches were only performed in new and creep-degraded specimens. Following the BS 8571:2018 standard an equation of the form in Equation (6.2) was fitted to the CTOD ($\delta_5$) versus $\Delta a$ data for constructing the tearing resistance curve. The CTOD at maximum load $\delta_m$ is an alternative measure for fracture toughness that was used as implemented in [36] to assess the tearing resistance of hydrogen-charged steel.

$$\delta_5 = m + l(\Delta a)^n \qquad (6.2)$$

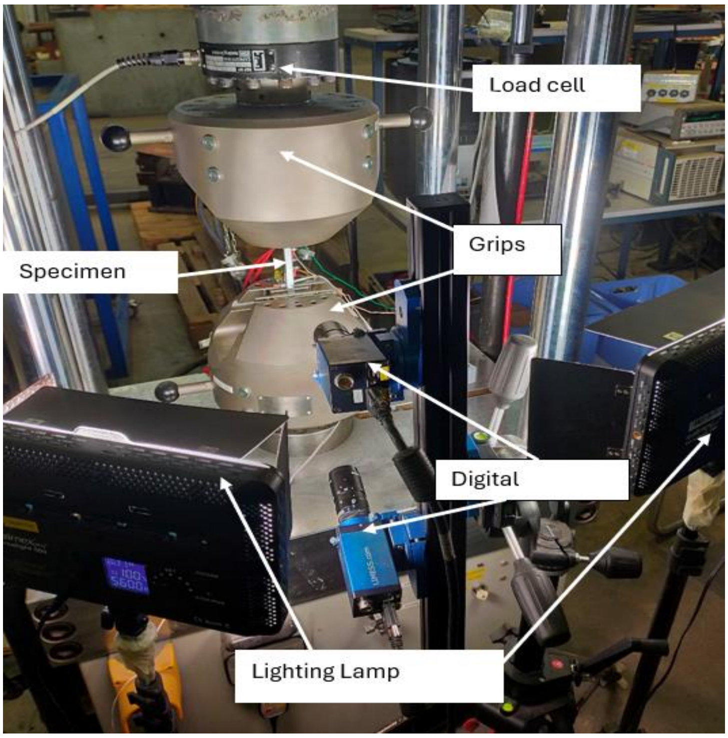

FIGURE 73: Set up to test SENT specimens under quasi-static tensile load, two DIC cameras are mounted in front of the loading machine.

TABLE 36: List of specimen codes, and conditions performed using SENT specimens.

| **Specimen treatment** | **$0^0$ notch angle** | **$22.5^0$ notch angle** | **$45^0$ notch angles** |
|---|---|---|---|
| New | N4-0, N5,0 | N1-22.5, N2-22.5, N3-22.5 | N6-45, N7-45, N8-45 |
| Creep degraded | C1, C2 | C3, C5 | C4, C6 |
| Isothermal aged 4 weeks | T4 | | |
| Isothermal aged 8 weeks | T8 | | |
| Isothermal aged 10 weeks | T10 | | |

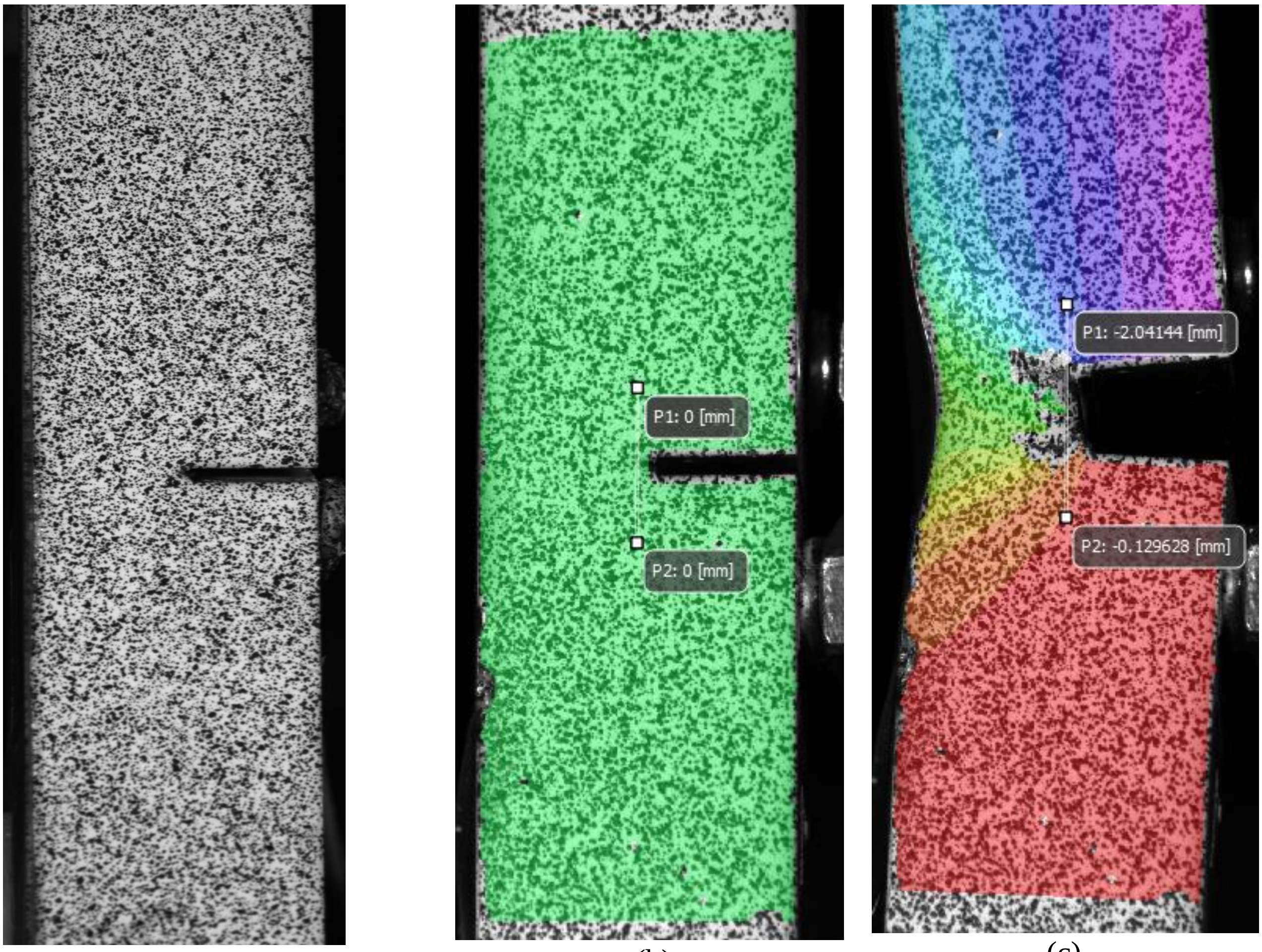

(a) (b) (c)

FIGURE 74: SENT specimen speckle pattern prepared for testing (a), virtual extensometer for δ5 at 1st DIC image when Force is 0 (b), 576th mage at maximum load (c).

The tested specimens were prepared for microstructure and fracture surface characterization. Microstructure analysis was done utilizing optical microscope while fracture morphology was observed using scanning electron microscopy (SEM). Polished specimens for microstructure were etched by dipping the surface in 2% nital (2% nitric acid and 95% ethanol) and then examined using a light optical microscope equipped with a digital camera and computer system. A scanning electron microscope (SEM) with an accelerated voltage of 30kV was used to analyze half of the specimens' fracture surfaces.

## 6.2. Results

### Creep and isothermal ageing

Creep curves can be used to visualize the time-dependent strain over a reference or gauge length. The creep rate significantly increases after approximately 140 hours, as illustrated in Figure 75 (a) and (b), indicating the onset of tertiary, unstable creep behaviour. At this creep duration, the strain reaches approximately 0.105. By assuming a 60% degradation threshold, the corresponding strain of 0.06 can be identified at 100 hours. This approach aligns with the material degradation classification categories 3 and 4 according to the method for evaluation of the structure condition and the methodology developed at the Institute for Ferrous Metallurgy, Poland.

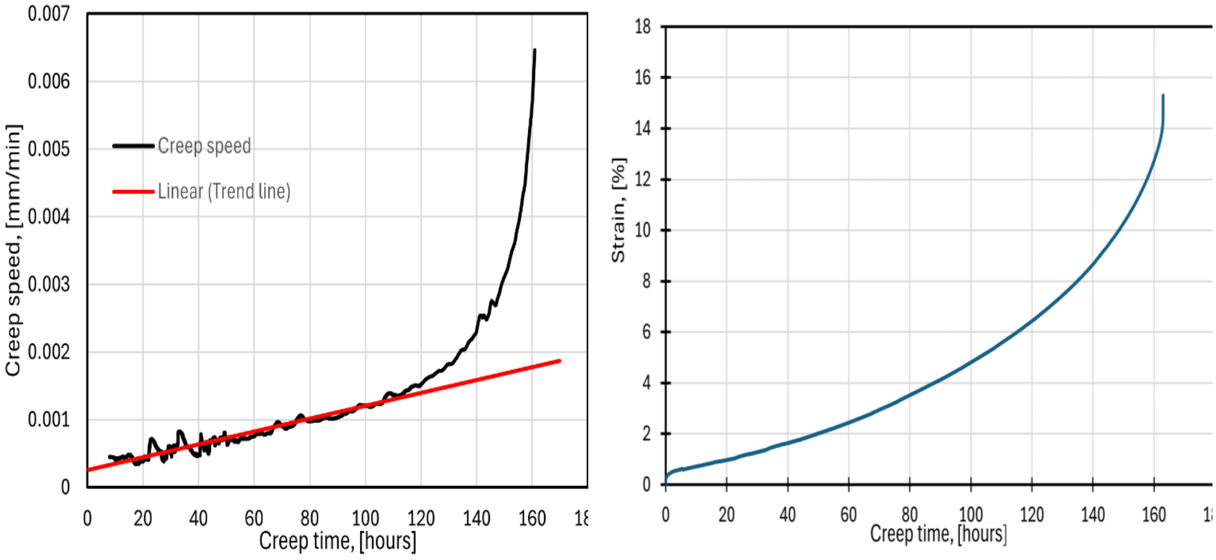

(a) (b)

FIGURE 75: Creep speed versus time curves of 14MoV6-3 steel samples (a), engineering strain versus creeping time (b).

During the primary creep stage, the creep rate diminishes with time. The decrease in creep rate during the primary creep stage may be due to strain hardening or fewer movable dislocations. In the secondary stage, the creep rate is constant. The steady-state creep rate refers to a balance between dislocation creation and recovery, resulting in hardness and softening. At high temperatures, diffusion leads to large recovery rates, which balance strain hardening and create secondary or steady-state creep. In the tertiary stage, the creep rate rises over time till rupture.

To forecast dissolution and precipitation behavior, Thermo-Calc software was used to determine the mole fraction of each precipitation phase based on temperature and the TCFE database. The Simulation results are seen in Figure 76. Mole fractions are presented on the Y axis as a function of temperature on the X axis predicting equilibrium phases at various temperature. Thermal ageing was done at a temperature constant of $650^0$ C ensuring there is no dissolution of precipitates as Cr-rich M23C6 carbides are expected to be present at $650^0$ C at the ageing temperature and dissolve at $680^0$ C.

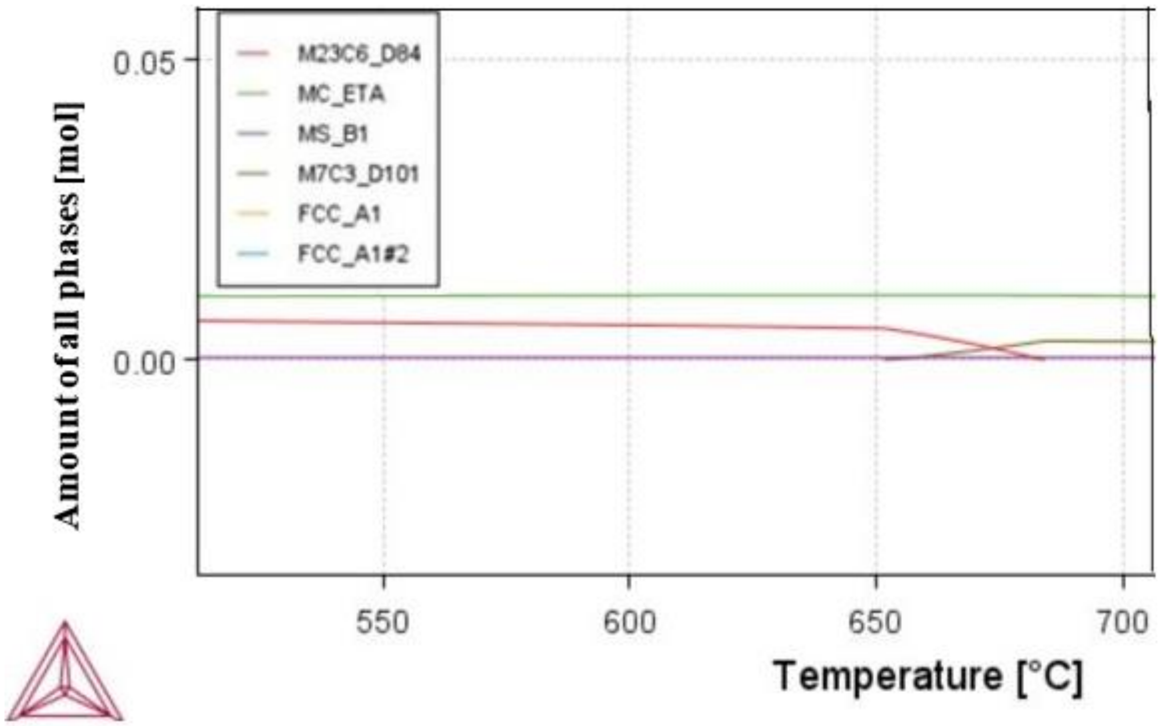

FIGURE 76: Calculated phase mole fraction of precipitates as a function of temperature.

**Fracture toughness**

Figure 77 (a) shows load vs displacement (LLD) response graphs. For all the specimens, there is a stable brittle crack extension with no pop-in or crack destabilization that suddenly causes the force to drop. It can be seen in the load-displacement graph that all new and both thermal and creep-degraded specimens have the same behaviour in the plastic region. This indicates that the plastic work dissipation by the applied load is similar. The difference is that the virgin specimens have a larger elastic component compared to the thermal degraded and creep-degraded specimens. At around 0.5 mm displacement, the loads of new and aged specimens start to diverge. The loads of the isothermal aged and the creep aged specimen start to diverge at a displacement of 0.75 mm.

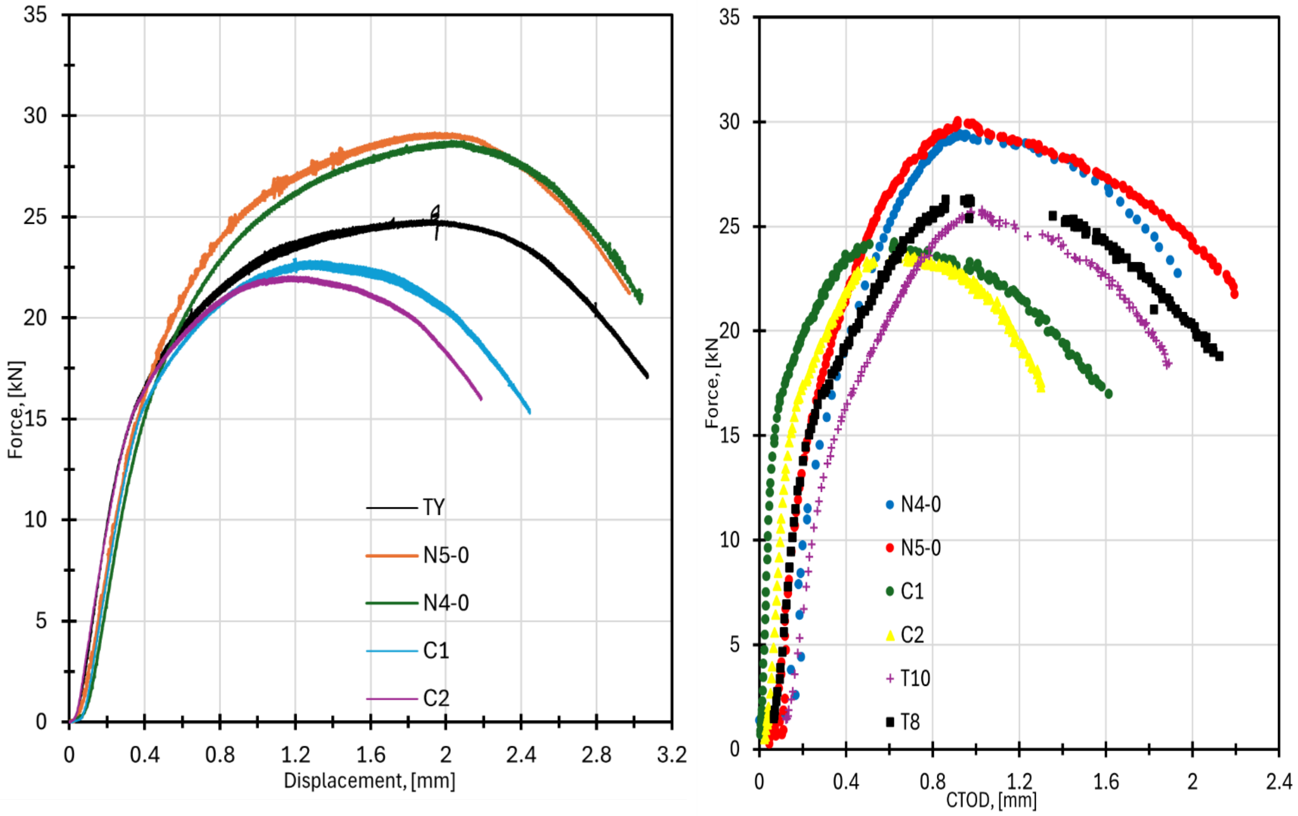

(a) (b)

Figure 77: Force vs displacement of tested SENT specimens (a), the plots of P versus CTOD from different ageing conditions (b).

Figure 77 (b) presents the force-CTOD curves obtained from the test of samples with ageing treatment. There is little scatter in the samples with the same treatment. During initial loading, the thermally aged specimens are the most ductile, but they have lower maximum load capacity compared to new specimens. Figure 78 (a) plots the effect of the crack inclination angle on the ductile tearing resistance of creep-degraded specimens. The straight-notched specimens have a low resistance to ductile tearing compared to tilted notches. Specimens with a 22.5° notch tilt show higher resistance than straight notches but lower than 45° tilt angles. The tilt reduces crack tip constrain leading to more resistance to crack propagation.  Furthermore, the tilt angle introduces a complex stress state and mixed-mode loading (mode I and III), resulting in delayed crack propagation and increased energy absorption.

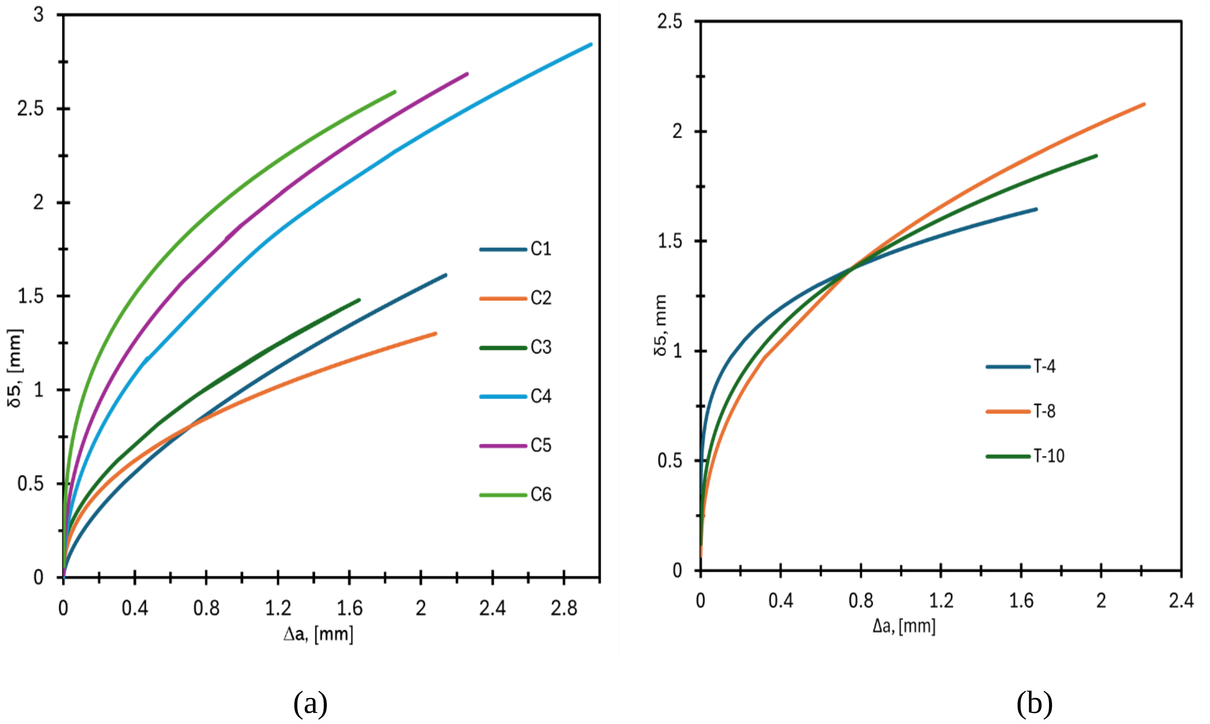

(a) (b)

FIGURE 78: CTOD - Δa resistance curve- of creep-degraded specimens with different notch tilt (a) and isothermal degraded specimens of different ageing durations (b)

Figure 78 (b) shows the CTOD-R curves for isothermal degraded specimens aged at 650$^0$C for 4, 8, and 10 weeks. Although the 4-week-aged specimen exhibits the highest resistance to crack extension for the initial crack propagation region (up to Δa≈1.0 mm) there is no other significant difference in ductile tearing behaviour with an increase in the ageing period. However, the final crack growth tends to increase with increasing degradation time. This is caused by the softening of the material, enabling higher ductility under crack propagation while experiencing degradation-induced loss of strength, which influences the fracture resistance of aged materials.

Figure 79 (a) compares the CTOD-R for new as-received and isothermally degraded specimens (T-4, T-8, T-10). The as-received specimens (N4-0 and N5-0) demonstrate higher CTOD values at larger crack extensions than degraded specimens. The isothermal ageing had a smaller effect on reduction in fracture resistance compared to creep degradation; instead, it led to a recovery in ductility at larger crack extensions, which can be attributed to microstructural softening due to prolonged thermal exposure.

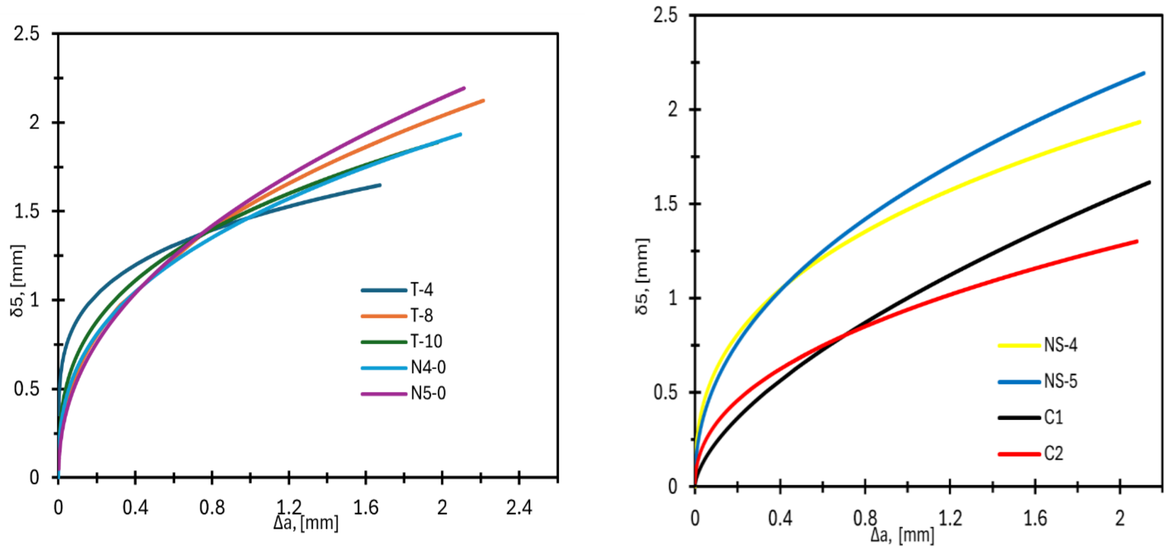

(a) (b)

FIGURE 79: CTOD-R curves for straight notched new and isothermally degraded (a), NEW and creep degraded (b) SENT specimens.

Figure 79 (b) compares the CTOD −Δa curves obtained from straight-notched new as received SENT specimens and straight-notched Creep degraded specimens. For both small crack extension, Δa ≤ 1 mm, and large values of crack growth, there is a significant decrease in the ductile tearing resistance due to creep degradation. The gap between the new and degraded curves widens as Δa increases, indicating that the effects of creep degradation are more pronounced at larger crack extensions. It is worth mentioning that specimens with the same conditions have the same tendency and scatter as expected. The scatter could be attributed to varying degrees of degradation, potentially due to differences in exposure conditions or localized material properties.

From load vs CTOD data the CTOD at maximum load, $P_{max}$ was calculated and listed in Table 37 the virgin as-received materials; the thermal-aged; and the creep-degraded specimens exhibit maximum forces in the ranges of $29.3 \le Pmax \le 31$; $25.7 \le Pmax \le 26.8$; and $23.5 \le Pmax \le 24.5$, kN respectively. Additionally, the as-received, creep-degraded, and isothermal-aged specimens show a similar scatter of maximum force. There is more percentage change in CTOD than maximum force for creep degraded material but for thermal degradation the ageing affects the load carrying capacity as compared to ductility. Figure 80 (a) Presents the maximum loads of the tested specimens while Figure 80 (b) presents the average CTOD at maximum loads ($\delta_m$) of the three ageing conditions.

TABLE 37: Average maximum loads and CTOD values at maximum loads of tested specimens with straight notches

| **Straight notched Specimen** | **Max force, kN** | **δm at max force** | **% change of maximum force** | **% change of δm** |
|---|---|---|---|---|
| New | 29.73 | 0.98 | | |
| Thermal | 26.30 | 0.93 | -11.55 | -5.19 |

| | | | | |
|---|---|---|---|---|
| Creep | 23.91 | 0.65 | -19.58 | -33.02 |

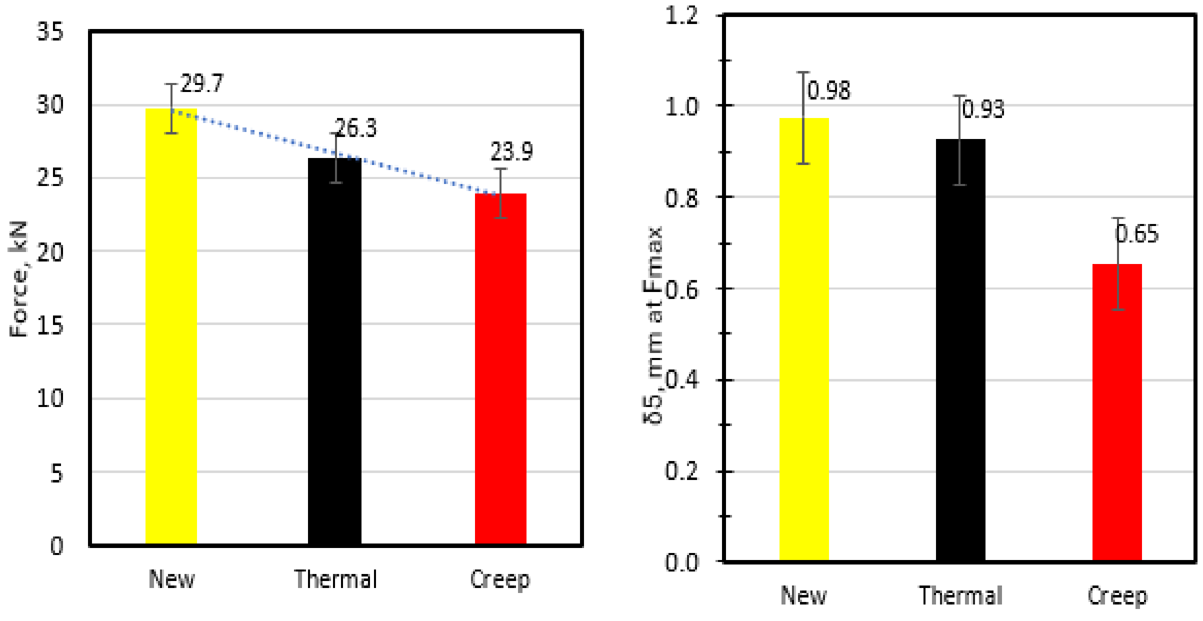

(a) (b)

FIGURE 80: Average maximums of the three specimen conditions (a) maximum loads (b) CTOD5 at maximum loads for three conditions of specimens.

The results in Table 38 compares the fracture performance of two types of specimens — one in a new (as received) condition and the other after being subjected to creep loading and provides insights into the influence of creep degradation on fracture characteristics of specimens with 45° tilted notches. It can be observed that straight notched specimens were more affected by creep degradation than tilted-notched specimens.

Table 38: Average maximum loads and CTOD values at maximum loads of tested specimens with $45^0$ tilted notches.

| **Specimens** | **Max F, kN** | **$\delta_m$, mm** |
|---|---|---|
| New | 30.9 | 1.21 |
| Creep degraded | 27.4 | 1.15 |
| % Change of Max load and $\delta_m$ after creep | -11.3 | -4.9 |

The as-received (new) specimens can withstand the highest maximum load compared to the creep-aged specimens with an 11.3% decrease after creep degradation. Similarly, the CTOD values followed a declining trend, with the new specimens achieving the highest value and creep-aged specimens showing a reduced value with a 4.8% reduction. The maximum force tolerated in straight notched specimens, reduced by 19.58% after creep degradation a much more reduction compared to 11.3 % in 45 degree tilted notch specimens.

**Fractography and microstructure**

Figure 81 presents the images of the fractured surfaces showing the crack fronts.

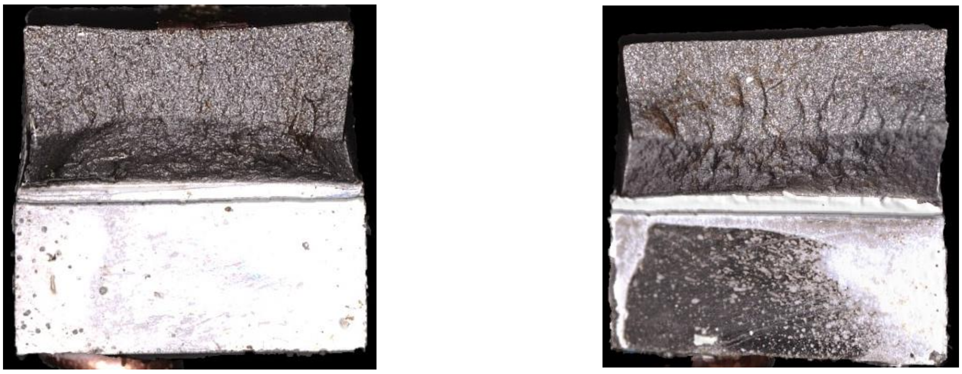

New as received straight notch (N4-0)

New as received 22.5 degree notch (N2-22.5)

Creep degraded straight notch (C1)

Creep degraded 22.5 degree notch (C3)

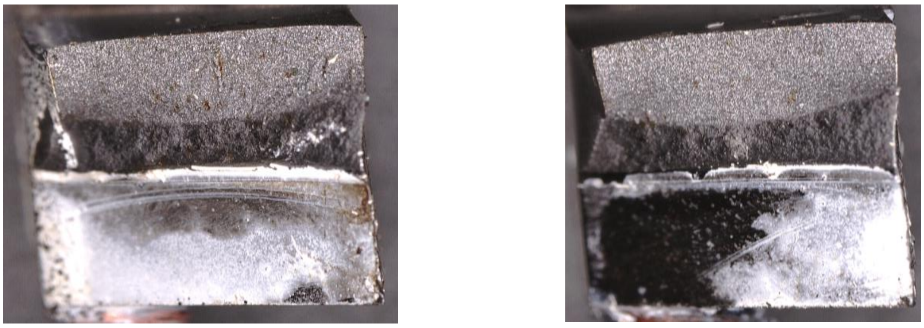

As received straight notch (N6-45)

As received straight notch (N7-45)

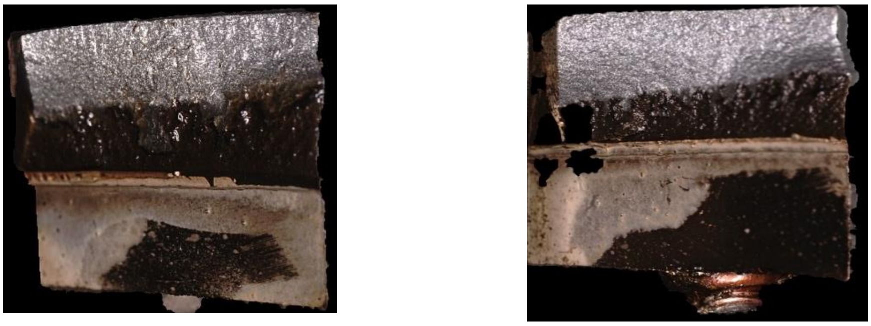

Creep aged 45-degree notch (4C)

Creep aged 45-degree notch (6C)

FIGURE 81: Fractography of fractured surfaces of new and creep-aged specimens.

While for the straight notched and 22.5 degree tilted notch there was no difference in crack front between the new and creep degraded specimens, the crack front of the creep degraded 45 degree tilted notch different from the new as received. In the new 45-degree notched specimens the cracks initiated in the edges propagated toward the midsection and were arrested (plane plane-strain state) resulting in a reversed crescent crack front (reversed crack tunnelling), in the creep degraded specimens the crack front is tilted on one side (plane strain) and advancing more on one side (plane-stress region).

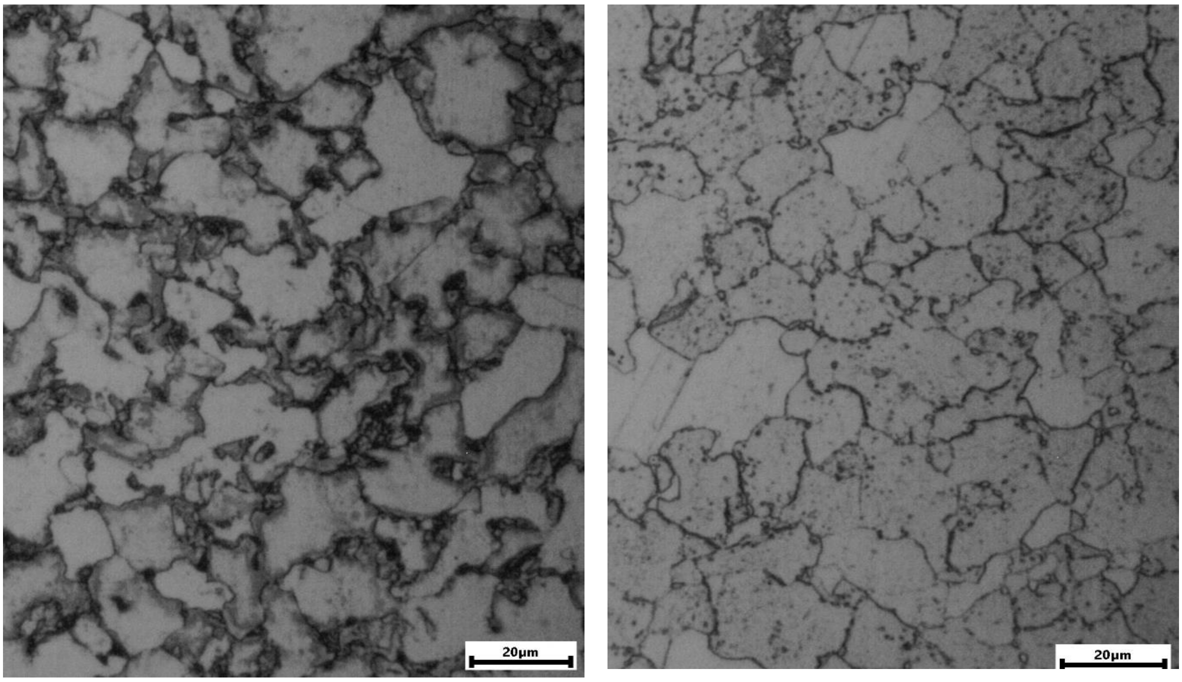

(a) New (b) Creep degraded (C1)

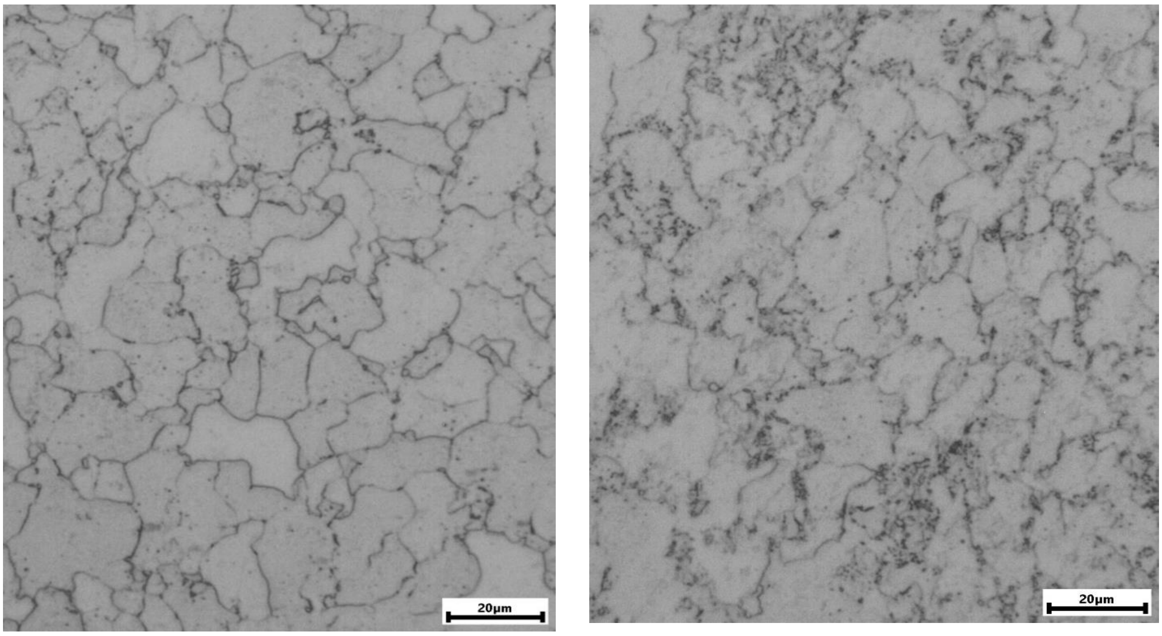

(c) Creep degraded (C3) (d) Isothermal Aged (TK)

FIGURE 82: Microstructure of new (a), creep degraded (b) and (c) and thermal aged (d) 14MoV6-3 steel as seen under light microscope.

Figure 82 shows the microstructure of the investigated specimens at 50X magnification. The initial microstructure features a mixture of bainite with ferrite, sometimes with a small amount of pearlite with a fine grain size and grains are homogeneously distributed. After thermal degradation and creep degradation, the structure image resembles the prolonged exploitation of ferrite with rather homogeneously distributed precipitations inside grains and chains of a significant number of precipitations on their boundaries. It is also observed that the grains coarsen compared to the virgin state.

Figure 83 shows the fracture morphology of the fractured surfaces just ahead of crack initiation blunting as examined using SEM at 500X magnification. Figure 83 (a) is the fractured surface of as received specimen. It has small and shallow dimples characterized by transgranular ductile dimple tearing resulting from the coalescence of microvoids.

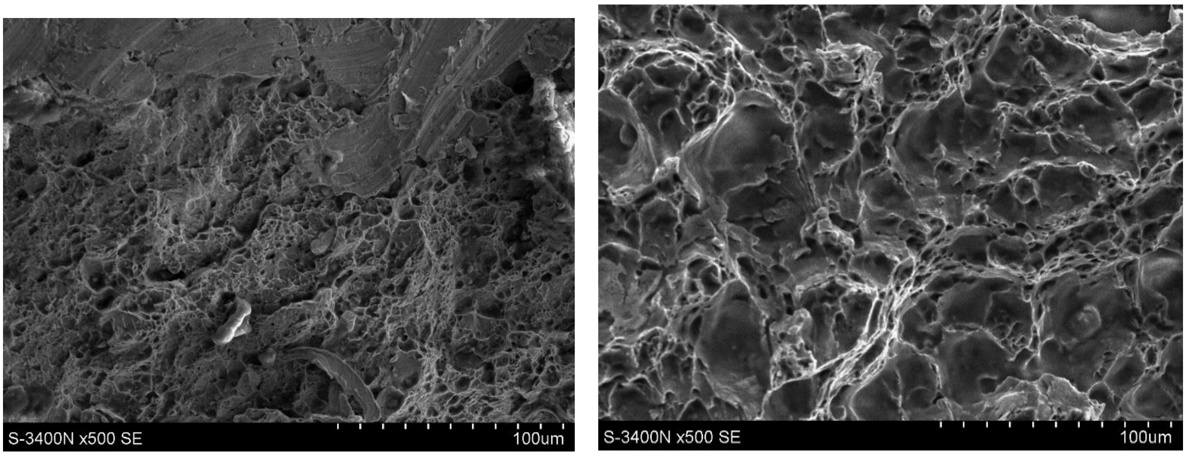

(a) New/Virgin

(b) Creep degraded 0 degree notch (C1)

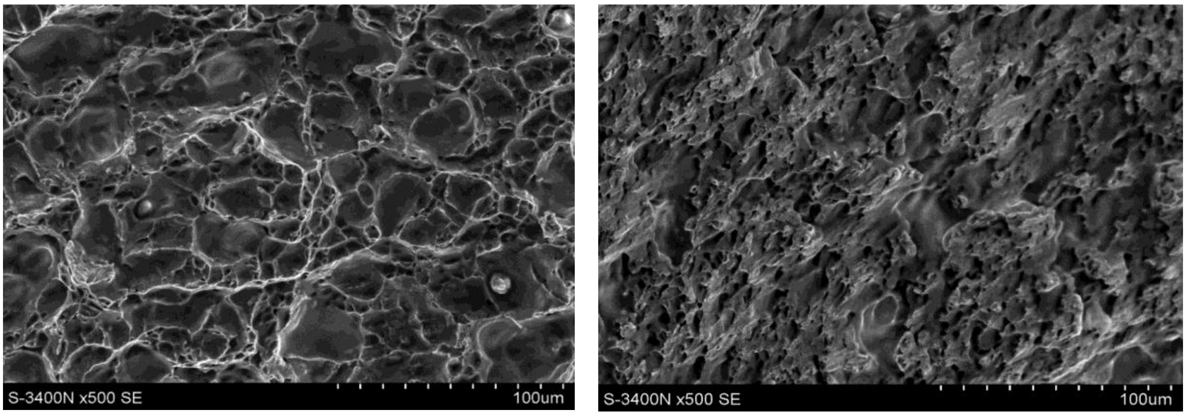

(c) Isothermal degraded (TK)

(d) Creep degree 45-degree notch (C6)

FIGURE 83: Fractographs of stable crack propagation zone located between the machined notch and the terminal crack front of fracture toughness specimens.

Figure 83 (b) shows creep degraded specimen with a straight notch. It is characterized by many large primary voids indicating low toughness even though the morphology appeared somehow ductile. This indicates the specimens underwent small-scale yielding near the fracture tip. Figure 83 (c) represents view on the fracture surface of the sample after the thermal exposition. The fracture mode features ductile dimple tearing along with areas of inter-lath decohesion. Smooth intercrystalline regions on the fracture surface indicate the embrittling effect of thermal exposure on fracture behaviour. None of the specimens' fractured surfaces had river patterns of transgranular cleavage hence the absence of brittle fracture.

### 6.3. Discussion

Compared to virgin specimens the 11.6% and 19.6% reduction in maximum loads of isothermal aged and creep-degraded specimens indicate creep has more detrimental effects on fracture toughness properties than thermal degradation. The reduction in mechanical properties due to ageing has been reported to be caused by precipitate distribution and formation of carbides as well as MnS particles For the creep-aged specimens, the significant decrease in fracture properties has been linked to M23C6 type carbides and MX type carbonitrides precipitation during ageing, leading to the change of the mechanical properties and fracture mode of the steel [181].

Isothermal ageing had a slight effect on the decrease in fracture toughness properties at room temperature as shown in Figure 79 (a). This behavior has been attributed to slow matrix recovery, minimal sub-grain dislocation density changes, and limited grain boundary growth, with hardness variations primarily influenced by precipitation processes. It can be concluded from this observation that high-temperature exposure without creep has a limited effect on the mechanical properties of 14MoV6-3 steel [119].

The results have shown that despite the reduction in fracture toughness, there is still some residual strength for service extension in both straight-notched and tilted-notched specimens. These findings are consistent with the findings of where CrMo-V welds were found to be repairable and functional to operate at $600^0$ C. Another investigation by the authors of this publication [24] investigated the fracture behaviour of 13HMF and L17HMF steel after lengthy operation durations in power boilers. They also concluded that while there was significant microstructural degradation, continued operation of the assessed components was viable and safe, even in minor cracks, if essential material was monitored continuously to avoid or reduce the likelihood of an uncontrolled failure.

In the equilibrium chart in Figure 76 the carbides M23C6_D84 represent the carbides of chromium Cr23C6 and manganese Mn23C6 according to the software nomenclature. They are replaced by carbides M73C3_D101 which are carbides of manganese Mn7C3 and chromium Cr7C3 during Isothermal degradation. Degradation of chromium carbides is one of the signs of materials ’long-term operation. It is reported that phase composition analysis of precipitates in the investigated steel initially normalized and tempered, reveals M3C and MC carbides, with occasional M2C. Prolonged operation at a temperature above the limit alters the type and form of these carbides. The precipitation at the grain boundary and the increase in grain size lowers the fracture toughness since there is nothing to block, deflect, or terminate crack propagation. Similar results were observed in [14] where Cr23C6 carbides were found in diverse sizes and forms at grain borders and in the grain at the start of deterioration. As the degradation time increased, the content of Cr23C6 carbides rose, and the size of Cr23C6 carbides at grain boundaries got coarser.

The more significant decrease in maximum load as shown in Figures 77 and 80 compared to CTOD suggests that creep degradation primarily affects the material’s load-carrying capacity rather than its overall ductility. This also aligns with observations from microstructural analysis, where significant changes in microstructure were observed but did not translate into a proportionally large impact on ductility or fracture toughness. The results from Tables 37 and 38 highlight the differences in mechanical performance between straight-notched and 45° tilted-notched specimens. The reduction in maximum load-carrying capacity after creep was more pronounced for the straight-notched specimens (19.6%) compared to the 45° tilted-notched specimens (11.2%). The decrease in δm after creep was less significant in the 45° tilted-notched specimens (-4.8%) than in the straight-notched specimens (-33%). The tilted geometry proved to be less sensitive to creep degradation as a mixed-mode stress state, allowing for more effective stress redistribution and energy dissipation during deformation. This orientation contributes to higher maximum load and CTOD values, even after creep conditions.

There is a significant increase in the final crack growth in the isothermal degraded specimens before it reaches fracture as observed in Figures 78 (a) and 79 (a). A similar observation was reported by [182], fracture elongation increased by 24% during tensile test of thermally aged specimens. This may be related to the combined effect of microstructural softening causing an increase in ductility and resistance to dislocation motions from the dislocation structure that results from the interaction of dislocations during thermal ageing. It has been reported in [27] that the elongation tends to increase continuously with increasing degradation time. This means that the material softened as the degradation progressed. The absence of significant loss of fracture resistance property in thermally aged specimens despite their deterioration of microstructure means with proper diagnostic supervision, these elements can often continue operating beyond their design life, depending on their residual life a finding that has also been reported in [91].

Creep service causes material structure changes as regards the decomposition of bainite and development of the carbides precipitation processes this causes the deterioration of the fracture toughness of steel as observed in this work. These findings are consistent with those reported in [117] the explored steam line material made of 14MoV6-3 has a lower impact toughness value after long-term exploitation than the minimum value needed for this material as in as received conditions according to German standards DIN17175. The fractographic investigation of fractured surfaces in Figure 83 revealed a dominant dimpled transgranular ductile fracture mode in all new and creep-degraded specimens. This was also reported in [119] where fractured specimens of prior short-term aged P92 steel revealed similar fracture behavior.

The behaviour of the crack front exhibited in Figures 81 in the new and creep-degraded specimens can be explained based on the material's response to the mixed-mode I/III loading conditions. For the new specimens, with a 45-degree notch, the crack propagation is suppressed at the center due to a higher plastic constraint while the edges experience a triaxial stress state which accelerates crack propagation near the side edges resulting in reverse tunneling. In the presence of creep damage, the stress field around the crack tip becomes asymmetric due to reduced ductility leading to suppressed out-of-plane plastic deformation (shear lips). This indicates that creep ageing results in tilted notched specimens losing crack-arresting properties on one of the free edges due to a change of fracture from plane stress state to plane strain state.

According to Figure 82 of the microstructure investigation, there is significant noticeable growth in grain size after both isothermal and creep degradation. Still, there is no significant difference in the growth of ferrite grain size in specimens after isothermal degradation and after creep degradation at elevated temperature. From the German standard VGB-TW 507 “Guidelines for the assessment of microstructure and damage development of creep exposed materials for pipes and boiler components". It can be concluded that both the creep degraded, and isothermal degraded specimens have undergone a significant degradation of microstructure that will forbid allowable service extension. But at the same time fracture toughness test results have demonstrated that there is very little loss of ductile tearing resistance after isothermal ageing. Fracture types in both creep-aged and isothermal-aged specimens follow the path of least resistance. In [26] it was reported that for operated steel, this is significantly influenced by grain boundary damage, including weakened cohesion due to carbide separation or complete bond loss from pore merging and intergranular microcrack initiation. The authors of [183] have demonstrated that the formation of large primary voids is hindered by the significant energy demand associated with their creation. Additionally, larger primary voids are found to enhance resistance to crack propagation. That explains the observations made in figure 83 where the specimen with large voids has a lower toughness.

The analysis indicates that creep damage has more impact in reducing fracture toughness on 14MoV6-3 steel compared to thermal degradation. While the creep crack test is the most precise way to measure creep damage, it can be time-consuming and costly. Furthermore, it is difficult to get samples directly from power plant components that operate in real-time. The application of the laboratory accelerated creep testing method to imitate materials after a specified operating time can be used to obtain specimens for fracture toughness testing and other mechanical properties. The thesis presented methodological issues related to the analysis of CTOD with different crack orientations. This is a very important aspect due to the difference in loading mode in different crack angles.

### 6.4. Summary and conclusion

This study examines the effects of high-temperature creep and thermal degradation on ductile tearing resistance using the Crack Tip Opening Displacement (CTOD) parameter. The investigated material is low-alloy steel 14MoV6-3. Due to the unavailability of material after prolonged in-service ageing accelerated ageing of virgin steel was done using two distinct ageing methods to simulate service-induced degradation in new steel specimens. High-temperature creep ageing was conducted in an electric furnace at 650°C and tensile stress of 60 MPa for 100 hours, while isothermal ageing was performed at 650°C under atmospheric conditions. The results of fracture toughness showed that the as-received specimens exhibited the highest CTOD at maximum load ($\delta m$ = 0.98 mm), followed by isothermally aged specimens ($\delta m$ = 0.93 mm), with creep-aged specimens showing the lowest value ($\delta_m$ = 0.65 mm), reflecting a 33% reduction in fracture toughness. Despite pronounced microstructural changes observed in isothermal ageing, the results revealed limited sensitivity of thermal degradation without creep to CTOD. Furthermore, no significant variation in fracture toughness was observed with increased ageing duration in isothermally aged specimens. Microstructural analyses using optical microscopy and Scanning Electron Microscopy (SEM) demonstrated comparable deterioration in creep-aged and isothermally aged specimens. However, the absence of fracture toughness degradation in the latter underscores the dominant role of creep in the deterioration of fracture toughness. The more significant decrease in maximum load after both thermal and creep ageing compared to CTOD suggests that creep degradation primarily affects the material's load-carrying capacity rather than its overall ductility. Although creep was found to have a mild effect on mixed mode fracture toughness was found to reduce the triaxial stress state at the edges for tilted notches changing fracture mode from plane stress to plane stain.

In this study, the effects of high-temperature creep and isothermal degradation on the ductile tearing resistance of 14MoV6-3 steel were investigated. The main conclusion was as follows:

1. Crack tip opening displacement showed very significant sensitivity to creep ageing, leading to higher crack propagation and lower crack growth resistance.
2. High-temperature isothermal degradation resulted in a significant transformation in the microstructure but there was no discernible change in ductile tearing resistance. Changes in precipitation processes and substructures do not prove deterioration of fracture toughness properties.
3. With high temperature creep the ductile tearing resistance decreased drastically. The creep reduced the $\delta_m$ by 33% and maximum loads by 19%. This means that the material becomes brittle as the degradation progresses.
4. The fracture toughness testing was conducted at room temperature, with a constant $a_0/W$ ratio. Thus, the presented results are limited to certain test conditions.
5. More creep ageing durations need to be examined so that an empirical model can be proposed to predict the change of ductile tearing resistance as a simple function of creeping time.
6. The tilted geometry proved to be less sensitive to creep degradation.
7. The more significant decrease in maximum load compared to CTOD suggests that creep degradation primarily affects the material's load-carrying capacity rather than its overall ductility.
8. Although knowledge of the structure and microstructural evolution is essential for assessing residual service life, it has several limitations as a tool for correcting material fracture toughness after degradation.

The findings of this investigation not only verify existing theories of creep-related deterioration in low-alloy steels but also give fresh insights into the influence of creep on ductile tearing resistance.

# CHAPTER 7: GENERAL DISCUSSION, CONCLUSION AND FUTURE PERSPECTIVES

Pressure vessel and boiler design is closely regulated given the safe operation criteria established by the corresponding codes. The thickness of the planned vessel wall is determined so that the stresses created in the structure stay within the elastic limit for the design temperature and pressure. By doing this, the excessive plastic deformations or rupture linked to the yield point surpassing be avoided. A pressure vessel's strength may be diminished by the presence of cracks. Once the fracture crack reaches its critical size, it may accelerate the expansion of pre-existing damage and ultimately lead to abrupt failure. Note that such failure typically occurs at stresses that are significantly lower than the yield strength of the material.

Industrial design and calculations assume a material free of defects, cracks, and internal cavities. This thesis assessed the impact of cracks and their potential progression on structural durability. The four goals outlined in Chapter 1 served as the inspiration for this work but its main aimy was to compare fracture properties of power plant steel grade using different specimen’s geometries from new, and those subjected to various ageing and degradation conditions. A survey of the advancements in fracture mechanics and fracture toughness testing and its contribution to predicting material failure has been presented in Chapters 1 and 2. Since the 1930s, fracture mechanics has matured as an engineering discipline, with gradual advancements in testing procedures rather than ground-breaking discoveries.

The study assessed the fracture toughness of power plant components made from 13HMF and L17HMF steel exposed to industrial conditions over extended periods (Chapter 3). Pressure systems' mechanical properties might deteriorate over time due to combined stresses and temperature exposure, limiting their residual life. The components analyzed were made from the valve chamber and piping sections. A combination of experimental and numerical approaches was employed, utilizing arc-shaped tension (AT) and single-edge notched tension (SENT) specimens. Finite element (FE) modelling in Abaqus provided valuable insights into stress distribution and crack propagation behaviour.

The fracture behaviour of SENT specimen geometry under mixed-mode loading was also examined utilizing the niche of Digital Image Correlation (DIC)-based test method to overcome the limitations of conventional clip gauge techniques (Chapter 4). SENT specimens with tilted notches highlighted the influence of crack tilt angles on fracture toughness.

The study also investigated the effects of accelerated high-temperature creep and isothermal degradation on the ductile tearing resistance of 14MoV6-3 steel. Maximum loads and CTOD parameters are measured and compared for the different ageing conditions.

The research was primarily experimental but was complemented by numerical simulations performed using Abaqus to validate the findings. The test results provided insights into the effects of creep and isothermal degradation on fracture resistance. The findings contribute to a deeper understanding of the fracture mechanisms in aged power plant steel, particularly under thermomechanical loading conditions. Moreover, this research broadens the application of Elastic-Plastic Fracture Mechanics (EPFM) in the inspection, assessment, and maintenance of engineering structures subjected to complex loading scenarios. The results demonstrate significant differences in the fracture behaviour of specimens based on their degradation and ageing condition. The following key conclusion can be drawn from the study:

1. Fracture toughness is an important material property that describes the ability of a material with a crack to resist fracture when applied force. The ISO and ASTM standards are now the most used standards for assessing fracture toughness as they offer reliability in ensuring precision in crack measurement methodologies, specimen geometry, and validity criteria. However, several obstacles remain, such as measuring fatigue crack development (FCG) and standardizing mixed-mode fracture testing as currently there is no developed standard for mixed mode fracture. SENT specimen geometry have low crack-tip constraint conditions like actual fractures in pressure containers and pipes which are frequently shallow and dominated by tensile stresses.
2. Arc-tension-shaped specimen geometries were machined for fracture testing after industrial condition degradation. Experimental testing was done by LLD using a traditional clip gauge extensometer, and the length of crack propagation was validated using the nine-point average method. Stress intensity factors were calculated and compared. The valve specimens demonstrated superior fracture toughness, indicating their ability to withstand higher stress concentrations before failure. Despite the microstructural degradation characterized by ferrite with homogeneously distributed precipitations inside grains and chains of the significant amount of precipitations on their boundaries, after more than 100, 000 hours of operation the results of fracture toughness showed that the material had enough strength for lifetime extension.
3. Mixed-mode fracture behaviour: The DIC-based experimental approach provided detailed insights into crack initiation and propagation under mixed-mode I/III loading, revealing the influence of notch orientation and stress intensity factors on fracture behaviour. An increase in the tilt angle increases the mode III opening component, resulting in higher fracture toughness. However, the fracture failure mechanism remained primarily contributed by mode I tensile stresses. The introduction of mode III shear loading does not significantly alter the fundamental fracture behaviour but contributes to increased ductility. The effect of creep on straight notched specimen was a 33.02 % reduction of CTOD5 at maximum load compared to 4.7 % reduction for 45% tilted notch specimens. Inclined notches are more resistant to effect of creep ageing.
4. Accelerated high-temperature creep and thermal ageing experiments revealed that creep exposure reduced crack growth resistance, with CTOD decreasing by 33% and maximum loads by 19%. The loads vs displacement (LLD) curves of new and both thermal and creep-degraded specimens have the same behaviour in the plastic region. The difference is that the new received has a larger elastic component compared to the thermal degraded and creep-degraded specimens. At some point around 0.5 mm displacement, the loads of new as received and the aged specimens start to diverge. The loads of the isothermal aged and the creep aged specimen start to diverge at a displacement of 0.75 mm. The findings indicate that creep ageing primarily affects the material’s load-carrying capacity rather than its overall ductility. Despite observable microstructural transformations, no significant deterioration in ductile tearing resistance was detected.

5. Validation through numerical simulations in Abaqus closely matched experimental results, confirming the accuracy of the test methodology and enhancing the predictive capabilities for assessing fracture performance in aged steel. The percentage error between experimental and numerical results was below 5% in all cases.
6. From the comparison of fracture toughness of isothermally aged pipes and creep degraded it was found that creep contributes to the probability of pipe failure more than high-temperature ageing. With increased isothermal degradation time the content of $Cr_{23}C_6$ carbides increased and the size of Cr23C6 carbides located at grain boundaries became coarse but fracture toughness was not significantly affected. However, the elongation tends to increase continuously with increasing degradation time. This means that the material softened as the degradation progressed.
7. The maximum force in the CMOD-force curves for new and isothermally aged materials are almost equal, but the new materials withstood slightly more force.

Overall, this research provides a foundation for future studies on the long-term structural integrity of thermally and mechanically degraded materials. Further work could explore advanced modelling techniques, extended service life assessments, and real-time monitoring approaches to enhance the predictive maintenance of industrial components.

## 7.1. Future Work

Some drawbacks and main findings of this thesis suggest numerous interesting areas for future research/developments. Based on the insights collected, the following major areas are recommended for further investigation:

1. This work only investigated the effect of creep and isothermal degradation but in actual boilers one of the most frequent types of loads are variable in time fields of forces and temperature fields which induce material degradation being the result of thermo-mechanical fatigue and creep at elevated temperature. A more comprehensive experimental and numerical study that include multiaxial creep-fatigue interactions should be done to improve predictive accuracy when assessing effect of long-term operation on deterioration of mechanical properties. Furthermore, from the literature review it was observed that fracture can occur during low temperature startup and transient conditions, attentions should be devoted to the influence of low temperatures on aged steel especially on HAZ which is the most brittle part. Furthermore, the fatigue crack propagation tests under mixed load conditions I+III needs to be conducted.
2. The boiler components typically fracture along welded joints. If the pressure from overheating exceeds the operational pressure, the welding joint becomes the weakest point due to stress concentration from the notched design structure. The boiler tank's welding junction has several problems, including spatter, crater, slag, and undercut. Double welding lines, with non-coincidence between start and end points, may result in residual tensile stress in the middle. Welding errors may cause boiler tank failure. Detailed studies of the fracture behaviour of welded joins and heat affected zone (HAZ) need to be done to find out the crack propagation on the weld joint of boiler components after creep ageing and thermal degradation.
3. Fracture toughness testing was done at room temperature conditions, yet the steel grade operates in elevated temperature. extending experimental research to higher operating temperature to examine fracture behaviour under harsh thermal settings, which simulate real-world power plant situations. Steel is known to be more ductile at elevated temperature therefore the results of room temperature are expected to vary with those at boiler operating temperatures.
4. It was difficult to monitor and measure crack mouth opening displacement of the tested SENT specimens using DIC because of loss of speckled pattern at the edges of the specimen during deformation. Therefore, it is recommended to develop more robust and reliable method of using DIC to measure CMOD.
5. Real structural health Monitoring using sensor-based approaches, such as acoustic emission and digital image correlation, to monitor crack growth and fracture processes in important components or in potential fracture areas.
6. Microstructural analysis of aged steel involves conducting comprehensive microstructural examinations, such as electron microscopy and phase analysis, to correlate fracture behaviour with underlying material alterations over time.
7. The in-plane mode II loading loading was not taken into consideration in this thesis. But boilers are engineering structures that are frequently subjected to mode II loading, which can

result in mixed-mode I-II fracture or more complex 3D mixed-mode fracture. The effect of mode II loading should be investigated.

8. A 3-dimensional digital image correlation approach is advised for the tests to measure the displacement or deformation under mode III loading. Standardization of mixed-mode fracture in complex geometries: Extending future research of mixed-mode I/III loading to more complex geometries and loading circumstances to increase the reliability of fracture evaluation techniques. There is currently no standard for determining fracture toughness of mixed mode fracture.
9. Collaborating with power plant operators to confirm findings in real-world scenarios and build Elastic plastic fracture mechanics-based maintenance and inspection techniques. The development of empirical models predicting changes in fracture toughness as a function of creep exposure would be useful in in-service life estimation and maintenance planning of power plant components, hence preventing unscheduled shutdowns.

These prospective research directions aim to refine the present methods of assessing structural integrity of ageing power plants by understanding of fracture development in ageing power plant steel, contributing to increased safety, reliability, and life extension of essential infrastructure.

# BIBLIOGRAPHY

[1] J. C. Newman, “The merging of fatigue and fracture mechanics concepts: A historical perspective,” *ASTM Spec. Tech. Publ.*, vol. 1321, pp. 3–51, 1997, doi: 10.1520/stp12300s.

[2] Ted. L. Anderson, *FRACTURE MECHANICS Fundamentals and Applications*, Third Edit. Taylor & Francis Group, 2005.

[3] S. D. Antolovich, A. Saxena, and W. W. Gerberich, “Fracture mechanics – An interpretive technical history,” *Mech. Res. Commun.*, vol. 91, pp. 46–86, 2018, doi: 10.1016/j.mechrescom.2018.03.003.

[4] J. M. Vasco-Olmo, F. A. Díaz, F. V. Antunes, and M. N. James, “Characterisation of fatigue crack growth using digital image correlation measurements of plastic CTOD,” *Theor. Appl. Fract. Mech.*, vol. 101, no. December 2018, pp. 332–341, 2019, doi: 10.1016/j.tafmec.2019.03.009.

[5] G. Liu *et al.*, “Typical Damage Prediction and Reliability Analysis of Superheater Tubes in Power Station Boilers Based on Multisource Data Analysis,” *Energies*, vol. 15, no. 3, 2022, doi: 10.3390/en15031005.

[6] J. Okrajni, K. Wacławiak, G. Junak, and M. Twardawa, “Stress – Strain Behavior and Fatigue of High-Temperature,” *Energies*, vol. 17, no. 2870, 2024.

[7] Badaruddin Soomro, Muhammad Irfan, Bilal Waseem, Sumaira Nosheen, Abdul Karim Aziz, and Hamza Butt, “Failure investigation into the boiler tubes of power plant,” *Int. J. Sci. Res. Arch.*, vol. 2, no. 2, pp. 028–036, 2021, doi: 10.30574/ijsra.2021.2.2.0048.

[8] B. Haghighat-shishavan, H. Firouzi-nerbin, and M. Nazarian-samani, “Failure analysis of a superheater tube ruptured in a power plant boiler : Main causes and preventive strategies,” *Eng. Fail. Anal.*, vol. 98, no. December 2018, pp. 131–140, 2019, doi: 10.1016/j.engfailanal.2019.01.016.

[9] B. Szybiński and P. Romanowicz, “Influence of crack presence on operating conditions of pressure vessels with flat endplates,” *J. KONES Powertrain Transp.*, vol. 23, no. 1, 2016.

[10] K. Wacławiak, B. Kipsang, B. V. Farahani, and W. De Waele, “Experimental and numerical assessment of fracture toughness variations in steam boiler components after a long period of operation,” *Int. J. Press. Vessel. Pip.*, vol. 209, no. May, 2024, doi: 10.1016/j.ijpvp.2024.105198.

[11] A. Singh, V. Sharma, S. Mittal, G. Pandey, D. Mudgal, and P. Gupta, “An overview of problems and solutions for components subjected to fireside of boilers,” *Int. J. Ind. Chem.*, vol. 9, no. 1, pp. 1–15, 2018, doi: 10.1007/s40090-017-0133-0.

[12] J. Trzeszczyński and E. Trzeszczyńska, “Conditional operation of boiler components working under creep conditions until replacement,” *Strength, Fract. Complex.*, vol. 15, no. 1, pp. 99–112, 2022, doi: 10.3233/SFC-228007.

[13] A. Jasiński, A. Zieliński, and H. Purzyńska, “RESIDUAL LIFE OF REPAIR WELDED JOINTS IN PIPELINES MADE OF 13HMF AFTER USE FOR NA RUROCIĄGACH WYKONANYCH Z 13HMF PO PRZEPRACOWANIU,” *Pr. Inst. Metal. Żelaza*, vol. 70, no. 3, pp. 2–10, 2018, doi: 10.32730/imz.0137-9941.18.3.1.

[14] J. Choi, C. S. Seok, S. Park, and G. Kim, “Effect of higherature degradation on microstructure evolution and mechanical properties of austenitic heat-resistant steel,” *J. Mater. Res. Technol.*, vol. 8, no. 2, pp. 2011–2020, 2019, doi: 10.1016/j.jmrt.2018.11.017.

[15] S. Mrozowska, J. A. Wendt, and K. Tomaszewski, “The challenges of poland’s energy transition,” *Energies*, vol. 14, no. 23, 2021, doi: 10.3390/en14238165.

[16] D. S. Bhiogade, “Ultra supercritical thermal power plant material advancements: A review,” *J. Alloy. Metall. Syst.*, vol. 3, no. July, p. 100024, 2023, doi: 10.1016/j.jalmes.2023.100024.

[17] N. A. Popova, E. L. Nikonenko, N. V. Ababkov, and A. N. Smirnov, “Service Life Effect on Structure and Phase Composition of DIN 14MoV63 Steel,” *Russ. Phys. J.*, vol. 63, no. 11, pp. 1898–1903, 2021, doi: 10.1007/s11182-021-02248-y.

[18] A. Zieliński, J. Dobrzański, and M. Dziuba-Kałuza, “Structure of welded joints of 14MoV6-3 and 13CrMo4-5 steel elements after design work time under creep conditions,” *Arch. Mater. Sci. Eng.*, vol. 61, no. 2, pp. 69–76, 2013.

[19] M. ziuba-Kałuża, A. Zieliński, J. Dobrzański, and M. Sroka, “G. Gerzy Okrajni, Kazimierz Mutwil, MarekCieśla (Politechnika Śląska, ‘WYTĘŻENIE I TRWAŁOŚĆ RUROCIĄGÓW PAROWYCH,’ GÓRNICTW,” *Arch. Mater. Sci. Eng.*, vol. 66, no. 1, pp. 21–30, 2014.

[20] A. Zieliński, “Assessment of loss in life time of the primary steam pipeline material after long-term service under creep conditions,” *J. Achiev. Mater. Manuf. Eng.*, vol. 54, no. 1, pp. 67–74, 2012.

[21] F. Masuyama, “History of power plants and progress in heat resistant steels,” *ISIJ Int.*, vol. 41, no. 6, pp. 612–625, 2001, doi: 10.2355/isijinternational.41.612.

[22] F. Abe, T.-U. K. And, and R. Viswanatha, *Creep-resistant steels*, 1st ed. New York: WOODHEAD PUBLISHING LIMITED, 2008.

[23] W. Karpa and A. Grginović, “(Not so) stranded: The case of coal in Poland,” *Energies*, vol. 14, no. 24, 2021, doi: 10.3390/en14248476.

[24] M. Widera, Z. Kasztelewicz, and M. Ptak, “Lignite mining and electricity generation in Poland: The current state and future prospects,” *Energy Policy*, vol. 92, pp. 151–157, 2016, doi: 10.1016/j.enpol.2016.02.002.

[25] M. Jakubowska, R. Chulist, L. Maj, and A. Sypien, “Analysis of the Creep Mechanism of Low-Alloy Steel in Terms of Plastic Deformation,” *J. Mater. Eng. Perform.*, 2024, doi: 10.1007/s11665-024-10229-8.

[26] H. Krechkovska *et al.*, “Substantiation of the critical structural and mechanical state of low-alloy heat-resistant steel from steam pipelines of thermal power plant,” *Eng. Fail. Anal.*, vol. 150, no. March, p. 107359, 2023, doi: 10.1016/j.engfailanal.2023.107359.

[27] M. van Rooyen, “Thermal power plant steel creep deformation measurement using digital image correlation,” Stellenbosch University, 2020.

[28] O. Cronvall, “Structural lifetime, reliability and risk analysis approaches for power plant components and systems,” VTT Technical Research Centre of Finland, Vuorimiehentie, 2011.

[29] S. T. R. N.Willems, J.T.Easely, *Strength of materials*. MCGraw-Hill Book Company, 1981.

[30] W. Khor, P. L. Moore, H. G. Pisarski, M. Haslett, and C. J. Brown, “Measurement and prediction of CTOD in austenitic stainless steel,” *Fatigue Fract. Eng. Mater. Struct.*, vol. 39, no. 11, pp. 1433–1442, 2016, doi: 10.1111/ffe.12487.

[31] P. R. Sreenivasan, “Inverse of Wallin ’ s relation for the effect of strain rate on the ASTM E-1921 reference temperature and its application to reference temperature estimation from Charpy tests,” *Nucl. Eng. Des.*, vol. 241, pp. 67–81, 2011.

[32] R. D. S. G. Campilho, K. Madani, and M. Belhouari, “Introduction to fracture mechanics,” *Fract. Mech. Adv. Res. Appl.*, pp. 1–15, 2024.

[33] X. Zhu and J. A. Joyce, “DigitalCommons @ University of Nebraska - Lincoln Review of fracture toughness ( G , K , J , CTOD , CTOA ) testing and standardization,” *Eng. Fract.*

*Mech.*, vol. 85, 2012, doi: 10.1016/j.engfracmech.2012.02.001.

[34] R. Shaikh, T. Khan, A. Inamdar, M. Jaweed, and B. Malik, "Review of Fracture Toughness ( G , K , J , CTOD , CTOA )," *IOSR J. Eng. (IOSR JEN)*, vol. c, pp. 62–66, [Online]. Available: http://www.iosrjen.org/.

[35] Ž. Božić, M. Mlikota, and S. Schmauder, "APPLICATION OF THE Δ K , Δ J AND Δ CTOD PARAMETERS IN FATIGUE CRACK GROWTH MODELLING," *Tech. Gaz.*, vol. 18, no. 3, pp. 459–466, 2011.

[36] C. Duan and S. Zhang, "Further investigation of J-CTOD relationship for clamped SET specimens based on finite element analyses – Part I: Homogeneous materials," *Theor. Appl. Fract. Mech.*, vol. 121, no. February, p. 103523, 2022, doi: 10.1016/j.tafmec.2022.103523.

[37] M. N. Silvestre, S. Hertelé, and D. F. B. Sarzosa, "On the experimental estimation of CTOD fracture parameter using SE(T) specimens based upon only one clip gauge measurement," *Eng. Fract. Mech.*, vol. 253, no. December 2020, p. 107856, 2021, doi: 10.1016/j.engfracmech.2021.107856.

[38] N. Gubeljak, M. D. Chapetti, J. Predan, and J. D. Landes, "CTOD-R curve construction from surface displacement measurements," *Eng. Fract. Mech.*, vol. 78, no. 11, pp. 2286–2297, 2011, doi: 10.1016/j.engfracmech.2011.05.002.

[39] M. Rund *et al.*, "Compatibility of fracture toughness results in the upper shelf region," in *Procedia Structural Integrity, The 3rd International Conference on Structural Integrity*, 2019, vol. 17, pp. 479–486, doi: 10.1016/j.prostr.2019.08.063.

[40] Y. Wang, W. Wang, B. Zhang, and C. Q. Li, "A review on mixed mode fracture of metals," *Eng. Fract. Mech.*, vol. 235, no. May, p. 107126, 2020, doi: 10.1016/j.engfracmech.2020.107126.

[41] N. Leitão and F. A. Gilabert, "A unified J-Integral-based procedure to investigate at different loading regimes the fracture by FEM simulations and image analysis," *J. Mech. Phys. Solids*, vol. 149, no. July 2020, p. 104318, 2021, doi: 10.1016/j.jmps.2021.104318.

[42] Y. Wang, W. Wang, B. Zhang, and C. Q. Li, "A new method to determine fracture resistance curve of steel under various in-plane loading," *Eng. Fract. Mech.*, vol. 248, no. March, p. 107701, 2021, doi: 10.1016/j.engfracmech.2021.107701.

[43] B. Tyson, P. Ding, and X. Wang, "Elastic compliance of single-edge-notched tension SE(T) (or SENT) specimens," *Frat. ed Integrita Strutt.*, vol. 30, no. June, pp. 95–100, 2014, doi: 10.3221/IGF-ESIS.30.13.

[44] B. S. Publication, "BSI Standards Publication Method of test for determination of fracture toughness in metallic materials using single edge notched tension ( SENT )," BS 8571:2014, 2014.

[45] T. B. Standards, "Method of test for determination of fracture toughness in metallic materials using single edge notched tension (SENT) specimens," 2018.

[46] B. Nyhus, M. L. Polanco, and O. Ørjasæther, "SENT SPECIMENS AN ALTERNATIVE TO SENB SPECIMENS," 2019, [Online]. Available: https://www.asme.org/terms-of-use.

[47] M. Paredes, T. Wierzbicki, and P. Zelenak, "Prediction of crack initiation and propagation in X70 pipeline steels," *Eng. Fract. Mech.*, vol. 168, pp. 92–111, 2016, doi: 10.1016/j.engfracmech.2016.10.006.

[48] E. Wang, W. De Waele, and S. Hertelé, "A complementary ηpl approach in J and CTOD estimations for clamped SENT specimens," *Eng. Fract. Mech.*, vol. 147, pp. 36–54, 2015, doi: 10.1016/j.engfracmech.2015.07.043.

[49] J. Kang, J. A. Gianetto, and W. R. Tyson, "Recent development in low-constraint fracture

toughness testing for structural integrity assessment of pipelines," *Front. Mech. Eng*, vol. 13, no. 4, pp. 546–553, 2018.

[50] C. Gustavo H. B. Donato, Ruggieri, "ESTIMATION PROCEDURE FOR J AND CTOD FRACTURE PARAMETERS USING THREE-POINT BEND SPECIMENS," *Proc. IPC2006 6th Int. Pipeline Conf.*, pp. 1–9, 2006.

[51] P. S. Lam, Y. Kim, and Y. J. Chao, "The non-constant CTOD/CTOA in stable crack extension under plane-strain conditions," *Eng. Fract. Mech.*, vol. 73, no. 8, pp. 1070–1085, 2006, doi: 10.1016/j.engfracmech.2005.12.008.

[52] I. Dzioba, P. Furmańczyk, and S. Lipiec, "The methods for determining the CTOD at crack initiation," *nżynieria Mater.*, vol. 3, no. 223, pp. 116–121, 2018.

[53] ASTM Standard, "Standard Test Methods for Tension Testing of Metallic Materials," vol. E8/E8M − 1, no. E8/E8M − 13a, 2018, doi: 10.1520/E0008.

[54] J. Zhang, L. Muys, S. De Tender, N. Micone, S. Hertelé, and W. De Waele, "Constraint corrected cycle-by-cycle analysis of crack growth retardation under variable amplitude fatigue loading," *Int. J. Fatigue*, vol. 125, no. April, pp. 199–209, 2019, doi: 10.1016/j.ijfatigue.2019.03.046.

[55] C. Qian, J. Liang, Y. Huang, J. Kang, and J. Gianetto, "Constraint effect on fracture toughness resistance curves of an X60 pipe steel," *Procedia Struct. Integr.*, vol. 37, no. 2019, pp. 926–933, 2022, doi: 10.1016/j.prostr.2022.02.027.

[56] B. K. Kipsang, K. Wacławiak, and W. De Waele, "Implementation of Recent Advances in Fracture Toughness Testing to Investigate Tearing Resistance of Heat-Resistant Steel 14MoV6-3," *Arch. Met. Mater.*, vol. 70, no. 1, pp. 317–324, 2025.

[57] J. Kowalski and J. Kozak, "THE EFFECT OF NOTCH DEPTH ON CTOD VALUES IN FRACTURE," *POLISH Marit. Res.*, vol. 25, no. 2, pp. 85–91, 2018, [Online]. Available: 10.2478/pomr-2018-005.

[58] W. K. Nowacki, Z. Nowak, P. Perzyna, and R. B. Pęcherski, "EFFECT OF STRAIN RATE ON DUCTILE FRACTURE. A NEW METHODOLOGY," *J. Theor. Appl. Mech.*, vol. 48, pp. 1003–1026, 2010.

[59] C. Pandey, M. M. Mahapatra, P. Kumar, and N. Saini, "Effect of strain rate and notch geometry on tensile properties and fracture mechanism of creep strength enhanced ferritic P91 steel," *J. Nucl. Mater.*, vol. 498, pp. 176–186, 2018, doi: 10.1016/j.jnucmat.2017.10.037.

[60] M. Graba, "NUMERICAL ANALYSIS OF THE INFLUENCE OF IN-PLANE CONSTRAINTS ON THE CRACK TIP OPENING DISPLACEMENT FOR SEN ( B ) SPECIMENS UNDER PREDOMINANTLY PLANE STRAIN CONDITIONS," *Int. J. Appl. Mech. Eng.*, vol. 21, no. 4, pp. 849–866, 2016, doi: 10.1515/ijame-2016-0050.

[61] B. Cotterell, "The past , present , and future of fracture mechanics," *Eng. Fract. Mech.*, vol. 69, pp. 533–553, 2002.

[62] K. Hectors and W. De Waele, "An X-FEM based framework for 3D fatigue crack growth using a B-spline crack geometry description," *Eng. Fract. Mech.*, vol. 261, 2022.

[63] ASTM, "Standard Test Method for Measurement of Fatigue Crack Growth Rates 1," vol. E647 − 15, no. E647 − 15, pp. 1–48, 2016, doi: 10.1520/E0647-15.2.

[64] M. Kadlec, P. HauŠild, J. Siegl, A. Materna, and J. Bystrianský, "Thermal fatigue crack growth in stainless steel," *Int. J. Press. Vessel. Pip.*, vol. 98, pp. 89–94, 2012, doi: 10.1016/j.ijpvp.2012.07.005.

[65] Y. Si, J. P. Rouse, and C. J. Hyde, "Potential difference methods for measuring crack

growth : A review," *Int. J. Fatigue*, vol. 136, no. March, 2020, doi: 10.1016/j.ijfatigue.2020.105624.

[66] D. Boronski, M. Kotyk, and P. Mackowiak, "Measurement method of crack length in compact tension type specimens made from the Al/Ti layered material.," *Maint. Probl.*, vol. 3, pp. 17–26, 2016.

[67] P. Štefane, S. Hertelé, S. Naib, W. De Waele, and N. Gubeljak, "Effects of Fixture Configurations and Weld Strength Mismatch on J-Integral Calculation Procedure for SE ( B ) Specimens," *Materials (Basel).*, vol. 15, no. 962, pp. 1–26, 2022.

[68] J. Bär, "Crack detection and crack length measurement with the DC potential drop method–possibilities, challenges and new developments," *Appl. Sci.*, vol. 10, no. 23, pp. 1–14, 2020, doi: 10.3390/app10238559.

[69] S. Wu and Z. Zhang, "Long term ageing effect on fracture toughness of the GTAW welded joints for nuclear power main pipelines," *Int. J. Press. Vessel. Pip.*, vol. 188, no. November, p. 104250, 2020, doi: 10.1016/j.ijpvp.2020.104250.

[70] M. Łomozik, "Structure and plastic properties of HAZ area in 13HMF steel after over 130 000 hours of operation while subjected to simulation welding thermal cycles," *Bulletin of the Institute of WeldingPoland*, vol. 4, no. 2013, 2017.

[71] R. G. Savioli and C. Ruggieri, "IMPROVED J AND CTOD ESTIMATION FORMULAS FOR C(T) FRACTURE SPECIMENS INCLUDING OVERMATCHED WELDMENTS," in *Proceedings of the ASME 2011 Pressure Vessels & Piping Division Conference PVP2011*, 2011, pp. 1–10.

[72] Z. Chen, P. Wang, F. Chen, and F. Wang, "Pressure reduction strategy based on a new CTOD model considering room temperature creep for X80 pipeline steel," *Eng. Fract. Mech.*, vol. 289, no. July, p. 109479, 2023, doi: 10.1016/j.engfracmech.2023.109479.

[73] M. A. Verstraete, W. De Waele, K. Van Minnebruggen, and S. Hertel, "Crack growth characterization in single-edge notched tension testing by means of direct current potential drop measurement," *Int. J. Press. Vessel. Pip.*, vol. 156, pp. 68–78, 2017, doi: 10.1016/j.ijpvp.2017.06.009.

[74] DET NORSKE VERITAS (DNV), "FRACTURE CONTROL FOR PIPELINE INSTALLATION METHODS INTRODUCING CYCLIC PLASTIC STRAIN," Høvik, Norway, 2006.

[75] Koen Van Minnebruggen, "PhD thesis. Experimental-Numerical Study on the Feasibility of Spirally Welded Pipes in a Strain Based Design Context Koen Van Minnebruggen," Ghent University, 2016.

[76] M. Graba, "A NUMERICAL ANALYSIS OF SELECTED ELASTIC-PLASTIC," *Int. J. Appl. Mech. Eng.*, vol. 22, no. 1, pp. 49–80, 2017, doi: 10.1515/ijame-2017-0004.

[77] E. Chvostová, J. Horváth, P. Konopík, S. Rzepa, and D. Melzer, "Optimization of test specimen dimensions for thermal power station exposure device," *IOP Conf. Ser. Mater. Sci. Eng.*, vol. 723, no. 1, 2020, doi: 10.1088/1757-899X/723/1/012009.

[78] P. K. and M. R. Jan Dzugan, "Fracture Toughness Determination with the Use of Miniaturized Specimens," *Contact Fract. Mech.*, 2018.

[79] J. Ast, M. Ghidelli, K. Durst, M. Göken, M. Sebastiani, and A. M. Korsunsky, "A review of experimental approaches to fracture toughness evaluation at the micro-scale," *Mater. Des.*, vol. 173, 2019, doi: 10.1016/j.matdes.2019.107762.

[80] K. Matocha, "The Use of Small Punch Tests for Determination of Fracture Behaviour of Ferritic Steels," *Procedia Eng.*, vol. 86, pp. 885–891, 2014, doi:

10.1016/j.proeng.2014.11.110.

[81] O. Dorazil, K. Matocha, J. Zhu, and Y. Chen, “The effect of long term exposition at 540 ◦ C on the empirical correlations for determination of mechanical properties of low alloy CrMoV steel from the results of Small Punch tests ഋ,” *Perspect. Sci.*, vol. 7, pp. 156–160, 2016, doi: 10.1016/j.pisc.2015.11.025.

[82] G. Mieczkowski and K. Molski, “Verification of brittle fracture criteria for bimaterial structures,” *acta Mech. Autom.*, vol. 8, no. 1, pp. 44–48, 2014, doi: 10.2478/ama-2014-0008.

[83] M. Kopec, “Fatigue Damage Development in 14MoV6-3 Steel for Power Plant Pipes Monitored by Digital Image Correlation,” *Acta Mech. Solida Sin.*, vol. 36, no. 3, pp. 405–417, 2023, doi: 10.1007/s10338-023-00387-y.

[84] Z. M, B. Z, and C. Z, “FRACTURE TOUGHNESS AND CRACK RESISTANCE OF STEAM PIPELINE STEEL IN INITIAL AND USED STATES,” *Strength Mater.*, vol. 36, no. 1, pp. 47–58, 2004.

[85] M. Sroka, A. Zieliński, M. Dziuba-Kałuża, M. Kremzer, M. Macek, and A. Jasiński, “Assessment of the residual life of steam pipeline material beyond the computational working time,” *Metals (Basel).*, vol. 7, no. 3, 2017, doi: 10.3390/met7030082.

[86] J. Dobrzański, A. Hernas, and G. Moskal, “Microstructural degradation in boiler steels: Materials developments, properties and assessment,” in *Power Plant Life Management and Performance Improvement*, E. J. Oakey, Ed. Gliwice: Woodhead Publishing Limited, 2011, pp. 222–271.

[87] R. Janulionis, G. Dundulis, and Albertas Grybenas Ferritic-martensitic, “Numerical Research of Fracture Toughness of Aged,” *Metals (Basel).*, 2020.

[88] N. Saini, C. Pandey, M. Mohan, H. K. Narang, R. S. Mulik, and P. Kumar, “A comparative study of ductile-brittle transition behavior and fractography of P91 and P92 steel,” *Eng. Fail. Anal.*, vol. 81, no. March, pp. 245–253, 2017, doi: 10.1016/j.engfailanal.2017.06.044.

[89] J. Blach, L. Falat, and P. Ševc, “Fracture characteristics of thermally exposed 9Cr – 1Mo steel after tensile and impact testing at room temperature,” *Eng. Fail. Anal.*, vol. 16, no. 5, pp. 1397–1403, 2009, doi: 10.1016/j.engfailanal.2008.09.003.

[90] V. Sklenicka, K. Kucharova, M. Svobodova, P. Kral, M. Kvapilova, and J. Dvorak, “Materials Characterization The e ff ect of a prior short-term ageing on mechanical and creep properties of,” *Mater. Charact.*, vol. 136, no. January, pp. 388–397, 2018, doi: 10.1016/j.matchar.2018.01.008.

[91] Czyrska-Filemonowicz, P. J. Ennis, and A. Zielinska-Lipiec, “High Chromium Creep Resistant Steels for Modern Power Plant Applications,” in *Metallurgy on the Turn of the 20th Century”, Committee of for Metallurgy of the Polish Academy of Sciences*, 2016, no. November, pp. 193–217.

[92] Pradeep Suman and S. Pal, “Microstructure Degradation after Prolonged Exploitation of Heatresistant Steel 14mov6-3,” *Int. J. Mod. Eng. Res.*, vol. 4, no. 6, pp. 42–46, 2014, [Online]. Available: http://www.ijmer.com/papers/Vol4_Issue6/Version-7/IJMER-46074246.pdf.

[93] P. J. Ennis, “Recent advances in creep-resistant steels for power plant applications,” vol. 28, no. August, pp. 709–730, 2003.

[94] X. F. Chen, R. K. Nanstad, and T. Eric, “Fracture Toughness in Metals,” *Mater. Sci. Technol. Div. Oak Ridge Natl. Lab. TennTenn*, no. April, pp. 19–23, 2014.

[95] S. Zhu *et al.*, “Evaluation of mechanical properties for saw welded p91&p92 pipes,” 2018.

[96] A. Thomas, P. Seliger, and T. Hauke, “Materials at High Temperatures Material behaviour and plant experience of P91 / P92 components,” *Mater. High Temp.*, vol. 3409, p. 0, 2017, doi: 10.1080/09603409.2017.1316957.

[97] G. Sasikala and S. K. Ray, “Evaluation of quasistatic fracture toughness of a modified 9Cr-1Mo ( P91 ) steel,” *Mater. Sci. Eng.*, vol. 479, no. A, pp. 105–111, 2008, doi: 10.1016/j.msea.2007.06.021.

[98] P. Yan and Z. Liu, “Materials Science & Engineering A Toughness evolution of 9Cr – 3W – 3Co martensitic heat resistant steel during long time aging,” *Mater. Sci. Eng. A*, vol. 650, pp. 290–294, 2016, doi: 10.1016/j.msea.2015.09.115.

[99] T. Yamada, “Mechanical property and microstructural change by thermal aging of SCS14A cast duplex stainless steel,” vol. 350, pp. 47–55, 2006, doi: 10.1016/j.jnucmat.2005.11.008.

[100] J. M. Hallen and A. Albiter, “Degradation of impact fracture during accelerated ageing of weld metal on microalloyed steel,” vol. 7116, 2010, doi: 10.1080/09507110903568760.

[101] T. Sang, D. A. Collins, T. G. Lach, and E. L. Carter, “Degradation of impact toughness in cast stainless steels during long-term thermal aging,” *J. Nucl. Mater.*, vol. 542, p. 152524, 2020, doi: 10.1016/j.jnucmat.2020.152524.

[102] F. Hafeez and A. Husain, “Diminutive Specimen Test Techniques for Predicting Mechanical Behavior of Metals-A Review,” *Int. J. Res. Emerg. Sci. Technol.*, vol. 2, no. 5, 2015.

[103] A. Orlova and V. Sklenic, “Microstructural development during high temperature creep of 9 % Cr steel,” *Mater. Sci. Eng.*, vol. 245, no. A245, pp. 39–48, 1998.

[104] R. Viswanathan and J. Stringer, “Failure Mechanisms of High Temperature Components in Power Plants,” *J. ENGI_NEERING Mater. Technol.*, vol. 122, no. July, 2000.

[105] D. Renowicz and M. Cieśla, “Crack initiation in steel parts working in boilers and steam pipelines,” *J. Achiev. Mater. Manuf. Eng.*, vol. 21, no. 2, pp. 49–52, 2007.

[106] R. Ranjeeth, D. Aditya, A. Gautam, S. P. Singh, and S. Bhattacharya, “Failure investigation of a water-wall tube of fossil-fuel fired boiler,” *Eng. Fail. Anal.*, vol. 155, no. October 2023, p. 107727, 2024, doi: 10.1016/j.engfailanal.2023.107727.

[107] E. S. Kim, “Fracture analysis of tube boiler for physical explosion accident,” *Forensic Sci. Int.*, vol. 278, pp. e1–e7, 2017, doi: 10.1016/j.forsciint.2017.07.036.

[108] G. Golaski and P. Wieczorek, “Precipitation of carbides in Cr-Mo-V cast steel after service and regenerative heat treatment,” *Arch. FOUNDRY Eng.*, vol. 9, no. 1, pp. 97–102, 2009.

[109] J. Ćwiek, “Evaluation of microstructure and mechanical properties of a steam turbine casing after long-term service,” *Achiev. Mater. Manuf. Eng.*, vol. 49, no. 1, pp. 27–34, 2011.

[110] G. Gerzy Okrajni, Kazimierz Mutwil, MarekCieśla (Politechnika Śląska, “WYTĘŻENIE I TRWAŁOŚĆ RUROCIĄGÓW PAROWYCH,” *GÓRNICTWO Odkryw.*, pp. 75–77, 2006.

[111] J. Okrajni, K. Mutwil, and M. Cieśla, “Steam pipelines ’ effort and durability,” *J. Achiev. Mater. Manuf. Eng.*, vol. 22, no. 2, pp. 63–66, 2007.

[112] L. Han, Y. Deng, and C. Liu, “The determination of J IC for polyethylene pipe using non-standard arc-shaped specimen,” *Int. J. Press. Vessel. Pip.*, vol. 76, pp. 647–651, 1999.

[113] G. Chen, J. Liu, J. Wang, and T. Zhang, “Effect of high temperature aging on microstructure and mechanical properties of HR3C heat resistant steel,” *Energy Mater. Mater. Sci. Eng. Energy Syst.*, vol. 9, no. 2, pp. 205–210, 2014, doi: 10.1179/1743284713Y.0000000347.

[114] G. Golański, “Mechanical Properties of G17CrMoV5 – 10 Cast Steel after Regenerative Heat Mechanical Properties of G17CrMoV5 – 10 Cast Steel after Regenerative Heat Treatment,” *Solid State Phenomena,Trans Tech Publ. Switz.*, vol. 147–149, no. May, p. p 732-737, 2019,

doi: 10.4028/www.scientific.net/SSP.147-149.732.

[115] D. Hodži and I. Hajro, “IMPACT TOUGHNESS OF STEAMLINE MATERIAL 14MoV6-3 AFTER LONG-TERM EXPLOITATION,” in *14th International Research/Expert Conference. “Trends in the Development of Machinery and Associated Technology,”* 2010, vol. 3, no. September, pp. 129–132.

[116] E. S. Ameh and B. O. Onyekpe, “Effect of High Strength Steel Microstructure on Crack Tip Opening Displacement,” *Am. J. Eng. Res.*, vol. 78, no. 7, pp. 72–78, 2016.

[117] D. Hodži and Ismar Hajro, “MICROSTRUCTURE DEGRADATION AFTER PROLONGED EXPLOITATION OF HEAT RESISTANT STEEL 14MoV6-3,” in *16th International Research/Expert Conference ”Trends in the Development of Machinery and Associated Technology”*, 2012, no. September, pp. 10–12.

[118] J. Dobrza, *Materials science interpretation of the life of steels for power plants*, vol. 3. 2011.

[119] V. Sklenicka, K. Kucharova, M. Svobodova, P. Kral, M. Kvapilova, and J. Dvorak, “The effect of a prior short-term ageing on mechanical and creep properties of P92 steel,” *Mater. Charact.*, vol. 136, no. January, pp. 388–397, 2018, doi: 10.1016/j.matchar.2018.01.008.

[120] L. Shi, J. J. Yu, C. Y. Cui, and X. F. Sun, “Materials Science & Engineering A Microstructural stability and tensile properties of a Ti-containing single-crystal Co – Ni – Al – W-base alloy,” vol. 646, pp. 45–51, 2015, doi: 10.1016/j.msea.2015.08.044.

[121] I. Aguirre and I. Ferreira, “Experimental and Numerical Analysis for Se ( B ) and Se ( T ) J-Integral Fracture Toughness Testing,” *8th Int. Congr. Mech. Eng.*, no. 1, pp. 1–7, 2005.

[122] B. V. Farahani, P. J. Tavares, J. Belinha, and P. M. G. P. Moreira, “Compact tension fracture specimen: Experimental and computational implementations on stress intensity factor,” *J. Strain Anal. Eng. Des.*, vol. 53, no. 8, pp. 630–647, 2018, doi: 10.1177/0309324718763189.

[123] I. Ameli *et al.*, “Determination of CMOD-force curves and R-curves in side-grooved single edge notched tensile (SENT) specimens in welded X42 pipeline steel,” *Int. J. Press. Vessel. Pip.*, vol. 163, no. May, pp. 68–74, 2018, doi: 10.1016/j.ijpvp.2018.04.003.

[124] X. Pan, J. Huang, Z. Gan, S. Dong, and W. Hua, “Analysis of mixed-mode i/ii/iii fracture toughness based on a three-point bending sandstone specimen with an inclined crack,” *Appl. Sci.*, vol. 11, no. 4, pp. 1–25, 2021, doi: 10.3390/app11041652.

[125] R. Seifi and N. Omidvar, “Fatigue crack growth under mixed mode I+III loading,” *Mar. Struct.*, vol. 34, pp. 1–15, 2013, doi: 10.1016/j.marstruc.2013.07.001.

[126] Y. Wang, W. Wang, B. Zhang, and C. Li, “A review on mixed mode fracture of metals,” *Eng. Fract. Mech.*, vol. 235, no. May, p. 107126, 2020, doi: 10.1016/j.engfracmech.2020.107126.

[127] A. G. Paradkar and S. V Kamat, “Fracture toughness of Ti – 15Al – 8Nb alloy under mixed mode I / III loading,” *Mater. Sci. Eng. A*, vol. 528, no. 9, pp. 3283–3288, 2011, doi: 10.1016/j.msea.2011.01.014.

[128] L. Shi and S. O. Oyadiji, “Determination of notch stress intensity factors for V-notched specimens under mode I loading using the 3D-Digital image correlation and strain energy approach,” *Theor. Appl. Fract. Mech.*, vol. 130, no. December 2023, p. 104307, 2024, doi: 10.1016/j.tafmec.2024.104307.

[129] Z. Wei, X. Deng, M. A. Sutton, J. Yan, C. S. Cheng, and P. Zavattieri, “Modeling of mixed-mode crack growth in ductile thin sheets under combined in-plane and out-of-plane loading,” *Eng. Fract. Mech.*, vol. 78, no. 17, pp. 3082–3101, 2011, doi: 10.1016/j.engfracmech.2011.09.004.

[130] P. Jin, X. Wang, H. Chen, Z. Liu, and X. Chen, “Analysis of mixed-mode Compact-Tension-

Shear (CTS) specimens with slanted propagating cracks," *Theor. Appl. Fract. Mech.*, vol. 127, no. May, p. 104037, 2023, doi: 10.1016/j.tafmec.2023.104037.

[131] M. R. Molteno and T. H. Becker, "Mode I-III decomposition of the j-integral from DIC displacement data," 2015.

[132] B. Jordan, V. Grolleau, and D. Mohr, "Using surround DIC to extract true stress–strain curve from uniaxial tension experiments," *Int. J. Solids Struct.*, vol. 268, no. October 2022, p. 112171, 2023, doi: 10.1016/j.ijsolstr.2023.112171.

[133] K. Samadian, S. Hertelé, and W. De Waele, "Measurement of CTOD along a surface crack by means of digital image correlation," *Eng. Fract. Mech.*, vol. 205, no. July 2018, pp. 470–485, 2019, doi: 10.1016/j.engfracmech.2018.11.015.

[134] I. Aguirre and I. Ferreira, "Experimental and Numerical Analysis for Se ( B ) and Se ( T ) J-Integral Fracture Toughness Testing," in *8th International Congress of Mechanical Engineering*, 2005, no. 1, pp. 1–7.

[135] H. Schreier, J. J. Orteu, and M. A. Sutton, *Image correlation for shape, motion and deformation measurements: Basic concepts, theory and applications*. Springer Science & Business Media., 2009.

[136] B. Zhang, W. Wang, H. Lei, X. Hu, and C. Q. Li, "Performance of digital image correction technique for mild steel with different strain hardening effects," *Theoretical and Applied Fracture Mechanics*, vol. 130. 2024, doi: 10.1016/j.tafmec.2024.104253.

[137] J. P. H. and R. M. S.V. Kamat, "COMBINED MODE I - MODE III FRACTURE TOUGHNESS OF ALUMINA PARTICULATE_REINFORCED ALUMINUM ALLOY-MATRIX COMPOSITES," *Scr. Metall.*, vol. 23, no. 58, pp. 523–528, 1989, [Online]. Available: https://www.unhcr.org/publications/manuals/4d9352319/unhcr-protection-training-manual-european-border-entry-officials-2-legal.html?query=excom 1989.

[138] ISO, *Metallic materials — Unified method of test for the determination of quasistatic fracture toughness*, vol. 2. 2016.

[139] B. V. Farahani, F. Q. de Melo, P. Tavares, and P. Moreira, "A fracture study of slanted cracks using the stress dead-zone hypothesis," *Fatigue Fract. Eng. Mater. Struct.*, vol. 43, no. 12, pp. 3012–3026, 2020, doi: 10.1111/ffe.13305.

[140] S. D. Pastrama, P. M. G. P. Moreira, P. M. S. T. Castro, and G. Jiga, "An Overdeterministic Algorithm for Stress Intensity Factor Calculation," *11th Port. Conf. Fract.*, no. February 2016, 2008.

[141] V. Richter-Trummer, P. M. G. P. Moreira, S. D. Pastrama, M. A. P. Vaz, and P. M. S. T. De Castro, "Methodology for in situ stress intensity factor determination on cracked structures by digital image correlation," *Int. J. Struct. Integr.*, vol. 1, no. 4, pp. 344–357, 2010, doi: 10.1108/17579861011099178.

[142] B. V. Farahani, P. J. Tavares, P. M. G. P. Moreira, and J. Belinha, "Stress intensity factor calculation through thermoelastic stress analysis, finite element and RPIM meshless method," *Eng. Fract. Mech.*, vol. 183, pp. 66–78, 2017, doi: 10.1016/j.engfracmech.2017.04.027.

[143] T. V. S. Chong, S. B. Kumar, M. O. Lai, and W. L. Loh, "Fracture capacity of modern pipeline girth welds with 3D surface cracks under extreme operating conditions," *Eng. Fract. Mech.*, vol. 146, pp. 139–160, 2015, doi: 10.1016/j.engfracmech.2015.07.032.

[144] M. Paredes, D. F. B. Sarzosa, R. Savioli, T. Wierzbicki, D. Y. Jeong, and D. C. Tyrell, "Ductile tearing analysis of TC128 tank car steel under mode I loading condition," *Theor. Appl. Fract. Mech.*, vol. 96, no. April 2017, pp. 658–675, 2018, doi:

10.1016/j.tafmec.2017.10.006.

[145] G. Murali, S. R. Abid, K. Al-Lami, N. I. Vatin, S. Dixit, and R. Fediuk, “Pure and mixed-mode (I/III) fracture toughness of preplaced aggregate fibrous concrete and slurry infiltrated fibre concrete and hybrid combination comprising nano carbon tubes,” *Constr. Build. Mater.*, vol. 362, no. June 2022, p. 129696, 2023, doi: 10.1016/j.conbuildmat.2022.129696.

[146] S. V. Kamat, M. Srinivas, and P. R. Rao, “Effect of temperature on the mode I and mixed mode I/III fracture toughness of SA333 steel,” *Mater. Sci. Eng. A*, vol. 528, no. 12, pp. 4141–4146, 2011, doi: 10.1016/j.msea.2011.01.117.

[147] Z. Shi *et al.*, “Acoustic emission and fracture morphology characteristics of thermal-damage granite under mixed mode I/III loading,” *Theor. Appl. Fract. Mech.*, vol. 133, no. PA, p. 104524, 2024, doi: 10.1016/j.tafmec.2024.104524.

[148] P. Miarka, A. S. Cruces, P. Lopez-Crespo, and W. De Corte, “Fracture process zone development and length assessment under the mixed-mode I/II load analysed by digital image correlation technique,” *Cem. Concr. Res.*, vol. 173, no. September 2022, p. 107261, 2023, doi: 10.1016/j.cemconres.2023.107261.

[149] K. Prasad, M. Srinivas, and S. V. Kamat, “Influence of mixed mode I/III loading on dynamic fracture toughness of mild steel at room and low temperatures,” *Mater. Sci. Eng. A*, vol. 590, pp. 54–59, 2014, doi: 10.1016/j.msea.2013.09.099.

[150] J. H. Yan, M. A. Sutton, X. Deng, Z. Wei, and P. Zavattieri, “Mixed-mode crack growth in ductile thin-sheet materials under combined in-plane and out-of-plane loading,” *Int. J. Fract.*, vol. 160, no. 2, pp. 169–188, 2009, doi: 10.1007/s10704-009-9420-x.

[151] M. L. Williams, “The bending stress distribution at the base of a stationary crack,” *J. Appl. Mech. Trans. ASME*, vol. 28, no. 1, pp. 78–82, 1960, doi: 10.1115/1.3640470.

[152] V. Gangwar, P. Basu, S. K. Acharyya, S. Dhar, S. Chakraborty, and A. Banerjee, “Dynamic deformation and fracture surface investigation of rolled homogenous armor steel through Charpy impact testing,” *Theor. Appl. Fract. Mech.*, vol. 133, no. PA, p. 104592, 2024, doi: 10.1016/j.tafmec.2024.104592.

[153] A. Królicka, D. Rozumek, G. Lesiuk, R. Kuziak, K. Radwański, and F. G. Caballero, “Fatigue crack growth rate under mixed-mode loading conditions (I+III) of a carbide-free bainitic steel designed for rail applications,” *Theor. Appl. Fract. Mech.*, vol. 134, no. February, 2024, doi: 10.1016/j.tafmec.2024.104683.

[154] D. R. H. Jones, “Creep failures of overheated boiler , superheater and reformer tubes,” *Eng. Fail. Anal.*, vol. 11, pp. 873–893, 2004, doi: 10.1016/j.engfailanal.2004.03.001.

[155] I. Dzioba, M. Gajewski, and A. Neimitz, “Studies of fracture processes in Cr e Mo e V ferritic steel with various types of microstructures,” *Int. J. Press. Vessel. Pip.*, vol. 87, no. 10, pp. 575–586, 2010, doi: 10.1016/j.ijpvp.2010.07.012.

[156] A. Maksimović, L. Milović, S. Bulatović, B. Z. E. Čević, A. Maksimović, and V. Aleksić, “Effect of temperature and specimen orientation on Charpy impact Effect of temperature and specimen orientation on Charpy impact toughness toughness,” *Procedia Struct. Integr.*, vol. 42, no. 2019, pp. 1475–1482, 2022, doi: 10.1016/j.prostr.2022.12.188.

[157] B. Aleksić, A. Grbović, L. Milović, A. Hemer, and V. Aleksić, “Numerical simulation of fatigue crack propagation : A case study of defected steam pipeline,” *Eng. Fail. Anal.*, vol. 106, no. March, p. 104165, 2019, doi: 10.1016/j.engfailanal.2019.104165.

[158] S. Cravero and C. Ruggieri, “Estimation procedure of J -resistance curves for SE ( T ) fracture specimens using unloading compliance,” *Eng. Fract. Mech.*, vol. 74, pp. 2735–2757, 2007, doi: 10.1016/j.engfracmech.2007.01.012.

[159] Tadeusz Jóźwik, “Effect of Austenitising on The Structure and Properties of Low-Alloy Cr-Mo-V Steels After Long-Term Operation In Creep Conditions for The Power Industry,” *Pr. Inst. Metal. Żelaza*, vol. 70, no. 2, pp. 2–18, 2018, doi: 10.32730/imz.0137-9941.18.2.01.

[160] M. Jakubowska, A. Wrobel, W. Manaj, and A. Sypien, “Degradation of microstructure and strength properties of heat-resistant steels operating under variable loads.,” *Int. J. Press. Vessel. Pip.*, p. 104916, 2023, doi: 10.1016/j.ijpvp.2023.104916.

[161] I. Čamagić, S. A. Sedmak, A. Sedmak, Z. Burzić, and M. Aranđelović, “The impact of the temperature and exploitation time on the tensile properties and plain strain fracture toughness, KIc in characteristic areas of welded joint,” *Frat. ed Integrita Strutt.*, vol. 12, no. 46, pp. 371–382, 2018, doi: 10.3221/IGF-ESIS.46.34.

[162] A. Dedov, “Assessment of Metal Condition and Remaining Life of In-service Power Plant Components Operating at High Temperature,” TALLINN UNIVERSITY OF TECHNOLOGY, 2007.

[163] ASTM E8/E8M − 13a, *Standard Test Methods for Tension Testing of Metallic Materials 1*. USA, 2013.

[164] M. A. Verstraete, W. De Waele, R. M. Denys, K. Van Minnebruggen, and S. Hertelé, “Constraint analysis of defects in strength mismatched girth welds of ( pressurized ) pipe and Curved Wide Plate tensile test specimens,” *Eng. Fract. Mech.*, vol. 131, pp. 128–141, 2014, doi: 10.1016/j.engfracmech.2014.07.018.

[165] G. Shen, J. A. Gianetto, and W. R. Tyson, “Measurement of J-R Curves Using Single-Specimen Technique on Clamped SE ( T ) Specimens,” in *Proceedings of the Nineteenth (2009) International Offshore and Polar Engineering Conference*, 2009, vol. 1, p. 880653.

[166] Y. Huang and W. Zhou, “Effects of crack front curvature on J-R curve testing using clamped SE(T) specimens of homogeneous materials,” *Int. J. Press. Vessel. Pip.*, vol. 134, pp. 112–127, 2015, doi: 10.1016/j.ijpvp.2015.05.001.

[167] European Commitee for Standardization, “EN 10216-2 Seamless steel tubes for pressure puropses - Technical delivery conditions - Part 2: Non-alloy and alloy steel tubes with specified elevated temperature properties,” 2002.

[168] A. Zieliński and J. Dobrzański, “Material properties and structure of thick-walled elements made of steel 7CrMoVTiB10-10 after long-term annealing,” *Arch. Mater. Sci. Eng.*, vol. 58, no. 1, pp. 5–12, 2012.

[169] J. Ćwiek, J. Łabanowski, and S. Topolska, “The effect of long-term service at elevated temperatures on structure and mechanical properties of Cr-Mo-V steel,” *Arch. Mater. Sci. Eng.*, vol. 49, no. 1, pp. 33–39, 2011.

[170] I. C. -Alagic, N. G. B, M. R. C, Z. C. C, and K. G. D, “Microstructural morphology effects on fracture resistance and crack tip strain distribution in Ti–6Al–4V alloy for orthopedic implant,” *Mater. Des.*, vol. 53, pp. 870–880, 2014.

[171] I. Dzioba, S. Lipiec, I. Dzioba, and S. Lipiec, “Evolution of the mechanical fields and fracture process of S355JR steel and fracture process Evolution of the mechanical fields of S355JR steel,” *Procedia Struct. Integr.*, vol. 16, pp. 97–104, 2019, doi: 10.1016/j.prostr.2019.07.027.

[172] M. Díaz-Cruz *et al.*, “Study of the Effect of Isothermal Aging on API 5L Grade B Steel Through Charpy Energy Testing and Electrochemical Evaluation,” *Arab. J. Sci. Eng.*, vol. 48, no. 12, pp. 16607–16622, 2023, doi: 10.1007/s13369-023-07804-x.

[173] V. Sklenicka, K. Kucharova, M. Svobodova, P. Kral, M. Kvapilova, and J. Dvorak, “The effect of a prior short-term ageing on mechanical and creep properties of P92 steel,” *Mater.*

*Charact.*, vol. 136, no. October 2017, pp. 388–397, 2018, doi: 10.1016/j.matchar.2018.01.008.

[174] M. E. A. El-azim *et al.*, “Creep fracture mechanism in welded joints of P91 steel Creep fracture mechanism in welded joints of P91 steel,” vol. 0836, 2013, doi: 10.1179/1743284713Y.0000000233.

[175] K. Sankhala, Z. Gauri, P. Sharma, and D. Kumar, “Study of Microstructure Degradation of Boiler Tubes Due To Creep for Remaining Life Analysis,” *Int. J. Eng. Res. Appl.*, vol. 4, no. 7, pp. 93–99, 2014.

[176] M. Négyesi, M. Kraus, V. Mareš, D. Kwon, and B. Strnadel, “Creep damaged microstructure and mechanical properties of Cr–Mo–V steel subjected to long-term service exposures,” *Int. J. Press. Vessel. Pip.*, vol. 206, no. July, 2023, doi: 10.1016/j.ijpvp.2023.105085.

[177] W. Zhang, T. Zhang, X. Wang, H. Chen, and J. Gong, “Remaining creep properties and fracture behaviour of P92 steel welded joint under prior low cycle,” *Integr. Med. Res.*, vol. 9, no. 4, pp. 7887–7899, 2020, doi: 10.1016/j.jmrt.2020.05.078.

[178] J. Piątkowski, B. Gajdzik, and A. Mesjasz, “Assessment of material durability of steam pipelines based on statistical analysis of strength properties - Selected models,” *Energies*, vol. 13, no. 14, 2020, doi: 10.3390/en13143633.

[179] S. Khayatzadeh, D. W. J. Tanner, C. E. Truman, P. E. J. Flewitt, and D. J. Smith, “Materials Science & Engineering A In fl uence of thermal ageing on the creep behaviour of a P92 martensitic steel,” *Mater. Sci. Eng. A*, vol. 708, no. August, pp. 544–555, 2017, doi: 10.1016/j.msea.2017.10.025.

[180] M. M. De Oliveira, A. A. Couto, G. F. C. Almeida, D. A. P. Reis, N. B. De Lima, and R. Baldan, “metals Mechanical Behavior of Inconel 625 at Elevated Temperatures,” doi: 10.3390/met9030301.

[181] G. Tian *et al.*, “Effect of long-term aging on the microstructure evolution and fracture mechanism of 9% Cr steels,” *Mater. Sci. Eng. A*, vol. 893, no. January, p. 146133, 2024, doi: 10.1016/j.msea.2024.146133.

[182] G. Pantazopoulos, A. Toulfatzis, A. Vazdirvanidis, and A. Rikos, “Analysis of the Degradation Process of Structural Steel Component Subjected to Prolonged Thermal Exposure,” *Metallogr. Microstruct. Anal.*, vol. 5, no. 2, pp. 149–156, 2016, doi: 10.1007/s13632-016-0273-1.

[183] Q. Guo, F. Lu, X. Liu, R. Yang, H. Cui, and Y. Gao, “Correlation of microstructure and fracture toughness of advanced 9Cr/CrMoV dissimilarly welded joint,” *Mater. Sci. Eng. A*, vol. 638, pp. 240–250, 2015, doi: 10.1016/j.msea.2015.04.011.

# APPENDIX: LIST OF PUBLICATIONS

## Publications

B. K. Kipsang, K. Wacławiak, and W. De Waele, "Implementation of Recent Advances in Fracture Toughness Testing to Investigate Tearing Resistance of Heat-Resistant Steel 14MoV6-3," *Arch. Met. Mater.*, vol. 70, no. 1, pp. 317–324, 2025.

K. Wacławiak, B. Kipsang, B. V. Farahani, and W. De Waele, "Experimental and numerical assessment of fracture toughness variations in steam boiler components after a long period of operation," *Int. J. Press. Vessel. Pip.*, vol. 209, May, 2024, doi: 10.1016/j.ijpvp.2024.105198.

Kipsang, B.K., & Wacławiak, K. (2023). Fracture toughness test methods and specimens: a comparative review of recent progress. In B. Balon (Ed.), Interdisciplinary research of young scientists (No. 987; pp. 232–247). Silesian University of Technology Publishing House. https://repolis.bg.polsl.pl/dlibra/publication/86320/edition/76772/content

## Conference Presentations

Kipsang, B. K., Farahani, B. F., Wacławiak, K., & de Waele, W. (2024). Investigation of influence of crack angle on mixed mode I/III fracture of power steel using 3D-digital image correlation. In A. Katunin (Ed.), Young Science Beyond Borders 2024 (p. 36). Polish Academy of Sciences. https://amu.pan.pl/ysbb/wp-content/uploads/sites/3/2024/12/YSBB2024-book-of-abstracts.pdf

Benard Kipsang, Behzad V. Farahani, Krzysztof Wacławiak, Wim De Waele, Investigation on Fracture Characteristics of 14MoV6-3 Power Plant Steel Under Mixed Mode I/III Loading Using 3D Digital Image Correlation, XXII International Scientific and Technical Conference on Design, Renovation Innovations and Modernization in the Energy Sector – (PIRE) 2024, Ustroń Poland

Benard Kipsang, Krzysztof Wacławiak, Wim De Waele,(2023) Effect of Accelerated Creep Aging on Ductile Tearing Resistance of 14MoV6-3 Steel , (Projektowanie, Innowacje i Remonty w Energetyce - Design, Innovation, Repair in Power Industry (PIRE), 2023, Ustron, Poland.